NASA Contractor Report 175024

A Numerical and Experimental Investigation of Electrothermal Aircraft Deicing

Kevin L. Leffel
The University of Toledo
Toledo, Ohio

January 1986

Prepared for
Lewis Research Center
Under Grant NAG 3-72

National Aeronautics and
Space Administration

SUMMARY

This study was composed of three parts. The first part involved the extension of an existing transient two-dimensional numerical code for an electrothermal deicer so that it would simulate the situation where a variable thickness ice layer existed at the outer surface. The Enthalpy Method was used to simulate the phase change, and Gauss-Seidel iteration was used to solve the resulting system of finite difference equations. A set of criteria were developed for determining when a variable thickness ice layer had an effect on deicer performance.

The second part of this study was the acquisition and analysis of experimental data. The test model consisted of a section of a Bell UH-1H helicopter blade equipped with an electrothermal deicer manufactured by the B. F. Goodrich Company. A total of fifty-two thermocouples were utilized to document the thermal response of the blade and deicer assembly. The tests were conducted in the Icing Research Tunnel at the NASA Lewis Research Center, and consisted of four phases: dry air tests; wet air tests; ice accretion tests; and deicing tests. A total of two hundred and eleven tests were run, from which ten readings, five dry runs and five deicing runs, were selected for further analysis. This re-

duced set of data were examined for thermocouple response consistency and, within experimental error, the thermocouple readings were found to be independent of the three cross-sections on the blade where measurements were taken. The dry run temperature responses at the abrasion shield showed test independence when correlated as $\Delta T/(\Delta T)_{avg}$ versus position. This was not true for the deicing runs. For both the dry and the deicing runs, the heater response, when correlated in the same manner, showed test independence for all ten runs. This behavior was a physical characteristic of the blade. In contrast, the response of the D-spar thermocouples was found to be almost entirely independent of position within each test. In the deicing runs, the experimental temperature response data clearly showed when melting, shedding or refreezing occurred. These tests illustrated that the criterion for shedding in the three cases where it did occur was that the abrasion shield interface temperature was 32-34°F.

The third part of this study concerned the validation of a one-dimensional transient thermal model of an electrothermal deicer by comparison of the predictions with the experimental data. The physical properties and the geometry of the test model were determined and used as input in the numerical simulation. Flat plate and cylindrical correlations were used to calculate the outer surface convection coefficients for both the dry and the deicing runs. The Enthalpy

Method was found to effectively model the phase change which occurred, and the ice shedding algorithm employed in the simulation was also evaluated. In general, the one-dimensional code showed good comparison with the experimental data, with the comparisons being better at the higher free-stream temperatures. The code definitely contains sufficient physical information so as to adequately model the thermal response of an electrothermal deicer assembly at positions where two-dimensional effects are small.

CONTENTS

A NUMERICAL AND EXPERIMENTAL INVESTIGATION OF ELECTROTHERMAL AIRCRAFT DEICING

PART I

INTRODUCTION

Ice accretion on aircraft components during flight has long been recognized as a serious aviation hazard. The presence of the ice decreases lift and increases drag, as well as increasing fuel and power requirements. Military and commercial aircraft that are not protected cannot fly in icing conditions. As a result, there is a continuing need for the development of systems that either prevent the ice from forming or remove it after accretion.

Preventing the formation of ice is known as anti-icing, while allowing it to form and then removing it is known as deicing. There are several ways of achieving either goal,

but some methods are better than others depending upon the particular application. The main thrust of the present work concerns the analysis of electrothermal deicing systems as applied to helicopter blades. As will soon become apparent, there are some limitations peculiar to this application that predicate a certain type of system. But first, a brief overview of the different anti-icing and deicing methods available is in order.

There are two commonly used types of anti-icing systems, chemical and thermal. Chemical systems use a freezing point depressant much like an antifreeze. The chemical is spread over the area to be protected, thereby lowering the freezing point and preventing ice accretion. This method is limited because of the difficulty encountered in maintaining a uniform distribution of the chemical over the surface. There is also a reservoir that frequently needs to be refilled, and holes used to transmit the antifreeze to the surface may become plugged. As a result, chemical systems are used mostly for windshield protection.

Thermal anti-icing prevents ice accretion by raising the surface temperature above the freezing temperature. Generally this is accomplished by passing hot compressed air through passages beneath the area to be protected. Energy requirements are quite high to achieve this. However, jet aircraft usually utilize this method because an ample supply

of hot compressed air may be bled from the first compressor stage of the engine.

Three types of deicing systems worthy of mention are: pneumatic boots, electromechanical impulse and electrothermal heating. A pneumatic boot is made of a flexible rubberlike material that is laminated to the area to be deiced. It is inflated like a ballon with compressed air, which mechanically breaks the ice from the surface. Boots are relatively simple and efficient, but they increase drag and require frequent maintenance to insure reliability.

Electromechanical impulse is a new method still in development. A series of electromagnets are pulsed in cycles, flexing a metal abrasion shield and thereby mechanically cracking off the ice. This method appears to be extremely energy efficient, but it has not yet been applied to helicopter blades because it is still in the developmental stage.

Electrothermal deicing uses electric heaters laminated to the area to be protected. Dynamic forces remove the ice after its adhesion to the blade surface is destroyed by melting a thin layer of ice next to the surface. The heaters may be cycled to reduce energy requirements. This method was first applied to deice propellers and lends itself particularly well to rotary wing aircraft.

Helicopters use electrothermal deicing exclusively to protect the blades. Using pneumatic boots on helicopters is still in the experimental stage. However, some success has been achieved, and boots may become commercially available in the near future. Electromechanical impulse is still in development and has not been applied to helicopters. At this time, electrothermal is the most advantageous method available to deice helicopter blades.

Electrothermal deicers are assembled in a composite construction. A wide variety of materials may be used but some are better suited than others. Baliga [1] and Stallabrass [2] have examined the effects of different materials and thicknesses. A typical example is shown in Figure 1 and consists of:

1. Substrate - This is actually the aircraft blade and can be made of many different types of materials. An aluminum alloy is considered here;
2. An inner layer of insulation - This is necessary to provide both thermal and electrical insulation. Resin impregnated cloth is commonly used for this purpose. A thickness of 0.01 to 0.02 inches is necessary to fulfill electrical insulation requirements;
3. Heater element - Woven mats or metal ribbons are used. Woven mats have thicknesses as great as 0.02 inches. Ribbons range from 0.001 to 0.005 inches in thickness. The individual elements are 0.5 to 1.0 inches wide;

4. Outer insulation - Good electrical insulators are usually poor conductors of heat. As a result the inner insulation has to be thicker than the outer insulation in order to direct most of the heat outward. A ratio of at least 2:1 has been recommended by Stallabrass; and
5. Abrasion Shield - This is necessary to protect the heater and insulation from the environment. Stainless steel is often used, ranging from 0.01 to 0.02 inches in thickness. Its high thermal conductivity serves to transmit heat laterally and reduce the effect of nonuniformities in heater output.

A major difficulty with this type of construction results from imperfect bonding between layers. Great care must be taken during the lamination process in order to prevent air gaps. However, small gaps usually do exist which inhibit the rate at which heat is transferred and, therefore, impede deicer performance.

Another difficulty that decreases performance is nonuniformity in heater output. Gaps exist between the heater elements in order to provide electrical insulation. These gaps are about 0.08 inches wide for woven mats and 0.04 inches wide for metal ribbons. These heater gaps cause hot and cold spots to occur at the abrasion shield-ice interface, which delays melting and subsequent shedding of the ice.

There are many factors that affect the design of electrothermal deicers. A combination of experimental data and analytical analysis is thought to be necessary in order to understand the physics occurring during the deicing process, and thus to be able to make recomendations concerning deicer design.

The first objective of the present study involved the incorporation of a variable ice thickness algorithm into an existing computer model. The second objective was the obtainment of experimental deicing data using the NASA Lewis Icing Research Tunnel. Finally, the third objective was to compare the experimental data with the heat transfer models developed by Baliga [1], Marano [3], and Chao [4] in order to determine the value of these models for use in electrothermal deicer design.

PART II

A SOLUTION TO THE VARIABLE ICE THICKNESS PROBLEM

Chapter 1

LITERATURE REVIEW

1.1 ANALYTICAL HISTORY

An analytical approach to the phase change problem was first proposed by Stefan (1889). Stefan dealt with the transition from solid to liquid or liquid to solid. These types of phase change problems are classically referred to as Stefan problems but are also known as ablation problems.

Arpaci [5] has formulated the classical ablation problem which involves a nonlinear boundary condition at the moving solid-liquid interface. This nonlinear equation at the interface complicates the problem immensely and makes an analytical solution very difficult. Reference [6] presents an extensive review of most of the analytical and numerical techniques used for phase change analysis.

Predicting temperatures in composite bodies is almost as formidable as the ablation problem. A Laplace Transform technique proposed by Carslaw and Jaeger [7] is effective for one or two layers. Finding the inverse transform is difficult for more than two layers. Campbell [8] proposed a method that uses an analogy between heat flow and the trans-

mission of electricity along a power line. Stallabrass [2] incorporated this method in verifying the accuracy of his numerical technique.

Chao [4] provides a more complete summary of the analytical techniques available for ablation problems and composite bodies. All of these methods are rendered impractical by the large number of calculations required for each temperature. The capacity of computers for executing large numbers of calculations inexpensively and efficiently makes them ideal tools for solving phase change and composite body problems.

1.2 NUMERICAL HISTORY

Recent interest in the electrothermal deicer problem has generated several numerical models. One-dimensional models were proposed by Stallabrass [2], Baliga [1] and Marano [3], and two-dimensional models have been developed by Stallabrass [2] and Chao [4]. All of the models consider phase change and use finite difference techniques.

Finite differencing is an approximate technique for solving boundary value problems. Carnahan, Luther and Wilkes [9] discuss the various differencing methods that are commonly used and their advantages and disadvantages. The finite difference method discretizes the continuous time and space domains into a grid of nodes. A system of difference

equations based on this grid replaces the governing differential equations and boundary conditions. This system of equations can be solved for a particular node at any point in time and space. Accuracy depends upon the particular solution method used and the grid spacing.

There are two basic classes of finite difference techniques: explicit and implicit. The explicit method uses only nodal values from the previous time step in the finite difference equations. A distinct advantage to this method is that the resulting set of equations can be solved directly for the nodal values at the present time step, without the use of inversion or iteration procedures. This reduces the total number of computations and saves on computer time. Explicit methods do not, however, guarantee convergence. The increments in time and space must satisfy the following equation: $\alpha\Delta t/(\Delta x)^2<1/2$, were α is the thermal diffusivity, and Δt and Δx are the time and space increments, respectively. This convergence criterion forces a time step of 0.001 seconds or less, which increases the number of calculations needed. Stallabrass [2] and Gent and Cansdale [10] used an explicit algorithm scheme which was forward differenced in time and central differenced in space. The truncation error for this method was first order in time and second order in space.

Implicit methods use nodal values from the present time step as well as from the previous time step. This forms a system of equations that must be either inverted or solved by iteration at each time step. An advantage of the implicit method is its unconditional stability, which allows a time step as large as 0.1 seconds. The governing energy equation for electrothermal analysis is a parabolic partial differential equation. Von Rosenberg [11] indicated that the Crank-Nicolson implicit method is the preferred method for this type of differential equation. The truncation error for this method is second order correct in both time and space. Baliga [1], Marano [3] and Chao [4] all employed the Crank-Nicolson implicit finite difference technique in their simulations.

Several numerical methods have been proposed for handling the phase change. Baliga [1] used a technique suggested by Bonacina et al. [12]. This approach modeled the latent heat effect with a large change in heat capacity over a small temperature interval around the melting point. The thermal conductivity was varied linearly over the interval. Stallabrass [2] accounted for the phase change by holding a node at the melting point until enough energy had been transferred to completely melt the nodal volume. Marano [3] and Chao [4] used the enthalpy method which is also known as the weak solution method. These methods to simulate the phase change are comparable, but the enthalpy method is preferred

because of its formalism and the ease with which it is applied. The enthalpy method is used in the present study and has been employed in a variety of problems in the recent literature [6,13,14,15,16].

The enthalpy method uses the conservation of energy equation formulated in terms of two dependent variables, temperature and enthalpy. Predicting the location of the solid-liquid interface is not required because this is determined by nodal enthalpy alone. The temperature at any node can be calculated from the known enthalpy-temperature relationship. This method requires the use of Gauss-Seidel iteration to solve the resulting set of difference equations. The equivalence of this method and the classical formulation of the ablation problem was proven by Atthey [14].

Temperatures predicted by the enthalpy method tend to oscillate about the true values once melting has started. This occurs because a node is held at the melting point for a finite period of time until the nodal volume melts. The techniques used by Stallabrass [2] and Baliga [1] also exhibit this phenomenon. Voller and Cross [13,16] have pointed out that this leads to unrealistic results and they have developed a criterion for deriving the true temperatures from the oscillating values using the nodal enthalpy. This criterion is discussed in the Appendix.

Chapter 2

FORMULATION OF THE NUMERICAL METHOD

2.1 METHOD OF APPROXIMATING THE VARIABLE ICE THICKNESS

The previously mentioned two-dimensional numerical simulation code developed by Chao [4] has the restriction of a constant ice layer thickness. In order to simulate blade sections that have variable ice layer thicknesses, a staircase approach was used in the present study.

This staircase approach approximates the ice shape with a series of discrete rectangular nodes. The x and y directions are discretized into dx and dy segments. If the ice-ambient interface passes above the centroid of a node, the node is added to the ice shape. If the interface passes below the centroid of a node, the node is not included. In this manner, a rough approximation of the ice shape is formed, as shown in Figure 2. This approximation may be improved by further decreasing the sizes of dx and dy. Ice accretion shapes usually have a rough surface that can be approximated rather naturally using this approach. It is also simple and easy to apply.

2.2 GOVERNING EQUATIONS AND BOUNDARY CONDITIONS

The assumptions made in formulating the mathematical model are:

1. The thermal and physical properties of the material composing each layer of the blade are different, but do not depend on temperature;
2. The ambient temperature, blade air temperature and all heat transfer coefficients are constant;
3. There is perfect thermal contact between each layer; and
4. The density change due to melting is negligible. In other words, the effect of the volume contraction of the ice as it melts is neglected.

Using these assumptions, the governing two-dimensional heat transfer equation can be reduced to:

$$\rho_j \bar{C}_{pj} \frac{\partial T_j}{\partial t} = K_j \left(\frac{\partial^2 T_j}{\partial x^2} + \frac{\partial^2 T_j}{\partial y^2} \right) + q_j \qquad (1)$$

where j represents the layer in question, as given by

j = 1: blade or substrate

j = 2: lower or inner insulation

j = 3: heater

j = 4: upper or outer insulation

j = 5: abrasion shield

and where

ρ_j = density of the j^{th} layer;

$\hat{C}_{pj}$ = specific heat capacity of the j^{th} layer;

T_j = temperature in the j^{th} layer;

K_j = thermal conductivity of the j^{th} layer;

q_j = rate of heat generation per unit volume of the j^{th} layer;

t = time variable; and

x,y = space coordinates.

The heat generation term, q_j, is zero for all layers except for the heater, where it becomes a function of time, $q_3(t)$.

A slightly different approach must be used for the ice layer (j = 6). The physical properties change as the ice melts. Because of this, the thermal conductivity, K_6, must be included within the first partial time derivative. The governing differential energy equation becomes:

$$\rho_6 \hat{C}_{p6} \frac{\partial T_6}{\partial T} = \frac{\partial}{\partial x}\left\{K_6 \frac{\partial T_6}{\partial x}\right\} + \frac{\partial}{\partial y}\left\{K_6 \frac{\partial T_6}{\partial y}\right\} \qquad (2)$$

At this point, it is advantageous to replace $\rho_6 \hat{C}_{p6} T_6$ with H_6, representing the enthalpy at positions within the ice layer. Carrying out this operation on equation (2):

$$\frac{\partial H_6}{\partial t} = \frac{\partial}{\partial x}\left(K_6 \frac{\partial T_6}{\partial x}\right) + \frac{\partial}{\partial y}\left(K_6 \frac{\partial T_6}{\partial y}\right) \qquad (3)$$

where

H_6 = enthalpy per unit volume within the ice-water layer;

T_6 = temperature within the ice-water layer; and

K_6 = thermal conductivity within the ice-water layer.

This equation is the governing equation for the enthalpy method. It can be used to solve for the temperature at any point within the ice layer. Enthalpy can be related to temperature using the following relationships:

$$H_6 = \begin{cases} \rho_s \hat{C}_{ps} T_6 & , T_6 < T_m \\ \\ \rho_l \hat{C}_{pl} (T_6 - T_m) + \rho_l (\hat{C}_{ps} T_m + L_f), & T_6 > T_m \end{cases} \quad (4)$$

where

ρ_s, $\hat{C}_{ps}$ = physical properties of the solid phase;

ρ_l, $\hat{C}_{pl}$ = physical properties of the liquid phase;

T_m = melting temperature; and

L_f = latent heat of fusion per unit mass.

Inverting equation (4) yields:

$$T_6 = \begin{cases} H_6/\rho_s \hat{C}_{ps} & , H_6 \leq H_{sm} \\ T_m & , H_{sm} < H_6 < H_{lm} \\ (H_6 - H_{lm})/\rho_l \hat{C}_{pl} + T_m & , H_6 \geq H_{lm} \end{cases} \quad (5)$$

with

$$\begin{aligned} H_{sm} &= \rho_s \hat{C}_{ps} T_m \\ H_{lm} &= \rho_l (\hat{C}_{ps} T_m + L_f) \end{aligned} \quad (6)$$

where H_{sm} and H_{lm} are the melting point enthalpies of ice and water, respectively.

The boundary conditions at the layer interfaces, inner ambient surface, and outer ambient surface are listed below.

1. At the interfaces between the layers, the temperature and heat fluxes are continuous:

$$T_j|_I = T_{j+1}|_I \qquad j = 1, \ldots, 5$$

$$-K_j \frac{\partial T_j}{\partial y_j}\bigg|_I = -K_{j+1} \frac{\partial T_{j+1}}{\partial y_{j+1}}\bigg|_I \qquad j = 1, \ldots, 5 \tag{7}$$

where I denotes the interface.

2. Newton's law of cooling is used at the inner surface-ambient and outer surface-ambient interfaces. For the lower or inner boundary:

$$K_j \frac{\partial T_j}{\partial y_j}\bigg|_1 = h_{b1} (T_j|_1 - T_{b1}), \quad j = 1 \tag{8}$$

where

h_{b1} = lower boundary convective heat transfer coefficient;

T_{b1} = lower ambient (blade air) temperature;

and the subscript, 1, denotes the lower surface. Correspondingly, for the upper or outer boundary:

$$-K_j \frac{\partial T_j}{\partial y_j}\bigg|_2 = h_{b2} (T_j|_2 - T_{b2}), \quad j = 6$$

where

h_{b2} = upper boundary heat transfer coefficient;

T_{b2} = upper surface (external flow) ambient temperature;

and the subscript 2 denotes the upper surface.

If there is a variable thickness ice shape at the upper surface, the boundary conditions are much more involved. There are actually three different boundary conditions possible depending upon the shape of the ice-ambient interface.

For a horizontal surface:

$$- K_6 \left.\frac{\partial T_6}{\partial y}\right|_2 = h_{b2} \left(T_6\big|_2 - T_{b2}\right) \tag{9a}$$

For a right-facing vertical surface:

$$- K_6 \left.\frac{\partial T_6}{\partial x}\right|_2 = h_{b2} \left(T_6\big|_2 - T_{b2}\right) \tag{9b}$$

For a left-facing vertical surface:

$$K_6 \left.\frac{\partial T_6}{\partial x}\right|_2 = h_{b2} \left(T_6\big|_2 - T_{b2}\right) \tag{9c}$$

The constants in equation (9) are defined as

h_{b2} = upper surface convective heat transfer coefficient;

T_{b2} = upper air (external flow) ambient temperature;

and the subscript, 2, denotes the upper ambient interface.

3. Insulated boundary conditions can be used to represent the symmetry at the centerline of the heater element and heater gap.

$$\left.\frac{\partial T_j}{\partial x}\right|_{g,j} = 0 \qquad , j = 1, \ldots, 6 \tag{10a}$$

$$\left.\frac{\partial T_j}{\partial x}\right|_{h,j} = 0 \qquad , j = 1, \ldots, 6 \tag{10b}$$

where the subscript, g, denotes the position of the gap centerline and h represents the position of the heater centerline.

The initial temperature distribution can be constant or a function of position. In this study, only a constant initial temperature distribution was considered.

These equations must be expressed in terms of dimensionless parameters. Those chosen were:

$$\theta \equiv \frac{T}{T_{ref}}, \quad \bar{x} \equiv \frac{x}{L}, \quad \bar{y} \equiv \frac{y}{L}, \quad \alpha_j \equiv \frac{K_j}{\rho_j \hat{C}_{pj}}$$

where

T_{ref} = the reference temperature (taken to be 32°F in this study);

L = the total thickness of the composite slab; and

α_j = the thermal diffusivity of the j^{th} layer.

These definitions were substituted into equations (1) through (10), resulting in the following set:

For each layer of the composite blade:

$$\frac{\partial \theta_j}{\partial t} = \frac{\alpha_j}{L^2}\left[\frac{\partial^2 \theta_j}{\partial \bar{x}^2} + \frac{\partial^2 \theta_j}{\partial \bar{y}^2}\right] + \frac{q_j}{\rho_j C_{pj} T_{ref}} \tag{11}$$

For the ice layer:

$$\frac{\partial H_6}{\partial t} = \frac{T_{ref}}{L}\left[\frac{\partial}{\partial \bar{x}}\left(K_6 \frac{\partial \theta_6}{\partial \bar{x}}\right) + \frac{\partial}{\partial \bar{y}}\left(K_6 \frac{\partial \theta_6}{\partial \bar{y}}\right)\right] \tag{12}$$

$$H_6 = \begin{cases} \rho_s \hat{C}_{ps}\, \theta_6\, T_{ref} & , \theta_6 < T_m \\ \rho_l \hat{C}_{pl}\, T_{ref}\,(\theta_6 - \theta_m) + \rho_l\,(\hat{C}_{ps}\, \theta_m\, T_{ref} + L_f), & \theta_6 > T_m \end{cases} \tag{13}$$

$$\theta_6 = \begin{cases} H_6/\rho_s \hat{C}_{ps}\, T_{ref} & , H_6 \leq H_{sm} \\ \theta_m & , H_{sm} < H_6 < H_{lm} \\ H_6/\rho_l \hat{C}_{pl}\, T_{ref} - \dfrac{1}{\hat{C}_{pl}}\left(\hat{C}_{ps}\, \theta_m + \dfrac{L_f}{T_{ref}}\right) + \theta_m & , H_6 \geq H_{lm} \end{cases} \tag{14}$$

At the layer interface points:

$$\theta_j\Big|_I = \theta_{j+1}\Big|_I \quad , j = 1, \ldots, 5 \tag{15a}$$

$$-K_j \frac{\partial \theta_j}{\partial \bar{y}_j}\Big|_I = -K_{j+1} \frac{\partial \theta_{j+1}}{\partial \bar{y}_{j+1}}\Big|_I \quad , j = 1, \ldots, 5 \tag{15b}$$

At the lower and upper boundaries:

$$K_j \frac{\partial \theta_j}{\partial \bar{y}_j}\Big|_1 = h_{b1} L\,(\theta_j\Big|_1 - \theta_{b1}) \quad , j = 1 \tag{16a}$$

$$-K_j \frac{\partial \theta_j}{\partial \bar{y}_j}\Big|_2 = h_{b2} L\,(\theta_j\Big|_2 - \theta_{b2}) \quad , j = 6 \tag{16b}$$

Lastly, the insulated boundary conditions at the heater and gap centerlines become:

$$\left.\frac{\partial \theta_j}{\partial \bar{x}}\right|_{g,j} = 0 \qquad j = 1, \ldots, 6 \tag{17a}$$

$$\left.\frac{\partial \theta_j}{\partial \bar{x}}\right|_{h,j} = 0 \qquad j = 1, \ldots, 6 \tag{17b}$$

2.3 NUMERICAL TECHNIQUE AND FINITE DIFFERENCE FORMULATION

Finite difference formulations require that the continuous time and space domains be discretized into a set of nodes on a grid. For this study, there are three dimensions to be discretized. The spatial coordinates, x and y, are divided into segments, Δx and Δy. The time coordinate, t, is discretized into Δt. The set of governing equations, initial conditions and boundary conditions must be cast into finite difference form. This set of equations is solved for each point of the spatial grid at each time step. A central difference scheme was employed, resulting in the following equations for the first and second partial space derivatives:

$$\left.\frac{\partial E_{i,k}}{\partial \bar{x}}\right|_j = \frac{E_{i+1,k} - E_{i-1,k}}{2\,\Delta\bar{x}} + O\,(\Delta\bar{x})^2 \tag{18}$$

$$\left.\frac{\partial^2 E_{i,k}}{\partial \bar{x}^2}\right|_j = \frac{E_{i+1,k} - 2E_{i,k} + E_{i-1,k}}{(\Delta\bar{x})^2} + O\,(\Delta\bar{x})^2 \qquad \text{where} \tag{19}$$

the i and k denote the nodal position on the two-dimensional grid of nodes, and the E represents any desired nodal

quantity. These are second-order accurate finite difference analogs. The first partial time derivative may be written in this form as:

$$\left.\frac{\partial E_{i,k}}{\partial t}\right|_j^o = \frac{E_{i,k} - E_{i,k}^{\Delta}}{\Delta t} + O(\Delta t)^2 \tag{20}$$

where the superscript Δ indicates the value from the previous time step and the superscript o denotes the value at the half time step between the previous and current time levels. Equation (20) is commonly known as the Crank-Nicolson formulation for the time derivative. The most advantageous aspect of this formulation is the higher accuracy resulting from a second-order truncation error. The spatial Crank-Nicolson analogy can be derived by taking the average of the present and previous time levels. The first and second spatial partial derivatives become:

$$\left.\frac{\partial E_{i,k}}{\partial \bar{x}}\right|_j^o = 1/2 \left(\left.\frac{\partial E_{i,k}}{\partial \bar{x}}\right|_j + \left.\frac{\partial E_{i,k}}{\partial \bar{x}}\right|_j^{\Delta}\right)$$

$$= \frac{E_{i+1,k} - E_{i-1,k} + E_{i+1,k}^{\Delta} - E_{i-1,k}^{\Delta}}{4\,\Delta\bar{x}} + O(\Delta\bar{x})^2 \tag{21}$$

$$\left.\frac{\partial^2 E_{i,k}}{\partial \bar{x}^2}\right|_j^o = 1/2 \left(\left.\frac{\partial^2 E_{i,k}}{\partial \bar{x}^2}\right|_j + \left.\frac{\partial^2 E_{i,k}}{\partial \bar{x}^2}\right|_j^{\Delta}\right)$$

$$= \frac{E_{i+1,k} - 2E_{i,k} + E_{i-1,k} + E_{i+1,k}^{\Delta} - 2E_{i,k}^{\Delta} + E_{i-1,k}^{\Delta}}{2\,(\Delta\bar{x})^2} + O(\Delta\bar{x})^2 \tag{22}$$

Equations (20) through (22) can be substituted into equations (11) through (17) to form a set of nodal equations that can be solved for any point within the discretized time and space grid.

2.3.1 Finite Difference Equations for the Composite Body

This study is based on the two-dimensional model developed by Chao [4] to study the effect of a gap in the heating element. A complete explanation of the derivation of the equations for the composite body has been presented in his dissertation. It will be reproduced here for the sake of completeness.

2.3.1.1 Equation for Points within a Layer

The first step in finding an equation that will represent nodes within a given layer is to substitute equations (20) and (21) into equation (11).

$$\frac{\theta_{i,k,j} - \overset{\Delta}{\theta}_{i,k,j}}{\Delta t} = \frac{\alpha_j}{2L^2}\left[\frac{\theta_{i+1,k,j} - 2\theta_{i,k,j} + \theta_{i-1,k,j} + \overset{\Delta}{\theta}_{i+1,k,j} - 2\overset{\Delta}{\theta}_{i,k,j}}{(\Delta\bar{x})^2} + \frac{\overset{\Delta}{\theta}_{i-1,k,j} + \theta_{i,k+1,j} - 2\theta_{i,k,j} + \theta_{i,k-1,j} + \overset{\Delta}{\theta}_{i,k+1,j} - 2\overset{\Delta}{\theta}_{i,k,j} + \overset{\Delta}{\theta}_{i,k-1,j}}{(\Delta\bar{y}_j)^2}\right] + \frac{q_j}{\rho_j \hat{C}_{pj} T_{ref}} \qquad j = 1, \ldots, 5 \tag{23}$$

This equation is solved for $\theta_{i,j,k}$, the desired nodal temperature.

$$\theta_{i,k,j} = A_j \left\{ \frac{\alpha_j}{2(L\Delta\bar{x})^2} \left[\theta_{i+1,k,j} + \theta_{i-1,k,j} + \theta^{\Delta}_{i+1,k,j} + \theta^{\Delta}_{i-1,k,j} \right] \right.$$

$$+ \frac{\alpha_j}{2(L\Delta\bar{y}_j)^2} \left[\theta_{i,k+1,j} + \theta_{i,k-1,j} + \theta^{\Delta}_{i,k+1,j} + \theta^{\Delta}_{i,k-1,j} \right] + B_j \, U^{n}_{i,k,j}$$

$$\left. + \frac{q_j''/L\Delta\bar{y}_j}{\rho_j C_{pj} T_{ref}} \right\} \qquad i = 2, \ldots, n-1, \quad j = 1, \ldots, 5 \tag{24}$$

The constants in equation (24) are defined as

$$A_j = \frac{1}{\frac{1}{\Delta t} + \frac{\alpha_j}{(L\Delta\bar{x})^2} + \frac{\alpha_j}{(L\Delta\bar{y}_j)^2}} \tag{25a}$$

$$B_j = \frac{1}{\Delta t} - \frac{\alpha_j}{(L\Delta\bar{x})^2} - \frac{\alpha_j}{(L\Delta\bar{y}_j)^2} \quad \text{and} \tag{25b}$$

q_j'' = the heat source per unit area, and equals $q_j L\Delta\bar{y}_j$.

Equation (24) is valid for all the nodes within the composite body except at the centerlines of the heater (i = n) and the gap (1 = 1). At these points, the insulated boundary condition, equation (17), must be satisfied. Finite differencing equation (17) results in:

$$U^{n}_{0,k,j} = \theta_{2,k,j} \qquad j = 1, \ldots, 6 \tag{26a}$$

$$\theta_{n+1,k,j} = \theta_{n-1,k,j} \qquad j = 1, \ldots, 6 \tag{26b}$$

Figures 3a and 3b show grid points at the centerline of the gap (i = 1) and at the centerline of the heater (i = n), respectively. Nodal equations for these points can be derived by substituting equation (26) into equation (24).

At the gap centerline:

$$i = 1,\ \theta_{1,k,j} = A_j \left(\frac{\alpha_j}{2(L\Delta\bar{x})^2}\left[2\,\theta_{2,k,j} + 2\,\theta^{\Delta}_{2,k,j}\right] + \frac{\alpha_j}{2(L\Delta\bar{y}_j)^2}\left[\theta_{1,k+1,j} + \theta_{1,k-1,j} + \theta^{\Delta}_{1,k+1,j} + \theta^{\Delta}_{1,k-1,j}\right] + B_j\,\theta^{\Delta}_{1,k,j} + \frac{q''_j/L\Delta\bar{y}_j}{\rho_j C_{pj} T_{ref}}\right)$$

$$j = 1, \ldots, 5 \qquad (27a)$$

At the heater centerline:

$$i = n,\ \theta_{n,k,j} = A_j\left(\frac{\alpha_j}{2(L\Delta\bar{x})^2}\left[2\,\theta_{n-1,k,j} + 2\theta^{\Delta}_{n-1,k,j}\right] + \frac{\alpha_j}{2(L\Delta\bar{y}_j)^2}\left[\theta_{n,k+1,j} + \theta_{n,k-1,j} + \theta^{\Delta}_{n,k+1,j} + \theta^{\Delta}_{n,k-1,j}\right] + B_j\,\theta^{\Delta}_{n,k,j}\right) \quad j = 1, \ldots, 5 \qquad (27b)$$

2.3.1.2 Equations at the Layer Interfacial Points

The interfacial boundary equations are derived by substituting equation (22) into equation (15b), and using equation (15a). Allowing (i,k) to denote the grid coordinates of an interfacial point yields:

$$\theta_{i,k,j} = \theta_{i,k,j+1}\ ,\quad \theta^{\Delta}_{i,k,j} = \theta^{\Delta}_{i,k,j+1}\ ,\quad j = 1, \ldots, 5 \qquad (28a)$$

$$-K_j\left(\frac{\theta_{i,k+1,j} - \theta_{i,k-1,j} + \theta^{\Delta}_{i,k+1,j} - \theta^{\Delta}_{i,k-1,j}}{4\,\Delta\bar{y}_j}\right) = -K_{j+1}\left(\frac{\theta_{i,k+1,j+1} - \theta_{i,k-1,j+1} + \theta^{\Delta}_{i,k+1,j+1} - \theta^{\Delta}_{i,k-1,j+1}}{4\,\Delta\bar{y}_{j+1}}\right) \qquad (28b)$$

It must be noted that temperatures $\theta_{i,k+1,j}$, $\theta^{\Delta}_{i,k+1,j}$,

$\theta_{i,k-1,j+1}$, and $\theta^{\Delta}_{i,k-1,j+1}$ are fictitious and have to be eliminated. This is accomplished by writing equation (24) for layers j and j+1.

$$\theta_{i,k+1,j} + \theta^{\Delta}_{i,k+1,j} = \frac{2(L\Delta\bar{y}_j)^2}{A_j\,\alpha_j}\Big\{\theta_{i,k,j} - A_j\Big[\frac{\alpha_j}{2(L\Delta\bar{x})^2}(\theta_{i+1,k,j} + \theta_{i-1,k,j} + \theta^{\Delta}_{i+1,k,j} + \theta^{\Delta}_{i-1,k,j}) + \frac{\alpha_j}{2(L\Delta\bar{y}_j)^2}(\theta_{i,k-1,j} + \theta^{\Delta}_{i,k-1,j}) + B_j\,\theta^{\Delta}_{i,k,j} + \frac{q''_j/L\Delta\bar{y}_j}{\rho_j C_{pj} T_{ref}}\Big]\Big\} \tag{29}$$

$$\theta_{i,k-1,j+1} + \theta^{\Delta}_{i,k-1,j+1} = \frac{2(L\Delta\bar{y}_{j+1})^2}{A_{j+1}\,\alpha_{j+1}}\Big\{\theta_{i,k,j+1} - A_{j+1}\Big[\frac{\alpha_{j+1}}{2(L\Delta\bar{x})^2}(\theta_{i+1,k,j+1} + \theta_{i-1,k,j+1} + \theta^{\Delta}_{i+1,k,j+1} + \theta^{\Delta}_{i-1,k,j+1}) + \frac{\alpha_{j+1}}{2(L\Delta\bar{y}_{j+1})^2}(\theta_{i,k+1,j+1} + \theta^{\Delta}_{i,k+1,j+1}) + B_{j+1}\theta^{\Delta}_{i,k,j+1} + \frac{q''_{j+1}/L\Delta\bar{y}_{j+1}}{\rho_{j+1} C_{pj+1} T_{ref}}\Big]\Big\} \tag{30}$$

Combining equations (28), (29) and (30) yields:

$$\theta_{i,k,j} = \frac{1}{\frac{2(L\Delta\bar{y}_j)^2}{A_j\,\alpha_j} + \frac{K_{j+1}\,\Delta\bar{y}_j\,2(L\Delta\bar{y}_{j+1})^2}{K_j\,\Delta\bar{y}_{j+1}\,A_{j+1}\,\alpha_{j+1}}}\Big\{\Big[\frac{(\Delta\bar{y}_j)^2}{(\Delta\bar{x})^2} + \frac{K_{j+1}\,\Delta\bar{y}_j(\Delta\bar{y}_{j+1})^2}{K_j\,\Delta\bar{y}_{j+1}\,(\Delta\bar{x})^2}\Big]$$
$$[\theta_{i+1,k,j} + \theta_{i-1,k,j} + \theta^{\Delta}_{i+1,k,j} + \theta^{\Delta}_{i-1,k,j}] + 2\,[\theta_{i,k-1,j} + \theta^{\Delta}_{i,k-1,j}]$$
$$+ \frac{2\,K_{j+1}\,\Delta\bar{y}_j}{K_j\,\Delta\bar{y}_{j+1}}[\theta_{i,k+1,j+1} + \theta^{\Delta}_{i,k+1,j+1}] + \Big[\frac{2(L\Delta\bar{y}_j)^2}{\alpha_j}\,B_j$$
$$+ \frac{2(L\Delta\bar{y}_{j+1})^2\,K_{j+1}\,\Delta\bar{y}_j}{\alpha_{j+1}\,K_j\,\Delta\bar{y}_{j+1}}\,B_{j+1}\Big]\theta^{\Delta}_{i,k,j} + \frac{2(L\Delta\bar{y}_j)^2}{\alpha_j}\,\frac{q''_j/L\Delta\bar{y}_j}{\rho_j C_{pj} T_{ref}}$$
$$+ \frac{2(L\Delta\bar{y}_{j+1})^2\,K_{j+1}\,\Delta\bar{y}_j\,q''_{j+1}/L\Delta\bar{y}_{j+1}}{\alpha_{j+1}\,\rho_{j+1}\,C_{pj+1}\,T_{ref}}\Big\} \quad i=2,\ \ldots,\ n-1,\ j=1,\ \ldots,\ 5 \tag{31}$$

This equation is applicable for the nodes at the interfaces between the layers. Once again, there are fictitious temperatures that must be eliminated at i = 1 and i = n. Substituting equation (26) into equation (31) yields:

At the gap centerline:

$$i=1,\ \theta_{1,k,j} = \frac{1}{\frac{2(L\Delta\bar{y}_j)^2}{A_j\ \alpha_j} + \frac{K_{j+1}\ \Delta\bar{y}_j}{K_j\ \Delta\bar{y}_{j+1}}\frac{2(L\Delta\bar{y}_{j+1})^2}{A_{j+1}\ \alpha_{j+1}}} \Bigg\{ 2\left[\frac{(\Delta\bar{y}_j)^2}{(\Delta\bar{x})^2} + \frac{(\Delta\bar{y}_{j+1})^2}{(\Delta\bar{x})^2}\frac{K_{j+1}\ \Delta\bar{y}_j}{K_j\ \Delta\bar{y}_{j+1}}\right]\left[\theta_{2,k,j} + \theta^{\Delta}_{2,k,j}\right] + 2\left[\theta_{1,k-1,j} + \theta^{\Delta}_{1,k-1,j}\right]$$

$$+ 2\frac{K_{j+1}\ \Delta\bar{y}_j}{K_j\ \Delta\bar{y}_{j+1}}\left[\theta_{1,k+1,j+1} + \theta^{\Delta}_{1,k+1,j+1}\right] + \left[\frac{2(L\Delta\bar{y}_j)^2}{\alpha_j}\ B_j + \frac{2(L\Delta\bar{y}_{j+1})^2}{\alpha_{j+1}}\frac{K_{j+1}\ \Delta\bar{y}_j}{K_j\ \Delta\bar{y}_{j+1}}\ B_{j+1}\right]\theta^{\Delta}_{1,k,j} + \frac{2(L\Delta\bar{y}_j)^2}{\alpha_j}\frac{q''_j/L\Delta\bar{y}_j}{\rho_j \hat{C}_{pj} T_{ref}}$$

$$+ \frac{2(L\Delta\bar{y}_{j+1})}{\alpha_{j+1}}\frac{K_{j+1}\ \Delta\bar{y}_j}{K_j\ \Delta\bar{y}_{j+1}}\frac{q''_{j+1}/L\Delta\bar{y}_{j+1}}{\rho_{j+1}\ \hat{C}_{pj+1}\ T_{ref}} \Bigg\} \qquad (32a)$$

At the heater centerline:

$$i=n,\ \theta_{n,k,j} = \frac{1}{\frac{2(L\Delta\bar{y}_j)^2}{A_j\ \alpha_j} + \frac{2(L\Delta\bar{y}_{j+1})^2}{\alpha_{j+1}\ A_{j+1}}\frac{K_{j+1}\ \Delta\bar{y}_j}{K_j\ \Delta\bar{y}_{j+1}}} \Bigg\{ 2\left[\frac{(\Delta\bar{y}_j)^2}{(\Delta\bar{x})^2} + \frac{(\Delta\bar{y}_{j+1})^2}{(\Delta\bar{x})^2}\frac{K_{j+1}\ \Delta\bar{y}_j}{K_j\ \Delta\bar{y}_{j+1}}\right]\left[\theta_{n-1,k,j} + \theta^{\Delta}_{n-1,k,j}\right] + 2\left[\theta_{n,k-1,j} + \theta^{\Delta}_{n,k-1,j}\right]$$

$$+ \frac{2K_{j+1}\Delta\bar{y}_j}{K_j\Delta\bar{y}_{j+1}}\left[\theta_{n-1,k,j} + \theta^{\Delta}_{n-1,k,j}\right] + \left[\frac{2(L\Delta\bar{y}_j)^2}{\alpha_j}\ B_j + \frac{2(L\Delta\bar{y}_{j+1})^2}{\alpha_{j+1}}\frac{K_{j+1}\ \Delta\bar{y}_j}{K_j\ \Delta\bar{y}_{j+1}}\ B_{j+1}\right]\theta^{\Delta}_{n,k,j} + \frac{2(L\Delta\bar{y}_j)^2}{\alpha_j}\frac{q''_j/L\Delta\bar{y}_j}{\rho_j \hat{C}_{pj} T_{ref}} + \frac{2(L\Delta\bar{y}_{j+1})^2}{\alpha_{j+1}}\frac{K_{j+1}\ \Delta\bar{y}_j}{K_j\ \Delta\bar{y}_{j+1}}\frac{q''_{j+1}/L\Delta\bar{y}_{j+1}}{\rho_{j+1}\hat{C}_{pj+1}T_{ref}} \Bigg\} \qquad (32b)$$

2.3.1.3 Equations for the Substrate-Ambient Interface

A representation of a node at the inner ambient interface is shown in Figure 4a. At the inner surface, j=1. Allowing (i,k) to denote an interfacial node at the lower surface, the convective boundary condition, equation (16a) becomes:

$$K_1 \left(\frac{\theta_{i,2,1} - \theta_{i,0,1} + \theta^{\Delta}_{i,2,1} - \theta^{\Delta}_{i,0,1}}{4\,\Delta\bar{y}_1}\right) = h_{b1}\, L \left(\frac{\theta_{i,1,1} + \theta^{\Delta}_{i,1,1}}{2} - \theta_{b1}\right) \tag{33}$$

Once again fictitious temperatures are encountered, $\theta_{i,0,1}$ and $\theta^{\Delta}_{i,0,1}$, and must be eliminated. Using equation (24) and letting k = 1, j = 1 and $q''_j = 0$, yields:

$$\theta_{i,1,1} = A_1 \left\{\frac{\alpha_1}{2(L\Delta\bar{x})^2}\left[\theta_{i+1,1,1} + \theta_{i-1,1,1} + \theta^{\Delta}_{i+1,1,1} + \theta^{\Delta}_{i-1,1,1}\right]\right.$$

$$\left. + \frac{\alpha_1}{2(L\Delta\bar{y}_1)^2}\left[\theta_{i,2,1} + \theta_{i,0,1} + \theta^{\Delta}_{i,2,1} + \theta^{\Delta}_{i,0,1}\right] + B_1\,\theta^{\Delta}_{i,1,1}\right\} \tag{34}$$

Substituting equation (34) into equation (33),

$$\theta_{i,1,1} = \frac{1}{\frac{2(L\Delta\bar{y}_1)^2}{A_1\,\alpha_1} + \frac{2h_{b1}\,L\Delta\bar{y}_1}{K_1}} \left\{\frac{(\Delta\bar{y}_1)^2}{(\Delta\bar{x})^2}\left(\theta_{i+1,1,1} + \theta_{i-1,1,1} + \theta^{\Delta}_{i+1,1,1} + \theta^{\Delta}_{i-1,1,1}\right)\right.$$

$$+ 2\left(\theta_{i,2,1} + \theta^{\Delta}_{i,2,1}\right) + \left[\frac{2(L\Delta\bar{y}_1)^2}{\alpha_1} B_1 - \frac{2\,h_{b1}\,L\Delta\bar{y}_1}{K_1}\right]\theta^{\Delta}_{i,1,1} +$$

$$\left.\frac{4\,h_{b1}\,L\Delta\bar{y}_1}{K_1}\,\theta_{b1}\right\} \quad i = 2, \ldots, n-1 \tag{35}$$

This equation is correct for all inner surface-ambient interface nodes except those at the gap and heater centerlines. For i = 1 and i = n, equation (26) must be substituted into equation (35).

At the gap centerline:

$$i=1,\ \theta_{1,1,1} = \frac{1}{\frac{2(L\Delta\bar{y}_1)^2}{A_1\alpha_1} + \frac{2h_{b1}L\Delta\bar{y}_1}{K_1}} \{2\frac{(\Delta\bar{y}_1)^2}{(\Delta\bar{x})^2}[\theta_{2,1,1} + \theta^{\Delta}_{2,1,1}] +$$

$$2[\theta_{1,2,1} + \theta^{\Delta}_{1,2,1}] + [\frac{2(L\Delta\bar{y}_1)^2}{\alpha_1}B_1 - \frac{2h_{b1}L\Delta\bar{y}_1}{K_1}]\theta^{\Delta}_{1,1,1} + \frac{4h_{b1}L\Delta\bar{y}_1}{K_1}\theta_{b1}\} \qquad (36a)$$

At the heater centerline:

$$i=n,\ \theta_{n,1,1} = \frac{1}{\frac{2(L\Delta\bar{y}_1)^2}{A_1\alpha_1} + \frac{2h_{b1}L\Delta\bar{y}_1}{K_1}} \{2\frac{(\Delta\bar{y}_1)^2}{(\Delta\bar{x})^2}[\theta_{n-1,1,1} + \theta^{\Delta}_{n-1,1,1}]$$

$$+ 2[\theta_{n,2,1} + \theta^{\Delta}_{n,2,1}] + [\frac{2(L\Delta\bar{y}_1)^2}{\alpha_1}B_1 - \frac{2h_{b1}L\Delta\bar{y}_1}{K_1}]\theta^{\Delta}_{n,1,1}$$

$$+ \frac{4h_{b1}L\Delta\bar{y}_1}{K_1}\theta_{b1}\} \qquad (36b)$$

2.3.1.4 Equations for the Abrasion Shield-Ambient Interface

When there is no ice on the abrasion shield, convective cooling may occur. A representative grid for this condition is shown in Figure 4b. Let j = 5 and allow (i,m) to denote the interfacial node. Representing the convective cooling boundary conditon, equation (16b), in finite difference form yields:

$$-K_5\left(\frac{\theta_{i,m+1,5} - \theta_{i,m-1,5} + \theta^{\Delta}_{i,m+1,5} - \theta^{\Delta}_{i,m-1,5}}{4\,\Delta\bar{y}_5}\right)$$

$$= h_{b2}L\left(\frac{\theta_{i,m,5} + \theta^{\Delta}_{i,m,5}}{2} - \theta_{b2}\right) \qquad (37)$$

Temperatures $\theta_{i,m-1,5}$ and $\theta^{\Delta}_{i,m-1,5}$ are fictitious and must be eliminated. The procedure is the same as for the inner convective surface. Using equations (24), (16b), and (26).

$$\theta_{i,m,5} = \frac{1}{\frac{2(L\Delta\bar{y}_5)^2}{A_5\,\alpha_5} + \frac{2h_{b2}L\Delta\bar{y}_5}{K_5}} \cdot \left(\frac{(\Delta\bar{y}_5)^2}{(\Delta\bar{x})^2}\left[\theta_{i+1,m,5} + \theta_{i-1,m,5} + \theta^{\Delta}_{i+1,m,5} + \theta^{\Delta}_{i-1,m,5}\right] + 2\left[\theta_{i,m-1,5} + \theta^{\Delta}_{i,m-1,5}\right] + \left[\frac{2(L\Delta\bar{y}_5)^2}{\alpha_5}B_5 - \frac{2h_{b2}L\Delta\bar{y}_5}{K_5}\right]\theta^{\Delta}_{i,m,5} + \frac{4h_{b2}L\Delta\bar{y}_5}{K_5}\theta_{b2}\right) \quad i=2, \ldots, n-1 \tag{38}$$

At the centerline of the gap:

$$i=1,\ \theta_{1,m,5} = \frac{1}{\frac{2(L\Delta\bar{y}_5)^2}{A_5\,\alpha_5} + \frac{2h_{b2}L\Delta\bar{y}_5}{K_5}}\left(2\frac{(\Delta\bar{y}_5)^2}{(\Delta\bar{x})^2}\left[\theta_{2,m,5} + \theta^{\Delta}_{2,m,5}\right] + 2\left[\theta_{1,m-1,5} + \theta^{\Delta}_{1,m-1,5}\right] + \left[\frac{2(L\Delta\bar{y}_5)^2}{\alpha_5}B_5 - \frac{2h_{b2}L\Delta\bar{y}_5}{K_5}\right]\theta^{\Delta}_{1,m,5} + \frac{4h_{b2}L\Delta\bar{y}_5}{K_5}\theta_{b2}\right) \tag{39a}$$

At the centerline of the heater:

$$i=n,\ \theta_{n,m,5} = \frac{1}{\frac{2(L\Delta\bar{y}_5)^2}{A_5\,\alpha_5} + \frac{2h_{b2}L\Delta\bar{y}_5}{K_5}}\left(2\frac{(\Delta\bar{y}_5)^2}{(\Delta\bar{x})^2}\left[\theta_{n-1,m,5} + \theta^{\Delta}_{n-1,m,5}\right] + 2\left[\theta_{n,m-1,5} + \theta^{\Delta}_{n,m-1,5}\right] + \left[\frac{2(L\Delta\bar{y}_5)^2}{\alpha_5}B_5 - \frac{2h_{b2}L\Delta\bar{y}_5}{K_5}\right]\theta_{n,m,5} + \frac{4h_{b2}L\Delta\bar{y}_5}{K_5}\theta_{b2}\right) \tag{40b}$$

2.3.2 Finite Difference Equations for the Ice Layer

2.3.2.1 Type 1 Element, Interior Node

Up to this point, a substitution method has been used exclusively to derive the governing finite difference equations. There is, however, an alternate energy approach that uses a nodal energy balance, and has been shown by Arpaci [5] to be equivalent to the substitution method. This alternate method considerably decreases the amount of algebraic manipulation necessary to reduce an equation to final form. It is also easier to physically understand what the equation represents. For these reasons, the nodal energy balance approach will be used from now on.

The type 1 element has conductive interfaces on all sides as shown in Figure 5a. Writing an energy balance for the nodal volume of Figure 7a, yields:

$$q_4 = q_1 + q_2 + q_3 + q_{STOR} \tag{41}$$

where

$$\begin{aligned} q_1 &= K_{\ell 1} \left.\frac{\partial T}{\partial x}\right|_{\ell i} \Delta y_6 \\ q_2 &= -K_{r1} \left.\frac{\partial T}{\partial x}\right|_{ri} \Delta y_6 \\ q_3 &= -K_{t1} \left.\frac{\partial T}{\partial y}\right|_{t1} \Delta x \\ q_4 &= -K_{b1} \left.\frac{\partial T}{\partial y}\right|_{b1} \Delta x \\ q_{STOR} &= \frac{\partial H}{\partial t} \Delta x \, \Delta y_6 \end{aligned} \tag{42}$$

with the subscript li denoting the left interface, ri denoting the right interface, ti denoting the top interface and bi denoting the bottom interface. The thermal conductivities at each interface vary with the phase present. Chao [4] approximated this effect by replacing these conductivities with average values depending upon the phase of adjacent nodes. The same method is used here.

K_{li} = KW_1 = Average conductivity between nodes (i,j) and (i-1,j).

K_{ri} = KW_2 = Average conductivity between nodes (i,j) and (i+1,j).

K_{ti} = KW_3 = Average conductivity between nodes (i,j) and (i,j+1).

K_{bi} = KW_4 = Average conductivity between nodes (i,j) and (i,j-1).

The partial derivatives in time and space of equation (42) may be approximated using the Crank-Nicolson finite difference algorithm at the half time step:

$$\left.\frac{\partial T}{\partial x}\right|_{\ell i} = \frac{T_{i,k,6} - T_{i-1,k,6} + T^{\Delta}_{i,k,6} - T^{\Delta}_{i-1,k,6}}{2\,\Delta x} + O(\Delta x) \qquad (44a)$$

$$\left.\frac{\partial T}{\partial x}\right|_{ri} = \frac{T_{i+1,k,6} - T_{i,k,6} + T^{\Delta}_{i+1,k,6} - T^{\Delta}_{i,k,6}}{2\,\Delta x} + O(\Delta x) \qquad (44b)$$

$$\left.\frac{\partial T}{\partial y}\right|_{ti} = \frac{T_{i,k+1,6} - T_{i,k,6} + T^{\Delta}_{i,k+1,6} - T^{\Delta}_{i,k,6}}{2\,\Delta y_6} + O(\Delta y_6) \qquad (44c)$$

$$\left.\frac{\partial T}{\partial y}\right|_{b1} = \frac{T_{1,k,6} - T_{1,k-1,6} + T^{\Delta}_{1,k,6} - T^{\Delta}_{1,k-1,6}}{2\,\Delta y_6} + O(\Delta y_6) \qquad (44d)$$

$$\frac{\partial H}{\partial t} = \frac{H_{i,k,6} - H^{\Delta}_{1,k,6}}{\Delta t} + O(\Delta t)^2 \qquad (44e)$$

Substituting equations (43) and (44) into (42) yields:

$$q_1 = KW_1 \left(\frac{T_{1,k,6} - T_{1-1,k,6}}{2\,\Delta x}\right) \Delta y_6 + KW^{\Delta}_1 \left(\frac{T^{\Delta}_{1,k,6} - T^{\Delta}_{i-1,k,6}}{2\,\Delta x}\right) \Delta y_6$$

$$q_2 = -KW_2\left(\frac{T_{1+1,k,6} - T_{i,k,6}}{2\,\Delta x}\right) \Delta y_6 - KW^{\Delta}_2\left(\frac{T^{\Delta}_{i+1,k,6} - T^{\Delta}_{1,k,6}}{2\,\Delta x}\right) \Delta y_6$$

$$q_3 = -KW_3\left(\frac{T_{i,k+1,6} - T_{i,k,6}}{2\,\Delta y_6}\right) \Delta x - KW^{\Delta}_3\left(\frac{T^{\Delta}_{i,k+1,6} - T^{\Delta}_{i,k,6}}{2\,\Delta y_6}\right) \Delta x$$

$$q_4 = -KW_4\left(\frac{T_{i,k,6} - T_{i,k-1,6}}{2\,\Delta y_6}\right) \Delta x - KW^{\Delta}_4\left(\frac{T^{\Delta}_{1,k,6} - T^{\Delta}_{1,k-1,6}}{2\Delta y_6}\right) \Delta x$$

$$q_{STOR} = \left(\frac{H_{1,k,6} - H^{\Delta}_{1,k,6}}{\Delta t}\right) \Delta x\, \Delta y_6 \qquad (45)$$

Substituting equation (45) into equation (41) and converting to dimensionless form yields:

$$H_{1,k,6} = H^{\Delta}_{i,k,6} + \frac{\Delta t\, T_{ref}}{2L^2}\left\{KW_4 \frac{\theta_{1,k-1,6}}{(\Delta \bar{y}_6)^2} + KW^{\Delta}_4 \left(\frac{\theta^{\Delta}_{1,k-1,6} - \theta^{\Delta}_{i,k,6}}{(\Delta \bar{y}_6)^2}\right) + KW_2 \frac{\theta_{i+1,k,6}}{(\Delta \bar{x})^2}\right.$$

$$+ KW_2^{\Delta} \left(\frac{\theta^{\Delta}_{i+1,k,6} - \theta^{\Delta}_{i,k,6}}{(\Delta\bar{y}_6)^2}\right) + KW_3 \frac{\theta_{i,k+1,6}}{(\Delta\bar{y}_6)^2}$$

$$+ KW_3^{\Delta} \left(\frac{\theta^{\Delta}_{i,k+1,6} - \theta^{\Delta}_{i,k,6}}{(\Delta\bar{y}_6)^2} + KW_1 \frac{\theta_{i-1,k,6}}{(\Delta\bar{x})^2}\right.$$

$$+ KW_1^{\Delta} \left(\frac{\theta^{\Delta}_{i-1,k,6} - \theta^{\Delta}_{i,k,6}}{(\Delta\bar{x})^2}\right) - \left[\frac{KW_1 + KW_2}{(\Delta\bar{x})^2}\right.$$

$$\left.\left. + \frac{KW_3 + KW_4}{(\Delta\bar{y}_6)^2}\right] \theta_{i,k,6}\right\} \qquad (46)$$

An equation for each phase is developed by incorporating equation (14) into equation (46) and solving for $H_{i,k,6}$.

For the solid phase:

$$H_{i,k,6} = \left\{1 + \frac{\Delta t}{2 \rho_s C_{ps} L^2} \left[\frac{KW_1 + KW_2}{(\Delta\bar{x})^2} + \frac{KW_3 + KW_4}{(\Delta\bar{y}_6)^2}\right]\right\}^{-1}$$

$$\left\{H^{\Delta}_{i,k,6} + \frac{\Delta t\, T_{ref}}{2L^2} \left[KW_4 \frac{\theta_{i,k-1,6}}{(\Delta\bar{y}_6)^2} + KW_4^{\Delta} \left(\frac{\theta^{\Delta}_{i,k-1,6} - \theta^{\Delta}_{i,k,6}}{(\Delta\bar{y}_6)^2}\right)\right.\right.$$

$$+ KW_2 \frac{\theta_{i+1,k,6}}{(\Delta\bar{x})^2} + KW_2^{\Delta} \left(\frac{\theta^{\Delta}_{i+1,k,6} - \theta^{\Delta}_{i,k,6}}{(\Delta\bar{x})^2}\right) + KW_3 \frac{\theta_{i,k+1,6}}{(\Delta\bar{y}_6)^2}$$

$$\left.\left. + KW_3^{\Delta} \left(\frac{\theta^{\Delta}_{i,k+1,6} - \theta^{\Delta}_{i,k,6}}{(\Delta\bar{y}_6)^2} + KW_1 \frac{\theta_{i-1,k,6}}{(\Delta\bar{x})^2} + KW_1^{\Delta} \left(\frac{\theta^{\Delta}_{i-1,k,6} - \theta^{\Delta}_{i,k,6}}{(\Delta\bar{x})^2}\right)\right]\right\} \qquad (47a)$$

For the melting point:

$$H_{i,k,6} = H^{\Delta}_{i,k,6} + \frac{\Delta t\, T_{ref}}{2L^2} \left\{KW_4 \frac{\theta_{i,k-1,6}}{(\Delta\bar{y}_6)^2} + \right.$$

$$+ KW_4^{\Delta} \left(\frac{\theta^{\Delta}_{i,k-1,6} - \theta^{\Delta}_{i,k,6}}{(\Delta\bar{y}_6)^2}\right) + KW_2 \frac{\theta_{i+1,k,6}}{(\Delta\bar{x})^2}$$

$$+ KW_2^{\Delta} \left(\frac{\theta^{\Delta}_{i+1,k,6} - \theta^{\Delta}_{i,k,6}}{(\Delta\bar{y}_6)^2}\right) + KW_3 \frac{\theta_{i,k+1,6}}{(\Delta\bar{y}_6)^2}$$

$$+ KW_3^{\Delta} \left(\frac{\theta^{\Delta}_{i,k+1,6} - \theta^{\Delta}_{i,k,6}}{(\Delta\bar{y}_6)^2}\right) + KW_1 \frac{\theta_{i-1,k,6}}{(\Delta\bar{x})^2}$$

$$+ KW_1^{\Delta} \left(\frac{\theta^{\Delta}_{i-1,k,6} - \theta^{\Delta}_{i,k,6}}{(\Delta\bar{x})^2} - \left[\frac{KW_1 + KW_2}{(\Delta\bar{x})^2} + \frac{KW_3 + KW_1}{(\Delta\bar{y}_6)^2} \right] \theta_m \right) \qquad (47b)$$

For the liquid phase:

$$H_{1,k,6} = \left\{ 1 + \frac{\Delta t}{2\, \rho_{\ell}\, C_{p\ell}\, L^2} \left[\frac{KW_1 + KW_2}{(\Delta\bar{x})^2} + \frac{KW_3 + KW_4}{(\Delta\bar{y}_6)^2} \right] \right\}^{-1} *$$

$$\left\{ H^{\Delta}_{i,k,6} + \frac{\Delta t\, T_{ref}}{2\, L^2} \left[KW_4 \frac{\theta_{1,k-1,6}}{(\Delta\bar{y}_6)^2} + KW_4^{\Delta} \left(\frac{\theta^{\Delta}_{i,k-1,6} - \theta^{\Delta}_{i,k,6}}{(\Delta\bar{y}_6)^2} \right) \right. \right.$$

$$+ KW_2 \frac{\theta_{1+1,k,6}}{(\Delta\bar{x})^2} + KW_2^{\Delta} \left(\frac{\theta^{\Delta}_{i+1,k,6} - \theta^{\Delta}_{i,k,6}}{(\Delta\bar{x})^2} \right)$$

$$+ KW_3 \frac{\theta_{i,k+1,6}}{(\Delta\bar{x})^2} + KW_3^{\Delta} \left(\frac{\theta^{\Delta}_{i,k+1,6} - \theta^{\Delta}_{i,k,6}}{(\Delta\bar{y}_6)^2} \right) + KW_1 \frac{\theta_{i-1,k,6}}{(\Delta\bar{x})^2}$$

$$+ KW_1^{\Delta} \left(\frac{\theta^{\Delta}_{i-1,k,6} - \theta^{\Delta}_{i,k,6}}{(\Delta\bar{x})^2} \right)$$

$$\left. \left. + \left[\frac{KW_1 + KW_2}{(\Delta\bar{x})^2} + \frac{KW_3 + KW_4}{(\Delta\bar{y}_6)^2} \right] \left[\frac{1}{C_{p\ell}} \left(\hat{C}_{ps}\, \theta_m + \frac{L_f}{T_{ref}} + \theta_m \right) \right] \right] \right\} \qquad (47c)$$

These equations are identical to those developed by Chao for a purely conductive node, and are second order accurate. This method is equivalent to the substitution method, but is more direct and easier to apply.

The insulated boundary conditions at the heater and gap centerlines are handled within the computer algorithm. For example, at the gap centerline (i = 1) the boundary condition is expressed in finite difference form as:

$$\theta_{\ell,k,6} = \theta_{0,k,6}$$

The fictitious quantity $\theta_{0,k,6}$ is replaced by $\theta_{2,k,6}$ in equation (47). At the heater centerline (i = n), the boundary condition becomes:

$$\theta_{n-1,k,6} = \theta_{n+1,k,6}$$

The nonexistent quantity, $\theta_{n+1,k,6}$, in equation (47) is replaced by $\theta_{n-1,k,6}$. This substitution process is handled entirely within the computer program, and reduces the total number of equations. It also simplifies the numerical model considerably.

2.3.2.2 Type 2 Element, Ice-Ambient Interface

This type of element is shown in Figure 5b. The same energy balance still applies, but one surface is now convective. The terms of equation (41) become:

$$q_1 = KW_1 \left(\frac{T_{i,k,6} - T_{i-1,k,6}}{2\,\Delta x}\right) \Delta y_6 + KW_1^{\Delta} \left(\frac{T^{\Delta}_{i,k,6} - T^{\Delta}_{i-1,k,6}}{2\,\Delta x}\right) \Delta y_6$$

$$q_2 = -KW_2\left(\frac{T_{i+1,k,6} - T_{i,k,6}}{2\,\Delta x}\right) \Delta y_6 - KW_2^{\Delta}\left(\frac{T^{\Delta}_{i+1,k,6} - T^{\Delta}_{i,k,6}}{2\,\Delta x}\right) \Delta y_6$$

$$q_3 = h_{b2} \left(\frac{T_{i,k,6} + T^{\Delta}_{i,k,6}}{2} - T_{b2}\right) \Delta x$$

$$q_4 = -KW_4\left(\frac{T_{i,k,6} - T_{i,k-1,6}}{2\,\Delta y_6}\right)\Delta x$$

$$- KW_4^{\Delta}\left(\frac{T^{\Delta}_{i,k,6} - T^{\Delta}_{i,k-1,6}}{2\Delta y_6}\right)\Delta x$$

$$q_{STOR} = \left(\frac{H_{i,k,6} - H^{\Delta}_{i,k,6}}{\Delta t}\right)\Delta x\,\Delta y_6 \qquad (48)$$

Substituting these into equation (41) and combining the result with equation (14) produces the final result for each phase.

For the solid phase:

$$H_{i,k,6} = \{1+\frac{\Delta t}{2L^2\,\rho_s\,C_{ps}}\left[\frac{KW_4}{(\Delta\bar{y}_6)^2} + \frac{KW_1 + KW_2}{(\Delta\bar{x})^2} + \frac{h_{b2}\,L}{\Delta\bar{y}_6}\right]\}^{-1} *$$

$$\{H^{\Delta}_{i,k,6} + \frac{\Delta t\,T_{ref}}{2L^2}\left[KW_4\,\frac{\theta_{i,k-1,6}}{(\Delta\bar{y}_6)^2} + KW_4^{\Delta}\left(\frac{\theta^{\Delta}_{i,k-1,6} - \theta^{\Delta}_{i,k,6}}{(\Delta\bar{y}_6)^2}\right)\right.$$

$$+ KW_2\,\frac{\theta_{i+1,k,6}}{(\Delta\bar{x})^2} + KW_2^{\Delta}\left(\frac{\theta^{\Delta}_{i+1,k,6} - \theta^{\Delta}_{i,k,6}}{(\Delta\bar{x})^2}\right) + KW_1\,\frac{\theta_{i-1,k,6}}{(\Delta\bar{x})^2}$$

$$\left. + KW_1^{\Delta}\left(\frac{\theta^{\Delta}_{i-1,k,6} - \theta^{\Delta}_{i,k,6}}{(\Delta\bar{x})^2}\right) + \frac{h_{b2}\,L}{\Delta\bar{y}_6}\,(2\,\theta_{b_2} - \theta^{\Delta}_{i,k,6})\right]\} \qquad (49a)$$

For the melting point:

$$H_{i,k,6} = H^{\Delta}_{i,k,6} + \frac{\Delta t\,T_{ref}}{2L^2}\left\{KW_4\,\frac{\theta_{i,k+1,6}}{(\Delta\bar{y}_6)^2} + KW_4^{\Delta}\,\left(\frac{\theta^{\Delta}_{i,k-1,6} - \theta^{\Delta}_{i,k,6}}{(\Delta\bar{y}_6)^2}\right)\right.$$

$$+ KW_2\,\frac{\theta_{i+1,k,6}}{(\Delta\bar{x})^2} + KW_2^{\Delta}\,\left(\frac{\theta^{\Delta}_{i+1,k,6} - \theta^{\Delta}_{i,k,6}}{(\Delta\bar{x})^2}\right)$$

$$+ KW_1\,\frac{\theta_{i-1,k,6}}{(\Delta\bar{x})^2} + KW_1^{\Delta}\,\left(\frac{\theta^{\Delta}_{i-1,k,6} - \theta^{\Delta}_{i,k,6}}{(\Delta\bar{x})^2}\right)$$

$$\left. + \frac{h_{b2}\,L}{\Delta\bar{y}_6}\,(2\,\theta_{b_2} - \theta^{\Delta}_{i,k,6}) - \left[\frac{KW_4}{(\Delta\bar{y}_6)^2} + \frac{KW_1 + KW_2}{(\Delta\bar{x})^2} + \frac{h_{b2}\,L}{\Delta\bar{y}_6}\right]\theta_m\right\} \qquad (49b)$$

For the liquid phase:

$$H_{i,k,6} = \{1 + \frac{\Delta t}{2L^2 \rho_\ell \dot{C}_{p\ell}} [\frac{KW_4}{(\Delta\bar{y}_6)^2} + \frac{KW_1 + KW_2}{(\Delta\bar{x})^2} + \frac{h_{b2}L}{\Delta\bar{y}_6}]\}^{-1} \cdot$$

$$\{H^{\Delta}_{i,k,6} + \frac{\Delta t\, T_{ref}}{2L^2} [KW_4 \frac{\theta_{i,k-1,6}}{(\Delta\bar{y}_6)^2} + KW^{\Delta}_4 (\frac{\theta^{\Delta}_{i,k-1,6} - \theta^{\Delta}_{i,k,6}}{(\Delta\bar{y}_6)^2})$$

$$+ KW_2 \frac{\theta_{i+1,k,6}}{(\Delta\bar{x})^2} + KW^{\Delta}_2 (\frac{\theta^{\Delta}_{i+1,k,6} - \theta^{\Delta}_{i,k,6}}{(\Delta\bar{x})^2}) + KW_1 \frac{\theta_{i-1,k,6}}{(\Delta\bar{x})^2}$$

$$+ KW^{\Delta}_1 (\frac{\theta^{\Delta}_{i-1,k,6} - \theta^{\Delta}_{i,k,6}}{(\Delta\bar{x})^2}) + \frac{h_{b2}L}{\Delta\bar{y}_6} (2\,\theta_{b2} - \theta_{i,k,6})$$

$$+ [\frac{KW_4}{(\Delta\bar{y}_6)^2} + \frac{KW_1 + KW_2}{(\Delta\bar{x})^2} + \frac{h_{b2}L}{\Delta\bar{y}_6}] [\frac{1}{\dot{C}_{p\ell}} (\dot{C}_{ps}\,\theta_m + \frac{L_f}{T_{ref}}) - \theta_m]]\} \qquad (49c)$$

The insulated boundary conditions at the heater and gap centerlines are handled within the computer algorithm in the same manner as the type 1 element.

2.3.2.3 Type 3 Element, Ice-Ambient Interface

This element has a convective surface on the left nodal interface and conductive surfaces on the others, as shown in Fig. 5c. The energy terms of equation (41) become:

$$q_1 = h_{b2} (\frac{T_{i,k,6} + T^{\Delta}_{i,k,6}}{2} - T_{b2})\, \Delta y_6$$

$$q_2 = -KW_2(\frac{T_{i+1,k,6} - T_{i,k,6}}{2\,\Delta x})\ \Delta y_6$$

$$- KW^{\Delta}_2(\frac{T^{\Delta}_{i+1,k,6} - T^{\Delta}_{i,k,6}}{2\,\Delta x})\ \Delta y_6$$

$$q_3 = -KW_3(\frac{T_{i,k+1,6} - T_{i,k,6}}{2\,\Delta y_6})\ \Delta x$$

$$- KW^{\Delta}_3(\frac{T^{\Delta}_{i,k+1,6} - T^{\Delta}_{i,k,6}}{2\,\Delta y_6})\ \Delta x$$

$$q_4 = -KW_4\left(\frac{T_{i,k,6} - T_{i,k-1,6}}{2\,\Delta y_6}\right)\Delta x$$

$$- KW_4^{\Delta}\left(\frac{T^{\Delta}_{i,k,6} - T^{\Delta}_{i,k-1,6}}{2\Delta y_6}\right)\Delta x$$

$$q_{STOR} = \left(\frac{H_{i,k,6} - H^{\Delta}_{i,k,6}}{\Delta t}\right)\Delta x\,\Delta y_6 \qquad (50)$$

Carrying out the substitution of these terms into equation (41), incorporating equation (14), and solving for $H_{i,k,6}$ yields the equations for each phase.

For the solid phase:

$$H_{i,k,6} = \{1 + \frac{\Delta t}{2\,\rho_s\,C_{ps}\,L^2}\left[\frac{KW_3 + KW_4}{(\Delta\bar{y}_6)^2} + \frac{KW_2}{(\bar{x})^2} + \frac{hb_2L}{\Delta\bar{x}}\right]\}^{-1} *$$

$$\{H^{\Delta}_{i,k,6} + \frac{\Delta t\,T_{ref}}{2L^2}\left[KW_4\,\frac{\theta_{i,k-1,6}}{(\Delta\bar{y}_6)^2} + KW_4^{\Delta}\left(\frac{\theta^{\Delta}_{i,k-1,6} - \theta^{\Delta}_{i,k,6}}{(\Delta\bar{y}_6)^2}\right)\right.$$

$$+ KW_3\,\frac{\theta_{i,k+1,6}}{(\Delta\bar{y}_6)^2} + KW_3^{\Delta}\left(\frac{\theta^{\Delta}_{i,k+1,6} - \theta^{\Delta}_{i,k,6}}{(\Delta\bar{y}_6)^2}\right) - KW_2\,\frac{\theta_{i+1,k,6}}{(\Delta\bar{x})^2}$$

$$\left. + KW_2^{\Delta}\left(\frac{\theta^{\Delta}_{i+1,k,6} - \theta^{\Delta}_{i,k,6}}{(\Delta\bar{x})^2}\right) + \frac{h_{b2}L}{\Delta\bar{x}}\,(2\,\theta_{b2} - \theta^{\Delta}_{i,k,6})\right]\} \qquad (51a)$$

For the melting point:

$$H_{i,k,6} = H^{\Delta}_{i,k,6} + \frac{\Delta t\,T_{ref}}{2L^2}\,KW_4\,\frac{\theta_{i,k-1,6}}{(\Delta\bar{y}_6)^2}$$

$$+ KW_4^{\Delta}\left(\frac{\theta^{\Delta}_{i,k-1,6} - \theta^{\Delta}_{i,k,6}}{(\Delta\bar{y}_6)^2}\right) + KW_3\,\frac{\theta_{i,k+1,6}}{(\Delta\bar{y}_6)^2}$$

$$+ KW_3^{\Delta}\left(\frac{\theta^{\Delta}_{i,k+1,6} - \theta^{\Delta}_{i,k,6}}{(\bar{y}_6)^2} + KW_2\,\frac{\theta_{i+1,k,6}}{(\bar{x})^2}\right.$$

$$\left. + KW_2^{\Delta}\left(\frac{\theta^{\Delta}_{i+1,k,6} - \theta^{\Delta}_{i,k,6}}{(\Delta\bar{x})^2}\right) + \frac{hb_2L}{\Delta\bar{x}}\,(2\,\theta_{b2} - \theta^{\Delta}_{i,k,6})\right.$$

$$\left. - \left[\frac{KW_3 + KW_4}{(\Delta\bar{y}_6)^2} + \frac{KW_2}{(\Delta\bar{x})^2} + \frac{hb_2L}{\Delta\bar{x}}\right]\theta_m\right\} \qquad (51b)$$

For the liquid phase:

$$H_{i,k,6} = \{1 + \frac{\Delta t}{2\rho_\ell \dot{C}_{p\ell} L^2}\left[\frac{KW_3 + KW_4}{(\Delta\bar{y}_6)^2} + \frac{KW_2}{(\Delta\bar{x})^2} + \frac{h_{b2}L}{\Delta\bar{x}}\right]\}^{-1} *$$

$$\{H^{\Delta}_{i,k,6} + \frac{\Delta t\, T_{ref}}{2L^2}\left[KW_4 \frac{\theta_{i,k-1,6}}{(\Delta\bar{y}_6)^2} + KW^{\Delta}_4 \left(\frac{\theta^{\Delta}_{i,k-1,6} - \theta^{\Delta}_{i,k,6}}{(\Delta\bar{y}_6)^2}\right)\right.$$

$$+ KW_3 \frac{\theta_{i,k+1,6}}{(\Delta\bar{y}_6)^2} + KW^{\Delta}_3 \left(\frac{\theta^{\Delta}_{i,k+1,6} - \theta^{\Delta}_{i,k,6}}{(\Delta\bar{y}_6)^2}\right) + KW_2 \frac{\theta_{i+1,k,6}}{(\Delta\bar{x})^2}$$

$$+ KW^{\Delta}_2 \left(\frac{\theta^{\Delta}_{i+1,k,6} - \theta^{\Delta}_{i,k,6}}{(\Delta\bar{x})^2}\right) + \frac{h_{b2}L}{\Delta\bar{x}} (2\,\theta_{b2} - \theta^{\Delta}_{i,k,6})$$

$$\left. + \left[\frac{KW_3 + KW_4}{(\Delta\bar{y}_6)^2} + \frac{KW_2}{(\Delta\bar{x})^2} + \frac{h_{b2}L}{\Delta\bar{x}}\right]\left[\frac{1}{\dot{C}_{p\ell}}\left(\dot{C}_{ps}\,\theta_m + \frac{L_f}{T_{ref}}\right) - \theta_m\right]\right\} \qquad (51c)$$

The insulated boundary condition at the heater centerline is handled within the computer algorithm in the same manner as the type 1 element. This type of element can never occur over the centerline of the gap (i=1).

2.3.2.4 Type 4 Element, Ice-Ambient Interface

Figure 5d shows a type 4 element. It has a convective surface on the right nodal interface and conductive surfaces on the others. The terms of the energy equation are:

$$q_1 = KW_1 \left(\frac{T_{i,k,6} - T_{i-1,k,6}}{2\,\Delta x}\right) \Delta y_6$$

$$+ KW^{\Delta}_1 \left(\frac{T^{\Delta}_{i,k,6} - T^{\Delta}_{i-1,k,6}}{2\,\Delta x}\right) \Delta y_6$$

$$q_2 = hb_2 \left(\frac{T_{i,k,6} + T^{\Delta}_{i,k,6}}{2} - T_{b2}\right) \Delta y_6$$

$$q_3 = -KW_3\left(\frac{T_{i,k+1,6} - T_{i,k,6}}{2\,\Delta y_6}\right)\Delta x - KW_3^{\Delta}\left(\frac{T^{\Delta}_{i,k+1,6} - T^{\Delta}_{i,k,6}}{2\,\Delta y_6}\right)\Delta x$$

$$q_4 = -KW_4\left(\frac{T_{i,k,6} - T_{i,k-1,6}}{2\,\Delta y_6}\right)\Delta x - KW_4^{\Delta}\left(\frac{T^{\Delta}_{i,k,6} - T^{\Delta}_{i,k-1,6}}{2\Delta y_6}\right)\Delta x$$

$$q_{STOR} = \left(\frac{H_{i,k,6} - H^{\Delta}_{i,k,6}}{\Delta t}\right)\Delta x\,\Delta y_6 \qquad (52)$$

Replacing the energy terms in equation (41) with equation (52), incorporating equation (14), and solving for $H_{i,k,6}$, results in the governing field equations for each phase.

For the solid phase:

$$H_{i,k,6} = \{1 + \frac{\Delta t}{2\,\rho_s\,C_{ps}\,L^2}\left[\frac{KW_4 + KW_3}{(\Delta\bar{y}_6)^2} + \frac{KW_1}{(\Delta\bar{x})^2} + \frac{hb_2L}{\Delta\bar{x}}\right]\}^{-1} *$$

$$\{H^{\Delta}_{i,k,6} + \frac{\Delta t\,T_{ref}}{2L^2}\left[KW_4\,\frac{\theta_{i,k-1,6}}{(\Delta\bar{y}_6)^2} + KW_4^{\Delta}\left(\frac{\theta^{\Delta}_{i,k-1,6} - \theta^{\Delta}_{i,k,6}}{(\Delta\bar{y}_6)^2}\right)\right.$$

$$+ KW_3\,\frac{\theta_{i,k+1,6}}{(\Delta\bar{y}_6)^2} + KW_3^{\Delta}\left(\frac{\theta^{\Delta}_{i,k+1,6} - \theta^{\Delta}_{i,k,6}}{(\Delta\bar{y}_6)^2}\right) + KW_1\,\frac{\theta_{i-1,k,6}}{(\Delta\bar{x})^2}$$

$$\left. + KW_1^{\Delta}\left(\frac{\theta^{\Delta}_{i-1,k,6} - \theta^{\Delta}_{i,k,6}}{(\Delta\bar{x})^2}\right) + \frac{hb_2L}{\Delta\bar{x}}\,(2\,\theta_{b2} - \theta^{\Delta}_{i,k,6})\right]\} \qquad (53a)$$

For the melting point:

$$H_{i,k,6} = H^{\Delta}_{i,k,6} + \frac{\Delta t\,T_{ref}}{2L^2}\left\{KW_4\,\frac{\theta_{i,k-1,6}}{(\Delta\bar{y}_6)^2}\right.$$

$$+ KW_4^{\Delta}\left(\frac{\theta^{\Delta}_{i,k-1,6} - \theta^{\Delta}_{i,k,6}}{(\Delta\bar{y}_6)^2}\right) + KW_3\,\frac{\theta_{i,k+1,6}}{(\Delta\bar{y}_6)^2}$$

$$KW_3^{\Delta}\left(\frac{\theta^{\Delta}_{i,k+1,6} - \theta^{\Delta}_{i,k,6}}{(\Delta\bar{y}_6)^2}\right) + KW_1\,\frac{\theta_{i-1,k,6}}{(\Delta\bar{x})^2}$$

$$+ KW_1^{\Delta} \left(\frac{\theta^{\Delta}_{i-1,k,6} - \theta^{\Delta}_{i,k,6}}{(\Delta\bar{x})^2}\right) + \frac{hb_2 L}{\Delta\bar{x}} (\theta_{b2} - \theta^{\Delta}_{i,k,6})$$

$$- \left[\frac{KW_4 + KW_3}{(\Delta\bar{y}_6)^2} + \frac{KW_1}{(\Delta\bar{x})^2} + \frac{hb_2 L}{\Delta\bar{x}}\right] \theta_m \} \qquad (53b)$$

For the liquid phase:

$$H_{i,k,6} = \{1 + \frac{\Delta t}{2 \rho_{\ell} C_{p\ell}} \left[\frac{KW_4 + KW_3}{(\Delta\bar{y}_6)^2} + \frac{KW_1}{(\Delta\bar{x})^2} + \frac{h_{b2} L}{\Delta\bar{x}}\right]\}^{-1} *$$

$$\{H^{\Delta}_{i,k,6} + \frac{\Delta t \, T_{ref}}{2L^2} [KW_4 \frac{\theta_{i,k-1,6}}{(\Delta\bar{y}_6)^2} + KW_4^{\Delta} \left(\frac{\theta^{\Delta}_{i,k-1,6} - \theta^{\Delta}_{i,k,6}}{(\Delta\bar{y}_6)^2}\right)$$

$$+ KW_3 \frac{\theta_{i,k+1,6}}{(\Delta\bar{y}_6)^2} + KW_3^{\Delta} \left(\frac{\theta^{\Delta}_{i,k+1,6} - \theta^{\Delta}_{i,k,6}}{(\Delta\bar{y}_6)^2}\right) + KW_1 \frac{\theta_{i-1,k,6}}{(\Delta\bar{x})^2}$$

$$+ KW_1^{\Delta} \left(\frac{\theta^{\Delta}_{i-1,k,6} - \theta^{\Delta}_{i,k,6}}{(\Delta\bar{x})^2}\right) + \frac{h_{b2} L}{\Delta\bar{x}} (2\theta_{b2} - \theta_{i,k,6})$$

$$+ \left[\frac{KW_4 + KW_3}{(\Delta\bar{y}_6)^2} + \frac{KW_1}{(\Delta\bar{x})^2} + \frac{h_{b2} L}{\Delta\bar{x}}\right] \left[\frac{1}{C_{p\ell}} \left(\hat{C}_{ps} \theta_m + \frac{L_f}{T_{ref}}\right) - \theta_m\right]\} \qquad (53c)$$

The insulated boundary condition over the heater gap centerline is handled the same as with a type 1 element. This type of element can never occur over the heater centerline ($i = n$).

2.3.2.5 Type 5 Element, Ice-Ambient Interface

This element has convective surfaces on the top and left side interfaces as shown in Figure 5e. The energy terms become:

$$q_1 = h_{b2} \left(\frac{T_{i,k,6} + T^{\Delta}_{i,k,6}}{2} - T_{b2}\right) \Delta y_6$$

$$q_2 = -KW_2\left(\frac{T_{i+1,k,6} - T_{i,k,6}}{2\,\Delta x}\right)\Delta y_6 - KW_2^{\Delta}\left(\frac{T^{\Delta}_{i+1,k,6} - T^{\Delta}_{i,k,6}}{2\,\Delta x}\right)\Delta y_6$$

$$q_3 = h_{b2}\left(\frac{T_{i,k,6} + T^{\Delta}_{i,k,6}}{2} - T_{b2}\right)\Delta x$$

$$q_4 = -KW_4\left(\frac{T_{i,k,6} - T_{i,k-1,6}}{2\,\Delta y_6}\right)\Delta x - KW_4^{\Delta}\left(\frac{T^{\Delta}_{i,k,6} - T^{\Delta}_{i,k-1,6}}{2\Delta y_6}\right)\Delta x$$

$$q_{STOR} = \left(\frac{H_{i,k,6} - H^{\Delta}_{i,k,6}}{\Delta t}\right)\Delta x\,\Delta y_6 \qquad (54)$$

Placing these terms into the energy balance, equation (41), incorporating equation (14), and solving for $H_{i,k,6}$ yields the governing field equation for each phase.

For the solid phase:

$$H_{1,k,6} = \{1 + \frac{\Delta t}{2\,\rho_s\,C_{ps}}\left[\frac{KW_4}{(\Delta\bar{y}_6)^2} + \frac{KW_2}{(\Delta\bar{x})^2} + h_{b2}L\left(\frac{1}{\Delta\bar{x}} + \frac{1}{\Delta\bar{y}_6}\right)\right]\}^{-1} *$$

$$\{H^{\Delta}_{1,k,6} + \frac{\Delta t\,T_{ref}}{2L^2}\left[KW_4\frac{\theta_{i,k-1,6}}{(\Delta\bar{y}_6)^2} + KW_4^{\Delta}\left(\frac{\theta^{\Delta}_{i,k-1,6} - \theta^{\Delta}_{i,k,6}}{(\Delta\bar{y}_6)^2}\right)\right.$$

$$+ KW_2\frac{\theta_{i+1,k,6}}{(\Delta\bar{x})^2} + KW_2^{\Delta}\left(\frac{\theta^{\Delta}_{i+1,k,6} - \theta^{\Delta}_{i,k,6}}{(\Delta\bar{x})^2}\right)$$

$$\left. + h_{b2}\,L(2\,\theta_{b2} - \theta^{\Delta}_{1,k,6})\left(\frac{1}{\Delta\bar{x}} + \frac{1}{\Delta\bar{y}_6}\right)\right]\} \qquad (55a)$$

For the melting point:

$$H_{1,k,6} = H^{\Delta}_{1,k,6} + \frac{\Delta t\,T_{ref}}{2L^2}\left\{KW_4\frac{\theta_{i,k-1,6}}{(\Delta\bar{x})^2}\right.$$

$$\left. + KW_4^{\Delta}\left(\frac{\theta^{\Delta}_{i,k-1,6} - \theta^{\Delta}_{i,k,6}}{(\Delta\bar{y}_6)^2}\right) + KW_2\frac{\theta_{i+1,k,6}}{(\Delta\bar{x})^2}\right.$$

$$+ KW_2^{\Delta} \left(\frac{\theta^{\Delta}_{i+1,k,6} - \theta^{\Delta}_{i,k,6}}{(\Delta\bar{x})^2}\right) + h_{b2} L (2\theta_{b2} - \theta^{\Delta}_{i,k,6})$$

$$\left(\frac{1}{\Delta\bar{x}} + \frac{1}{\Delta\bar{y}_6}\right) - \left[\frac{KW_4}{(\Delta\bar{y}_6)^2} + \frac{KW_2}{(\Delta\bar{x})^2} + h_{b2}L\left(\frac{1}{\Delta\bar{x}} + \frac{1}{\Delta\bar{y}_6}\right)\right]\theta_m\Big) \qquad (55b)$$

For the liquid phase:

$$H_{i,k,6} = \{1 + \frac{\Delta t}{2\rho_{\ell} C_{p\ell} L^2}\left[\frac{KW_4}{(\Delta\bar{y}_6)^2} + \frac{KW_2}{(\Delta\bar{x})^2} + h_{b2} L\left(\frac{1}{\Delta\bar{x}} + \frac{1}{\bar{y}6}\right]\right\}^{-1} *$$

$$\{H^{\Delta}_{i,k,6} + \frac{\Delta t\, T_{ref}}{2L^2}\left[KW_4 \frac{\theta_{i,k-1,6}}{(\Delta\bar{y}_6)^2} + KW_4^{\Delta}\left(\frac{\theta^{\Delta}_{i,k-1,6} - \theta^{\Delta}_{i,k,6}}{(\Delta\bar{y}_6)^2}\right)\right.$$

$$+ KW_2 \frac{\theta_{i+1,k,6}}{(\Delta\bar{x})^2} + KW_2^{\Delta}\left(\frac{\theta^{\Delta}_{i+1,k,6} - \theta^{\Delta}_{i,k,6}}{(\Delta\bar{x})^2}\right)$$

$$+ h_{b2} L(2\theta_{b2} - \theta^{\Delta}_{i,k,6})\left(\frac{1}{\Delta\bar{x}} + \frac{1}{\Delta\bar{y}_6}\right) + \left[\frac{KW_4}{(\Delta\bar{y}_6)^2}\right.$$

$$\left.\left.\left. + \frac{KW_2}{(\Delta\bar{x})^2} + h_{b2} L\left(\frac{1}{\Delta\bar{x}}\frac{1}{\Delta\bar{y}_6}\right)\right]\left[\frac{1}{C_{p\ell}}\left(\hat{C}_{ps}\theta_m + \frac{L_f}{T_{ref}}\right) - \theta_m\right]\right]\right\} \qquad (55c)$$

The insulated boundary condition at the heater centerline is handled in the same manner as for a type 1 element. This element cannot exist over the gap centerline (i = 1).

2.3.2.6 Type 6 Element, Ice-Ambient Interface

Figure 5f shows the type 6 element which has convective surfaces on the top and right side nodal interfaces. The energy terms for this situation are:

$$q_1 = KW_1\left(\frac{T_{i,k,6} - T_{i-1,k,6}}{2\,\Delta x}\right)\Delta y_6$$

$$+ KW_1^{\Delta}\left(\frac{T^{\Delta}_{i,k,6} - T^{\Delta}_{i-1,k,6}}{2\,\Delta x}\right)\Delta y_6$$

$$q_2 = hb_2 \left(\frac{T_{i,k,6} + T^{\Delta}_{i,k,6}}{2} - T_{b2}\right) \Delta y_6$$

$$q_3 = h_{b2} \left(\frac{T_{i,k,6} + T^{\Delta}_{i,k,6}}{2} - T_{b2}\right) \Delta x$$

$$q_4 = -KW_4 \left(\frac{T_{i,k,6} - T_{i,k-1,6}}{2\,\Delta y_6}\right) \Delta x$$

$$- KW^{\Delta}_4 \left(\frac{T^{\Delta}_{i,k,6} - T^{\Delta}_{i,k-1,6}}{2\Delta y_6}\right) \Delta x$$

$$q_{STOR} = \left(\frac{H_{i,k,6} - H^{\Delta}_{i,k,6}}{\Delta t}\right) \Delta x\, \Delta y_6 \qquad (56)$$

Substituting equation (56) into equation (41), incorporating equation (14), and solving for $H_{i,k,6}$ yields the three governing equations corresponding to each phase.

For the solid phase:

$$H_{i,k,6} = \left\{1 + \frac{\Delta t}{2\rho_s C_{ps} L^2}\left[\frac{KW_4}{(\Delta\bar{y}_6)^2} + \frac{KW_1}{(\Delta\bar{x})^2} + h_{b2} L\left(\frac{1}{\Delta\bar{x}} + \frac{1}{\Delta\bar{y}_6}\right)\right]\right\}^{-1} *$$

$$\left\{H^{\Delta}_{i,k,6} + \frac{\Delta t\, T_{ref}}{2L^2}\left[KW_4 \frac{\theta_{i,k-1,6}}{(\Delta\bar{y}_6)^2} + KW^{\Delta}_4 \left(\frac{\theta^{\Delta}_{i,k-1,6} - \theta^{\Delta}_{i,k,6}}{(\Delta\bar{y})^2}\right)\right.\right.$$

$$+ KW_1 \frac{\theta_{i-1,k,6}}{(\Delta\bar{x})^2} + KW^{\Delta}_1 \left(\frac{\theta^{\Delta}_{i-1,k,6} - \theta^{\Delta}_{i,k,6}}{(\Delta\bar{x})^2}\right)$$

$$\left.\left. + h_{b2} L(2\,\theta_{b2} - \theta^{\Delta}_{i,k,6})\left(\frac{1}{\Delta\bar{x}} \quad \frac{1}{\Delta\bar{y}_6}\right)\right]\right\} \qquad (57a)$$

For the melting point:

$$H_{i,k,6} = H^{\Delta}_{i,k,6} + \frac{\Delta t\, T_{ref}}{2L^2}\left\{KW_4 \frac{\theta_{i,k-1,6}}{(\Delta\bar{y}_6)^2}\right.$$

$$\left. + KW^{\Delta}_4 \left(\frac{\theta^{\Delta}_{i,k-1,6} - \theta^{\Delta}_{i,k,6}}{(\Delta\bar{y}_6)^2}\right) + KW_1 \frac{\theta_{i-1,k,6}}{(\Delta\bar{x})^2}\right.$$

$$+ KW_1^{\Delta} \left(\frac{\theta^{\Delta}_{i-1,k,6} - \theta^{\Delta}_{i,k,6}}{(\Delta\bar{x})^2}\right) + h_{b2}\, L(2\theta_{b2} - \theta^{\Delta}_{i,k,6})$$

$$\left(\frac{1}{\Delta\bar{x}} + \frac{1}{\Delta\bar{y}_6}\right) - \left[\frac{KW_4}{(\Delta\bar{y}_6)^2} + \frac{KW_1}{(\Delta\bar{x})^2} + h_{b2}\, L\left(\frac{1}{\Delta\bar{x}} + \frac{1}{\Delta\bar{y}_6}\right)\right] \theta_m \Big\} \qquad (57b)$$

For the liquid phase:

$$H_{i,k,6} = \left\{1 + \frac{\Delta t}{2\rho_{\ell}\, C_{p\ell}\, L^2}\left[\frac{KW_4}{(\Delta\bar{y}_6)^2} + \frac{KW_1}{(\Delta\bar{x})^2} + h_{b2}\, L\left(\frac{1}{\Delta\bar{x}} + \frac{1}{\Delta\bar{y}_6}\right)\right]\right\}^{-1} *$$

$$\left\{H^{\Delta}_{i,k,6} + \frac{\Delta t\, T_{ref}}{2L^2}\left[KW_4 \frac{\theta_{i,k-1,6}}{(\Delta\bar{y}_6)^2} + KW_4^{\Delta}\left(\frac{\theta^{\Delta}_{i,k-1,6} - \theta^{\Delta}_{i,k,6}}{(\Delta\bar{y}_6)^2}\right)\right.\right.$$

$$+ KW_1 \frac{\theta_{i-1,k,6}}{(\Delta\bar{x})^2} + KW_1^{\Delta}\left(\frac{\theta^{\Delta}_{i-1,k,6} - \theta^{\Delta}_{i,k,6}}{(\Delta\bar{x})^2}\right)$$

$$+ h_{b2}\, L(2\theta_{b2} - \theta_{i,k,6})\left(\frac{1}{\Delta\bar{x}} + \frac{1}{\Delta\bar{y}_6}\right) + \left[\frac{KW_4}{(\Delta\bar{y}_6)^2} + \frac{KW_1}{(\Delta\bar{x})^2}\right.$$

$$\left.\left. + h_{b2}\, L\left(\frac{1}{\Delta\bar{x}} + \frac{1}{\Delta\bar{y}}\right)\right]\left[\frac{1}{C_{p\ell}}\left(\hat{C}_{ps}\,\theta_m - \frac{L_f}{T_{ref}}\right) - \theta_m\right]\right\} \qquad (57c)$$

The insulated boundary condition over the heater gap centerline is handled the same as for a type 1 element. This element cannot occur over the heater centerline (i = n).

2.3.2.7 Type 7 Element, Ice-Ambient Interface

This type of element has convective surfaces on the left and right nodal interfaces and conductive surfaces on the top and bottom interfaces as shown in Figure 6a. The energy terms are:

$$q_1 = h_{b2}\left(\frac{T_{i,k,6} + T^{\Delta}_{i,k,6}}{2} - T_{b2}\right) \Delta y_6$$

$$q_2 = hb_2 \left(\frac{T_{i,k,6} + T^{\Delta}_{i,k,6}}{2} - T_{b2}\right) \Delta y_6$$

$$q_3 = -KW_3\left(\frac{T_{i,k+1,6} - T_{i,k,6}}{2\,\Delta y_6}\right) \Delta x$$

$$- KW^{\Delta}_3\left(\frac{T^{\Delta}_{i,k+1,6} - T^{\Delta}_{i,k,6}}{2\,\Delta y_6}\right) \Delta x$$

$$q_4 = -KW_4\left(\frac{T_{i,k,6} - T_{i,k-1,6}}{2\,\Delta y_6}\right) \Delta x$$

$$- KW^{\Delta}_4\left(\frac{T^{\Delta}_{i,k,6} - T^{\Delta}_{i,k-1,6}}{2\Delta y_6}\right) \Delta x$$

$$q_{STOR} = \left(\frac{H_{i,k,6} - H^{\Delta}_{i,k,6}}{\Delta t}\right) \Delta x\, \Delta y_6 \qquad (58)$$

Substituting equation (58) into the energy balance, equation (41), incorporating equation (14), and solving for $H_{i,k,6}$ produces the governing equations for the three phases.

For the solid phase:

$$H_{i,k,6} = \{1 + \frac{\Delta t}{2\rho_s C_{ps} L^2}\left[\frac{KW_3 + KW_4}{(\Delta\bar{y}_6)^2} + \frac{2\,h_{b2}\,L}{\Delta\bar{x}}\right]\}^{-1}$$

$$\{H^{\Delta}_{i,k,6} + \frac{\Delta t\, T_{ref}}{2L^2}\left[\frac{2\,h_{b2}\,L}{\Delta\bar{x}}\,(2\,\theta_{b2} - \theta^{\Delta}_{i,k,6}) + KW_3\,\frac{\theta_{i,k+1,6}}{(\Delta\bar{y}_6)^2}\right.$$

$$+ KW^{\Delta}_3\left(\frac{\theta^{\Delta}_{i,k+1,6} - \theta^{\Delta}_{i,k,6}}{(\Delta\bar{y}_6)^2}\right) + KW_4\,\frac{\theta_{i,k-1,6}}{(\Delta\bar{y}_6)^2}$$

$$\left. + KW^{\Delta}_4\left(\frac{\theta^{\Delta}_{i,k-1,6} - \theta^{\Delta}_{i,k,6}}{(\Delta\bar{y}_6)^2}\right)\right]\} \qquad (59a)$$

For the melting point:

$$H_{i,k,6} = H^{\Delta}_{i,k,6} + \frac{\Delta t\, T_{ref}}{2L^2}\left\{\frac{2\, h_{b2}\, L}{\Delta \bar{x}}\,(2\,\theta_{b2} - \theta^{\Delta}_{i,k,6})\right.$$

$$+ KW_3\,\frac{\theta_{i,k+1,6}}{(\Delta \bar{y}_6)^2} + KW^{\Delta}_3\left(\frac{\theta^{\Delta}_{i,k+1,6} - \theta^{\Delta}_{i,k,6}}{(\Delta \bar{y}_6)^2}\right) + KW_4\,\frac{\theta_{i,k-1,6}}{(\Delta \bar{y}_6)^2}$$

$$\left. + KW^{\Delta}_4\left(\frac{\theta^{\Delta}_{i,k-1,6} - \theta^{\Delta}_{i,k,6}}{(\Delta \bar{y}_6)^2}\right) - \left[\frac{2\, h_{b2}}{\Delta \bar{x}} + \frac{KW_3 + KW_4}{(\Delta \bar{y}_6)^2}\right]\theta_m\right\} \qquad (59b)$$

For the liquid phase:

$$H_{i,k,6} = \left\{1 + \frac{\Delta t}{2\rho_\ell\, C_{p\ell}\, L^2}\left[\frac{2\, h_{b2}}{\Delta \bar{x}} + \frac{KW_3 + KW_4}{(\Delta \bar{y}_6)^2}\right]\right\}^{-1} *$$

$$\left\{H_{i,k,6} + \frac{\Delta t\, T_{ref}}{2L^2}\left[\frac{2\, hb_2 L}{\Delta \bar{x}}\,(2\,\theta_{b2} - \theta^{\Delta}_{i,k,6}) + KW_3\,\frac{\theta_{i,k+1,6}}{(\Delta \bar{y}_6)^2}\right.\right.$$

$$+ KW^{\Delta}_3\left(\frac{\theta^{\Delta}_{i,k+1,6} - \theta^{\Delta}_{i,k,6}}{(\Delta \bar{y}_6)^2}\right) + KW_4\,\frac{\theta_{i,k-1,6}}{(\Delta \bar{y}_6)^2}$$

$$+ KW^{\Delta}_4\left(\frac{\theta^{\Delta}_{i,k-1,6} - \theta^{\Delta}_{i,k,6}}{(\Delta \bar{y}_6)^2}\right) + \left[\frac{2\, h_{b2}\, L}{\Delta \bar{x}} + \frac{KW_3 + KW_4}{(\Delta \bar{y}_6)^2}\right]$$

$$\left.\left[\frac{1}{C_{p\ell}}\left(\dot{C}_{ps}\,\theta_m + \frac{L_f}{T_{ref}}\right) - \theta_m\right]\right]\right\} \qquad (59c)$$

The insulated boundary condition does not apply here because this type of element can never occur over the heater or gap centerlines (i = 1 or n).

2.3.2.8 Type 8 Element, Ice-Ambient Interface

Figure 6b shows the type 8 element, which has convective surfaces on the right, left, and top sides and a conductive nodal interface on the bottom. The energy terms for these conditions are:

$$q_1 = h_{b2} \left(\frac{T_{i,k,6} + T^{\Delta}_{i,k,6}}{2} - T_{b2}\right) \Delta y_6$$

$$q_2 = hb_2 \left(\frac{T_{i,k,6} + T^{\Delta}_{i,k,6}}{2} - T_{b2}\right) \Delta y_6$$

$$q_3 = h_{b2} \left(\frac{T_{i,k,6} + T^{\Delta}_{i,k,6}}{2} - T_{b2}\right) \Delta x$$

$$q_4 = -KW_4 \left(\frac{T_{i,k,6} - T_{i,k-1,6}}{2\,\Delta y_6}\right) \Delta x$$

$$- KW^{\Delta}_4 \left(\frac{T^{\Delta}_{i,k,6} - T^{\Delta}_{i,k-1,6}}{2\Delta y_6}\right) \Delta x$$

$$q_{STOR} = \left(\frac{H_{i,k,6} - H^{\Delta}_{i,k,6}}{\Delta t}\right) \Delta x \, \Delta y_6 \qquad (60)$$

Introducing these terms into the energy balance, equation (41), incorporating the temperature enthalpy relationship, equation (14), and solving for $H_{i,k,6}$ yields the governing equation for each phase.

For the solid phase:

$$H_{i,k,6} = \left\{1 + \frac{\Delta t}{2\rho_s C_{ps} L^2}\left[\frac{KW_4}{(\Delta \bar{y}_6)^2} + h_{b2} L \left(\frac{2}{\Delta \bar{x}} + \frac{1}{\Delta \bar{y}_6}\right)\right]\right\}^{-1} *$$

$$\left(H^{\Delta}_{i,k,6} + \frac{\Delta t\, T_{ref}}{2L^2}\left[KW_4 \frac{\theta_{i,k-1,6}}{(\Delta \bar{y}_6)^2} + KW^{\Delta}_4 \left(\frac{\theta^{\Delta}_{i,k-1,6} - \theta^{\Delta}_{i,k,6}}{(\Delta \bar{y}_6)^2}\right)\right.\right.$$

$$\left.\left. + h_{b2} L \left(2\,\theta_{b2} - \theta_{i,k,6}\right) \left(\frac{2}{\Delta \bar{x}} + \frac{1}{\Delta \bar{y}_6}\right)\right]\right\} \qquad (61a)$$

For the melting point:

$$H_{i,k,6} = H^{\Delta}_{i,k,6} + \frac{\Delta t\ T_{ref}}{2L^2}\ KW_4\ \frac{\theta_{i,k-1,6}}{(\Delta\bar{y}_6)^2}$$

$$+ KW^{\Delta}_4\ \left(\frac{\theta^{\Delta}_{i,k-1,6} - \theta^{\Delta}_{i,k,6}}{(\Delta\bar{y}_6)^2}\right) + h_{b2}\,L\,(2\,\theta_{b2} - \theta^{\Delta}_{i,k,6})\ \left(\frac{2}{\Delta\bar{x}} + \frac{1}{\Delta\bar{y}_6}\right)$$

$$- \left[\frac{KW_4}{(\Delta\bar{y}_6)^2} + h_{b2}\,L\,\left(\frac{2}{\Delta\bar{x}} + \frac{1}{\Delta\bar{y}_6}\right)\right]\theta_m\Big\} \qquad (61b)$$

For the liquid phase:

$$H_{i,k,6} = \left\{1 + \frac{\Delta t}{2\rho_{\ell}\,C_{p\ell}\,L^2}\left[\frac{KW_4}{(\Delta\bar{y}_6)^2} + h_{b2}\,L\left(\frac{2}{\Delta\bar{x}} + \frac{1}{\Delta\bar{y}_6}\right)\right]\right\}^{-1} *$$

$$\Big\{H^{\Delta}_{i,k,6} + \frac{\Delta t\ T_{ref}}{2L^2}\left[KW_4\ \frac{\theta_{i,k-1,6}}{(\Delta\bar{y}_6)^2} + KW^{\Delta}_4\ \left(\frac{\theta^{\Delta}_{i,k-1,6} - \theta^{\Delta}_{i,k,6}}{(\Delta\bar{y}_6)^2}\right)\right.$$

$$+ h_{b2}\,L\,(2\,\theta_{b2} - \theta^{\Delta}_{i,k,6})\ \left(\frac{2}{\Delta\bar{x}} + \frac{1}{\Delta\bar{y}_6}\right) + \left[\frac{KW_4}{(\Delta\bar{y}_6)^2}\right.$$

$$\left.\left. + h_{b2}\,L\left(\frac{2}{\Delta\bar{x}} + \frac{1}{\Delta\bar{y}_6}\right)\right]\left[\frac{1}{C_{p\ell}}\left(\hat{C}_{ps}\,\theta_m + \frac{L_f}{T_{ref}}\right) - \theta_m\right]\right]\Big\} \qquad (61c)$$

The insulated boundary conditions at the heater and gap centerlines are of no concern because this type of element can never occur at these positions.

2.3.2.9 Type 9 Element, Abrasion Shield-Ice Interface

The final type of element occurs at the abrasion shield-ice interface, as shown in Figure 6c. Figure 7b shows this type of node and the associated energies passing into and out of the element. The energy balance equation is slightly more involved:

$$q^4 = q_1^a + q_1^i + q_2^a + q_2^i + q_3 + q_{STOR} \tag{62}$$

The energy terms of this equation are:

$$q_1^a = K_5 \left(\frac{T_{1,k,5} - T_{1-1,k,5} + T^{\Delta}_{1,k,5} - T^{\Delta}_{1-1,k,5}}{2\Delta x}\right) \frac{\Delta y_5}{2}$$

$$q_1^i = KW_1 \left(\frac{T_{i,k,6} - T_{i-1,k,6}}{2\Delta x}\right) \frac{\Delta y_6}{2}$$

$$+ KW_1 \left(\frac{T^{\Delta}_{i,k,6} - T^{\Delta}_{i-1,k,6}}{2\Delta x}\right) \frac{\Delta y_6}{2}$$

$$q_2^a = -K_5 \left(\frac{T_{i+1,k,5} - T_{i,k,5} + T^{\Delta}_{i+1,k,5} - T^{\Delta}_{i,k,5}}{2\Delta x}\right) \frac{\Delta y_5}{2}$$

$$q_2^i = -KW_2 \left(\frac{T_{i+1,k,6} - T_{i,k,6}}{2\Delta x}\right) \frac{\Delta y_6}{2}$$

$$- KW_2^{\Delta} \left(\frac{T^{\Delta}_{i+1,k,6} - T^{\Delta}_{i,k,6}}{2\Delta x}\right) \frac{\Delta y_6}{2}$$

$$q_3 = -KW_3 \left(\frac{T_{i,k+1,6} - T_{i,k,6}}{2\Delta y_6}\right) \Delta x - KW_3^{\Delta} \left(\frac{T^{\Delta}_{i,k+1,6} - T^{\Delta}_{i,k,6}}{2\Delta y_6}\right) \Delta x$$

$$q_4 = -K_5 \left(\frac{T_{i,k,5} - T_{i,k-1,5} + T^{\Delta}_{i,k,5} - T^{\Delta}_{i,k-1,5}}{2\Delta y_5}\right) \Delta x$$

$$q_{STOR} = \left(\frac{H_{i,k,6} - H^{\Delta}_{i,k,6}}{\Delta t}\right) \frac{\Delta x \, \Delta y_6}{2} + \rho_5 C_{p5} \left(\frac{T_{i,k,6} - T^{\Delta}_{i,k,6}}{\Delta t}\right) \frac{\Delta x \Delta y_5}{2} \tag{63}$$

Substituting these terms into equation (62), incorporating the enthalpy-temperature relationship, equation (14), and solving for $H_{i,k,6}$ yields the final governing equations for the three phases.

For the solid phase:

$$H_{1,k,6} = \left(1 + \frac{\rho_5 \hat{C}_{p5}}{\rho_s \hat{C}_{ps}} + \frac{\Delta t}{2\rho_s \hat{C}_{ps} L^2}\right) \left[\frac{2 K_5}{\Delta \bar{y}_5 \Delta \bar{y}_6} + \frac{2 KW_3}{(\Delta \bar{y}_6)^2}\right.$$

$$+ \frac{KW_1 + KW_2}{(\Delta\bar{x})^2} + \frac{\Delta\bar{y}_5}{\Delta\bar{y}_6} \frac{2K_5}{(\Delta\bar{x})^2}]]^{-1} * \{H^{\Delta}_{i,k,6} + \rho_5 C_{p5} T_{ref}$$

$$\theta^{\Delta}_{i,k,6} \frac{\Delta\bar{y}_5}{\Delta\bar{y}_6} + \frac{T_{ref}\,\Delta t}{2L^2} [2K_5 \frac{\theta_{i,k-1,5}}{\Delta\bar{y}_5\,\Delta\bar{y}_6}$$

$$+ 2K_5 (\frac{\theta_{i,k-1,5} - \theta_{i,k,5}}{\Delta\bar{y}_5\,\Delta\bar{y}_6}) + 2KW_3 \frac{\theta_{i,k+1,6}}{(\Delta\bar{y}_6)^2}$$

$$+ 2KW^{\Delta}_3 (\frac{\theta^{\Delta}_{i,k+1,6} - \theta^{\Delta}_{i,k,6}}{(\Delta\bar{y}_6)^2}) + KW_2 \frac{\theta_{i+1,k,6}}{(\Delta\bar{x})^2}$$

$$+ KW^{\Delta}_2 (\frac{\theta^{\Delta}_{i+1,k,6} - \theta^{\Delta}_{i,k,6}}{(\Delta\bar{x})^2}) + K_5 \frac{\Delta\bar{y}_5}{\Delta\bar{y}_6} (\frac{\theta_{i+1,k,5} + \theta^{\Delta}_{i+1,k,5} - \theta^{\Delta}_{i,k,5}}{(\Delta\bar{x})^2})$$

$$+ KW_1 \frac{\theta_{i-1,k,6}}{(\Delta\bar{x})^2} + KW^{\Delta}_1 (\frac{\theta^{\Delta}_{i-1,k,6} - \theta^{\Delta}_{i,k,6}}{(\Delta\bar{x})^2})$$

$$+ K_5 \frac{\Delta\bar{y}_5}{\Delta\bar{y}_6} (\frac{\theta_{i-1,k,5} + \theta^{\Delta}_{i-1,k,6} - \theta^{\Delta}_{i,k,5}}{(\Delta\bar{x})^2})]\} \qquad (64a)$$

For the melting point:

$$H_{i,k,6} = H^{\Delta}_{i,k,6} + \rho_5 \hat{C}_{p5} \frac{\Delta\bar{y}_5}{\Delta\bar{y}_6} \theta^{\Delta}_{i,k,6}$$

$$+ \frac{T_{ref}\,\Delta t}{2L^2} \{2K_5 (\frac{\theta_{i,k-1,5} + \theta^{\Delta}_{i,k-1,5} - \theta^{\Delta}_{i,k,5}}{\Delta\bar{y}_5\,\Delta\bar{y}_6})$$

$$+ 2KW_3 \frac{\theta_{i,k+1,6}}{(\Delta\bar{y}_6)^2} + 2KW^{\Delta}_3 (\frac{\theta^{\Delta}_{i,k+1,6} - \theta^{\Delta}_{i,k,6}}{(\Delta\bar{y}_6)^2}) + KW_2 \frac{\theta_{i+1,k,6}}{(\Delta\bar{x})^2}$$

$$+ KW^{\Delta}_2 (\frac{\theta^{\Delta}_{i+1,k,6} - \theta^{\Delta}_{i,k,6}}{(\Delta\bar{x})^2}) + K_5 \frac{\Delta\bar{y}_5}{\Delta\bar{y}_6} (\frac{\theta_{i+1,k,5} + \theta^{\Delta}_{i+1,k,5} - \theta^{\Delta}_{i,k,5}}{(\Delta\bar{x})^2})$$

$$+ KW_1 \frac{\theta_{i-1,k,6}}{(\Delta\bar{x})^2} + KW^{\Delta}_1 (\frac{\theta^{\Delta}_{i-1,k,6} - \theta^{\Delta}_{i,k,6}}{(\Delta\bar{x})^2})$$

$$+ K_5 \frac{\Delta\bar{y}_5}{\Delta\bar{y}_6} (\frac{\theta_{i-1,k,5} - \theta^{\Delta}_{i,k,5} + \theta^{\Delta}_{i-1,k,5}}{(\Delta\bar{x})^2}) - [\rho_5 \hat{C}_{p5} T_{ref} \frac{\Delta\bar{y}_5}{\Delta\bar{y}_6}$$

$$+ \frac{\Delta t\, T_{ref}}{2L^2} (\frac{2K_5}{\Delta\bar{y}_5\,\Delta\bar{y}_6} + \frac{2KW_3}{(\Delta\bar{y}_6)^2} + \frac{KW_1 + KW_2}{(\Delta\bar{x})^2} + \frac{\Delta\bar{y}_5}{\Delta\bar{y}_6} \frac{2K_5}{(\Delta\bar{x})^2})] \theta_m\}$$

(64b)

For the liquid phase:

$$H_{i,k,6} = \{1 + \frac{\rho_5 \hat{C}_{p5}}{\rho_\ell C_{p\ell}} \frac{\Delta\bar{y}_5}{\Delta\bar{y}_6} + \frac{\Delta t}{2\rho_\ell C_{p\ell} L^2} [\frac{2K_5}{\Delta\bar{y}_5 \Delta\bar{y}_6} + \frac{2KW_3}{(\Delta\bar{y}_6)^2}$$

$$+ \frac{KW_1 + KW_2}{(\Delta\bar{x})^2} + \frac{\Delta\bar{y}_5}{\Delta\bar{y}_6} \frac{2K_5}{(\Delta\bar{x})^2}]\}^{-1} * \{H^{\Delta}_{i,k,6}$$

$$+ \rho_5 \hat{C}_{p5} T_{ref} \theta^{\Delta}_{i,k,5} \frac{\Delta\bar{y}_5}{\Delta\bar{y}_6} + \frac{\Delta t\, T_{ref}}{2L^2} [2K_5 \frac{\theta_{i,k-1,5}}{\Delta\bar{y}_5 \Delta\bar{y}_6}$$

$$+ 2K_5 (\frac{\theta^{\Delta}_{i,k-1,5} - \theta^{\Delta}_{i,k,5}}{\Delta\bar{y}_5 \Delta\bar{y}_6}) + 2KW_3 \frac{\theta_{i,k+1,6}}{(\Delta\bar{y}_6)^2}$$

$$+ 2KW^{\Delta}_3 (\frac{\theta^{\Delta}_{i,k+1,6} - \theta^{\Delta}_{i,k,6}}{(\Delta\bar{y}_6)^2}) + KW_2 \frac{\theta_{i+1,k,6}}{(\Delta\bar{x})^2}$$

$$+ KW^{\Delta}_2 (\frac{\theta^{\Delta}_{i+1,k,6} - \theta^{\Delta}_{i,k,6}}{(\Delta\bar{x})^2}) + K_5 \frac{\Delta\bar{y}_5}{\Delta\bar{y}_6} \frac{\theta_{i+1,k,5}}{(\Delta\bar{x})^2}$$

$$+ K_5 \frac{\Delta\bar{y}_5}{\Delta\bar{y}_6} (\frac{\theta^{\Delta}_{i+1,k,5} - \theta^{\Delta}_{i,k,5}}{(\Delta\bar{x})^2}) + KW_1 \frac{\theta_{i-1,k,6}}{(\Delta\bar{x})^2}$$

$$+ KW^{\Delta}_1 (\frac{\theta^{\Delta}_{i-1,k,6} - \theta^{\Delta}_{i,k,6}}{(\Delta\bar{x})^2}) + K_5 \frac{\Delta\bar{y}_5}{\bar{y}_6} \frac{\theta_{i-1,k,5}}{(\Delta\bar{x})^2}$$

$$+ K_5 \frac{\Delta\bar{y}_5}{\Delta\bar{y}_6} (\frac{\theta^{\Delta}_{i-1,k,5} - \theta^{\Delta}_{i,k,5}}{(\Delta\bar{x})^2})] + [\rho_5 \hat{C}_{p5} T_{ref} \frac{\Delta\bar{y}_5}{\Delta\bar{y}_6}$$

$$+ \frac{T_{ref}\, \Delta t}{2L^2} (\frac{2K_5}{\Delta\bar{y}_5 \Delta\bar{y}_6} + \frac{2KW_3}{(\Delta\bar{y}_6)^2} + \frac{KW_1 + KW_2}{(\Delta\bar{x})^2}$$

$$+ \frac{\Delta\bar{y}_5}{\Delta\bar{y}_6} \frac{2K_5}{(\Delta\bar{x})^2})] [\theta_m - \frac{1}{C_{p\ell}} (\hat{C}_{ps} \theta_m + \frac{L_f}{T_{ref}})]\}$$

(64c)

These equations are identical to those developed by Chao [4] for the abrasion shield-ice interface, further validating the energy balance approach.

2.4 NUMERICAL SOLUTION BY COMPUTER IMPLEMENTATION

2.4.1 Gauss-Seidel Point Iterative Method

The Crank-Nicolson finite differencing formulation results in a set of simultaneous algebraic equations that must be solved at each point in the spatial grid for each time step. There are several methods available for solving the matrices resulting from the set of simultaneous equations. Some use matrix inversions, and others use iterative processes. An iterative process is necessary for the ice layer because the nodal phase condition, solid, liquid, or ice, is not known in advance. The Gauss-Seidel point iterative method was chosen because it was already incorporated by Chao [4] in solving for the composite body nodal temperatures. He had also used it for the ice layer.

The Gauss-Seidel iterative process starts for each time step with an initial approximation derived from the previous time step. The equations are solved for the desired nodal quantity, enthalpy or temperature, as can be seen from the final equations for the ice layer and the composite body. The initial approximation is improved by passing through the spatial grid and solving the equations at each point. This process is repeated many times, eventually resulting in a converged set of values satisfying the set of equations for the spatial grid of nodes.

For this study, the iteration process was considered to be converged when the difference between the previous and present iteration was less than 0.01%. Once this criterion was met, the iterative process was started for the next time step, using the final converged matrix of values from the previous time step as the initial values.

The Crank-Nicolson formulation results in an unconditionally stable set of equations. Reference [9] contains a more complete discussion of the suitability and stability of the method.

2.4.2 Numerical Program Algorithm

A complete flow chart for the computer program is shown in Figures 8 and 9. It is identical to Chao's since this study was based on his work. The main program is almost identical to Chao's, except for a few changes necessary to allow incorporation of the variable ice thickness subroutine. Parts of the original program pertaining to the ice layer were replaced by the new variable ice thickness algorithm.

All of the features of the original Chao program are still present except for ice shedding. Information pertaining to this has been eliminated from the input data set. However, the original shedding algorithm has not been deleted from the program and could be made operational.

Chapter 3

DISCUSSION OF RESULTS

3.1 VERIFICATION OF THE VARIABLE ICE THICKNESS ALGORITHM

The first step in validating the variable ice thickness algorithm was to compare it to Marano's [3] and Chao's [4] numerical models for the case of two-dimensional conditions with uniform ice thickness. These comparisons were made in order to make sure that the program correctly handled the base case of constant thickness ice. Heater gaps were included in many of the two-dimensional runs. For all cases, the variable ice thickness model simplified correctly and yielded virtually identical results.

Another approach was used in validating the results for variable thickness ice layers. Symmetrical ice shapes were run to see if symmetrical temperature distributions resulted. In all of the cases studied, a symmetrical temperature distribtion was observed.

3.2 VARIABLE ICE THICKNESS PROGRAM RESULTS

As a preliminary step towards implementing the two-dimensional code for a variable thickness ice layer, Marano's one-dimensional code was run for a deicer model with various ice layer thicknesses. The object of these runs was to aid in the determination of relevant changes in thermal transients due to ice layer thickness. This information can be provided using the one-dimensional model with much less cpu time than with a two-dimensional code.

Figure 10 is the plot obtained from results generated with Marano's code using the deicer model of Table 1. The temperature rise of the ice-abrasion shield interface is plotted against time for a heater power density of 25 W/in^2 and for various uniform ice layer thicknesses. The external convection coefficient is 200 $BTU/hr\text{-}ft^2\text{-}^\circ F$. Temperature rise is defined as the total rise to 32 °F from the initial temperature in the ice layer. Phase change is not considered.

There are several features of this plot that must be noted. The most important aspect is that the curves for ice thicknesses of 0.5, 0.25, and 0.125 inches are identical. This shows that, for these thicknesses, the outer convective surface has no influence on the time it takes for the ice-abrasion shield interface to reach 32° F. The curve corresponding to this set of ice thicknesses will be called the "base curve."

Two other important features will be called the "critical thickness" and the "deviation temperature rise." The critical thickness is the minimum thickness of ice that will not result in a deviation from the base curve. In Figure 10, the critical thickness is approximately 0.125 in. For ice thicknesses above 0.125 inches, the temperature rise versus deicing time curve will not deviate from the base curve. For ice thicknesses below 0.125 inches, the curve will deviate from the base curve at the deviation temperature rise. The deviation temperature rise for 0.0625 inches is 42 °F, and for 0.0313 inch thick ice it is 37°F.

Two points from Figure 10 were chosen as a way of demonstrating the conditions under which a variable ice thickness model is necessary to provide accurate results. The first is a point on the base curve at a thickness of 0.125 inches and a temperature rise of 60 °F (initial temperature at -28° F). The second point is on the 0.0625 inch curve at a temperature rise of 60° F. It is important to note that the second point is below the critical thickness and above the deviation temperature rise. It does not lie on the base curve.

Figures 11 and 12 show the two-dimensional variable thickness ice layer results for two mean ice layer thicknesses, 0.125 and 0.0625 inches, respectively. The initial temperature for each case is -28 °F, so that these figures

correspond to the two points mentioned above. The ice length in each case is 0.25 and 0.125 inches, respectively, and there is no heater gap. For each mean thickness, five cases of a sloped ice layer are presented, where the slope of the ice shape is designated by 0 , 10 , 20 , 30 , and 40° The location of the melt line is indicated as a function of time.

These figures clearly show the relationship between ice geometry, critical thickness, and deicer performance. For a set of conditions corresponding to a point on the base curve, Figure 11, where the mean ice thickness is greater or equal to the critical thickness, the ice geometry has a limited effect on deicer performance. Note that even with drastic changes in ice shape, where a significant portion of the ice is less than the critical thickness, there is relatively little effect on deicer performace as is shown by the gradual slope of the melt curves and the relatively constant melt times. For these cases a one-dimensional solution should provide sufficiently accurate results.

The effect on deicer performance is very pronounced when the conditions do not correspond to a point on the base curve, Figure 12, where the mean ice thickness is less than the critical thickness. The variation from the 0 ° case to the 40 ° case takes one from good deicer performance to almost no deicing at all. This plainly illustrates the need

for a two-dimensional code capable of handling a variable ice layer thickness to accurately predict the thermal transients for cases not corresponding to points on the base curve.

The base curve, critical thickness, and deviation temperature rise appear to be excellent parameters for comparing various deicer designs. For similar power inputs and external conditions, these parameters will be functions of deicer configuration and design only. The magnitudes of these values can be easily found using Marano's [3] one-dimensional code if the heater gap is not a consideration, or Chao's [4] two-dimensional code if the heater gap is a consideration.

Chapter 4

CONCLUSIONS AND RECOMMENDATIONS

A variable ice thickness algorithm was successfully applied to Chao's [4] two-dimensional transient numerical model of electrothermal deicer performance. The new model has been shown to be equivalent to Marano's [3] and Chao's [4] one and two-dimensional models for uniform ice thickness. It generates consistent and uniform results for variable thickness ice layers and allows location of the ice-liquid interface at any point in time.

Determining the conditions under which a variable thickness ice layer has an effect on deicer performance proved to be difficult. An analysis using a one-dimensional model has been shown to be useful in determining these conditions. This analysis has shown that a one-dimensional model is sufficient for problems where the mean ice thickness is equal to or greater than the critical thickness. It has also shown that a two-dimensional analysis is necessary in cases where the mean ice thickness is less than the critical thickness. The results illustrate that the thinner the mean thickness of the ice, the more important the ice shape becomes in order to predict the movement of the melt interface.

Further research in this area should be directed toward developing a model that can approximate the actual two-dimensional blade geometry in addition to the variable ice thickness. A numerical model being developed at The University of Toledo for this purpose is nearing completion. It uses a coordinate transformation technique to model the blade geometry, and the enthalpy method is used to model the phase change.

PART III

EXPERIMENTAL TESTING AND RESULTS

Chapter 5

EXPERIMENTAL HISTORY

Until recently, there has been very little experimental information available concerning the thermal behavior of an electrothermal deicer. Commercial manufacturers often possess such information, but consider it proprietary and do not publish it in the open literature. The existing available information comes from both laboratory and flight test data.

Gent and Cansdale [10] have published experimental transient temperature profiles from laboratory deicer pads. They used these results to validate their one-dimensional computer model. Marano [3] also used these results for the same purpose. The significance of this data is limited because the deicer pads tested were flat plate models of full size helicopter blade-deicer constructions. Actual deicers may not respond in the same manner during flight conditions. Flight test or wind tunnel data is thought to be more pertinent.

An early attempt at obtaining flight test data involved a UH-1H helicopter equipped with an electrothermal deicing system on the main and tail rotors [17]. Blade surface temperature was recorded during dry and icing conditions.

Transient data was not established because only peak temperatures were recorded during the deicing cycle. This information was not detailed enough to allow a rigorous evaluation of one and two-dimensional numerical models.

A very recent and detailed investigation promises to provide valuable flight data. Electrothermal deicing tests of a Royal Air Force HC-Mk1 Chinook helicopter have been conducted [18] by the Boeing-Vertol Company. One of the blades was equipped with both internal and external temperature sensors. Tests were run during both dry and icing conditions. A preliminary analysis of the flight data using the Baliga [1] one-dimensional computer model was conducted. The Baliga model tended to overpredict the actual temperatures, but the overall correlation appeared to be quite good.

Due to this lack of avilable experimental data which was needed to evaluate The University of Toledo computer codes, the tests described in the following chapter were conducted.

Chapter 6

FORMULATION OF THE EXPERIMENTAL METHOD

6.1 OBJECTIVE

During the past few years, icing research sponsored by the NASA Lewis Research Center has yielded several analytical computer programs developed for the prediction of the thermal behavior of an electrothermal deicer. Both one and two dimensional models have been developed, and different approaches have been used. It has not been possible, however, to validate these codes because an experimental database for electrothermal deicer performance has never been established. Therefore, a main objective of the experimental testing was to develop an experimental database, thereby providing a standard against which the computer codes could be compared. In so doing, the limitations of the mathematical models could be determined.

Another objective of this testing was to further document the ice accretion process and the resulting ice shapes. A computer program is being developed at NASA Lewis that will allow the prediction of an ice shape for a given set of conditions. Information collected during the testing would be useful in validating this numerical model of the ice accretion process.

Finally, a more general directive of the test was to record the thermal response of the blade during two different sets of conditions. The first was a condition of evaporative cooling while the blade was running wet at temperatures above the freezing point. The second was an icing condition at temperatures below the freezing point. The entire thermal response, beginning with the onset of the spray, was to be recorded. This information would enable quantitative interpretations to be made concerning the physics occurring during the icing and deicing operations.

Accomplishing these objectives would go far in establishing an experimental database documenting the thermal behavior of an electrothermal deicer. It would also provide much information concerning the thermodynamic response of an airfoil to icing and convective cooling conditions.

6.2 TEST PLAN

A UH-1H (NACA 0012) helicopter blade was outfitted with an electrothermal deicer designed and manufactured by the B. F. Goodrich Company. The resulting composite blade was heavily instrumented with thermocouples during the lamination process. The model was then mounted on the oscillating rig in the test section of the Icing Research Tunnel (IRT) at NASA Lewis. Data acquisiton consisted of subjecting the blade, which was held stationary in the present tests, to a

wide range of aerodynamic and icing conditions and recording the response.

The test conditions necessary to satisfy the objectives resulted in a four phase test program. The first phase was a dry test with no spray. Runs both with and without heat were recorded. These runs were meant to provide information on thermocouple consistency and performance, and to document the blade thermal behavior under tunnel flow conditions.

The second phase consisted of running the blade wet at temperatures above freezing, both with and without heat. The entire process temperatures, from the onset of the spray, were recorded for all runs. Those runs with heat were meant to provide information on the thermal response of the deicer while running wet. Those tests without heat were meant to record the effect of convective cooling on the blade temperature.

Phase three was an ice accretion documentation test. The heaters were not activated, which allowed the operators to enter the tunnel and record the ice shape after the ice accretion process was completed. Both tracings and photographs of the ice shapes and their cross sections were recorded. This phase was vital because the ice shapes would be lost during the deicing tests.

The final phase comprised the deicing tests. Icing conditions during these tests were meant to match those during the ice accretion documentation tests. This would allow positive identification of the ice shapes lost during shedding.

There were two parts to the deicing tests. The first part involved a simultaneous cycling of the eight heater zones, in which all of the heater zones were turned on and off at the same time. The second part consisted of a phased cycling of the heater zones. Each zone was cycled with different turn-on and turn-off times. The data analyzed in the present study was taken during the simultaneous cycling part of the testing. All of the testing was done during the period from January 31 to March 1, 1985.

6.3 INSTRUMENTATION

The model construction started with a section of a UH-1H (NACA 0012) helicopter blade. The blade was mostly aluminum with a stainless steel abrasion shield, as shown in Figure 13. The electrothermal deicer consisted of a layer of epoxy/glass insulation, a copper heater element, another layer of epoxy/glass insulation, and a stainless steel abrasion shield. The layers of the deicer were laminated to the blade using epoxy adhesive. A detailed description of the UH-1H blade and electrothermal deicer construction is presented in Figure 14 and Table 2.

The heater consisted of eight individual zones, 1.0 inch wide, which were electrically insulated from each other. Each zone was divided into a winding sub-element, 0.165 inches wide, with a gap 0.061 inches wide, which was necessary for electrical insulation. Subdividing the zones resulted in a more uniform heater output. A single heater zone layout is illustrated in Figure 15. The heater element was manufactured by B. F. Goodrich using an etching process, and was attached to a backing material that prevented damage.

Instrumentation consisted of afixing thermocouples to the blade and deicer in three layers and at three planes, as shown in Figures 16, 17, and 18. The planes were labeled AA, BB, and CC, corresponding to an upper plane, a middle plane, and a lower plane, respectively. The three layers of thermocouples were placed at the inner side of the D-spar, the inner side of the heater mat, and the outer side of the abrasion shield.

The inner side of the D-spar had eight thermocouples positioned one inch apart as closely as possible to the center of the heater zones. Thermocouples on the mat were positioned one inch apart in the center of each of the eight zones, and were attached to the center of the heater subelements rather than over a gap, as shown in Figure 15. A total of eleven thermocouples were attached, one inch apart,

to the outer surface of the abrasion shield. Eight were centered over heater zones, and the remaining three were spaced over an unheated portion of the blade.

All of the thermocouples were constructed of chromel and alumel wire, 0.003 inches in diameter. Those at the heater and substrate were spot welded at the junction and then attached to the desired location. The abrasion shield thermocouples were fabricated by drilling a hole through the abrasion shield, inserting the thermocouple wires, spot welding the junction, and dressing the surface.

After fabrication, the thermocouples were calibrated at two temperatures. The first was at room temperature, 74 °F, and the second was at 32 °F using an ice bath. In both cases, the thermocouples read within ± 1°F.

After a few preliminary bench tests, it became apparent that many of the thermocouples were inaccurate. The thermocouples were very fragile, and several had been damaged during the lamination process. Figures 16, 17, and 18 indicate the twenty-seven thermocouples that were disregarded as a result of this initial testing. These thermocouples were not used later in this study.

During the testing, the thermocouples were interfaced with the Escort II data acquisition system. This system considerably simplified the data acquisition, allowing large

numbers of thermocouple readings to be recorded quickly and efficiently. The Escort II system was operated in superplex mode, and initially scanned the fifty-four thermocouple readings once every 0.3 seconds. After operating the system for a few initial tests, it became apparent that 0.3 seconds per scan was producing more data than could be efficiently processed. The scan time was increased to 0.9 seconds, afterwhich no further problems were encountered.

A special computer program, IRT1D009, was developed that transferred the readings from Escort to an IBM 370 computer. Once the readings were transferred to the 370, they were copied onto tape for permanent storage. The computer program also processed several different types of graphical plots of the experimental data. This program was capable of storing, retrieving, and modifying the experimental database.

The heater zones for the simultaneous cycling portion of the deicing tests were connected to three different power supplies. The top three zones, the zone below the stagnation point, and the bottom four zones formed the three independent groups. This arrangement allowed different power densities to be applied to different portions of the heater.

6.4 DETERMINING THE TEST CONDITIONS

As mentioned previously, the testing was divided into four phases. The test matrix for each phase is presented in Tables 3 through 6. The definitions of the symbols representing the conditions are as follows:

V_∞ = test section air velocity (miles/hr.);

T_∞ = tunnel air stagnation temperature (°F);

α = blade angle of attack (degrees);

P1 = power supplied to bottom four heater zones (Watts/in.^{2});

P2 = power supplied to top three heater zones (Watts/in.^{2});

P3 = power supplied to heater zone just below the stagnation point (Watts/in.^{2});

t_{on} = heater on time (sec.);

t_{off} = heater off time (sec.);

n = number of heater cycles;

d = droplet diameter (microns);

LWC = liquid water content (g/m^3); and

t_{ice} = time of ice accretion (min.).

Selection of the test condition matrix was somewhat arbitrary. Duplication of a set of test conditions was avoided,

and the individual conditions were varied as much as possible. The most stringent criterion was the matching of icing conditions between the ice accretion documentation tests and the deicing tests.

6.5 TEST PROCEDURE

6.5.1 Phase I - Dry Air Tests

The procedure for the dry air tests was:

1. Establish the desired conditions for V_∞, α, and T_∞;
2. Allow the blade to reach equilibrium at T_∞;
3. Set the on/off times and power densities for the eight heater zones;
4. Activate the Escort data acquisition system and record the initial temperature distribution;
5. Turn on the heaters; and
6. Turn the heaters off, deactivate Escort, and return the tunnel to idle speed.

Steps 3 and 5 were skipped if an unheated run was desired.

Initially, the heaters were turned off if they reached temperatures greater than 160°F. After a few tests, it was found that they could tolerate much higher transient temperatures. An upper limit of about 200°F was then allowed before cutting power to the heater zones. There were a total of 46 dry runs, 35 being with heat applied, and 11 without heat.

6.5.2 Phase II - Wet Air Tests

The test procedure for the second phase was:

1. Establish the desired conditions for V_∞, α, and T_∞ ;
2. Allow the blade to reach equilibrium at T_∞ ;
3. Set the on/off times and power densities for the eight heater zones;
4. Activate the Escort data acquisition system and record the initial temperature distribution;
5. Turn on the cloud spray with the desired conditions of LWC and d;
6. Record the temperature response of the blade for five minutes;
7. Turn on the heaters; and
8. Turn the heaters off after the desired number of cycles, deactivate Escort, and turn the spray off.

Steps 3 and 7 were skipped if an unheated run was desired. In this case, Escort was deactivated after equilibrium was reached. There were a total of 45 wet runs, 10 runs being with heat applied and 35 runs being without heat. The same temperature limit for the heater zones was enforced as for the Phase I tests.

6.5.3 Phase III - Accretion Documentation Tests

The ice accretion documentation tests were performed as follows:

1. Establish the desired conditions for V_∞, α, and T_∞ ;
2. Allow the blade to reach equilibrium at T_∞ ;
3. Activate the Escort data acquisition system and record the initial temperature distribution;
4. Turn on the cloud spray with the desired conditions of LWC and d;
5. Allow the ice accretion process to continue for five minutes from spray activation;
6. Turn off the spray and deactivate Escort;
7. Return the tunnel to idle speed;
8. Enter the tunnel and document ice accretion by tracing profiles and photographing ice cross-sections; and
9. Remove the remaining accreted ice.

The accreted ice profiles were traced by sectioning the ice shape with a steam knife and inserting a cardboard template into the slot. A line was then drawn around the shape onto the cardboard. This was sufficient for recording the general ice shape, but fell short with regard to the details of the ice structure.

Another method was developed because of the presence of the electrothermal deicer. The deicer was turned on just long enough to destroy the ice adhesion at the abrasion shield surface. The ice shape was then carefully removed and sectioned with a steam knife. These sections were then pho-

tographed next to a scale in order to provide a dimensional reference. Almost all of the ice structure detail was preserved if enough care was exercised in its removal. This process resulted in some interesting and unique photographs. There were a total of 30 ice accretion documentation runs.

6.5.4 Phase IV - Deicing Tests

The procedure for the simultaneous heater zone activation tests was:

1. Establish the desired conditions for V_∞, α , T_∞ ;
2. Allow the blade to reach equilibrium at T_∞ ;
3. Set the on/off times and power densities for the eight heater zones;
4. Activate the Escort data acquisition system and record the initial temperature distribution;
5. Turn on the cloud spray with the desired conditions of LWC and d;
6. Record the temperature response of the blade for t_{ice} minutes;
7. Turn on the heaters; and
8. Turn the heaters off after the desired number of cycles, deactivate Escort, and turn the spray off.

The same heater temperature restrictions as for the Phase I and II tests were enforced in order to prevent heater burnout.

An identical procedure was used for the phased heater zone activation tests except for step 3, which was;

3. Set zonal phase lags, on/off times, and power densities.

There were 72 simultaneous heater cycling tests and 27 phased heater cycling tests.

Chapter 7

DISCUSSION OF RESULTS

7.1 PHYSICAL DESCRIPTION AND ANALYSIS OF THE EXPERIMENTAL DATA

A vast amount of data was acquired during the testing. There were a total of 211 tests over a wide range of conditions. A breakdown as to the types and numbers of the tests is included in the test matrix. For obvious reasons, it was not possible to analyze every one of the tests. It was necessary to reduce the data to an analyzable set. This was accomplished in two steps. A preliminary set of about 30 readings was randomly selected from the database. This set was studied in order to get a feel for the general physical trends that were occurring in the data. The second step was a further reduction to ten readings, allowing a detailed comparison to the numerical simulation models. The temperature versus time curves from these ten readings for selected thermocouples are shown in Figures 19 through 28. Figures 19 through 23 represent the dry heat tests, and Figures 24 through through 28 are the deicing tests. Many of the general physical characteristics and trends about to be discussed are shown on these figures.

7.1.1 General Physical Description

7.1.1.1 Dry Runs

The abrasion shield temperature response for the dry runs was observed to be very dependent upon the external flow conditions. This was expected since the external heat transfer coefficient was relatively large at the outer surface. Because of this, the abrasion shield was always at the flow freestream stagnation temperature before heat was applied.

In contrast, the initial readings of the heater and D-spar thermocouples were never at the flow freestream stagnation temperature. This behavior resulted from not allowing the blade to cold soak for long enough periods of time between runs. Residual heat from previous runs had a tendency to remain in the blade. A low convection coefficient at the inner surface coupled with the relatively large mass of the D-spar caused this condition.

In general, the temperature response at any layer was strongly influenced by the heater power density and on/off times. Most of the influence was in maximum temperature magnitude. At a given layer, the shapes of the temperature versus time curves were quite similar for different positions and conditions.

7.1.1.2 Deicing Runs

The thermal response at the abrasion shield for the deicing runs was visibly different from that for the dry runs. The initial temperature was seldom at the freestream stagnation temperature or consistent from cross-section to cross-section. This behavior was caused by a fluctuation in temperature at the onset of ice accretion.

Two types of fluctuations occured. A rise in temperature due to a latent heat effect, or a dip in temperature due to convective cooling. A correlation relating the type of fluctuation to icing conditions or position was not found. In either case, the largest deflection occurred at the onset of ice accretion, afterwhich the temperature tended to approach the ambient.

The D-spar and heater behaved in much the same manner as for the dry runs. At the heater, some of the readings showed a slight temperature deflection at the onset of ice accretion. The effect was similar to, but much more limited than at the abrasion shield. The D-spar never showed this behavior and appeared to be quite independent of the outer surface conditions.

7.1.2 Reducing the Database to an Analyzable Set

Narrowing the database down to an analyzable set that could be compared to the numerical models was necessary. A total of ten runs was chosen for the final database. This number was completely arbitrary. Five dry runs and five deicing runs were chosen. A set of criteria was used in selecting the ten readings. The deicing runs were chosen first using the following guidelines:

1. The runs were limited to a 0° angle of attack;
2. As wide a variety of ice shapes as possible was desired;
3. Runs chosen were limited to those for which the ice shape was definitely known; and
4. If possible, runs where shedding occurred were chosen.

Based on the set of deicing runs chosen, a set of dry runs with heat was chosen using the following restrictions:

1. Limit to a 0° angle of attack;
2. Attempt to match the conditions as closely as possible with those of the deicing runs already chosen;
3. Try to get a wide range of temperatures; and
4. As a last resort, vary the heater power densities.

The ten readings chosen and the conditions for each are shown in Table 7. Figures 19 through 28 present the temperature profiles for these cases. A general overview of the

temperature profiles of this set showed that it was representative and consistent with the physical trends already noted.

7.1.3 Thermocouple Response as Related to Consistency

An important part of validating the thermocouple readings was to check for consistency. Behavior should be similar from reading to reading or position to position. If a thermocouple exhibited erratic behavior for any of the ten readings, it was discarded.

For example, thermocouples 59 and 64 exhibited consistent behavior for the dry runs but not for the deicing runs. Thermocouple 59 did not respond at all in the deicing runs, and thermocouple 64 did not appear to behave consistently with respect to those at other positions. This was considered erratic behavior. Thermocouple 75 did not respond at all in the deicing runs, and thermocouple 76 did not respond in the dry runs and appeared to give inconsistent readings in the deicing runs.

The judgement as to whether or not a thermocouple was consistent or erratic was somewhat arbitrary. Disregarding a thermocouple was not usually critical because of the presence of duplicates for each position. It was safer to just disregard a thermocouple if there was any doubt about its validity. This had an effect only on the deicing tests, and involved thermocouples 64 and 76, which were disregarded.

7.1.4 Thermocouple Response as Related to Cross-Section Dependency

7.1.4.1 Dry Runs

To aid in analyzing the data, cross-section dependency between planes AA, BB, and CC was tested by plotting all three thermocouples for a given position on one graph. Some of the positions had only one good thermocouple.

As was mentioned previously, the calibration showed that the thermocouples were accurate within ± 1°F. This made the experimental error range 2°F for the dry runs. Thermocouple readings were considered to be cross-section independent if they were within 2 °F of each other at a given position for all three cross-sections.

Most of the thermocouple readings at the abrasion shield and the D-spar were within 2°F of each other for the three cross-sections at a given position. This behavior indicated that the thermocouple readings were cross-section independent for the abrasion shield and D-spar. There were no duplicates at the heater, so this analysis did not apply.

7.1.4.2 Deicing Runs

At first, the deicing runs appeared to be cross section-dependent at the abrasion shield. The peak magnitude of the thermal response varied from cross-section to cross-section at a given position. After further study, however, the

cross-section discrepancies appeared to be caused by differences in initial temperature. These differences were caused by the onset of ice accretion, as discussed in a previous section. A different approach was necessary to analyze the deicing runs.

The new approach used the temperature difference from initial to peak temperature in the cross-section comparisons. A temperature rise parameter, ΔT, was defined as the total rise from initial to peak temperature. Using this parameter in the cross-section comparisons removed the initial temperature dependency.

Before ΔT could be compared amongst the cross-sections, the experimental temperature error range needed to be established. As for the dry runs, the accuracy of any temperature measurement was within $\pm 1°F$, so that the error range of each measurement was $2°F$. Therefore, the experimental temperature difference error range was $4°F$.

Most of the temperature differences at the abrasion shield for the three cross-sections were within $4°F$ of each other at a given position. This indicated that the abrasion shield thermocouples were cross-section independent. In other words, the response at one cross-section would be representative of the other two cross-sections for a given position.

This analysis was not necessary for the heater and the D-spar. There were no duplicates at the heater and the ice accretion temperature fluctuation did not penetrate to the D-spar. The D-spar behaved exactly the same as in the dry runs, with a few exceptions.

These exceptions were due to the presence of one inch wide anti-icers at the top and bottom of the heater mat. Their presence was meant to prevent ice bridging, which could delay or stop ice from shedding. After long periods of time, the initial temperature at cross-sections AA and CC began to rise above cross-section BB. Heat from the anti-i-cers was being conducted to the D-spar. Eventually, it reached the thermocouples at cross-sections AA and CC. This phenomenon was intensified by the high thermal conducitivity of the aluminum.

Overall, a minority of readings showed this effect. Most of the substrate thermocouples behaved very similar to the dry runs.

7.1.4.3 Establishing a Representative Set of Thermocouples

Having shown that the thermocouple readings were cross-section independent allowed the selection of a representa-tive group. This was an important step as it eliminated considering cross-sections during the numerical model vali-dation.

The representative set of thermocouples is shown in Table 8. The middle cross-section, BB, was chosen at the D-spar. This cross-section was least affected by heat conducted from the anti-icers for the deicing runs. There was no choice at the heater because there were no duplicates. At the abrasion shield, the top cross-section was chosen if possible. The middle cross-section was chosen if there was not a good thermocouple at the top cross-section for a given position. These decisions were not extremely critical since the thermocouple response had been shown to be cross-section independent.

7.1.5 Thermocouple Response as Related to Position

An analysis studying the relationship between thermocouple response and position was in order. The object of this analysis was to look for and explain any physical trends in relation to position that were occurring in the experimental data.

7.1.5.1 Dry Runs

A definite positional trend was noted at the abrasion shield for the dry runs. It was noted to occur for all of the readings. A technique was used to bring this trend onto the same order of magnitude for all five of the dry readings.

The temperature rise, ΔT, from initial to peak temperature was measured and tabulated for each position and every run. They were brought onto the same order of magnitude by dividing by the average temperature rise, $(\Delta T)avg$, for each run. This technique produced surprisingly consistent results, as may be seen in Figure 29.

This plot shows a physical trend consistent for all of the dry runs. Positions 1 through 3 show an increasing magnitude in ΔT. There are no heaters at these positions, and lateral heat conduction is solely responsible for the increasing trend. Position 4 shows a sudden increase in ΔT due to the start of the heater zones. Positions 4 through 11 have heater zones.

Starting at position 4, the curve slopes downward to a minimum at position 6, the stagnation point. The curve then starts back up and increases from positions 6 through 8. The curve is almost symmetrical about a cusp at the stagnation point. This was caused by the flow symmetry and a convection coefficient which increased to a maximum at the stagnation point. The UH-1H blade is a symmetrical airfoil and there was a 0° angle of attack.

Progressing from position 8 to 9 shows a dip in the curve. This was possibly caused by an air gap running the length of the blade somewhere between the heater and the abrasion shield. An air gap would impede heat flow to the ab-

rasion shield and result in a lower peak temperature. However, it is also possible that this dip could have been a consequence of the flow behavior around the blade.

The curve continues to rise from position 9 to 11. This corresponds to the further development of the boundary layer. Correspondingly, for a flat plate in parallel flow, the convection coefficient decreases with increasing distance from the leading edge. This trend occurs whether the flow is laminar or turbulent.

The curve in Figure 29 is a physical characteristic of the blade. This hypothesis is supported by the agreement of the curve for all five of the dry runs. Heater on-times, power densities, and external flow conditions change, but the curve remains similar from reading to reading.

The same analysis used for the abrasion shield was carried out for the heater thermocouples. Once again, a consistent trend from reading to reading surfaced in the experimental data, as shown in Figure 30.

This curve shows that the temperature rise, ΔT, oscillates in a sinusoidal manner about the average temperure rise, $(\Delta T)avg$, in relation to position. This behavior was probably caused by a combination of variations in heater zone power output and varying contact resistances. The contact resistances were most likely induced by air gaps in the

construction. The data appear to indicate that this curve is a physical characteristic of the blade. It changes very little despite changes in heater power density and on/off times.

In contrast to the abrasion shield and heater, the D-spar thermocouple temperature profiles for each test were almost identical despite position. For example, a thermocouple at the inside of the D-spar at position 6 produced the same profile as a thermocouple at position 10. Even the brass noseblock at the stagnation point had no visible effect.

This position independence was caused by the construction and physical characteristics of the D-spar. The D-spar is a single piece of aluminum extrusion, and aluminum has a very high thermal conductivity. Energy conducted to the spar was evenly distributed throughout almost instantaneously. At any point in time, a sort of equilibrium existed around the D-spar resulting in position independent temperature profiles.

7.1.5.2 Deicing Runs

The dry run analysis did not apply to the deicing runs. Conditions between runs varied because of the different ice shapes at the outer surface. A consistent physical trend from run to run did not occur. As a result, a different approach was used in the analysis of the deicing runs.

The temperature rise, ΔT, was plotted versus position for each cycle. The melting point was included on the curves. The melting point temperature rise was calculated by taking the difference between the melting point, 32 °F, and the initial temperature. Graphs for each of the deicing runs are presented on Figures 31 through 35.

Figure 31 shows a set of curves from reading 197, for which the IRT temperature was 31 °F. Recorded absolute temperatures for this test are given on Figure 24. The temperature rise begins at position 3. There were no heater zones at positions 1, 2 or 3, so this temperature increase at position 3 was entirely due to lateral heat conduction.

Positions 5, 6, and 7 are in the water droplet impingement zone. Prior to heater activation, there was a glaze ice shape over these regions. The ice cap was shed before the peak temperature was reached. It did not reform before the next cycle because the abrasion shield was too warm. Position 6, the stagnation point, was not the point of lowest temperature as it was in the dry runs. Figures 24e, f and g illustrate the melting and shedding that occurred at positions 5, 6 and 7 at 32°F. The slight change in slope that is evident in the abrasion shield temperature just after the heater is turned on is characteristic of this phenomena.

Moving on to positions 8, 9, and 10 in Figure 31 shows a steady increase in temperature rise. This was probably due to the development of a turbulent boundary layer and decreasing convection coefficient.

Reading 209 is shown on Figure 32, with the absolute temperatures given on Figure 25. The IRT temperature for this reading was 28°F. This test is similar to reading 197. An ice cap was formed before each of the three cycles. However, it was shed before the temperature peak at the abrasion shield was attained for all three cycles. The same trends and physical explanations apply as in reading 197. Positions 1 and 2 show evidence of lateral conduction. Figure 25f at position 6 clearly illustrates that melting and shedding occurred at 32°F during the first two cycles. Figure 25e at position 5 illustrates that melting and shedding occurred during all three cycles. The response at position 7, Figure 25g, does not show a clear enough change in slope to indicate these effects.

Reading 213 is also similar to reading 197, and is presented on Figure 33. The IRT temperature for this reading was 24°F. Absolute temperatures are given on Figure 26. Ice was formed prior to each of the three cycles but was shed before the temperature peaked. The ice covered positions 6 and 7 on the blade. The physical explanation of the trends is the same as in reading 197. Figures 26f and g

show that melting and shedding occurred at positions 6 and 7 at 32°F during the first cycle.

Reading 234 is different from the previous readings in that shedding did not occur. The ice continued to build and increase in thickness during all three cycles. The first cycle in this test was 20/60, and the next two cycles were 30/60. The approximate ice shape is shown in the temperature rise versus position plot, Figure 34, and the absolute temperatures are given on Figure 27. The IRT temperature reading was 16°F. Starting at position 1 on Figure 34, the temperature increases to position 3. There were no heaters at these positions, and the rise was entirely due to lateral heat conduction.

An interesting feature on this plot is the decrease in temperature rise from position 3 to position 4. There is a heater at position 4, but not at position 3. There is no immediate explanation for this behavior.

Positions 5 through 7 are beneath the ice cap. The temperature rises for these positions are almost symmetrical about the stagnation point. Position 6 is not a minimum for the heated zones because it is not a convective interface as it was in the dry runs. It should be noted that melting appeared to occur at positions 5 through 7 for all three cycles, and yet shedding did not take place. Moving outside the ice cap from position 8 to 10 shows an increasing temp-

C.2

erature rise. This is characteristic of a developing turbulent boundary layer and a decreasing convection coefficient. Figures 27e, f and g are interesting in that they illustrate that melting and refreezing occurred at positions 5 and 7 during the second and third cycles, whereas position 6 does not show the required change in slope, even though the temperature exceeded 32°F.

Reading 275, Figures 35 and 28, was like reading 234 in that shedding did not occur. The IRT temperature was -3° F. Only at position 5 during the third cycle did melting and refreezing occur. This is evident from Figures 35 and 28e. A rime ice shape was formed prior to the first heater cycle and continued to grow during the second and third cycles. Positions 4 through 8 were covered by the ice cap.

Lateral heat conduction effects are evident from positions 1 through 3 in Figure 35. A lack of symmetry under the ice cap is apparent. This might have been caused by nonuniform ice adhesion. Imperfect ice adhesion could cause a contact resistance, thereby impeding the rate of heat transfer to the ice. The high degree of anti-symmetry may have also been caused by inconsistencies in the ice physical properties. Rime ice is a somewhat porous substance. Differences in the quantity of air at different positions could change the thermal conductivity and heat capacity drastically.

Progressing outside the ice cap from position 9 to 10 shows an increasing temperature rise. As before, this was probably induced by a developing turbulent boundary layer and decreasing convection coefficient.

A thin layer of frost was observed on the blade at positions outside the water droplet impingement zone. It was probably condensed onto the blade by the passing moisture laden air. The frost appeared in a more or less random pattern, largely depending upon the ice shape. A thermocouple at any one position might or might not be covered by frost. This introduced another aspect of uncertainty when studying temperature profiles at the abrasion shield.

It should be mentioned that water runback was also evident in many of the ice accretion and deicing tests.

Many of the dry run physical trends at the heaters were observed in the deicing runs. This suggested using the dry run analysis for the deicing runs and produced Figure 36. Comparing this curve to that for the dry runs, Figure 30, shows that they are almost identical. This behavior supports the idea that this response is a physical characteristic of the blade. It also implies that the heater response, when correlated in this manner, is independent of the outer surface conditions.

The D-spar thermocouples responded in a manner almost identical to the dry runs. The temperature profile for each test was independent of position. The brass at the nose-block produced no discernable deviations.

The approximate ice shapes and thicknesses for all of the deicing tests (197, 209, 213, 234, 275) are shown in Figure 37. It should again be mentioned that these ice shapes were determined during the ice accretion documentation tests. The same IRT conditions were repeated, as closely as possible, for the deicing tests. The only case where a slight difference occurred was in reading 197. In this case, the deicing test was run with a droplet diameter of 18.4 (Figure 24), whereas the accretion test involved a droplet diameter of 23.1 (Figure 37).

Chapter 8

CONCLUSIONS AND RECOMMENDATIONS

Experimental data were recorded in the NASA Lewis Icing Research Tunnel documenting the thermal behavior of a UH-1H helicopter blade fitted with an electrothermal deicer pad manufactured by the B. F. Goodrich Company. The testing was done in four phases: dry air tests; wet air tests; ice accretion tests; and deicing tests. Originally, there were eighty-one thermocouples in the deicer assembly. Bench and consistency tests reduced this number, resulting in a final total of fifty-two thermocouples that were used in the analysis. These thermocouples proved to be numerous enough and in such a variety of locations that an accurate record of the thermal response of the blade and deicer pad was obtained.

A total of two hundred and eleven IRT readings were taken, from which ten readings, five dry runs and five deicing runs, were selected for further analysis. Only a zero degree angle of attack was considered. The purposes of the analysis were: (1) to examine the thermal response of the deicer assembly for information on how flow conditions affected the temperature transients (dry runs), and on how ice accretion and the presence of ice affected the temperature

profiles (deicing runs); (2) to investigate, as much as possible, the physics of deicing; and (3) to provide a reduced database for comparison with mathematical models. The thermocouple readings from this set of runs were found to behave consistently and, within experimental error, were found to be independent of the three cross-sections on the blade where measurements were taken. This meant that the thermocouple response at a given position was the same at cross-sections AA, BB and CC, which allowed the selection of a representative set of thermocouples. This further simplified the analysis.

For the dry runs, the magnitude of the peak temperature at the abrasion shield interface was found to depend upon position in a manner consistent for all five readings. Plots of $\Delta T/(\Delta T)avg$ showed test independence at each blade position. Symmetry around the stagnation point was evident, as was a decreasing heat transfer coefficient with arc length along the blade surface. The deicing abrasion shield ΔT values were not test independent due to the different ice shapes, but showed moderate symmetry about the stagnation point. Two-dimensional effects were only noticed at the three blade positons that did not have heater elements.

For both the dry and the deicing runs, the heater response, when correlated as $\Delta T/(\Delta T)avg$ versus position, showed test independence for all ten runs. This behavior was a physical characteristic of the blade.

In contrast, the response of the D-spar thermocouples was found to be almost entirely independent of position within each test. Energy transferred to the D-spar was quickly conducted around the D-spar so that its temperature was position independent. This behavior was caused by the high thermal conductivity of the aluminum, and represents a multidimensional effect.

In the deicing runs, melting and shedding occurred in three cases (tests 197 with freestream temperature 31° F, 209 with freestream temperature 28°F, 213 with freestream temperature 24°F) before the maximum temperatures were reached. In reading 197, ice did not reform before the second cycle; for readings 209 and 213, ice reformed and shed at similar times during the second and third cycles as in the first cycle. For the last two deicing runs (tests 234 at 16°F, 275 at -3 °F), the ice did not shed, although temperatures in reading 234 indicated that some melting had occurred. The occurrence of melting, refreezing,and/or shedding was documented in the temperature response of the abrasion shield thermocouples.

The tests illustrated that the criterion for shedding in the three cases where it did occur was that the abrasion shield interface temperature was 32-34°F. The ice shapes for these cases (glaze ice) were like frozen slush, and horns were evident which experienced high aerodynamic shear forces which aided the ice removal.

Test 234 at 16 °F appeared to show that melting at some positions occurred, but the ice shape was such that the surface stress was much less than in the previous three cases. The ice in this test exhibited both glaze and rime characteristics.

As the tests were run with the primary purpose being to document the thermal response of the deicer pad, an evaluation of the performance of the deicer was difficult. The power density in reading 234 was too low (8 W/in^2) and the cycle used in reading 275 was too short (10/30), when combined with the resulting ice shapes, to obtain the necessary interface temperatures and conditions for shedding to occur.

Finally, the experimental data indicated that the thermodynamic process of ice accretion had an effect on the thermal response of the deicer. This was evidenced by the inflection noted to occur at the onset of ice accretion. However, this might have been an effect that would occur only in the IRT. It has not yet been determined how well the water spray in the tunnel emulates the supercooled water droplets which occur in nature.

Further research should be directed toward studying a larger set of deicer runs with a wider variety of conditions in order to further assess deicer performance and the thermal response of the assembly. Particularly, more angles of attack should be considered. In addition, the oscillating

blade tests should be conducted since the environmental conditions would then more closely approximate in-flight conditions.

PART IV

COMPARISON OF EXPERIMENTAL RESULTS WITH NUMERICAL CODES

Chapter 9

THE VALIDATION OF NUMERICAL CODES

9.1 OBJECTIVE

As was discussed in the Introduction, the third objective of the present study was to compare the experimental data with the numerical codes developed at The University of Toledo by Baliga [1], Marano [3] and Chao [4]. This comparison, or model validation, was necessary (1) in order to verify that the model contained sufficient physics to describe the thermal behavior of a real deicer pad; and (2) so that contact resistances, etc., could be added to the model , if necessary, to properly characterize the construction of a real deicer pad, i.e., to calibrate the model for a real case as versus a perfectly or theoretically constructed deicer. The major result hoped for is that models will result that can accurately be used for electrothermal deicer design.

It was decided that initial comparisons of the experimental data would be made with the one-dimensional model of Marano [3] in order to determine the blade locations where a one-dimensional model would provide accurate predictions. A. Peterson [18] of Boeing-Vertol has reported success with

the Baliga [1] one-dimensional model, but Marano's code was felt to be more accurate in simulating the phase change since it uses the Enthalpy Method to determine the location of the phase interface. Thus, Marano's code was chosen for the initial comparisons with the experimental data.

9.2 DETERMINING THE ONE-DIMENSIONAL NUMERICAL MODEL INPUT PARAMETERS

9.2.1 Modeling the Blade Geometry

There are some obvious limitations in using a one-dimensional approximation in modeling electrothermal aircraft deicing. An electrothermal deicer and blade construction potentially constitutes a three-dimensional transient thermal problem. However, it is important to recognize which portions, if any, of a blade may be effectively modeled using a one-dimensional transient numerical simulation.

One way of looking at a one-dimensional geometry is to consider it as a finite thickness flat plate with infinite boundaries in the other two directions . If the heat generation is uniform over the entire plate surface, energy will travel only inward. A boundary or discontinuity in geometry too close to the point of interest causes an edge effect. The problem is then no longer one-dimensional. A one-dimensional model is a good approximation as long as the actual geometry emulates a flat plate and has no end or edge effects.

The flate plate analogy works best along the side of the D-spar, at positions 8 through 10 (Figure 19). The blade curvature is relatively low, and the layer thicknesses are constant. These positions are far enough from any discontinuities in geometry to insure minimal edge effects. Therefore, the best correlation should occur at this portion of the blade.

The other positions depart from the one-dimensional analogy in varying degrees. Position 11 emulates the flat plate geometry but loses energy to an adjacent unheated zone. Position 7 is right at the corner of the D-spar, and position 6 is affected by the brass noseblock. A somewhat marginal correlation should occur at these positions.

Positions 1 through 5 were not utilized in the numerical/experimental correlation. There was no heater at positions 1 to 3, and any thermal response was due to lateral heat conduction only. This effect cannot be modeled using a one-dimensional simulation. Due to symmetry, the response for positions 4 and 5 was almost identical to positions 6 and 7, except for test 275. Modeling only positions 6 through 11 reduced the total CPU time without sacrificing important information.

9.2.2 Modeling the Composite Body

Two cross-sections were possible depending upon the portion of the blade being modeled. Table 2a lists the physical cross-section and properties used as input for the composite body from positions 7 through 11. At position 6, the brass was included, resulting in the cross-section of Table 2b. The electrothermal deicer construction was the same for both cross-sections. A total of 83 nodes were used in the composite body without the brass, and 95 nodes were used with the brass. A breakdown of the number of the nodes used per layer is included in the tables.

The thermal properties presented on these tables are published values that may vary from the actual values. Some of the properties were not firmly established. For example, the adhesive used in constructing the UH-1H blade was specified as FM1000 film adhesive manufactured by the American Cyanimid Company. The thermal conductivity and heat capacity of this substance was not known. A company representative suggested using values for unfilled epoxy resin.

On the other hand, many of the properties are probably quite accurate. Those for copper, aluminum, and stainless steel have been established to a high degree of accuracy. The only uncertainty comes from determining the grade of metal actually used in the blade.

After running a few preliminary comparisons, it became apparent that slightly increasing the thermal conductivities and heat capacities of the composite blade materials improved the numerical/experimental correlation. For all of the dry and deicing runs, the thermal properties input into the computer program were increased by a maximum of five percent. This was not regarded as an excessive or unrealistic approximation.

Another parameter input into the computer simulation was the zonal heater power density. The heater power density varied from position to position due to zonal variations in electrical resistance, and the densities given in Tables 3, 4, 6 and 7 are the nominal values. Actual power densities at each position for all ten readings are presented in Table 9.

9.2.3 Modeling the Ice

The ice shapes accreted during the deicing tests were lost when the blade deiced. The ice thickness for a given position had to be known. As stated previously, this information was obtained by matching the icing conditions for the deicing tests with those from the ice accretion documentation tests. The approximate ice shapes for the five runs are shown in Figure 37. The ice shapes for Readings 234 and 275 at 2.5 minutes of accretion time were obtained by taking

one-half of the thickness recorded in ice accretion tests 173 and 181, respectively, at a time of 5 minutes. This calculation assumed a linear rate of ice growth.

Readings 197, 209, and 213 were ice shedding runs. Marano's [3] program handles shedding as a sudden removal of all of the ice and water. The ice is shed when half a specified node is melted. In other words, the ice is shed when the melt-ice interface is halfway through a particular node. This particular node will be called the deice node and is part of the program input. Its value is somewhat arbitrary. The thickness of a single node must be considered when selecting the deice node.

The deice node can be any node within the ice layer. The abrasion shield interface is specified as node 1 of the ice layer. If node 1 is chosen, the ice is shed as soon as the interface reaches 32°F. The phase change algorithm is not employed. Specifying node 2 or above causes the program to enter the phase change algorithm before shedding.

A large number of nodes is desirable in the ice layer. The enthalpy method causes a plateau at 32°F when the ice melts. This occurs, as previously discussed, because each node is held at 32°F until the entire nodal volume melts. Decreasing the nodal thickness decreases the length of time over which the plateau occurs. If a large number of nodes is used, the plateau is not descernable on a temperature

versus time plot. A total of ninety nodes was used in the ice layer. Generally, this was enough to avoid the plateau.

There was some uncertainty in the ice thermal properties. The thermal conductivity of ice varies a relatively large amount over the experimental temperature range. Properties at 32°F were used because phase change occurred in most of the deicing runs.

Another aspect that has an effect on ice thermal properties is air trapped in the ice microstructure. Small bubbles, a few thousands of an inch in diameter, are probably trapped during accretion. Some types of ice may contain more air than others. For all of the deicing runs, air was not taken into account in the ice thermal properties.

9.2.4 Determining the Outer and Inner Surface Convection Coefficients

The outer surface convection coefficients at points other than the stagnation point were calculated using flat plate correlations [19]. Both laminar and turbulent flow were considered. The equation used for laminar flow was:

$$h_o = 0.332 \frac{k}{x} \sqrt{Re_x} (Pr)^{1/3} \qquad Re_x < 5 \times 10^5 \qquad (65)$$

The equation for turbulent flow was:

$$h_o = 0.51\ (T_m)^{0.3}\left[\frac{(1.69\ \rho v)^{0.8}}{x^{0.2}}\right] \qquad Re_x > 2 \times 10^6 \qquad (66)$$

where:

h_o = Outer surface convection coefficient, in BTU/hr-ft^2-°F;

k = Thermal conductivity of air, in BTU/hr-ft-°F;

x = Distance along the blade surface from the stagnation point, in feet;

Re_x = Reynolds number based on the distance, x, from the stagnation point;

Pr = Prandtl number of the air flowing over the blade;

T_m = Film temperature of the air flowing over the blade, in degrees Rankine;

ρ = Density of the air flowing over the blade, in lbm/ft^3; and

v = Local velocity of the air flowing over the blade, in ft/sec.

All of the air properties were calculated at the film temperature, T_m. The film temperature was approximated as the average between the initial and peak temperature for a given position at the abrasion shield. It varied from position to position.

Local velocities were used in both equations for a specific position at the blade surface. These velocities were calculated using an inviscid analysis for a NACA 0012 airfoil [20]. The local velocities were always higher than the freestream velocities for the positions studied.

The stagnation point coefficient was approximated using a cylinder in cross-flow correlation. The equation was taken from the same source [19]:

$$h_o = 1.14 \frac{k}{D} \sqrt{Re_D} (Pr)^{0.4} \left[1 - \left(\frac{\theta}{90°} \right)^3 \right], \quad 0 < \theta < 60° \quad (67)$$

where:

h_o = Stagnation point convection coefficient, in BTU/hr-ft^2-°F;

k = Thermal conductivity of the air flowing over the cylinder, in BTU/hr-ft-°F;

D = Cylinder diameter, in feet;

Re_D = Reynolds number of the air flowing about the cylinder, based on D; and

θ = Angle that specifies position around the cylinder with 0° at the stagnation point, in degrees.

The air properties were taken at the freestream flow stagnation temperature. The Reynolds Number was calculated using the freestream flow velocity, and the diameter, D, was based on the leading edge radius of curvature.

Convection coefficients for the deicing runs were calculated in the same manner. The turbulent flow flat plate correlation was used with air properties at the freestream flow temperature. Neglecting the presence of the ice shape, the local velocities were calculated using an inviscid analysis for a NACA 0012 blade. The cylinder in cross-flow correlation was used at the leading edge based on the leading edge radius. As will be seen, these approximations produced acceptable results for most of the data.

Unlike the outer blade surface, the inner surface did not experience forced convection. It was more like a free convective surface. Free convective surfaces usually have coefficients ranging from 1 to 10 BTU/hr-ft^2-°F. A value of 1 BTU/hr-ft^2-°F was used in the numerical simulation.

9.3 COMPARING THE NUMERICAL MODEL TO THE EXPERIMENTAL DATA

9.3.1 Dry Runs

Having established the input parameters, the next step was to compare the numerical and experimental data. Marano's [3] one-dimensional model was run for all of the dry runs at positions 6 through 11. The results of the compari-

sons are shown in Figures 38 through 42. The thermocouple positions were modeled by plotting nodes at the spar-ambient interface, the inner glue-heater interface, and the abrasion shield-ambient interface. Included in each figure are the following parameters:

T_∞ = Freestream flow stagnation temperature, in °F;

Pz = Heater power density for a specific zone, in W/in^2;

h_o = Outer surface convection coefficient, in BTU/hr-ft^2-°F;

t_{on} = Heater on time, in seconds;

x = Distance from the stagnation point, in inches; and

Re_x = Reynolds number based on the distance from the stagnation point.

These parameters, except Re_x and x , were used to generate the numerical data. Also included in Figures 38 through 42 are the following symbols used to differentiate between the various curves:

ABX = Experimental data at the abrasion shield;

HX = Experimental data at the heater;

SX = Experimental data at the D-spar;

ABS = Numerical simulation data at the abrasion shield;

HS = Numerical simulation data at the heater; and

SS = Numerical simulation data at the D-Spar.

The Reynolds Number was an important parameter to consider. According to Reference [19], transition from laminar to turbulent flow starts at a Reynolds Number of 5×10^5 and ends at a Reynolds Number of 2×10^6. Most of the Reynolds Numbers were below the transition point. This would imply that the flow was laminar, and that laminar coefficients should have been used.

After a few trial comparisons, it become apparent that the laminar coefficients were too low. Likewise, the turbulent coefficients were too high. A combination of two problems probably caused this discrepancy. First, using flat plate and cylindrical correlations to calculate convection coefficients for an airfoil is only an approximation. Second, tunnel turbulence probably lowered the transition Reynolds Number and raised the coefficients in general.

Despite this discrepancy, the values used in the numerical/experimental correlation fell between the laminar and turbulent values calculated using the flat plate and cylindrical correlations. Convection coefficients at 65 percent of the fully turbulent values were used for readings 92, 93, and 94, and 42 percent of the turbulent values were necessary for readings 70 and 76.

Studying Figures 38 through 42 reveals an inconsistent trend in the numerical/experimental correlation. The numerical data overpredict the experimental heater temperature in readings 92, 93, and 94, but underpredict the experimental heater temperature in readings 70 and 76. This behavior can possibly be attributed to an error in the measured heater power output for readings 70 and 76.

The input heater voltage was supposed to be at 10V for readings 70 and 76. At first, the power source voltmeter was used to set the desired voltage. However, it became apparent after a few readings that the power source voltmeter was not accurate enough. An external digital voltmeter, accurate to a tenth of a volt, was used to fine tune the input voltages for readings 92, 93, and 94, but not readings 70 and 76. The input voltage for readings 70 and 76 was probably higher than 10V.

This also possibly explains why 42 percent of the fully turbulent convection coefficients were necessary in readings 70 and 76 as compared to 65 percent for readings 92, 93, and 94. A lower than actual heater power density in the numerical model would mean less energy was reaching the abrasion shield. A lower external convection coefficient was necessary to match the experimental data.

As expected, the one-dimensional model appears to be most accurate at positions 8, 9, and 10. At position 11, the nu-

merical data overpredicted the experimental data due to lateral heat conduction. Except for the heater temperature in Reading 94, the numerical data matched the experimental data surprisingly well at position 7. The effect of the change in geometry at the D-spar was minimized by the high conductivity of aluminum.

At position 6, there is a noticable breakdown in the one-dimensional analogy at the D-spar. The numerical data severely underpredicted the experimental temperature profile of the D-spar. This occurred because the brass noseblock included in the simulation acted as a huge heat sink. As discussed previously, the experimental D-spar temperature profiles were position independent due to lateral heat conduction around the D-spar. This phenomenon could not be modeled using a one-dimensional simulation.

The heater temperature was consistently overpredicted by the numerical data for readings 92, 93, and 94. It was thought that a 0.001 inch thick layer of capton, which was between the thermocouple and the heater, was affecting the measurment of the actual heater temperature. An attempt at modeling this geometry was made by plotting the numerical temperature profile at a node about 0.001 inches into the glue layer away from the heater. The effect on the numerical data was found to be negligble, as shown in Figure 43.

9.3.2 Deicing Runs

There were two goals to the simulation comparisons for the deicing runs. The first was to verify the Enthalpy Method as an effective model of the phase change. The second was to evalute the accuracy of the numerical ice shedding algorithm.

Reading number 234 was an excellent run to use for testing the Enthalpy Method. Ice shedding did not occur, and the abrasion shield temperatures exceeded 32°F under the ice cap. Positions 5, 6 and 7 were the only positions covered by ice, and positions 5 and 7 showed reasonable symmetry. Thus, only positions 6 and 7 were modeled.

The composite body was modeled in the same manner as in the dry runs, except ice was included. The thermocouple positions were numerically modeled by nodes at the inner ambient-spar interface, the inner glue-heater interface, and the outer ambient-abrasion shield interface. The numerical and experimental comparison results for positions 6 and 7 are presented in Figures 44 through 48 for readings 197, 209, 213, 234, and 275, respectively. Included on these figures are the pertinent test conditions;

T_∞ = Freestream flow stagnation temperature, in °F;

P_z = Heater power density for a particular position, in W/in^2;

h_o = Outer surface convection coefficient, in BTU/hr-ft^2-°F;

t_{on} = Heater on time, in seconds;

t_{off} = Heater off time, in seconds; and

IT = Ice thickness at a particular position.

These parameters were important input parameters for the numerical simulation.

Using the pertinent input parameters and the composite body of Table 2a with an ice layer, Figure 47, parts e through g, resulted for position 7 for reading 234. There does not appear to be any phase change in the first cycle; however, phase change is clearly evident in the second and third cycles, as was discussed above in Chapter 7, section 7.1.5.2. Good agreement between the experimental and numerical data resulted. The experimental results clearly illustrate slope changes in the abrasion shield temperature, signifying that melting and refreezing at 32°F did occur in the second and third cycles.

An outer surface convection coefficient of 145 BTU/hr-ft^2 - °F was used to obtain these results. This was over twice that calculated using the turbulent flat plate analogy with

local velocities given by an NACA 0012 inviscid analysis. This coefficient may have been too high. The ice at position 7 was probably thinner than 1/16 inch, in which case a lower coefficient would have produced equivalent results.

The stagnation point convection coefficient was calculated using the cylinder in cross flow correlation with the airfoil leading edge radius. Using this coefficient along with the other pertinent input parameters produced Figure 47, part a, for the first cycle at position 6. Even though the experimental data shows abrasion shield temperatures above 32°F, no change in slope is evident, meaning that the phase change predicted by the numerical simulation did not occur in the experimental data. Two possible explanations can be offered for these results.

The first explanation is that, considering the experimental data to be reliable, this phenomenon was caused by an air gap over the abrasion shield thermocouple at position 6. Accreted ice is suspected as being a porous substance. Small air bubbles can be trapped in the ice microstructure during the accretion process. These bubbles are random in size and occurrence, causing a random effect on thermocouple response. Ice adhesion and density probably vary from position to position.

The air effect was modeled by placing a 0.002 inch gap of air between the abrasion shield and the ice at position 6.

Including the air produced much better agreement, as may be seen in Figure 47, parts b through d. This figure supports the conclusion that air trapped in the ice during accretion can have a major effect on the thermal response of the abrasion shield.

The second explanation concerns the previously mentioned independence of sections AA, BB and CC on the blade. At position 6, thermocouple 65 (Figure 27f) in section BB was chosen as the representative thermocouple since thermocouple 54 had been eliminated by bench testing and thermocouple 76 in section CC had been disregarded based on consistency. Going back to the original readings at position 6, as shown in Figure 49a, illustrates that if thermocouple 76 had been chosen, then no difference would have been observed between the experimental and theoretical results in Figures 47a, b and c. I.e., the predicted melting, which is evident in the response of thermocouple 76, did occur experimentally. Similar reasoning can be used at position 7 between thermocouples 55 (Figure 27g) and 77 (Figure 49b). Thermocouple 55 shows melting in Figures 47, parts f and g, whereas thermocouple 77 gives evidence of an air gap.

The most plausible description of the physics that occurred in reading 234 is that section BB shows an air gap (thermocouple 65) at position 6 and melting (thermocouple 66) at position 7. Correspondingly, section CC shows melt-

ing (thermocouple 76) at position 6 and an air gap (thermocouple 77) at position 7. This would explain why no shedding occured at either cross-section in reading 234.

As in the dry runs, the experimental D-spar temperature at position 6 exceeded the simulation results.

Having demonstrated the validity of the phase change algorithm allowed the verification of the shedding algorithm. Readings 197, 209, and 213 were ice shedding runs. The pertinent input parameters were the same, plus the following parameters;

DI = Deice node; and
MT = Melt thickness, in inches.

As discussed previously, the deice node determines when shedding occurs.

The outer surface convection coefficients were calculated as if the ice was not there. The flat plate turbulent correlation using local velocities from an inviscid analysis of an NACA 0012 was used at position 7. The stagnation point value, at position 6, was calculated using the cylinder in cross-flow correlation with the leading edge radius and freestream velocity. These coefficients were appropriate once the ice was shed.

Results from the numerical simulation as compared to the experimental data are presented in Figures 44 through 46 for readings 197, 209, and 213, respectively. Deicing occurred in the numerical data at the change in slope in the curve as indicated in Figure 44 for reading 197. Those simulations that had the deice node at node 1 did not enter the phase change algorithm.

A change in slope in most of the experimental curves, as indicated in the plots, signifies the actual point of ice shedding. The test log indicated that shedding occurred at about ten seconds in all three runs. An accurate measurement was not taken. The numerical deicing point could be made to match the experimental deicing point by reducing the value of the deice node.

The second cycle was modeled in reading 197. Ice did not accrete during the second cycle because the abrasion shield temperature was too high. In the second cycle, the abrasion shield was a convective interface and the convection coefficient was calculated as stated above. As may be seen in Figure 44, parts b and d, this approximation generated a good correlation.

The second and third cycles were not modeled in readings 209 and 213 because of the complexities introduced by the ice accretion process. Thermodynamic effects of ice accretion were not employed in Marano's program. Besides that,

the ice shapes for the second and third cycles were not documented. These discrepancies would have allowed a marginal, at best, correlation.

As can be seen, the simulation results compared very favorably with the experimental results for readings 197, 209 and 213. As in the dry runs, the experimental D-spar temperature at position 6 exceeded the simulation results in all cases.

Reading 275 was the only deicing run to be numerically modeled all the way around the blade from position 6 through position 11. The outer surface convection coefficients were calculated using the flat plate and cylindrical correlations along with the NACA 0012 inviscid analysis.

From the experimental data, no shedding occurred and melting is evident only at position 5 during the third cycle, as was discussed in section 7.1.5.2 in Chapter 7. As may be seen in Figure 48a, the numerical simulation overpredicted the experimental temperature at the abrasion shield by a significant amount at position 6, and also predicted a large amount of phase change in the third cycle which did not occur. Again, the experimental D-spar temperature was much higher than the predicted value. At position 7, the abrasion shield prediction is much closer, but the heater simulation is much higher than the measured value. The simulation would have fit the temperatures at position 5

much better (Figure 28e). Positions 8 through 11 exhibit a good correlation, as presented in Figures 48c through 48f.

Chapter 10

CONCLUSIONS AND RECOMMENDATIONS

A one-dimensional numerical model developed by Marano [3] was compared to an experimental database derived from tests performed in the Icing Research Tunnel at the NASA Lewis Research Center. The experimental database used in the comparisons consisted of thermocouple readings from five dry runs and five deicing runs, and was representative of a much larger set of readings. Input to the simulation was modified to match experimental test conditions at a variety of blade positions, thereby allowing an effective comparison.

For the dry runs, temperature responses at positions 6 through 11 were simulated. Positions 1 through 3 had no heater elements, so any energy transferred to these positions was due to two-dimensional effects. These could not be modeled using a one-dimensional code. Positions 4 and 5 were also not modeled as their experimental thermal responses showed reasonable symmetry with those from positions 7 and 8. For the deicing runs, the temperature responses for the stagnation point and any positions on the lower side of the blade where ice had accreted were modeled. Again, because the experimental data was taken at a zero degree angle of attack, the assumption of symmetry was used for the cor-

responding ice covered positions on the top of the blade. Their thermal response had shown moderate symmetry, and these corresponding positions were also not modeled. As was shown in the simulations of readings 234 and 275 in Chapter 9, this latter assumption probably should not have been made, and all positions under the ice should have been simulated.

In general, the simulation was found to overpredict the experimental data, especially at the heater element. This overprediction was possibly due to the effects of blade curvature and lateral heat conduction, neither of which were modeled by the one-dimensional simulation. A position at which the simulation consistently underpredicted the experimental data occurred at the inner side of the D-spar beneath the stagnation point. This behavior was caused by a breakdown in the one-dimensional analogy at this point.

Flat plate and cylindrical correlations were used, with an inviscid analysis of a NACA 0012 airfoil, in calculating the outer surface convection coefficients. Coefficients falling between the laminar and turbulent values were used for the dry runs, and fully turbulent values were used for the deicing runs. A free convection coefficient was used at the inner blade surface. These values generated adequate results in most cases.

The dry run simulation comparisons achieved moderate suc-
ss. The abrasion shield temperatures showed good agree-
nt, as did the substrate comparisons at positions other
an the stagnation point. The predicted heater tempera-
res were too high, as stated, but these temperatures were
e most sensitive ones with respect to the power intensity.
r predictive purposes, using the flat plate and cylinder
at transfer coefficients, it appeared that the one-dimen-
onal model can be used to model the thermal response of
e deicer assembly. The experimental data did not appear
show any other two-dimensional effects for positions 6
rough 11. It would also be expected that the model would
edict better at the higher ambient temperatures since the
ermal gradients were less. Runs 70 and 76 were at 17°F
l -4°F, and were modeled quite well except for the heater
position 6, whereas runs 92, 93 and 94 were all for am-
nt temperatures of -15°F. For these latter cases, agree-
t was not as good. No indications became evident during
comparison process that imperfect contact between layers
present in the deicer assembly. This would have neces-
ated the addition of contact resistances to the simula-
n code.

For the deicing runs, the Enthalpy Method was shown to
quately model the phase change which occurred at the ab-
ion shield - ice interface. Evidence has been presented
ch indicates that air gaps may have occurred at this in-

terface in reading 234, thereby delaying phase change · preventing ice shedding. The onset of phase change and, refreezing was discernable in the temperature versus t plots as a sudden change in slope at 32°F.

The Enthalpy Method and the deicing criteria set forth Marano's code were found to be adequate in modeling t first cycle of ice shedding. Experimental ice shedding c curred in readings 197, 209 and 213 when the abrasion shie - ice interface temperature was 32-34°F. Subsequent cycl were not modeled because an ice accretion model was not i cluded in the simulation. Ice shedding was discernable the experimental and numerical temperature versus time plc as a sudden increase in slope following change in phas The melt thickness at which shedding occurred in the simul tion was always less than 0.005 inches. As in the dry run no contact resistances had to be added to the numeric code.

In general, the one-dimensional code of Marano show good comparison with the experimental data, with the compa isons being better at the higher freestream temperatures This code definitely contains sufficient physical informa- tion so as to adequately model the thermal response of the electrothermal deicer assembly at positions where two-dime sional effects are small.

Further research should be directed toward three areas. The first effort should be spent toward expanding the present investigation to include more deicing run experimental data constituting a wider set of conditions. The question of cross-section independence of the thermocouple readings for the deicing runs should be re-examined, and all blade positions that are covered by the accreted ice should be modeled. Two-dimensional simulations developed at The University of Toledo should also be employed and evaluated. The second effort should be directed toward modifying Marano's code to include an internally calculated heat transfer coefficient at the outer surface, and also, if possible, an ice accretion model. Finally, the third effort should be set toward acquiring the flight test data compiled by the Boeing-Vertol Company during tests of an RAF HC-Mk1 Chinook helicopter equipped with electrothermal deicers on the main rotors. This data would provide invaluable information in regard to the differences between the tunnel thermal response and the in-flight response of an electrothermal deicer.

REFFERENCES

1. Baliga, G., "Numerical Simulation of One-Dimensional Heat Transfer in Composite Bodies with Phase Change," M. Sc. Thesis, Univ. of Toledo, Toledo, Ohio, 1980.

2. Stallabrass, J. R., "Thermal Aspects of De-Icer Design," presented at The International Helicopter Icing Conference, Ottawa, Canada, 1972.

3. Marano, J. J., "Numerical Simulation of an Electrothermal De-Icer Pad," M. Sc. Thesis, The University of Toledo, Toledo, Ohio, May, 1982.

4. Chao, D. F., "Numerical Simulation of Two-Dimensional Heat Transfer in Composite Bodies with Application to De-icing of Aircraft Components," Ph.D. Thesis, The University of Toledo, Toledo, Ohio, November, 1983.

5. Arpaci, Conduction Heat Transfer, Addison-Wesley, Reading, Massachusetts, 1966.

6. Ockenden, J. R., and W. R. Hodgkins (editors), Moving Boundary Value Problems in Heat Flow and Diffusion, Oxford Univ. Press, Oxford, 1975.

7. Carslaw, H. S., and J. C. Jaeger, Conduction of Heat in Solids, Clarendon Press, Oxford, 1959.

8. Campbell, W. F., "A Rapid Analytical Method for Calculating the Early Transient Temperature in a Composite Slab," NRC Lab Report MT-32, 1956.

9. Carnahan, B., Luther, H. A., and J. O. Wilkes, Applied Numerical Methods, Wiley, New York, 1969.

10. Gent, R. W., and J. T. Cansdale, "One-Dimensional Treatment of Thermal Transients in Electrically De-Iced Helicopter Rotor Blades," RAE Technical Report 80159, 1980.

11. von Rosenberg, D. V., Methods for the Numerical Solution of Partial Differential Equations, American Elsevier, 1969.

12. Bonacina, C., Comini, G., Fasano, A. and N. Primicerio, "Numerical Solution of Phase Change Problems," Int. J. Heat & Mass Trans., 10, p. 1825, 1973.

13. Voller, V. R., Cross, M., and P. G. Walton, "Assessment of Weak Solution Numerical Techniques for Solving Stefan Problems," 172, Department of Mathematics & Computer Studies, Sunderland Polytechnic, U.K., 1979.

14. Atthey, D. R., "A Finite Difference Scheme for Melting Problems," J. Inst. Math. Appl. 13, 353, 1974.

15. Shamsunder, N., and E. M. Sparrow, "Analysis of Multidimensional Conduction Phase Change Via the Enthalpy Model, "J. Heat Transfer 75, 333, 1975.

16. Voller, V., and M. Cross, "Accurate Solutions of Moving Boundary Value Problems Using the Enthalpy Method," Int. J. Heat & Mass Trans., 24, p. 545, 1981.

17. Cotton, R. H., "Icing Tests of a UH-1H Helicopter with an Electrothermal Ice Protection System Under Simulated and Natural Icing Conditions," U. S. Army Research and Technology Laboratories, Report USARTL-TR-78-48, 1978.

18. Peterson, Andrew A., "Thermal Analysis Techniques for Design of VSTOL Aircraft Rotor Ice Protection," AIAA 23rd Aerospace Sciences Meeting, Reno, Nevada, Report AIAA-85-0340, 1985.

19. SAE Aerospace Applied Thermodynamics Manual, Society of Automotive Engineers, Inc., Second Edition, October 1969.

20. Abbott, Ira H., von Doenhoff, Albert E., and Louis S. Stivers, Jr., "Summary of Airfoil Data", NACA Report 824, 1945.

TABLE 1

Deicer Model Used in Variable Thickness Ice Layer Program
Sample Runs

Layer	Thickness (in.)	Thermal Conductivity (BTU/hr-ft-°F)	Thermal Diffusivity (ft^2/hr)
Aluminum D-Spar	0.0870	66.5	1.65
Epoxy/Glass Insulation	0.0200	0.220	0.00870
Point Heater	0.0000	----	----
Epoxy/Glass Insulation	0.0200	0.220	0.00870
Stainless Steel Abrasion Shield	0.0120	8.70	0.150
Ice	Variable	1.32	0.0469

Heater Power Density = 25 W/in^2
Outer Convection Coefficient = 200 $BTU/hr\text{-}ft^2\text{-}°F$
Inner Convection Coefficient = 10 $BTU/hr\text{-}ft^2\text{-}°F$
Ambient Temperature = -28 °F
Initial Temperature = -28 °F

TABLE 2

Physical Construction and Thermal Properties of Materials Used in the Helicopter Blade and Electrothermal Deicer

a. Sides of the Blade (Positions 7 through 11)

Layer	Nodes	Thickness (in.)	Thermal Conductivity (BTU/hr-ft-°F)	Thermal Diffusivity (ft^2/hr)
Abrasion Shield Stainless Steel	6	0.030	8.7	0.15
Adhesive Epoxy	4	0.0168	0.1	0.0058
Insulation Epoxy/Glass	4	0.0138	0.22	0.0087
Adhesive Epoxy	4	0.0082	0.1	0.0058
Heater Element Copper	4	0.0065	60.0	1.15
Adhesive Epoxy	4	0.0082	0.1	0.0058
Insulation Epoxy/Glass	4	0.138	0.22	0.0087
Adhesive Epoxy	2	0.0082	0.1	0.0058
Blade Skin Stainless Steel	4	0.02	8.7	0.15
Film Adhesive FM 1000	3	0.01	0.1	0.0058
Doubler Aluminum	10	0.05	102	2.83
Film Adhesive FM1000	3	0.01	0.1	0.0058
D-Spar Aluminum	31	0.175	102	2.83

b. Stagnation Point (Position 6)

Layer	Nodes	Thickness (in.)	Thermal Conductivity (BTU/hr-ft-°F)	Thermal Diffusivity (ft^2/hr)
Abrasion Shield Stainless Steel	6	0.030	8.7	0.15
Adhesive Epoxy	4	0.0168	0.1	0.0058
Insulation Epoxy/Glass	4	0.0138	0.22	0.0087
Adhesive Epoxy	2	0.0082	0.1	0.0058
Heater Element Copper	2	0.0065	60.0	1.15
Adhesive Epoxy	2	0.0082	0.1	0.0058
Insulation Epoxy/Glass	4	0.138	0.22	0.0087
Adhesive Epoxy	2	0.0082	0.1	0.0058
Blade Skin Stainless Steel	4	0.02	8.7	0.15
Film Adhesive FM 1000	3	0.01	0.1	0.0058
Noseblock Brass	38	0.7	64.15	1.32
Film Adhesive FM1000	3	0.01	0.1	0.0058
D-Spar Aluminum	21	0.125	102	2.83

TABLE 3

Test Matrix Conditions for the Dry Runs

Escort Leading	V_∞ (MPH)	T_∞ (°F)	α (Deg.)	P1	P2	P3 (W/in^2)	t_{on}/t_{off} (Sec.)	n
57	50	64	0	0	0	0	-----	-
60	50	33	0	0	0	0	-----	-
61	50	26	0	0	0	0	-----	-
62	200	19	2	0	0	0	-----	-
64	200	20	2	6.5	6.5	6.5	30/30	1
65	200	20	2	14	14	14	30/30	1
66	200	20	2	24	24	24	10/30	1
67	200	20	6	0	0	0	-----	-
68	200	20	6	14	14	14	10/30	1
69	120	17	0	0	0	0	-----	-
70	120	17	0	2.9	2.9	2.9	30/30	1
71	120	17	0	16	16	16	10/30	1
73	50	5	0	0	0	0	-----	-
74	64	-3	0	0	0	0	-----	-
75	275	-4	0	0	0	0	-----	-
76	275	-4	0	2.9	2.9	2.9	30/30	1
77	275	-4	0	16	16	16	30/30	1
78	275	-4	0	16	16	16	10/30	4
79	275	-4	6	0	0	0	-----	-
80	275	-4	6	2.9	2.9	2.9	30/30	1
81	275	-4	6	16	16	16	30/30	1
82	275	-4	6	16	16	16	10/30	4
86	100	-9	0	0	0	0	-----	-
87	200	-10	6	8	8	8	30/30	1
88	200	-11	6	16	16	16	30/30	1
89	200	-11	6	24	24	24	20/30	1
90	200	-12	2	24	24	24	20/30	1
91	200	-11	4	24	24	24	20/30	1
92	120	-15	0	8	8	8	30/30	1
93	120	-15	0	16	16	16	30/30	1
94	120	-15	0	24	24	24	20/30	1
95	120	-15	0	16	16	24	20/30	1
96	120	-15	0	8	8	24	20/30	1
97	120	-15	0	0	0	24	20/30	1
98	120	-16	2	24	24	24	20/30	1
99	120	-15	4	24	24	24	20/30	1
100	120	-15	6	8	8	8	20/30	1
101	120	-15	6	16	16	16	30/30	1
102	120	-15	6	24	24	24	20/30	1
103	120	-15	6	24	24	24	30/30	4
105	120	-14	6	16	24	16	20/30	1
106	120	-15	6	16	24	16	20/30	2
107	120	-15	6	8	24	8	20/30	2
108	120	-15	6	0	24	0	20/30	2
109	120	-16	6	8	8	8	30/30	2
110	120	-15	6	8	8	8	180/100	1

TABLE 4

Test Condition Matrix for the Wet Runs

Escort Reading	V_∞ (MPH)	T_∞ (°F)	α (Deg.)	P1 (W/in^2)	P2 (W/in^2)	P3 (W/in^2)	t_{on}/t_{off} (Sec.)	n	LWC (g/m^3)	d (μm)
115	120	57	0	0	0	0	-----	-	1.07	16.8
116	120	56	0	24	24	24	20/30	1	1.07	16.8
120	120	61	0	24	24	24	10/30	1	1.07	16.8
121	120	53	4	0	0	0	-----	-	1.07	16.8
122	120	47	6	0	0	0	-----	-	1.07	16.8
123	120	47	6	0	0	0	-----	-	1.02	11.7
124	120	49	4	0	0	0	-----	-	1.02	11.7
125	120	46	2	0	0	0	-----	-	1.02	11.7
126	120	46	0	0	0	0	-----	-	1.02	11.7
127	120	46	0	0	0	0	-----	-	2.49	35.4
128	120	50	2	0	0	0	-----	-	2.49	35.4
129	120	46	4	0	0	0	-----	-	2.49	35.4
130	120	47	6	0	0	0	-----	-	2.49	35.4
131	120	48	6	0	0	0	-----	-	2.24	23.6
132	120	45	4	0	0	0	-----	-	2.24	23.6
133	120	45	2	0	0	0	-----	-	2.24	23.6
134	120	47	0	0	0	0	-----	-	2.24	23.6
135	200	46	0	0	0	0	-----	-	1.20	18.8
136	200	46	0	16	16	16	20/30	1	1.20	18.8
137	200	47	2	0	0	0	-----	-	1.20	18.8
138	200	47	2	16	16	16	20/30	1	1.20	18.8
139	200	49	4	16	16	16	30/30	1	1.20	18.8
140	200	50	4	0	0	0	-----	-	1.20	18.8
141	200	50	6	0	0	0	-----	-	1.20	18.8
142	200	50	6	16	16	16	30/30	1	1.20	18.8
143	200	49	6	0	0	0	-----	-	1.10	14.8
144	200	46	4	0	0	0	-----	-	1.10	14.8
145	200	45	2	0	0	0	-----	-	1.10	14.8
146	200	43	0	0	0	0	-----	-	1.10	14.8
147	200	44	0	0	0	0	-----	-	0.96	18.0
148	200	45	0	16	16	16	30/30	1	0.96	18.0
149	200	44	2	0	0	0	-----	-	0.96	18.0
150	200	45	2	16	16	16	30/30	1	0.96	18.0
151	200	44	4	0	0	0	-----	-	0.96	18.0
152	200	45	4	16	16	16	30/30	1	0.96	18.0
153	200	44	6	0	0	0	-----	-	0.96	18.0
154	200	44	6	16	16	16	30/30	1	0.96	18.0
155	280	49	6	0	0	0	-----	-	0.36	11.0
156	280	49	4	0	0	0	-----	-	0.36	11.0
157	280	48	2	0	0	0	-----	-	0.36	11.0
158	280	48	0	0	0	0	-----	-	0.36	11.0
159	280	48	0	0	0	0	-----	-	1.17	20.0
160	280	48	2	0	0	0	-----	-	1.17	20.0
161	280	47	4	0	0	0	-----	-	1.17	20.0
162	280	49	6	0	0	0	-----	-	1.17	20.0

TABLE 5

Test Condition Matrix for the Ice Accretion Documentation Tests

Escort Reading	V_∞ (MPH)	T_∞ (°F)	α (Deg.)	LWC (g/m^3)	d (μm)	t_{ice} (min)
163	200	34	0	1.2	23.1	5
164	200	31	0	1.2	23.1	5
---	200	31	2	1.2	23.1	5
---	200	31	4	1.2	23.1	5
---	280	31	0	1.0	16.8	5
---	200	29	0	1.2	23.7	5
170	200	24	0	1.2	23.7	5
171	100	24	0	2.7	38.5	5
172	100	24	2	2.7	38.5	5
---	100	16	0	2.2	19.2	5
174	100	16	2	2.2	19.2	5
175	170	5	0	1.7	19.2	5
176	170	5	4	1.7	19.2	5
177	100	2	2	2.3	25.6	5
178	100	4	4	2.3	25.6	5
179	100	0	0	1.8	15.0	5
180	100	1	2	1.8	15.0	5
181	250	-2	0	1.2	20.0	5
182	250	-2	2	1.2	20.0	5
183	280	31	0	1.0	20.0	5
185	250	28	0	1.0	20.0	5
186	200	24	0	1.0	20.0	5
187	150	21	0	1.0	20.3	5
188	100	19	0	1.0	19.9	5
189	280	-3	0	1.0	15.1	5
190	280	-3	2	1.0	15.1	5
191	200	-10	0	1.2	20.0	5
192	200	-11	2	1.2	20.0	5
---	120	-11	0	1.1	15.3	5
---	120	-11	2	1.1	15.3	5

TABLE 6

Test Condition Matrix for the Deicing Tests

a. Simultaneous Heater Zone Cycling Test

Escort Reading	V_∞ (MPH)	T_∞ (°F)	α (Deg.)	P1	P2	P3 (W/in^2)	t_{on}/t_{off} (Sec.)	n	LWC (g/m^3)	d (μm)	t_{ice} (min)
196	200	31	0	8	8	8	60/60	1	1.2	18.4	5
197	200	31	0	16	16	16	10/30	2	1.2	18.4	5
198	200	31	2	8	8	8	10/30	1	1.2	18 4	5
199	200	31	2	16	16	16	10/60	2	1.2	18.4	5
200	200	31	2	8	8	8	10/60	2	1.2	18.4	5
201	200	31	4	8	8	8	10/60	1	1.2	18.4	5
202	200	31	4	16	16	16	10/60	1	1.2	18.4	5
204	280	31	0	16	16	16	10/60	1	1.0	14.5	5
205	280	31	0	8	8	8	10/60	1	1.0	14.5	5
206	280	31	0	8	8	8	10/60	1	1.0	14.5	5
207	280	31	0	16	16	16	10/60	1	1.0	14.5	5
209	250	28	0	16	16	16	10/60	3	1.0	20.0	5
210	250	28	0	8	8	8	10/60	3	1.0	20.0	5
211	200	24	0	8	8	8	10/60	3	1.0	20.0	5
212	200	24	0	8	8	8	20/60	3	1.0	20.0	5
213	200	24	0	16	16	16	20/60	3	1.0	20.0	5
214	150	21	0	16	16	16	20/60	3	1.0	20.3	5
215	150	21	0	16	16	16	20/60	3	1.0	20.3	5
216	100	20	0	16	16	16	20/60	3	1.0	19.9	5
217	100	20	0	24	24	24	10/60	3	1.0	19.9	5
218	170	5	0	24	24	24	10/60	3	1.7	23.1	5
219	170	6	0	24	24	24	10/60	3	1.7	23.1	2.5
223	200	29	0	8	8	8	10/60	3	1.2	19.0	2.5
225	200	29	0	16	16	16	10/60	3	1.2	19.0	2.5
226	200	24	0	8	8	8	10/30	4	1.2	19.0	2.5
227	200	23	0	16	16	16	10/30	3	1.2	19.0	2.5
228	100	24	0	8	8	8	10/30	3	2.7	29.3	2.5
229	100	24	0	16	16	16	10/30	3	2.7	29.3	2.5
230	100	25	0	24	24	24	10/30	3	2.7	29.3	2.5
231	100	25	2	8	8	8	10/30	3	2.7	29.3	2.5
232	100	24	2	16	16	16	20/40	3	2.7	29.3	2.5
233	100	24	2	24	24	24	10/40	3	2.7	29.3	2.5
234	100	16	0	8	8	8	20,30/60	3	2.2	19.2	2.5
238	200	29	0	16	16	16	10/60	3	1.2	19.0	5
239	200	29	0	8	8	16	10/60	3	1.2	19.0	5
240	200	29	0	0	0	16	10/60	3	1.2	19.0	5
241	100	16	0	16	16	16	20/60	3	2.2	19.2	2.5
242	100	16	0	24	24	24	10/60	3	2.2	19.2	2.5
243	100	16	2	24	24	24	10/60	3	2.2	19.2	2.5
244	100	16	2	16	16	16	20/60	4	2.2	19.2	2.5
245	100	16	2	8	8	8	30/60	4	2.2	19.2	2.5
246	100	-1	2	8	8	8	30/60	4	1.8	15.0	2.8
247	100	-1	2	16	16	16	20/60	4	1.8	15.0	2.5
251	170	5	0	24	24	24	10/60	4	1.7	19.7	2.5

252	170	5	0	16	16	16	20/60	4	1.7	19.7	2.5
253	170	5	0	8	8	8	30/30	4	1.7	19.7	2.5
254	170	5	0	16	16	24	10/60	4	1.7	19.7	2.5
255	170	5	0	8	8	24	10/60	2	1.7	19.7	2.5
256	170	5	4	24	24	24	10/60	2	1.7	19.7	2.5
257	170	5	4	16	16	16	30/30	4	1.7	19.7	2.5
258	170	5	4	8	8	8	60/30	4	1.7	19.7	2.5
259	100	2	2	8	8	8	60/30	3	2.3	25.6	2.5
260	100	2	2	16	16	16	30/30	4	2.3	25.6	2.5
261	100	2	2	24	24	24	10/30	4	2.3	25.6	2.5
262	100	2	4	24	24	24	10/30	4	2.3	25.6	2.5
263	100	2	4	16	16	16	30/30	4	2.3	25.6	2.5
264	100	2	4	8	8	8	60/30	4	2.3	25.6	2.5
265	100	-1	0	8	8	8	60/30	4	2.3	25.6	2.5
266	100	-1	0	16	16	16	30/30	4	2.3	25.6	2.5
267	100	-1	0	24	24	24	10/30	4	2.3	25.6	2.5
269	100	-1	2	8	8	8	60/30	3	1.8	15.0	2.5
270	100	-1	2	16	16	16	30/30	3	1.8	15.0	2.5
271	100	-1	2	24	24	24	10/30	3	1.8	15.0	2.5
272	250	-1	0	8	8	8	60/30	3	1.2	20.0	2.5
274	250	-2	0	16	16	16	30/30	4	1.2	20.0	2.5
275	250	-3	0	24	24	24	10/30	4	1.2	20.0	2.5
277	250	-3	2	8	8	8	60/30	3	1.2	20.0	0.5
278	250	-2	2	16	16	16	30/30	3	1.2	20.0	0.5
280	250	-2	2	24	24	24	10/10	8	1.2	20.0	0.5
281	280	-3	0	8	8	8	60/30	3	1.0	15.1	2.5
282	280	-4	0	16	16	16	20/10	10	1.0	15.1	0.5
283	280	-4	0	24	24	24	10/10	12	1.0	15.1	---

b. Phased Heater Cycling Test

Escort Reading	V_∞ (MPH)	T_∞ (°F)	α (Deg.)	P (W/in^2)	HC	t_{on}/t_{off} (Sec.)	n	LWC (g/m^3)	d (μm)	t_{ice} (min)
286	200	29	0	8	1	10/60	3	1.2	19.0	2.5
287	200	29	0	8	1	10/60	1	1.2	19.0	2.5
288	100	24	0	8	1	10/60	3	2.7	29.3	2.5
289	100	24	0	8	1	10/60	3	2.7	29.3	2.5
290	100	24	0	16	1	10/60	3	2.7	29.3	2.5
291	100	16	0	16	1	10/60	3	2.2	19.2	2.5
292	100	16	0	8	1	10/60	3	2.2	19.2	2.5
293	100	-1	0	16	1	10/60	3	1.8	15.0	2.5
294	100	-1	0	16	1	10/60	3	1.8	15.0	2.5
295	200	-11	0	16	1	10/60	3	1.2	20.0	2.5
298	200	29	0	8	2	10/40	3	1.2	19.0	2.5
300	200	29	0	8	2	10/40	3	1.2	19.0	5.0
301	200	24	0	16	1	10/60	3	1.0	20.0	2.5
302	200	24	0	24	1	10/60	3	1.0	20.0	2.5
303	200	24	0	8	2	10/40	3	1.0	20.0	2.5
304	200	24	0	16	2	10/40	3	1.0	20.0	2.5
305	100	16	0	16	2	10/40	3	2.2	19.2	2.5
306	100	16	0	24	3	20/40	3	2.2	19.2	2.5
307	100	16	0	16	3	20/40	3	2.2	19.2	2.5

308	100	16	0	24	3	20/40	3	2.2	19.2	2.5
309	170	5	0	24	3	20/40	4	1.7	19.7	2.5
310	100	0	0	24	3	20/40	4	1.8	15.0	2.5
311	100	0	0	24	3	20/40	4	1.8	15.0	5
312	100	0	2	24	3	20/40	4	1.8	15.0	5
313	200	-11	2	24	3	20/40	3	1.2	20.0	2.5
314	200	-13	0	24	3	20/40	3	1.2	20.0	2.5
315	200	-11	0	24	4	-----	3	1.2	20.0	2.5

P = Nominal Heater Power Density
HC = Heater Configuration

There were four heater configurations. See Figure 50.

TABLE 7

Test Conditions for those Readings Chosen for the Numerical and Experimental Data Comparisons

Escort Reading	V_∞ (MPH)	T_∞ (°F)	α (Deg.)	P (W/in^2)	t_{on}/t_{off} (Sec.)	n	LWC (g/m^3)	d (μm)	t_{ice} (min)
70	120	17	0	2.9	30/30	1	---	---	---
76	275	-4	0	2.9	30/30	1	---	---	---
92	120	-15	0	8	30/30	1	---	---	---
93	120	-15	0	16	30/30	1	---	---	---
94	120	-15	0	24	20/30	1	---	---	---
197	200	31	0	16	10/30	2	1.2	18.4	5
209	250	28	0	16	10/60	3	1.0	20.0	5
213	200	24	0	16	20/60	3	1.0	20.0	5
234	100	16	0	8	20,30/60	3	2.2	19.2	2.5
275	250	-3	0	24	10/30	3	1.2	20.0	2.5

TABLE 8

Presentation of the Thermocouples Chosen as the Representative Set

Position Around Blade	Thermocouple Number AB	H	S
1	49	--	--
2	50	--	--
3	62	--	--
4	63	25	9
5	53	26	10
6	65	27	11
7	55	28	12
8	56	x	13
9	57	x	14
10	58	39	15
11	x	32	16

- Indicates that a thermocouple is not present at the specified location.

x Indicates that all of the thermocouples at the specified location were innacurate or discarded.

AB = Abrasion Shield
H = Heater
S = D-Spar

TABLE 9

Presentation of the Zonal Dependent Heater Power Densities

a. Dry Runs

Position Around Blade	Heater zone	Power Density (W/in^2) Reading Number 70	76	92	93	94
1	-	----	----	----	----	----
2	-	----	----	----	----	----
3	-	----	----	----	----	----
4	8	2.87	2.87	7.90	15.8	23.8
5	7	2.87	2.87	7.91	15.9	23.8
6	6	2.86	2.86	7.87	15.8	23.7
7	5	2.89	2.89	7.97	16.0	24.0
8	4	2.96	2.96	8.14	16.3	24.5
9	3	2.91	2.91	8.03	16.1	24.2
10	2	2.97	2.97	8.20	16.4	24.7
11	1	2.97	2.97	8.20	16.4	24.7

b. Deicing Runs

Position Around Blade	Heater zone	Power Density (W/in^2) Reading Number 197	209	213	234	275
1	-	----	----	----	----	----
2	-	----	----	----	----	----
3	-	----	----	----	----	----
4	8	15.8	15.8	15.8	7.90	23.8
5	7	15.9	15.9	15.9	7.91	23.8
6	6	15.8	15.8	15.8	7.87	23.7
7	5	16.0	16.0	16.0	7.97	24.0
8	4	16.3	16.3	16.3	8.14	24.5
9	3	16.1	16.1	16.1	8.03	24.2
10	2	16.4	16.4	16.4	8.20	24.7
11	1	16.4	16.4	16.4	8.20	24.7

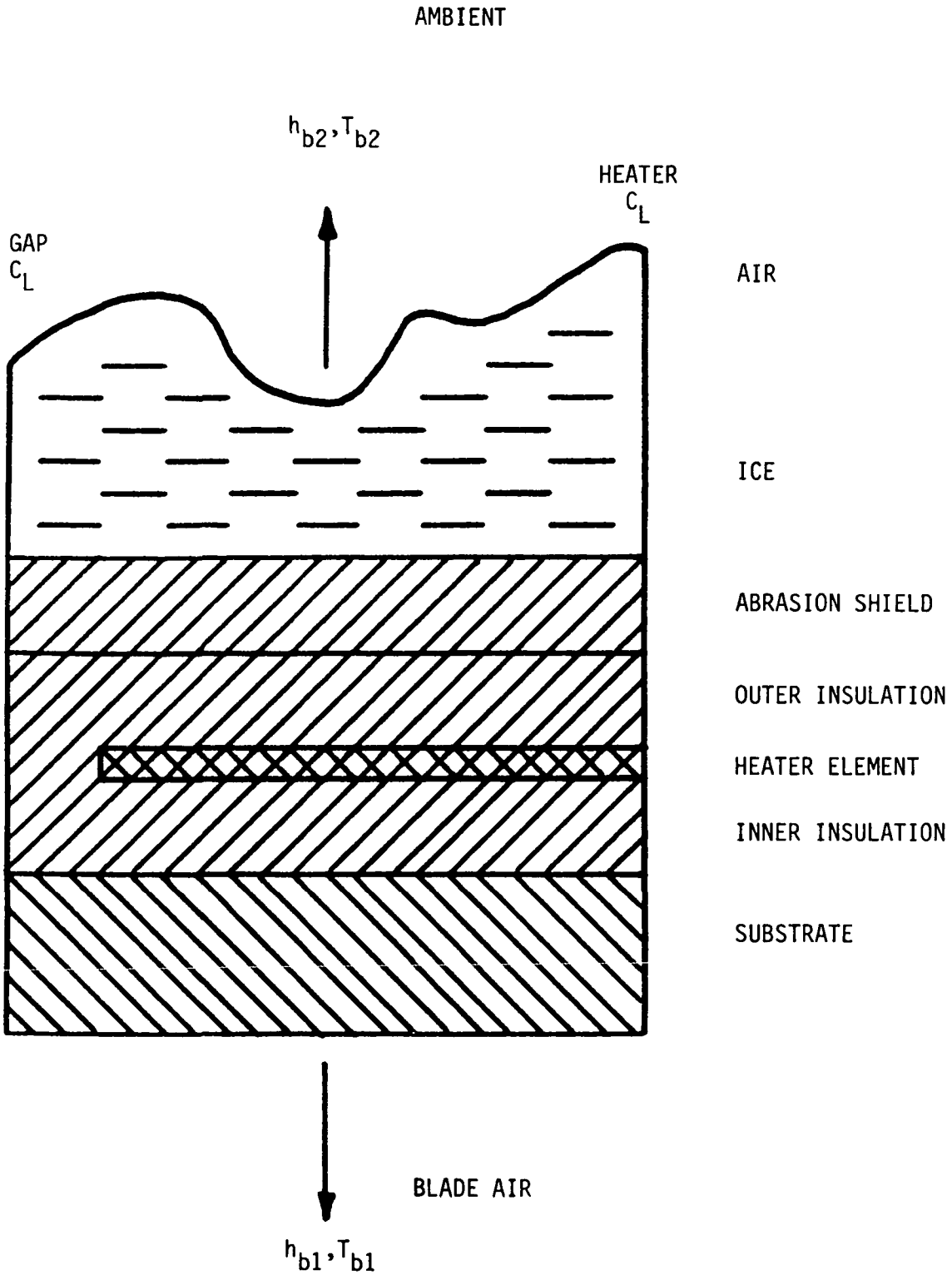

Figure 1. Two-Dimensional Deicer Model

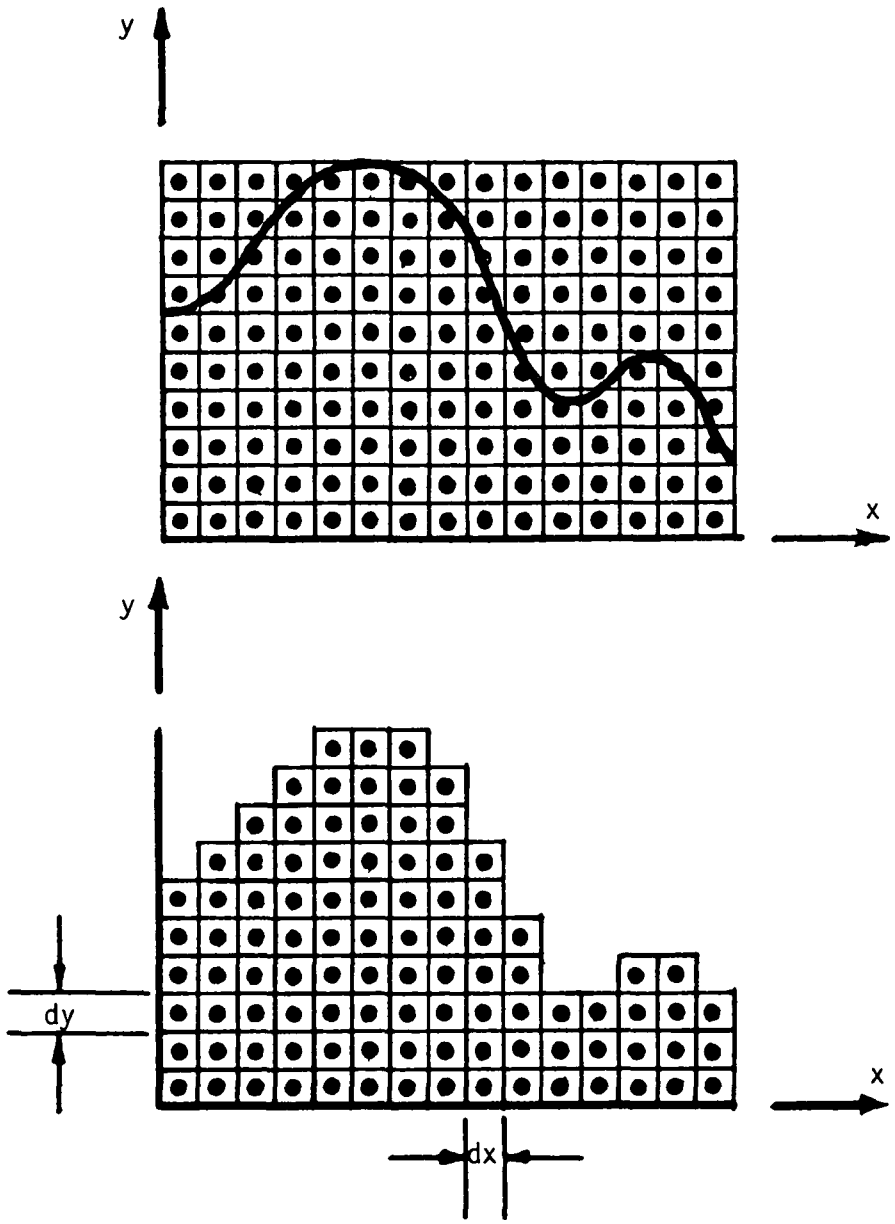

Figure 2. Method of Approximating the Variable Thickness Ice Layer

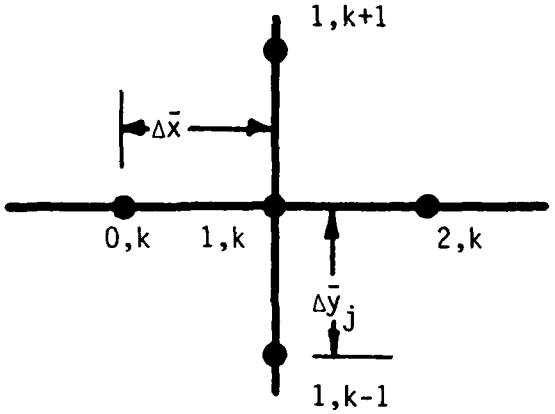

a. Interior Mesh Point at the Center of the Gap

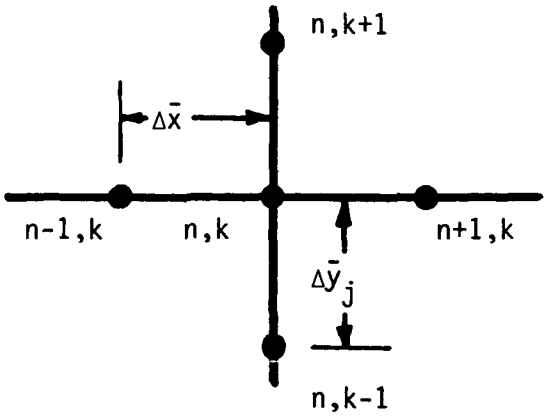

b. Interior Mesh Point at the Center of the Heater

Figure 3. Finite Difference Grid at Selected Points

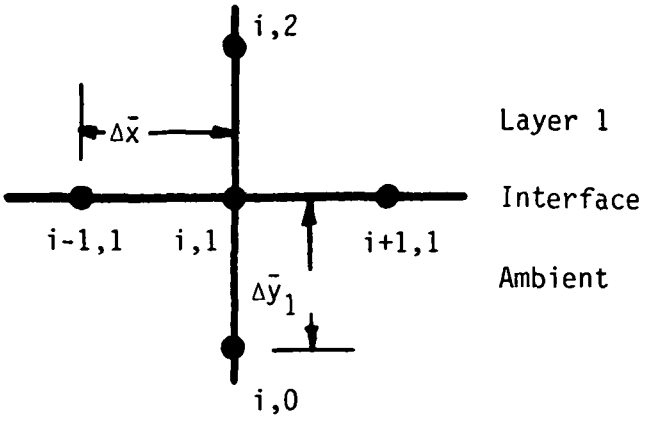

a. Substrate-Ambient Interface

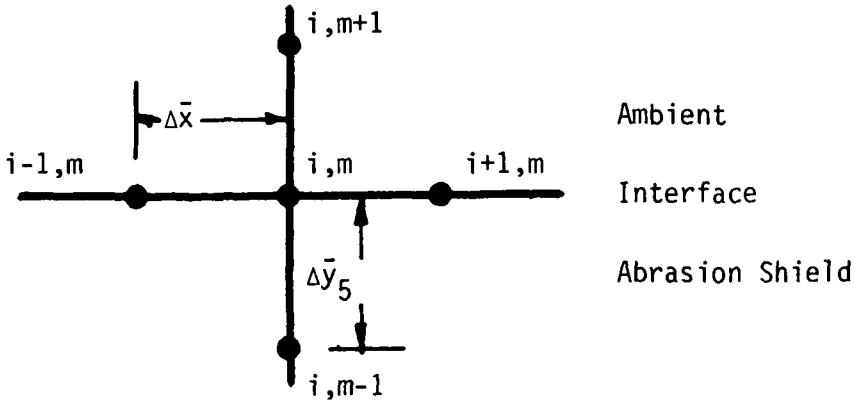

b. Abrasion Shield-Ambient Interface

Figure 4 . Finite Difference Grid at Selected Points

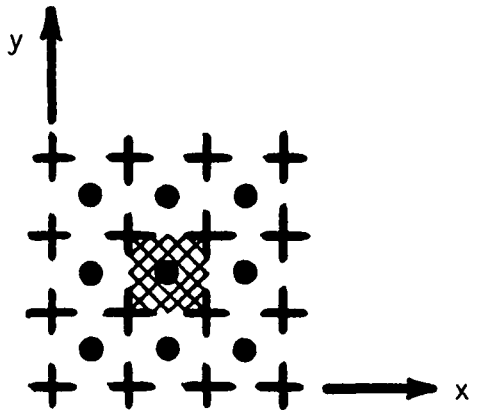

a. Type 1 Element

$$-KW_3 \frac{\partial T}{\partial y} = h_{b2}(T-T\infty)$$

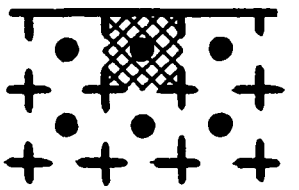

b. Type 2 Element

$$KW_1 \frac{\partial T}{\partial x} = h_{b2}(T-T\infty)$$

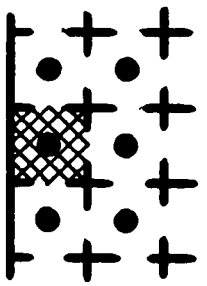

c. Type 3 Element

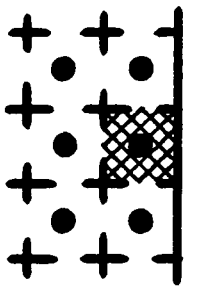

$$-KW_2 \frac{\partial T}{\partial x} = h_{b2}(T-T\infty)$$

d. Type 4 Element

$$-KW_3 \frac{\partial T}{\partial y} = h_{b2}(T-T\infty)$$

$$KW_1 \frac{\partial T}{\partial x} = h_{b2}(T-T\infty)$$

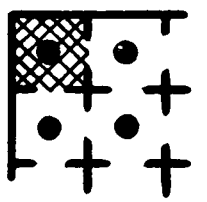

e. Type 5 Element

$$-KW_3 \frac{\partial T}{\partial y} = h_{b2}(T-T\omega)$$

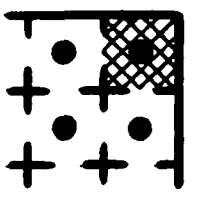

$$KW_2 \frac{\partial T}{\partial x} = h_{b2}(T-T\infty)$$

f. Type 6 Element

Figure 5. Nodal Boundary Configurations for the Variable Thickness Ice Layer

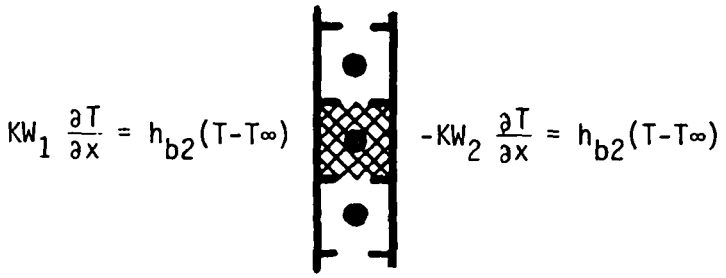

a. Type 7 Element

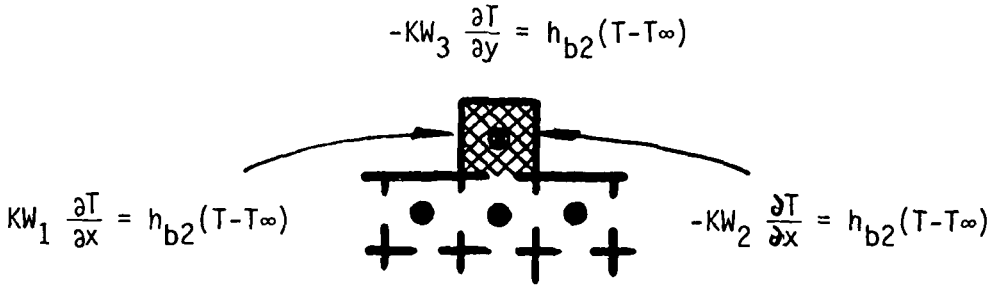

b. Type 8 Element

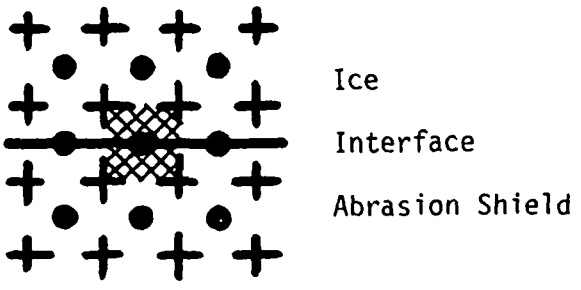

c. Type 9 Element

Figure 6. Nodal Boundary Configurations for the Variable Thickness Ice Layer

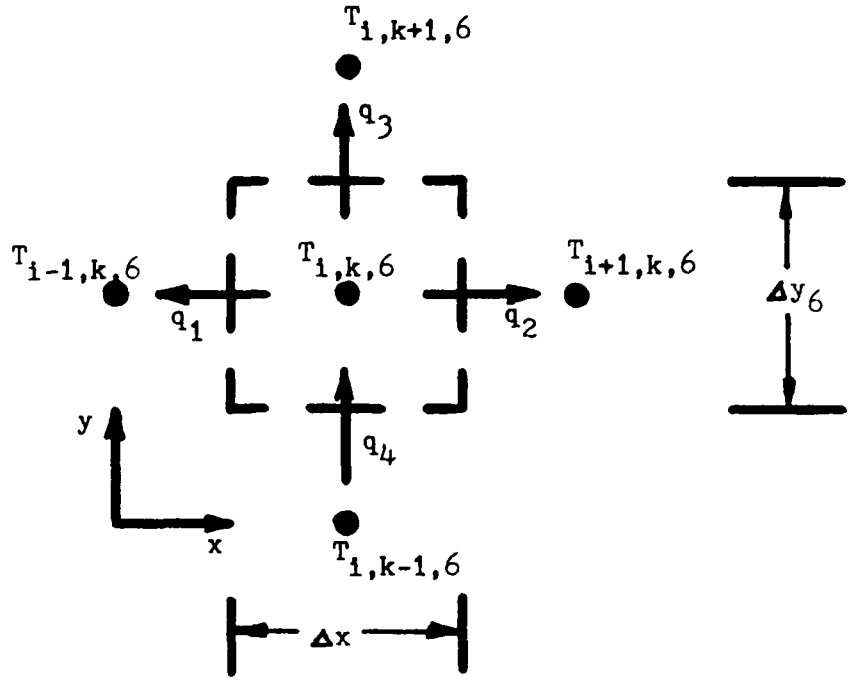

a. Interior Ice Node

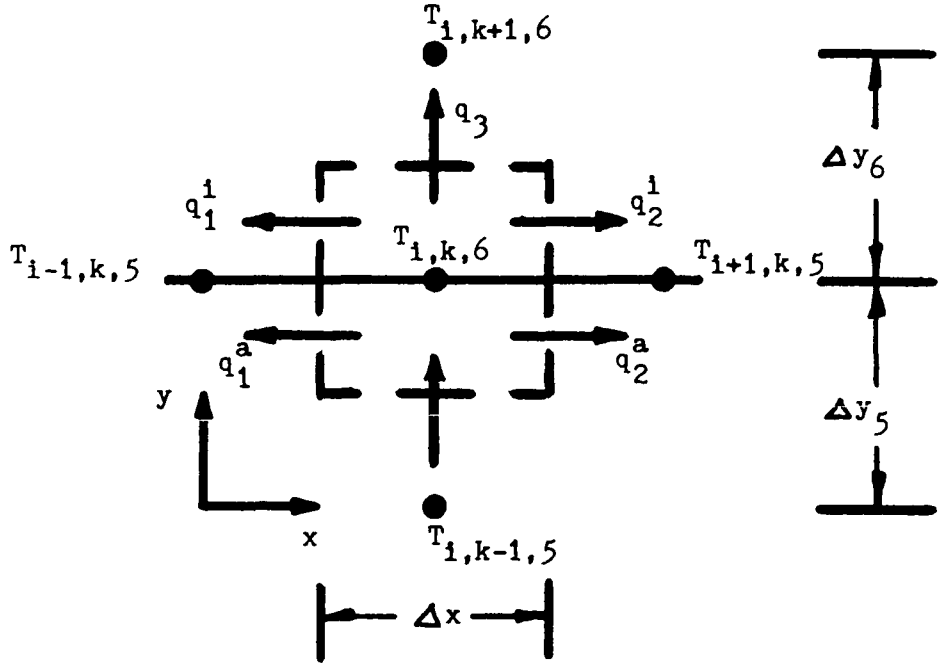

b. Ice-Abrasion Shield Interface

Figure 7. The Nodal Energy Balance

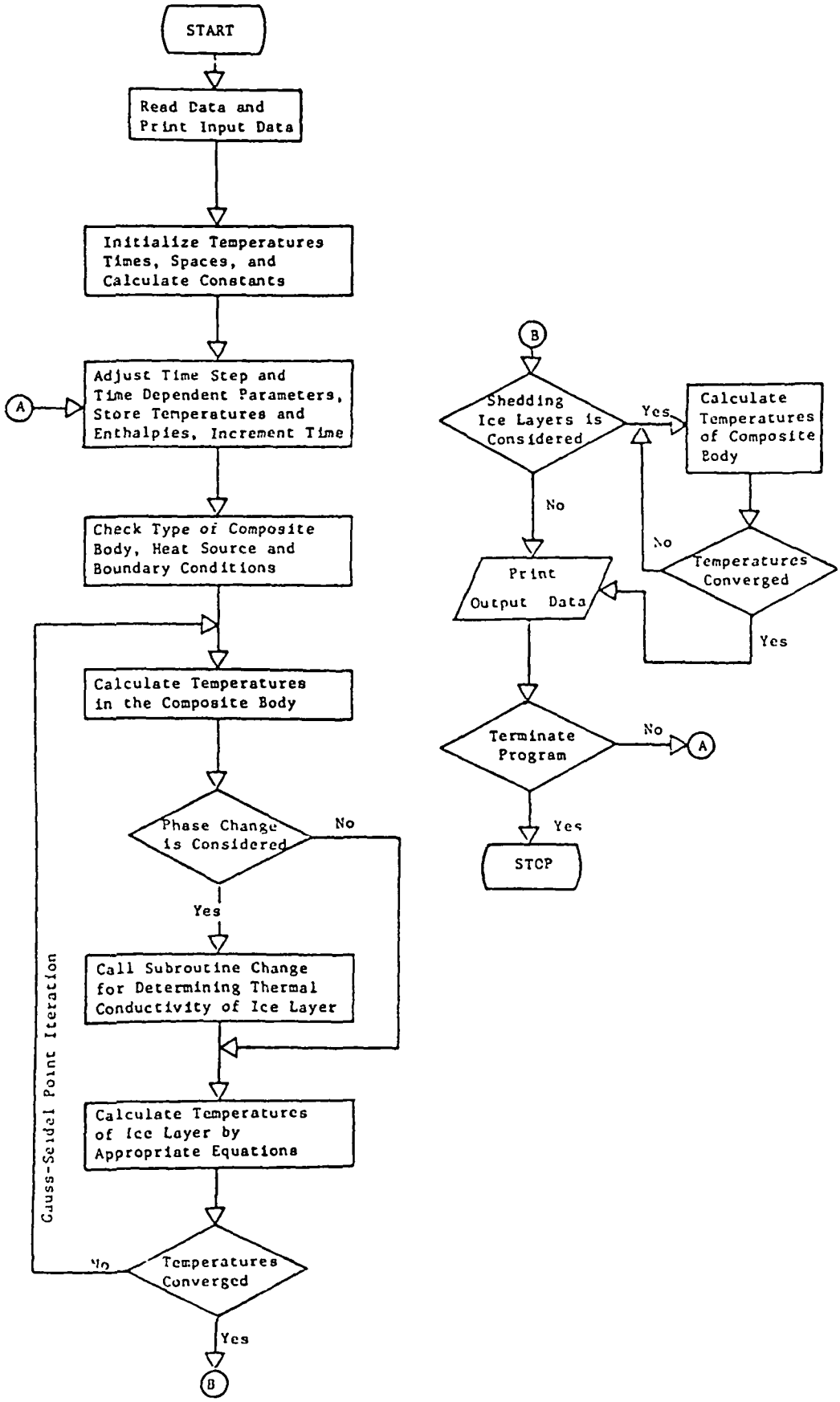

Figure 8. Flow Chart for the Computer Program

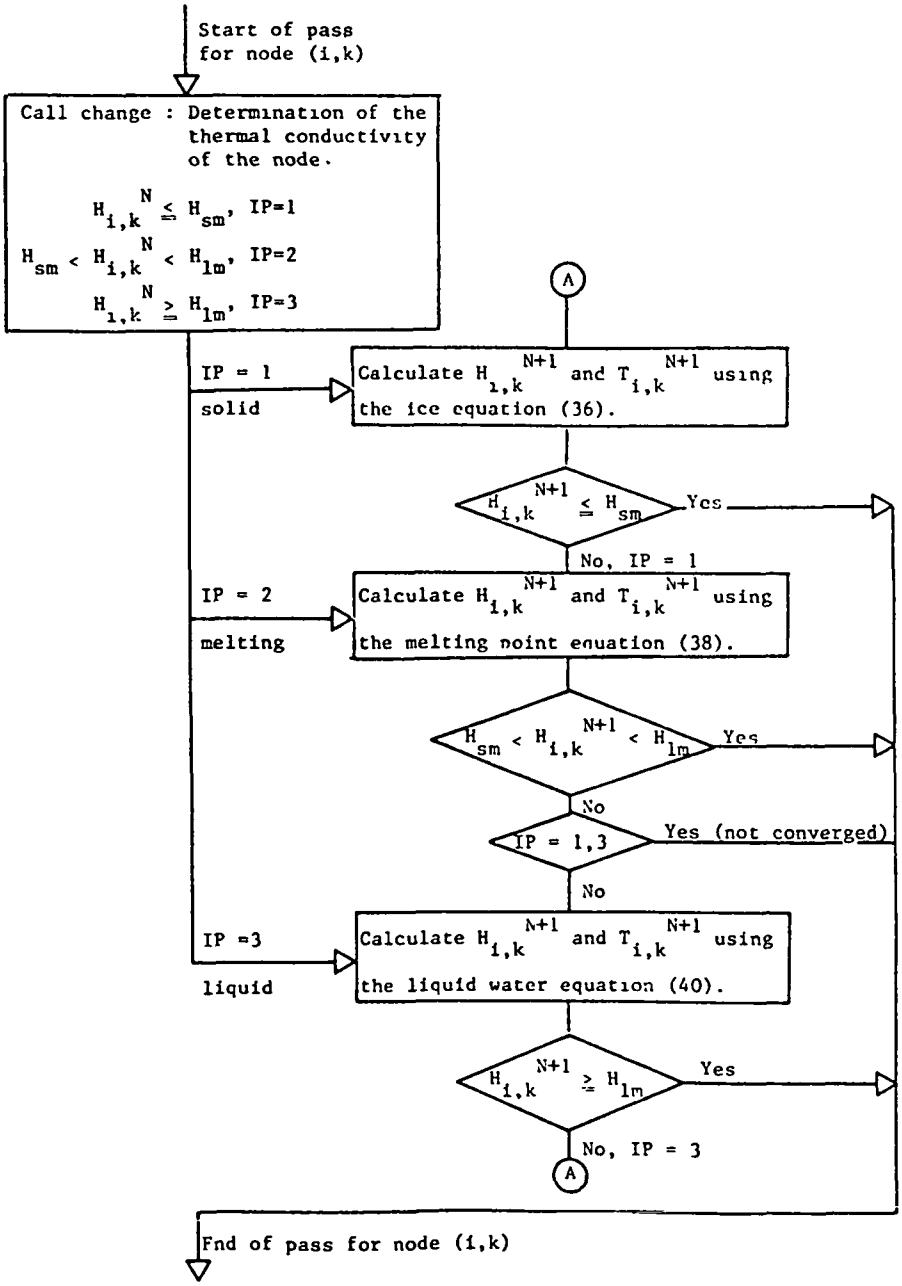

Figure 9. Flow Chart for the Enthalpy Method

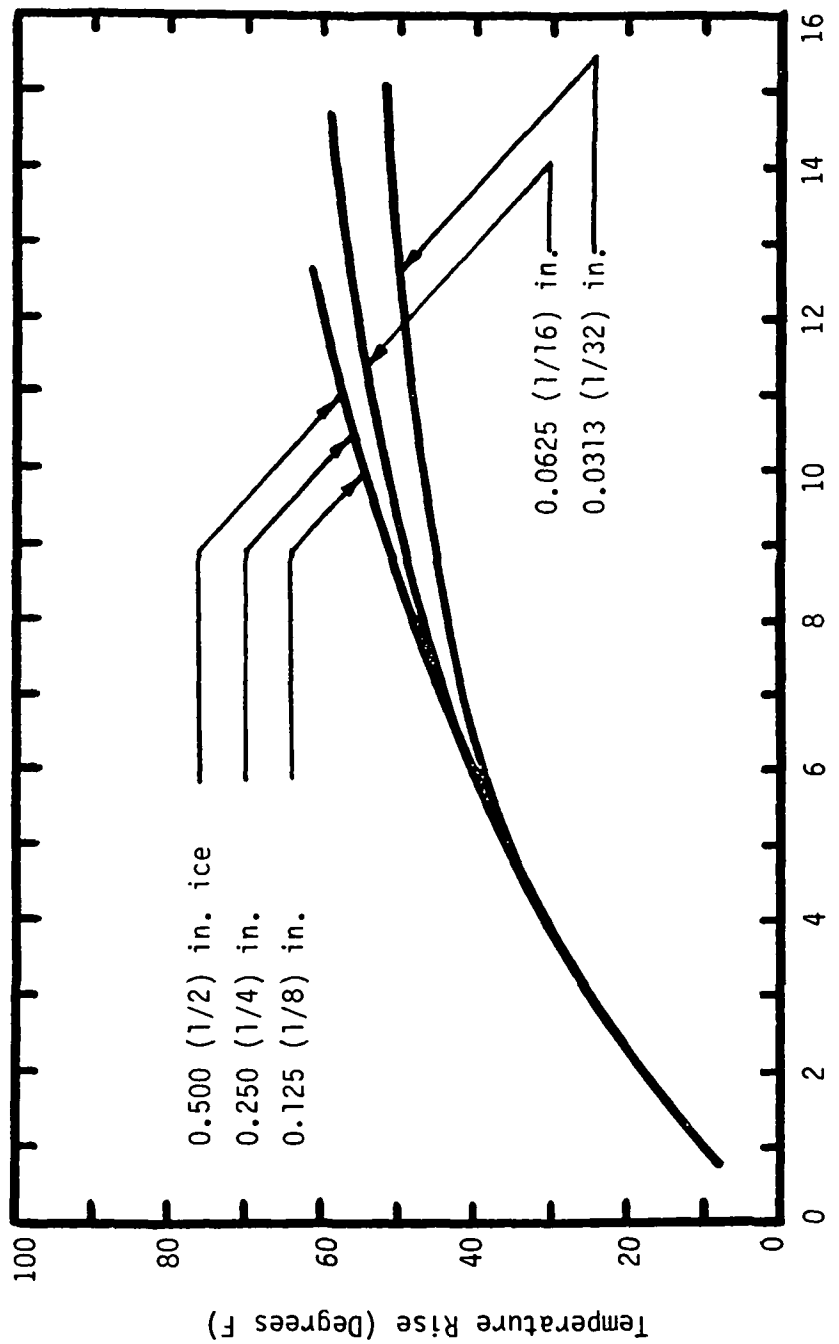

Figure 10. Deicing Time Predictions Using Marano's 1-D Code With No Phase Change

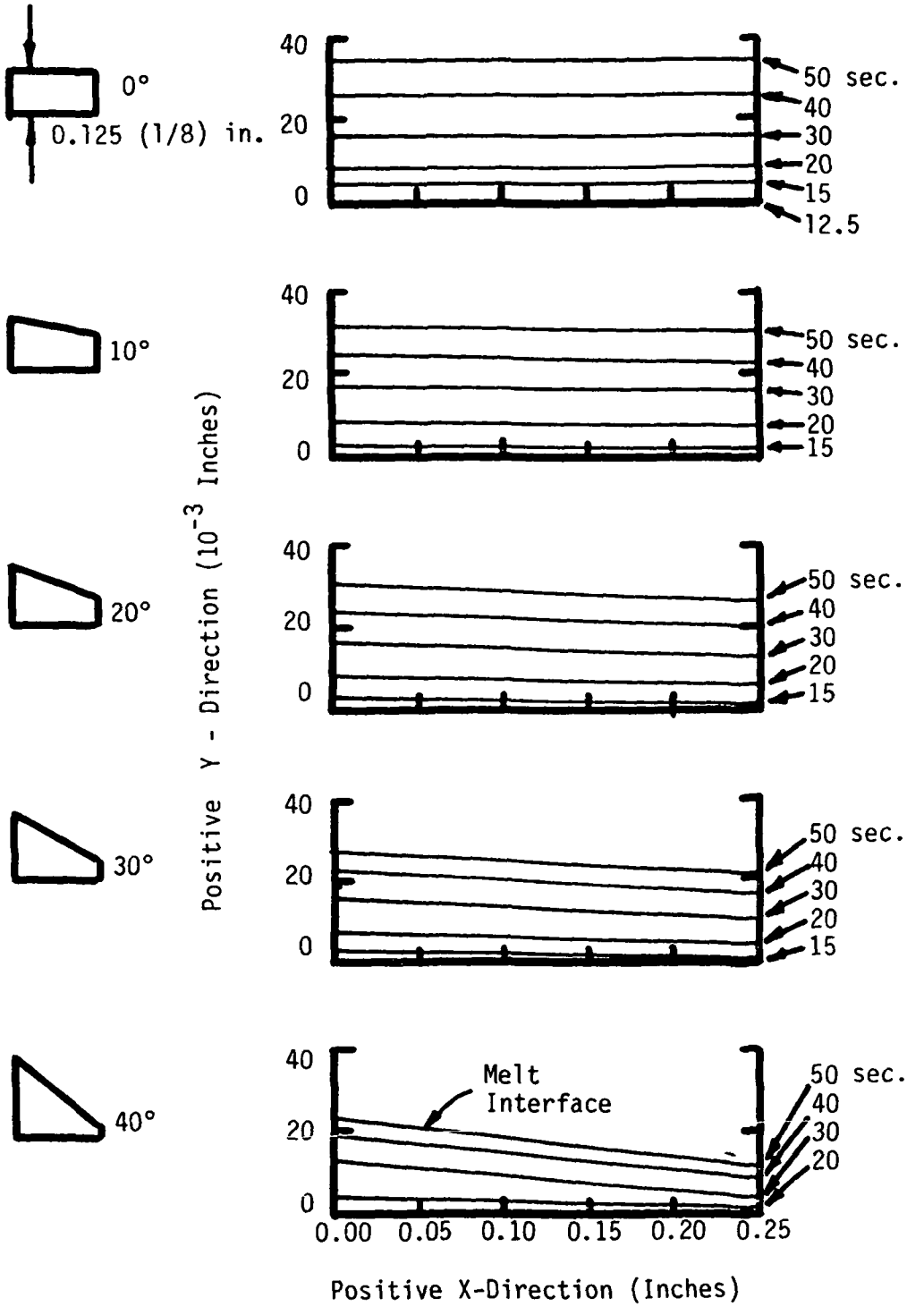

Figure 11. Progression of Melt Interface for Various Ice Shapes With a Mean Ice Thickness of 0.125 (1/8) Inches

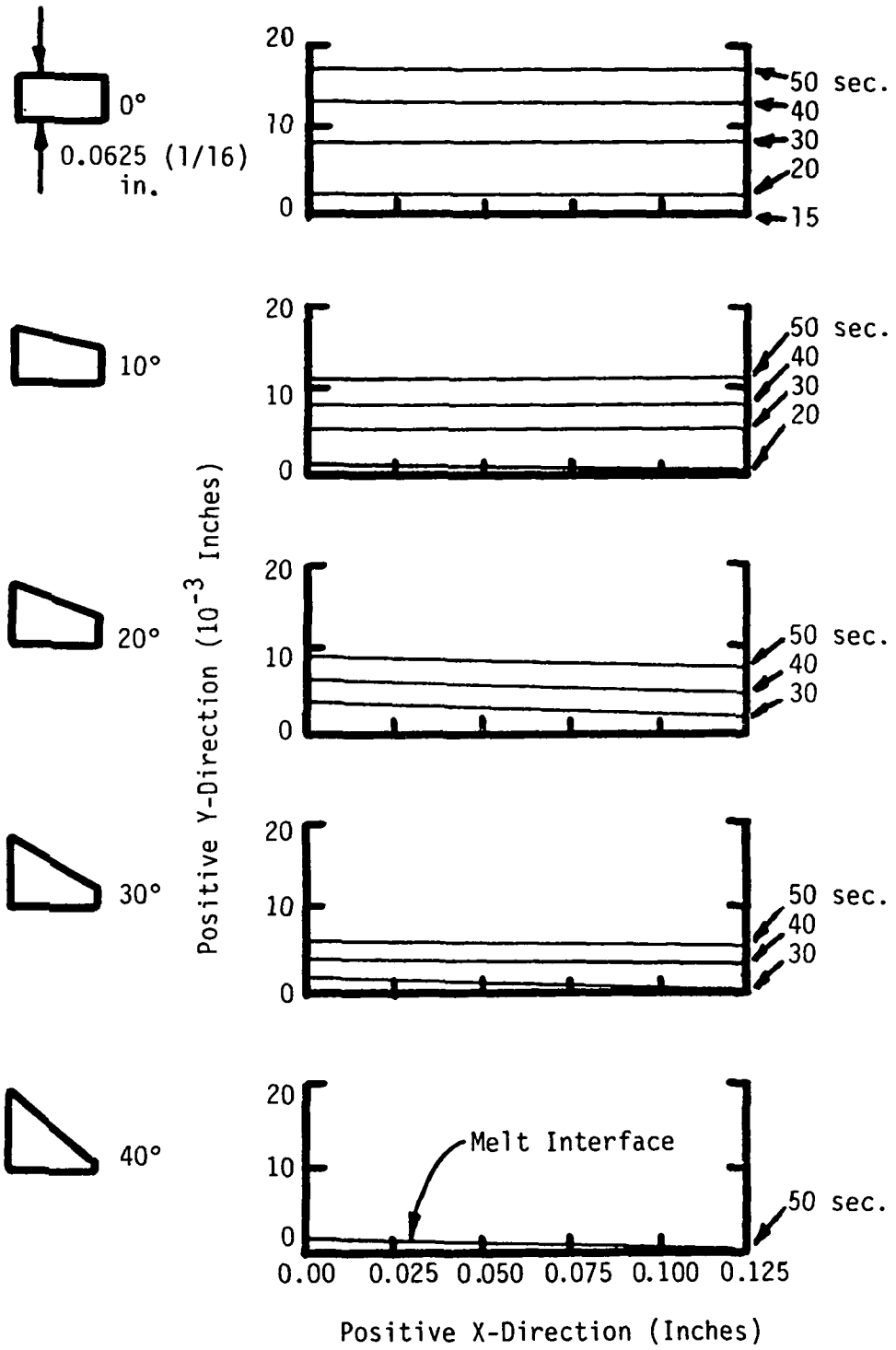

Figure 12. Progression of Melt Interface for Various Ice Shapes with a Mean Ice Thickness of 0.0625 (1/16) Inches

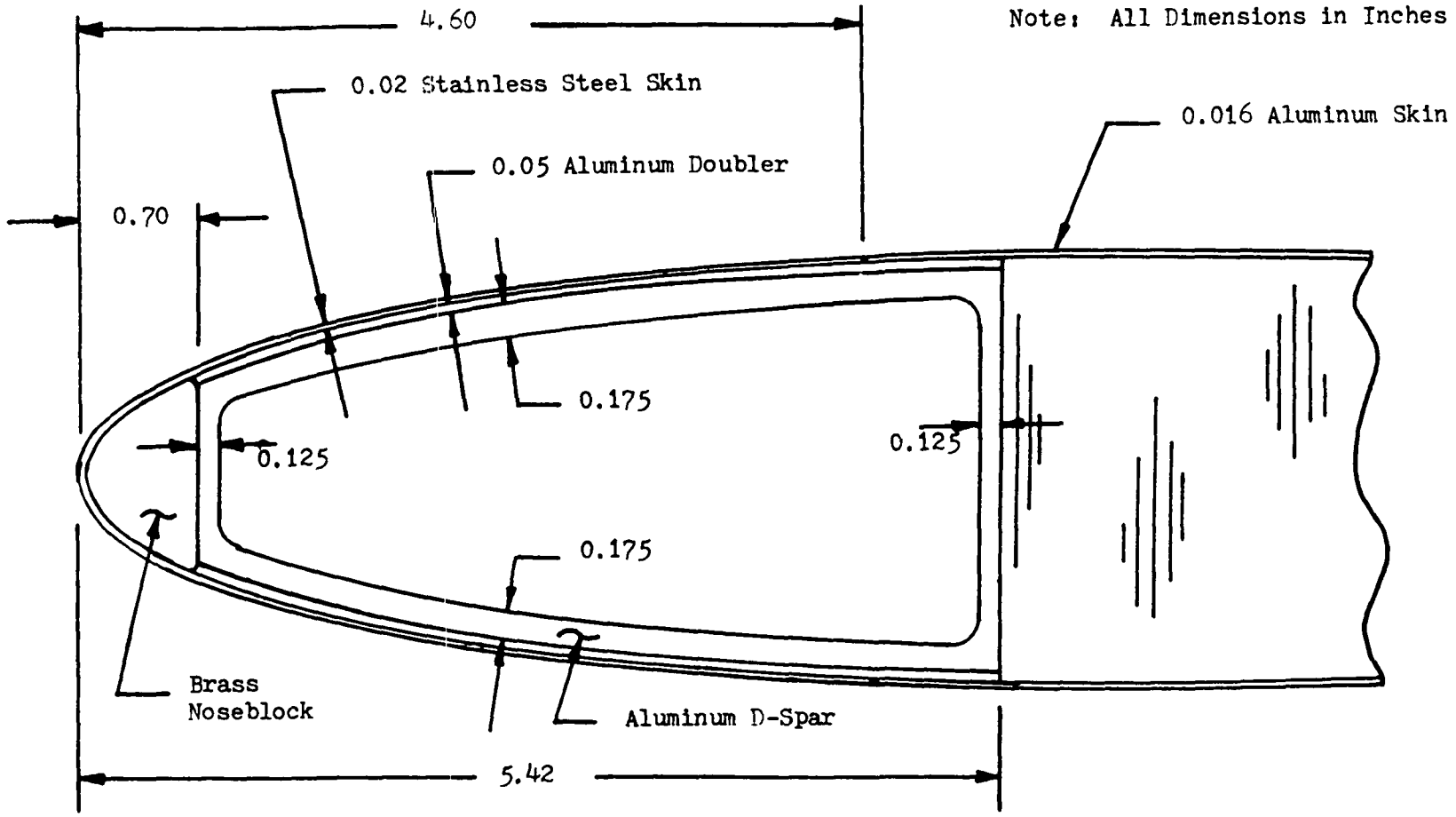

Figure 13. Details of a UH-1H Helicopter Blade Construction
(All Dimensions in Inches)

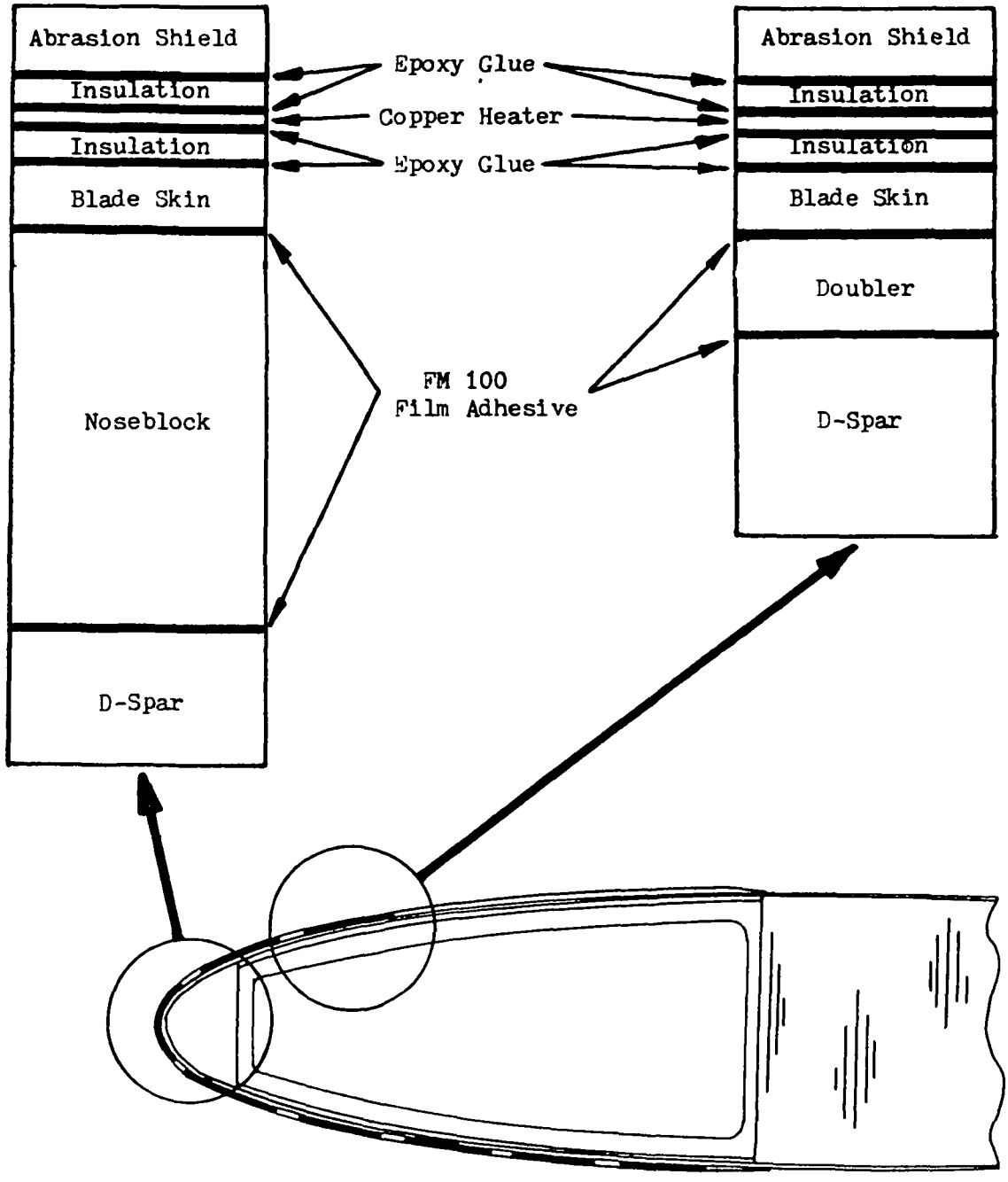

Figure 14. Details of the Electrothermal Deicer and Blade Construction

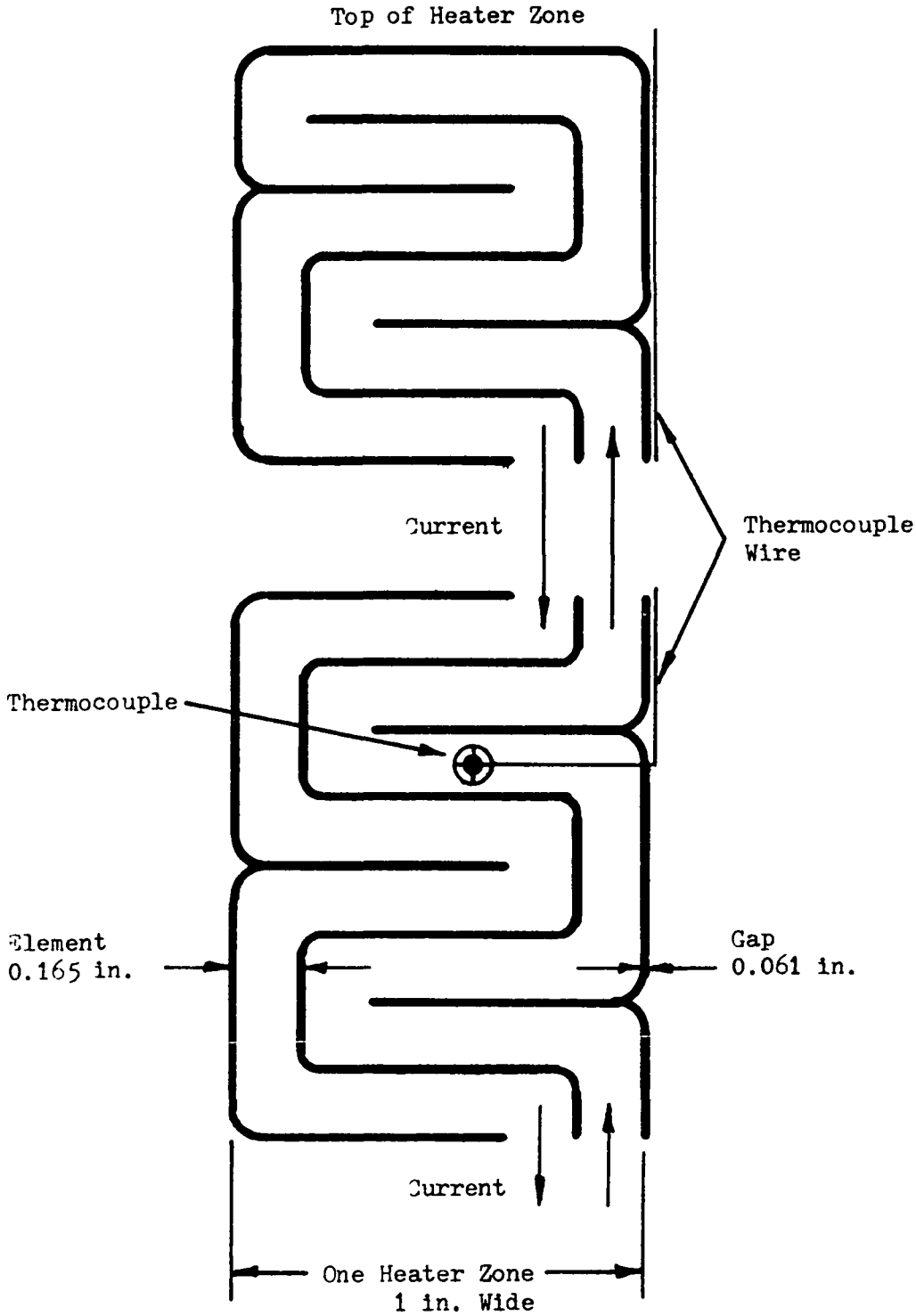

Figure 15. Details of a Heater Zone and Thermocouple Construction

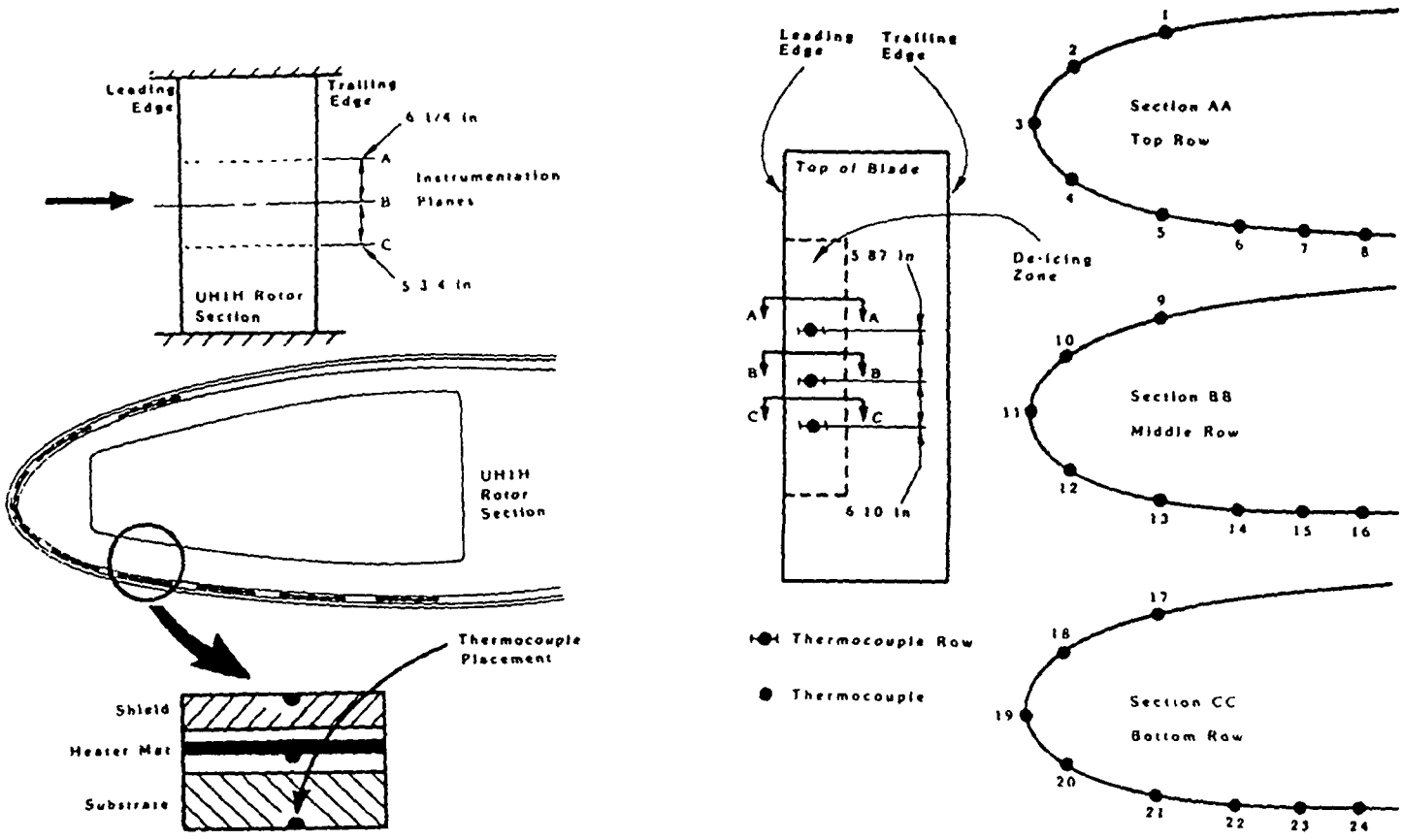

Figure 16. Thermocouple Location and Numbering for Thermocouples on the Inner Side of the D-Spar

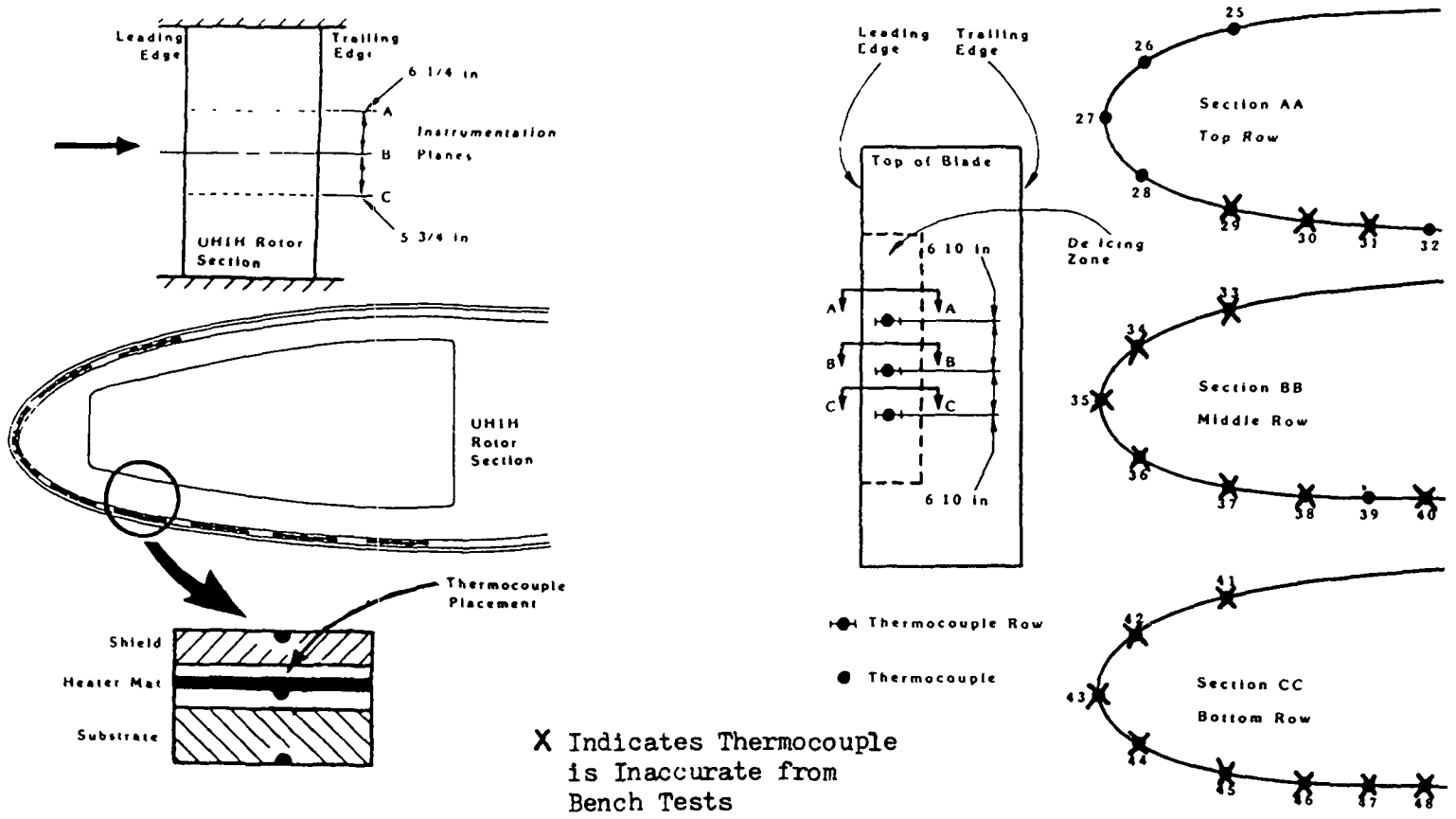

X Indicates Thermocouple is Inaccurate from Bench Tests

Figure 17. Thermocouple Location and Numbering for Thermocouples Laminated to the Inner Side of the Heater Mat

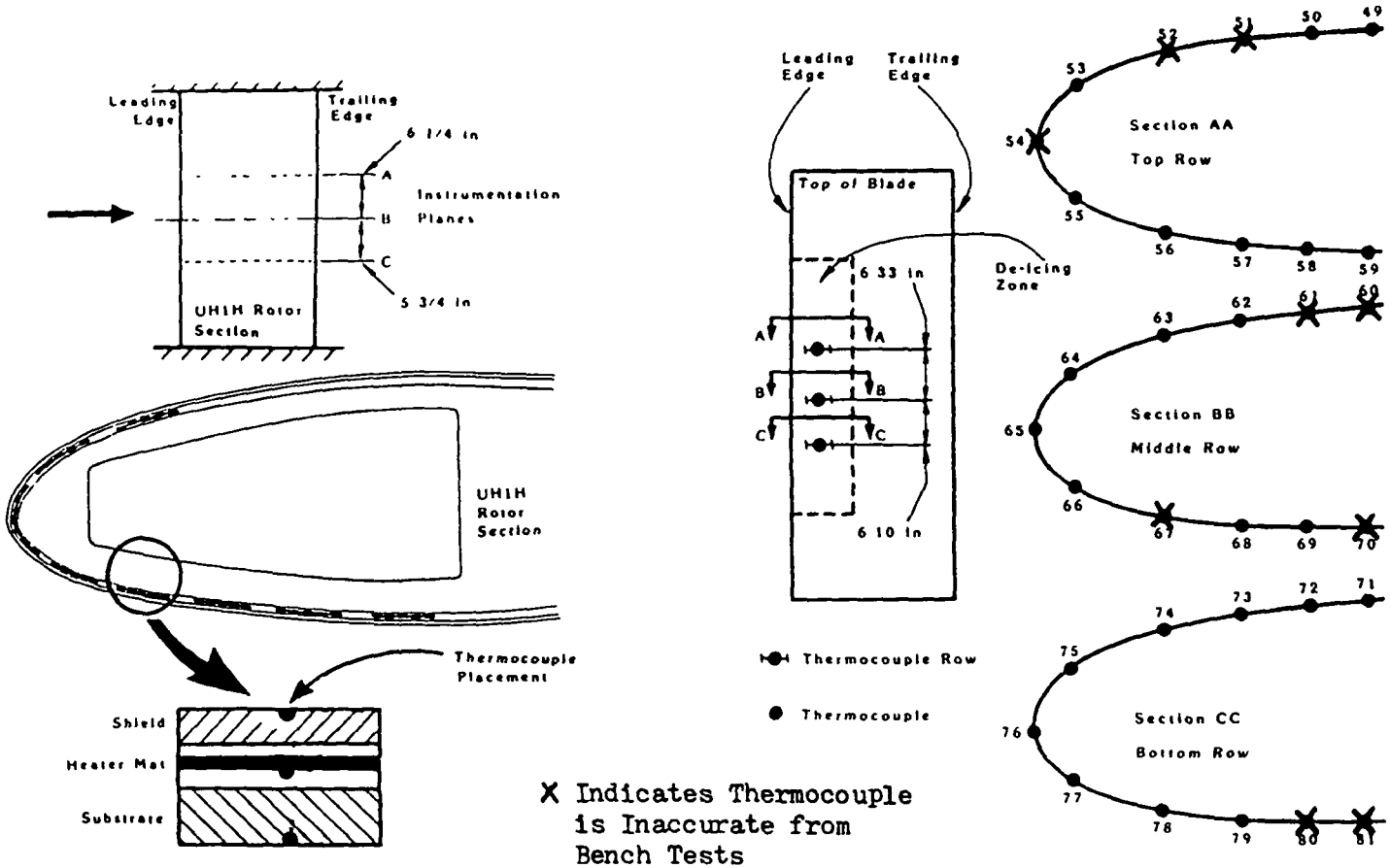

Figure 18. Thermocouple Location and Numbering for Thermocouples at the Outer Side of the Abrasion Shield

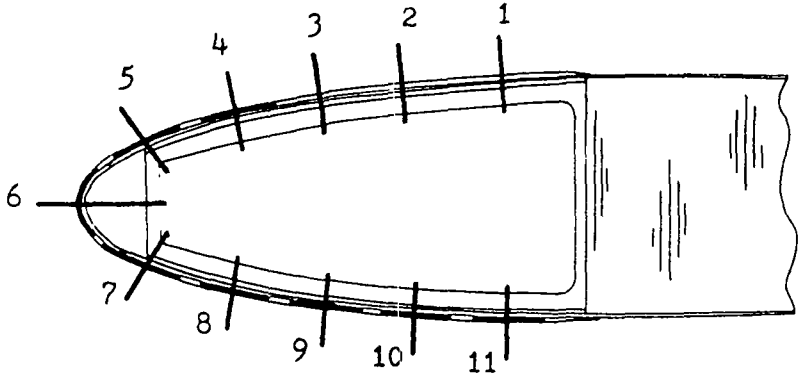

Position Around Blade

V_∞ = 120
T_∞ = 17
α = 0
P = 2.9
t_{on}/t_{off} = 30/30
n = 1

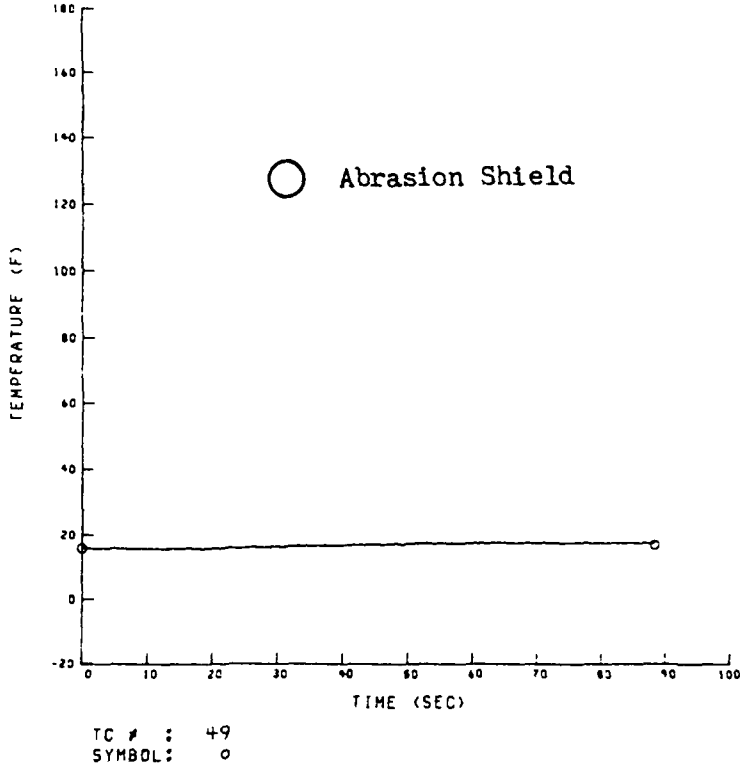

a. Position 1

Figure 19. Response of Selected Thermocouples for Escort Reading 70

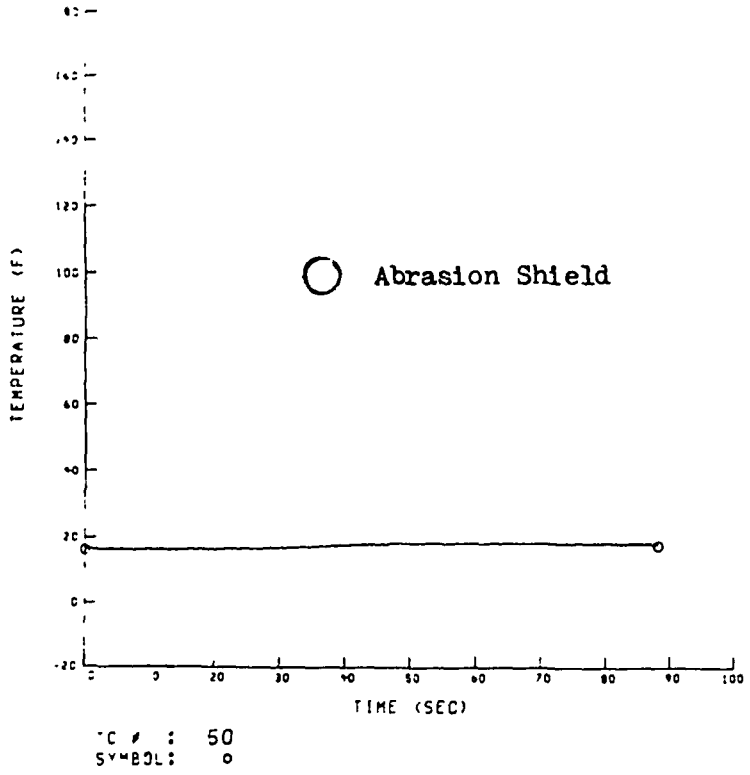

b. Position 2

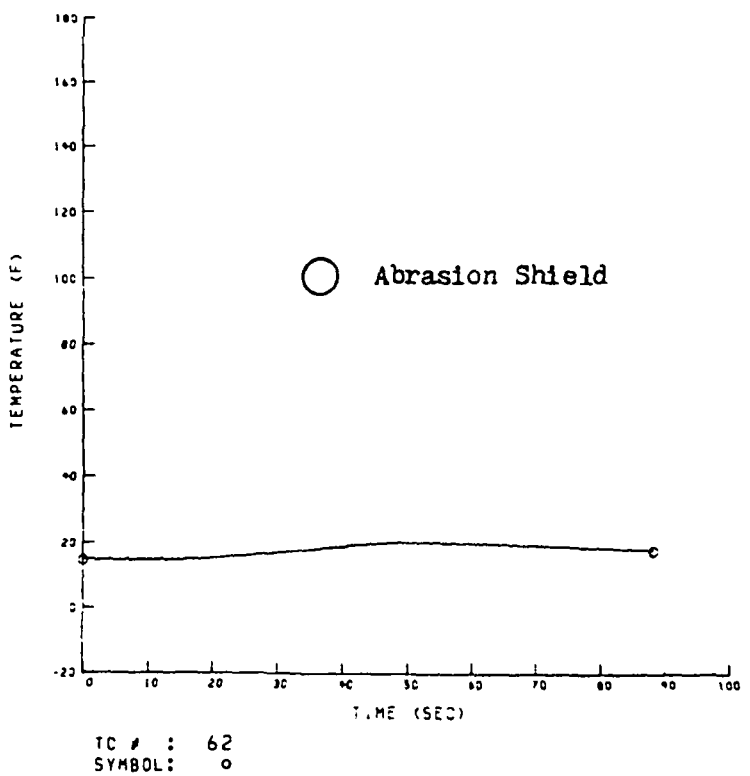

c. Position 3

Figure 19. (Reading 70 Continued)

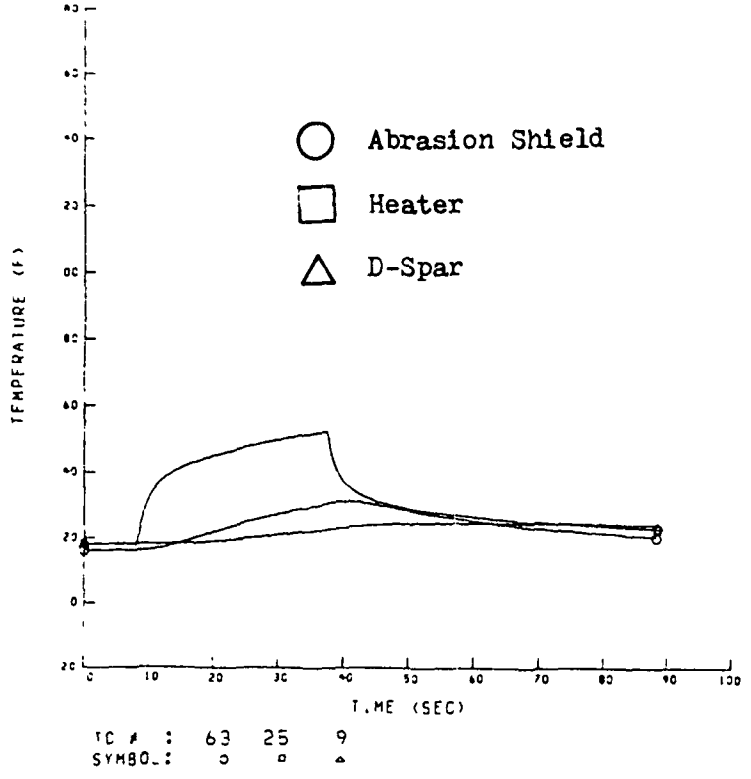

d. Position 4

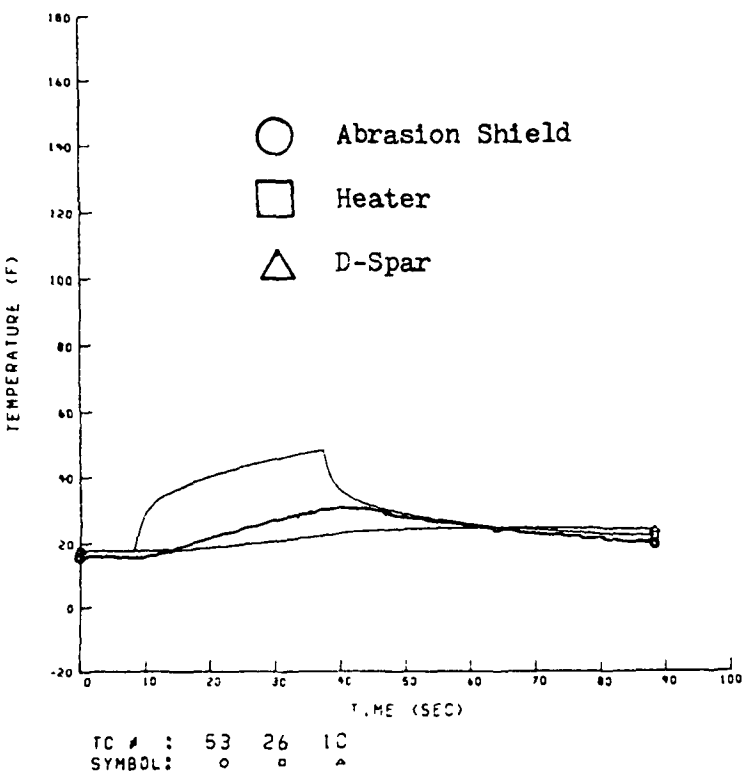

e. Position 5

Figure 19. (Reading 70 Continued)

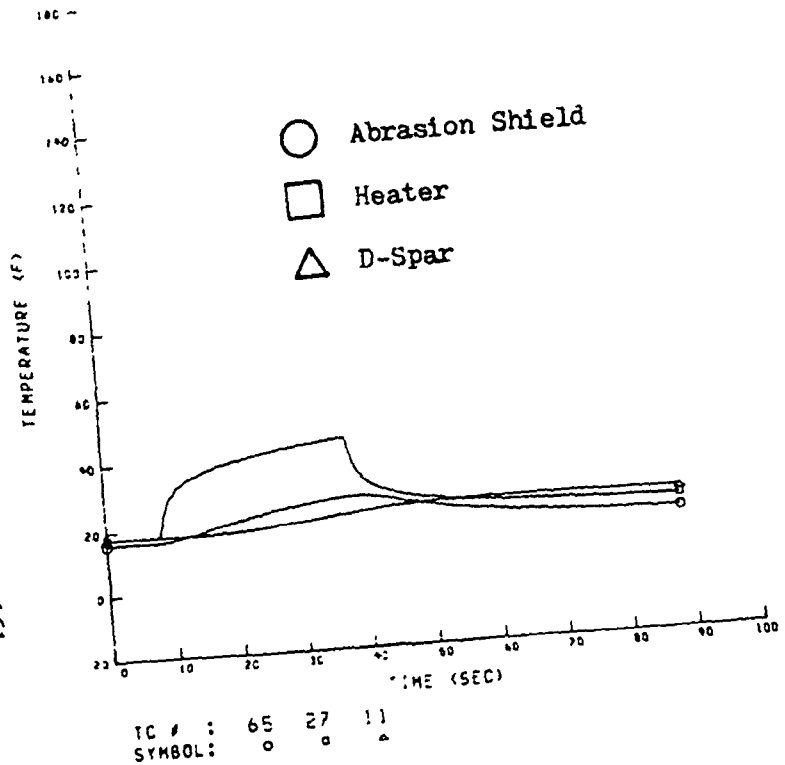

f. Position 6

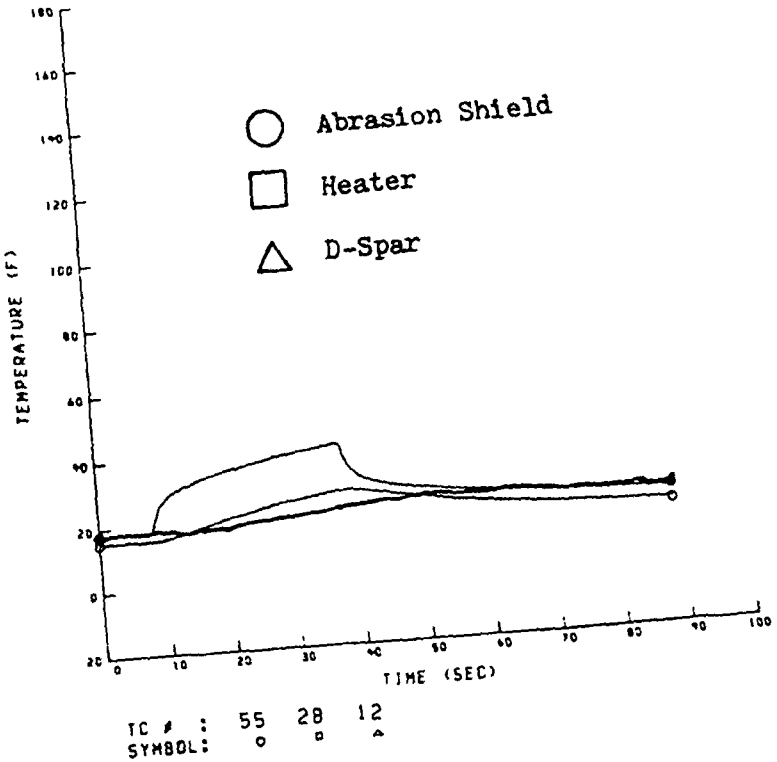

g. Position 7

Figure 19. (Reading 70 Continued)

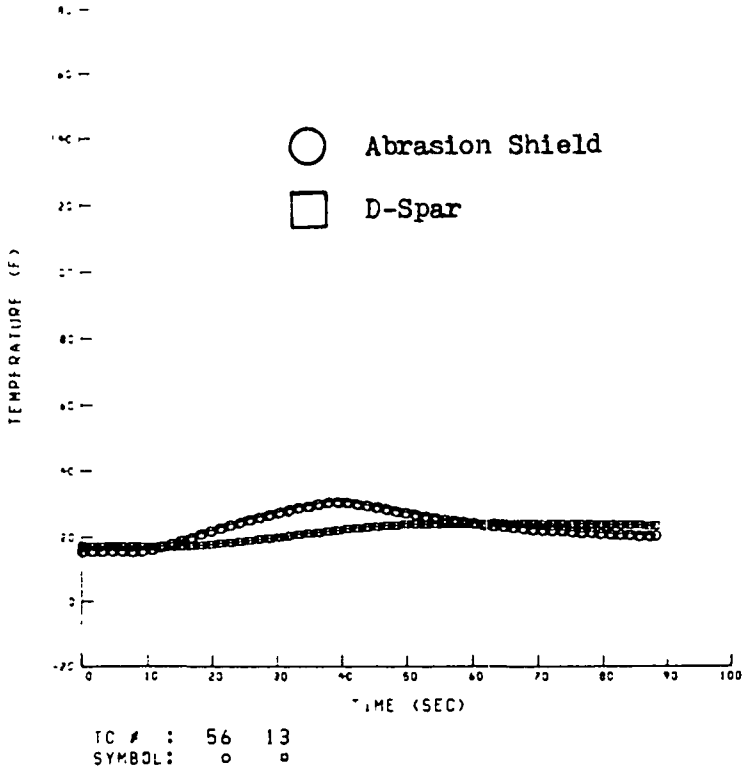

h. Position 8

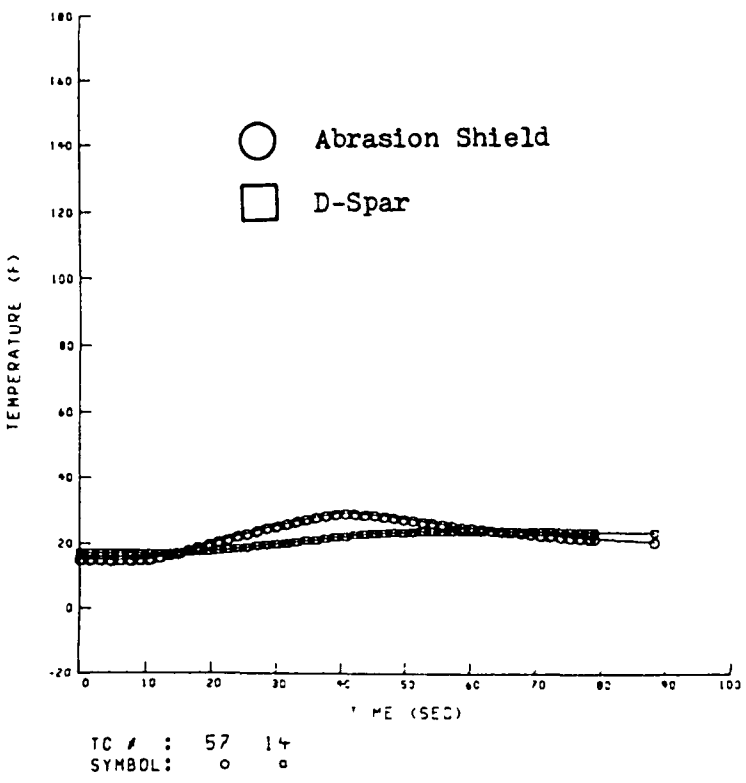

i. Position 9

Figure 19. (Reading 70 Continued)

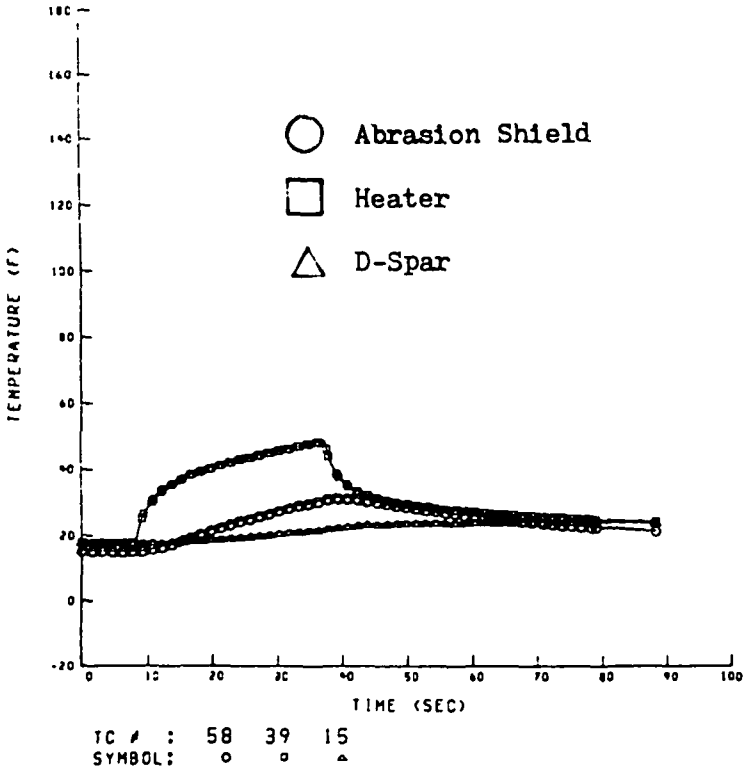

j. Position 10

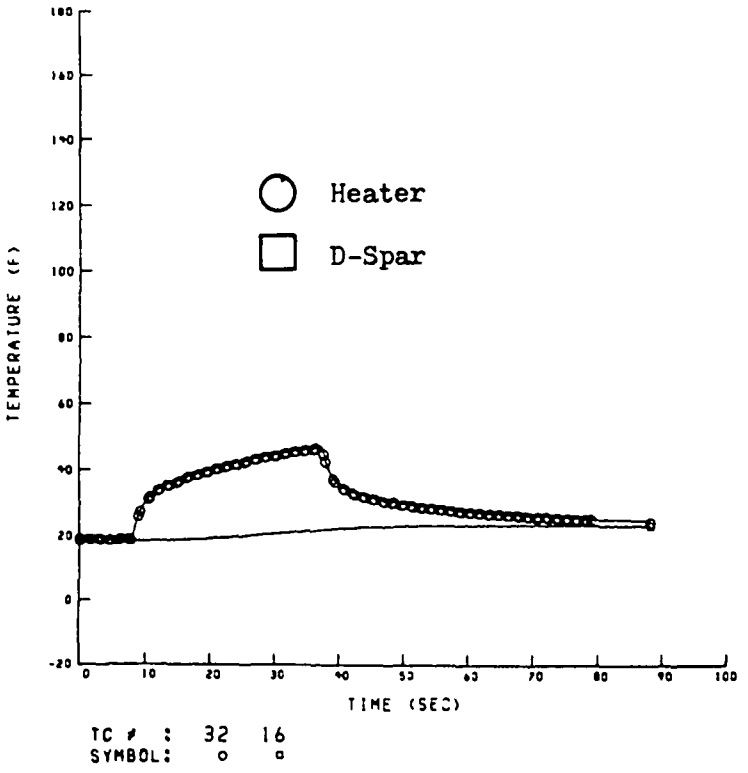

k. Position 11

Figure 19. (Reading 70 Continued)

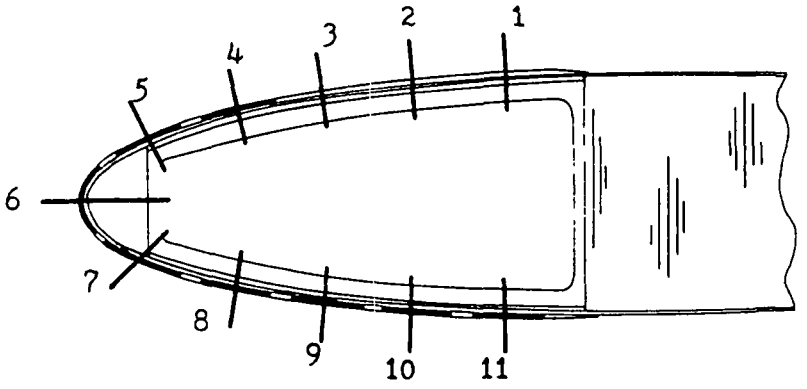

Position Around Blade

V_∞ = 275
T_∞ = -4
α = 0
P = 2.9
t_{on}/t_{off} = 30/30
n = 1

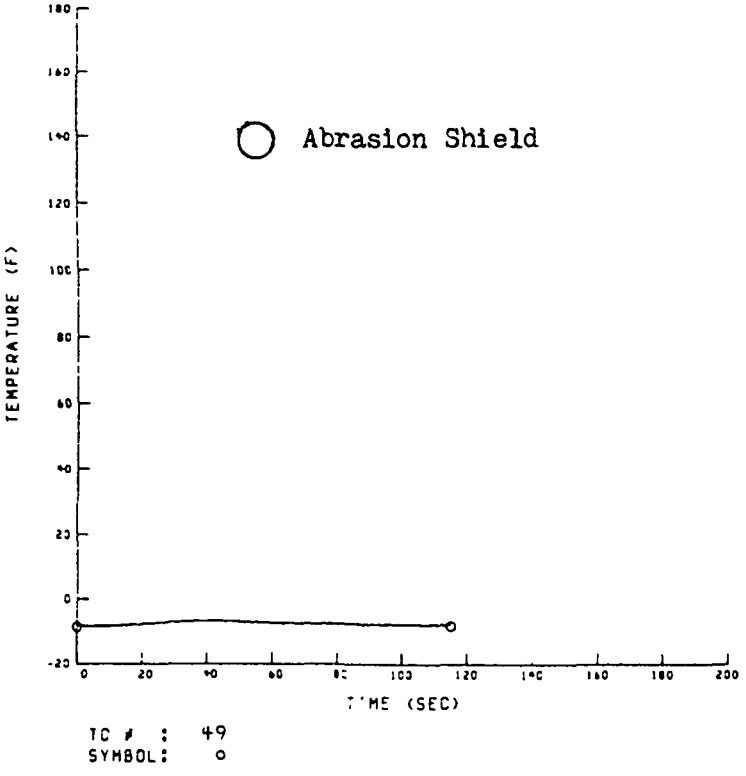

a. Position 1

Figure 20. Response of Selected Thermocouples for Escort Reading 76

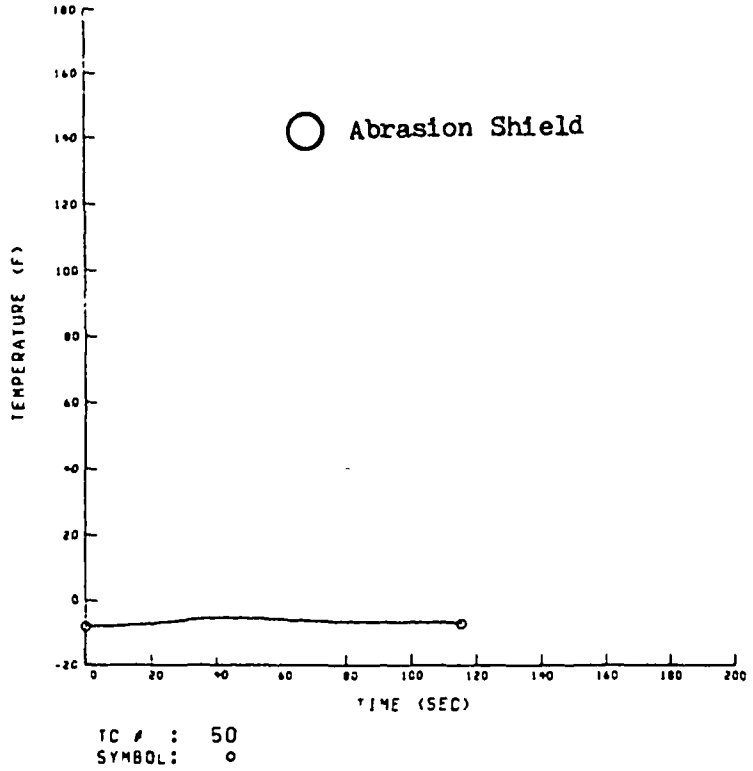

b. Position 2

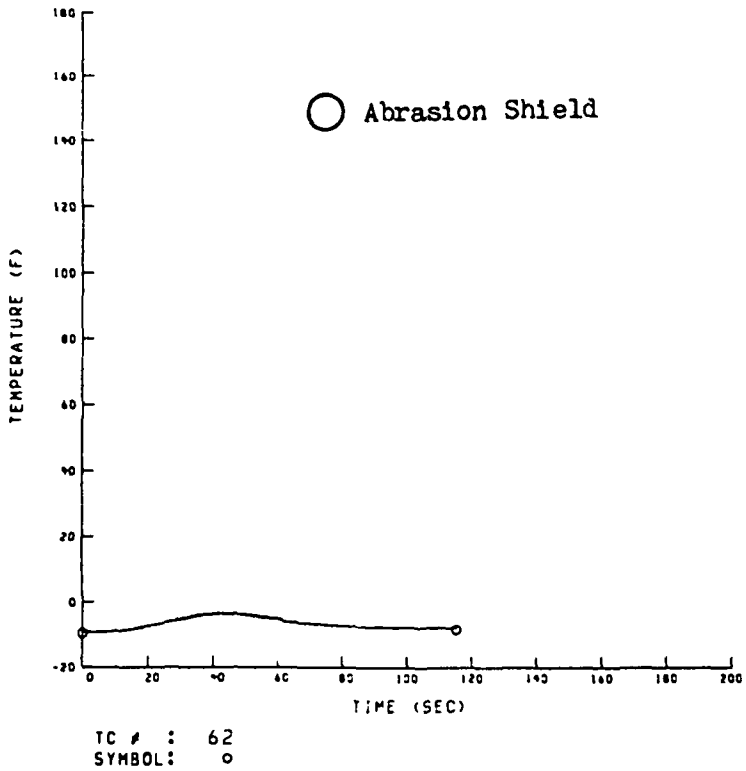

c. Position 3

Figure 20. (Reading 76 Continued)

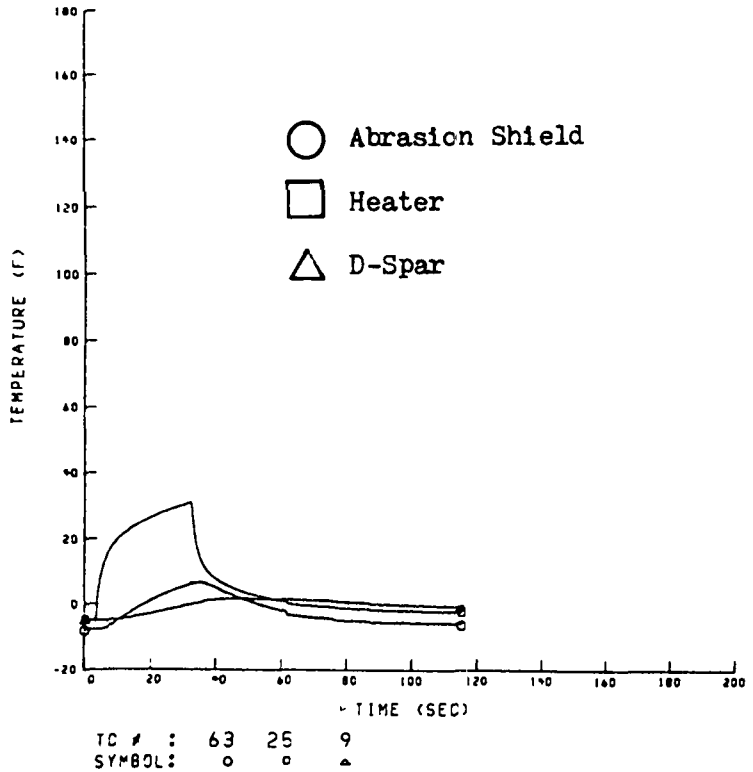

d. Position 4

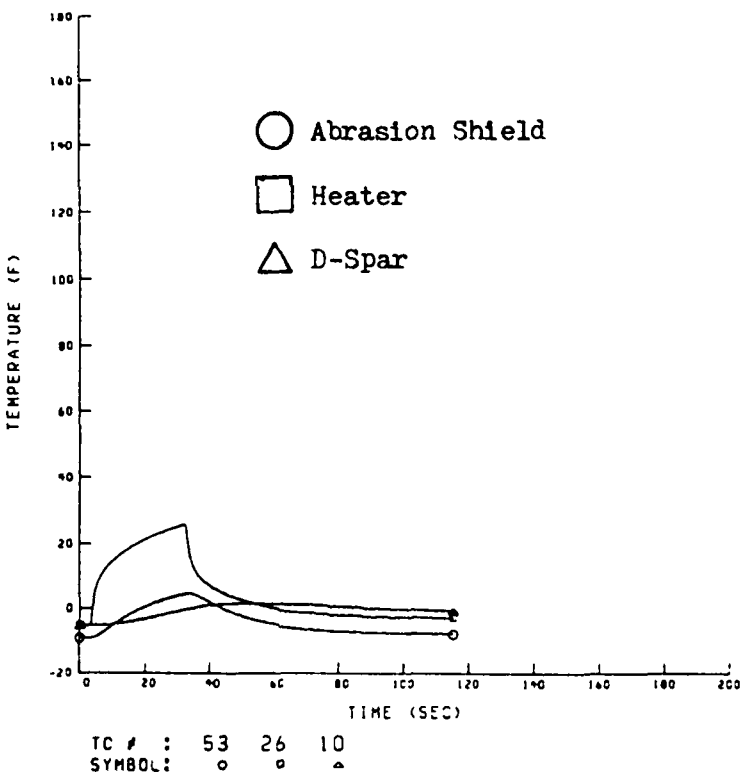

e. Position 5

Figure 20. (Reading 76 Continued)

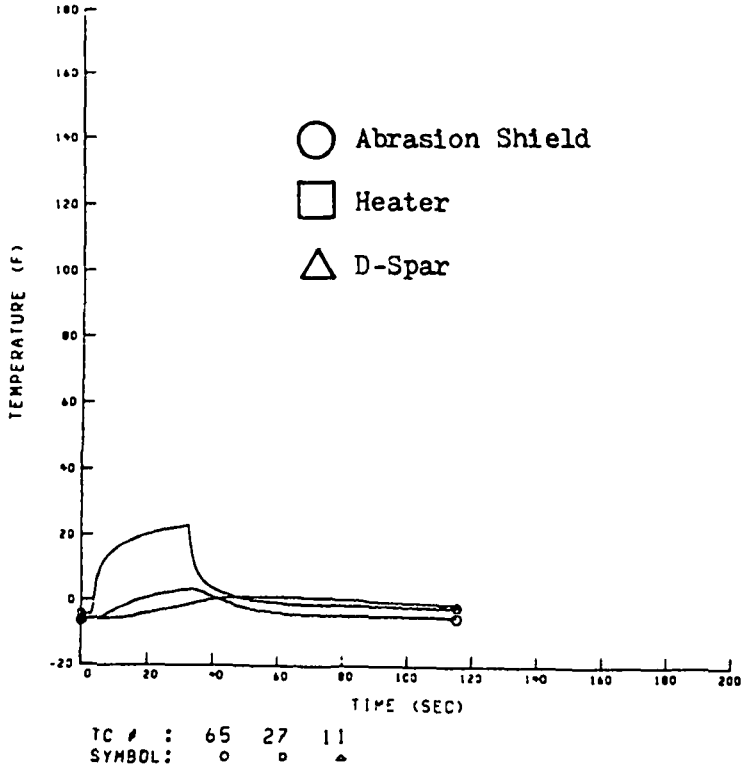

f. Position 6

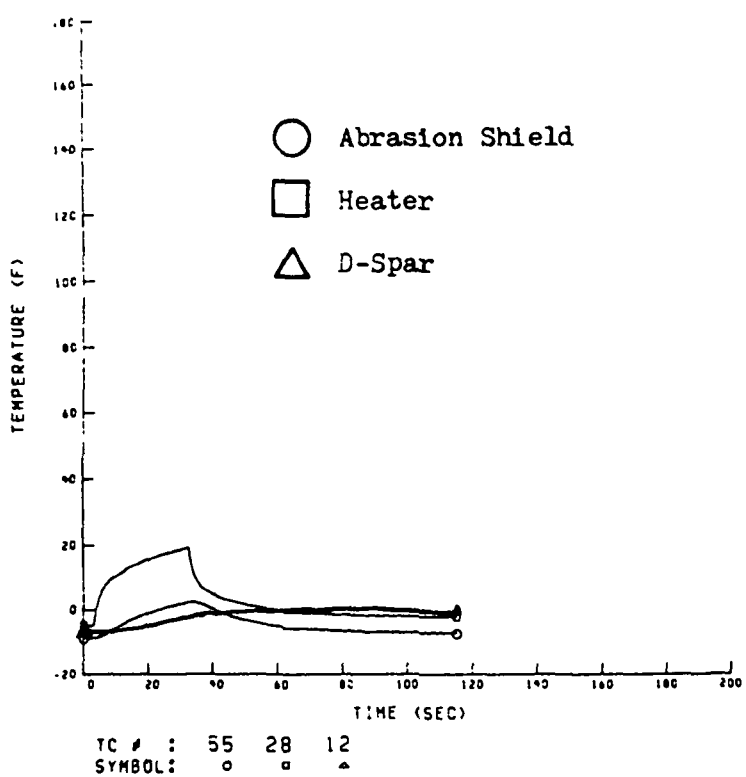

g. Position 7

Figure 20. (Reading 76 Continued)

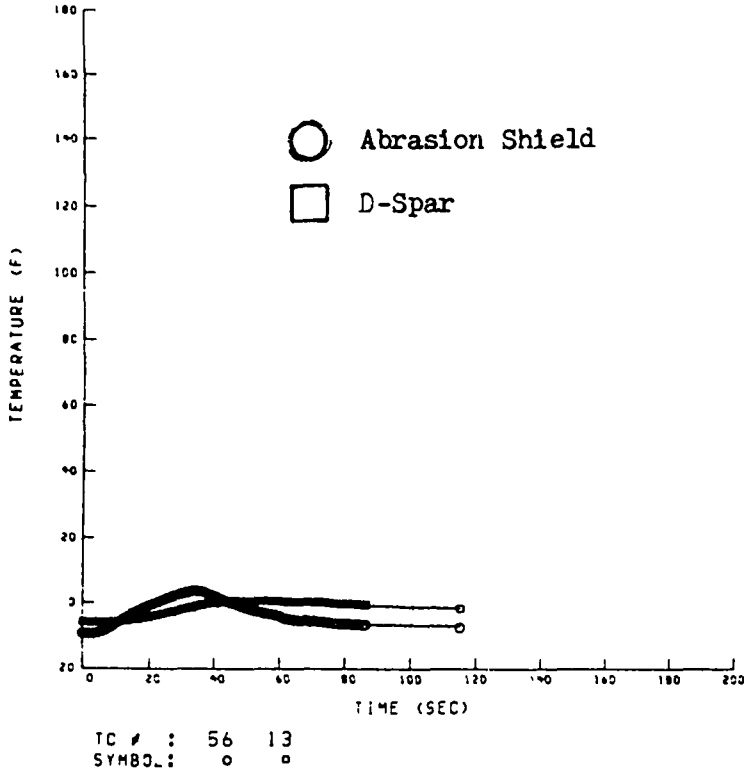

h. Position 8

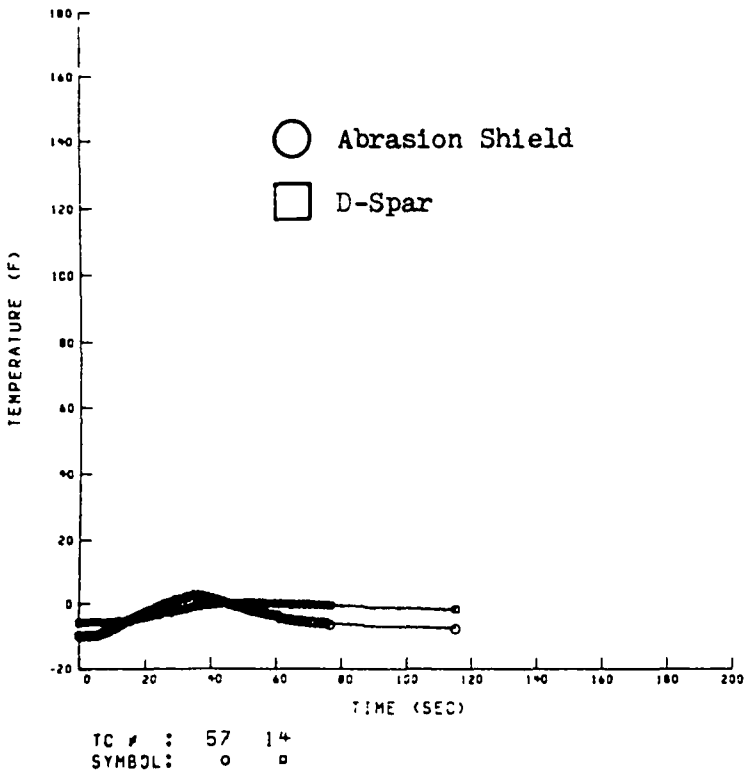

i. Position 9

Figure 20. (Reading 76 Continued)

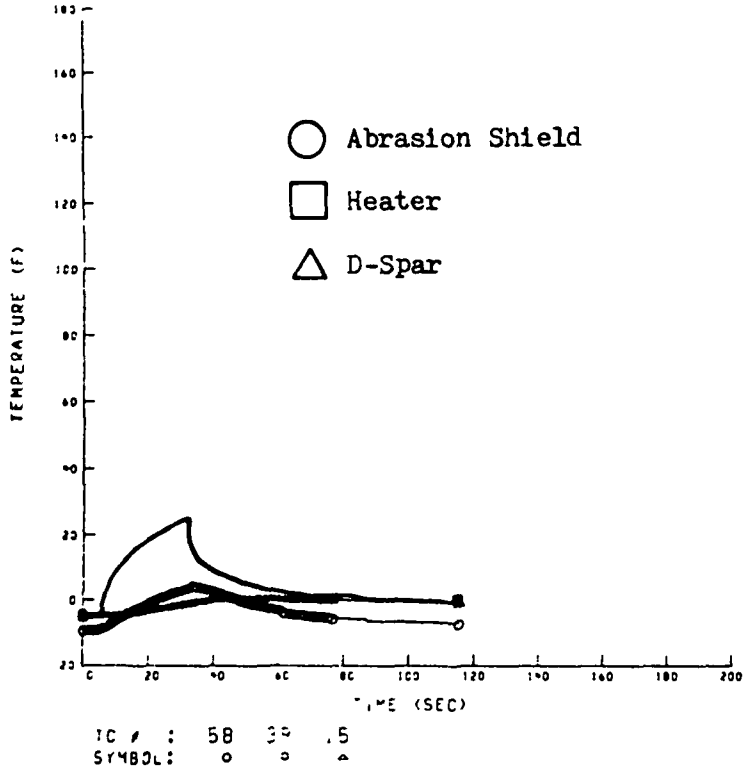

j. Position 10

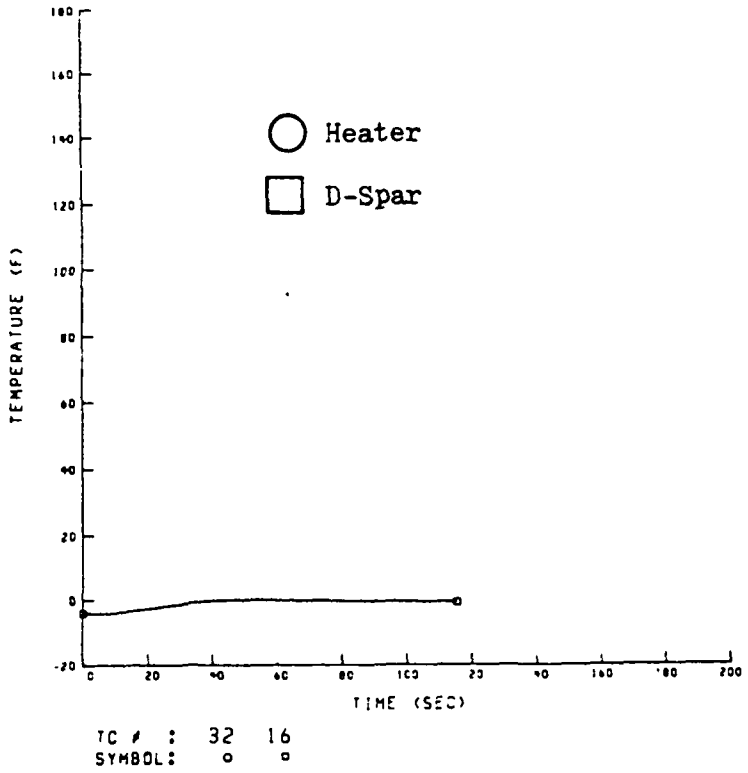

k. Position 11

Figure 20. (Reading 76 Continued)

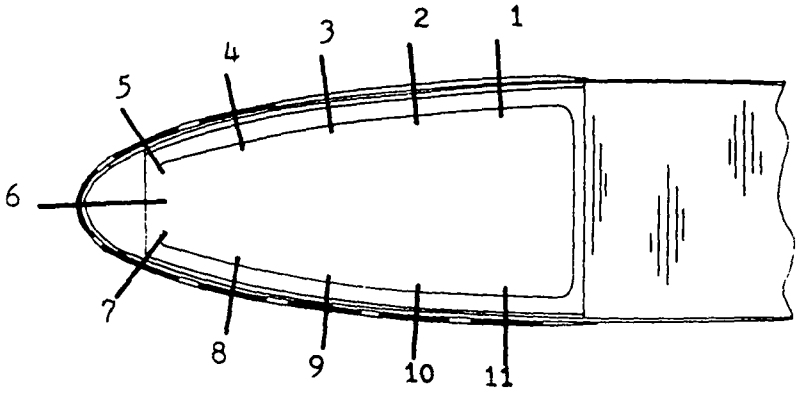

Position Around Blade

V_∞ = 120
T_∞ = -15
α = 0
P = 8.0
t_{on}/t_{off} = 30/30
n = 1

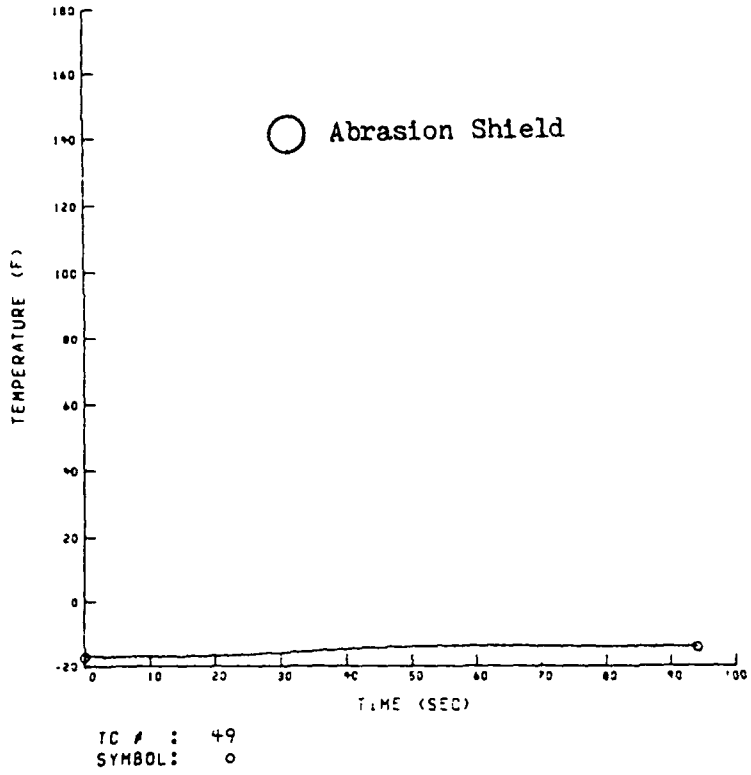

a. Position 1

Figure 21. Response of Selected Thermocouples for Escort Reading 92

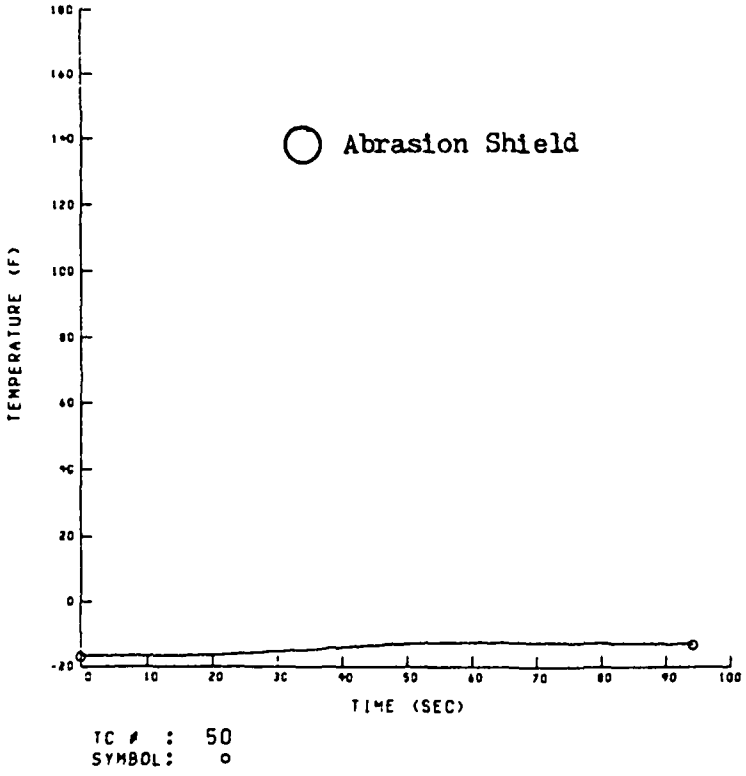

b. Position 2

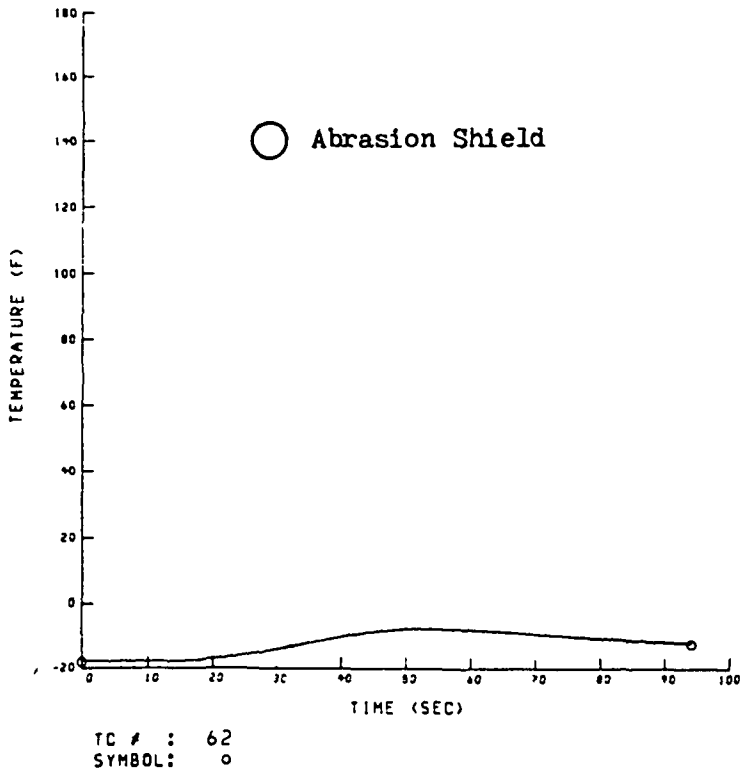

c. Position 3

Figure 21. (Reading 92 Continued)

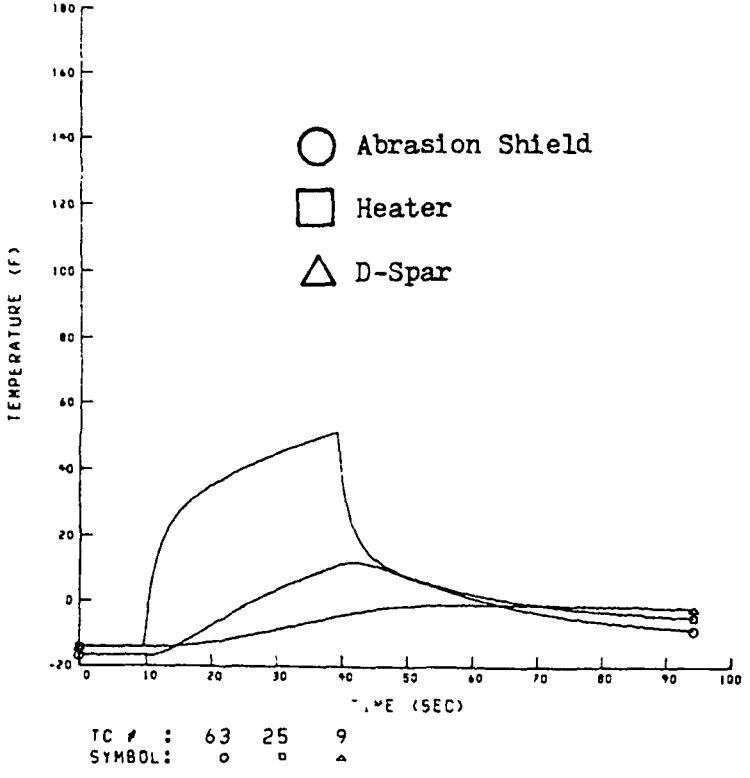

d. Position 4

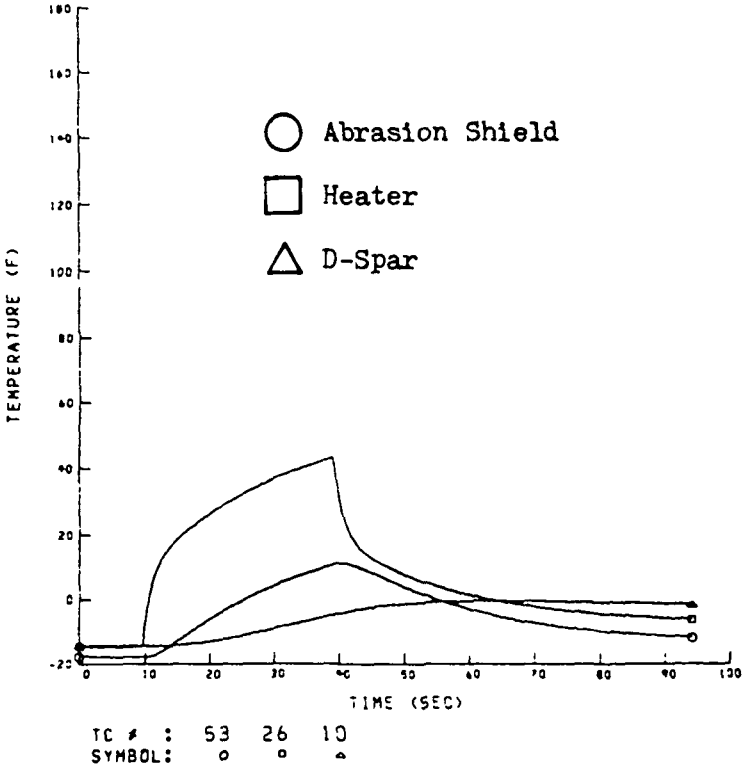

e. Position 5

Figure 21. (Reading 92 Continued)

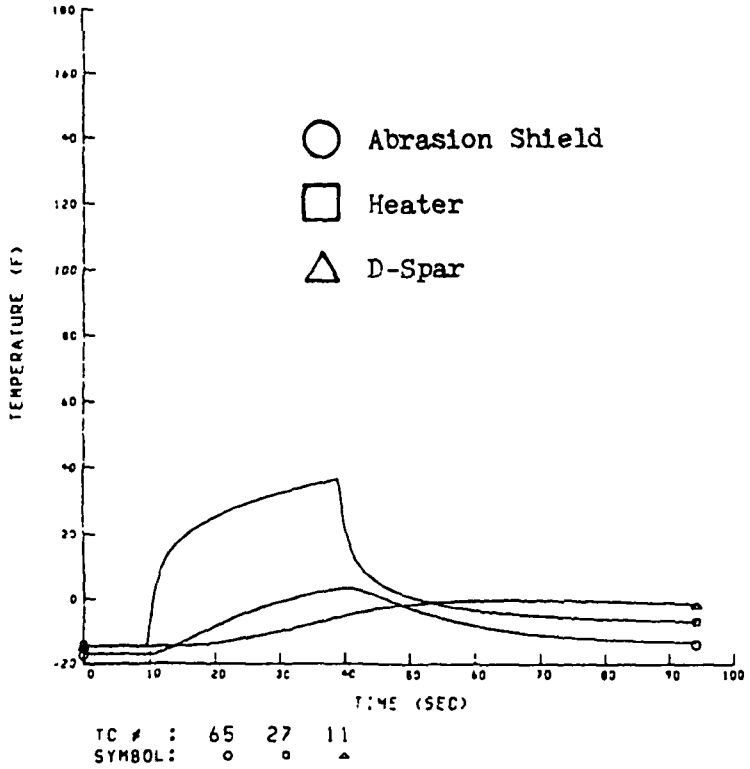

f. Position 6

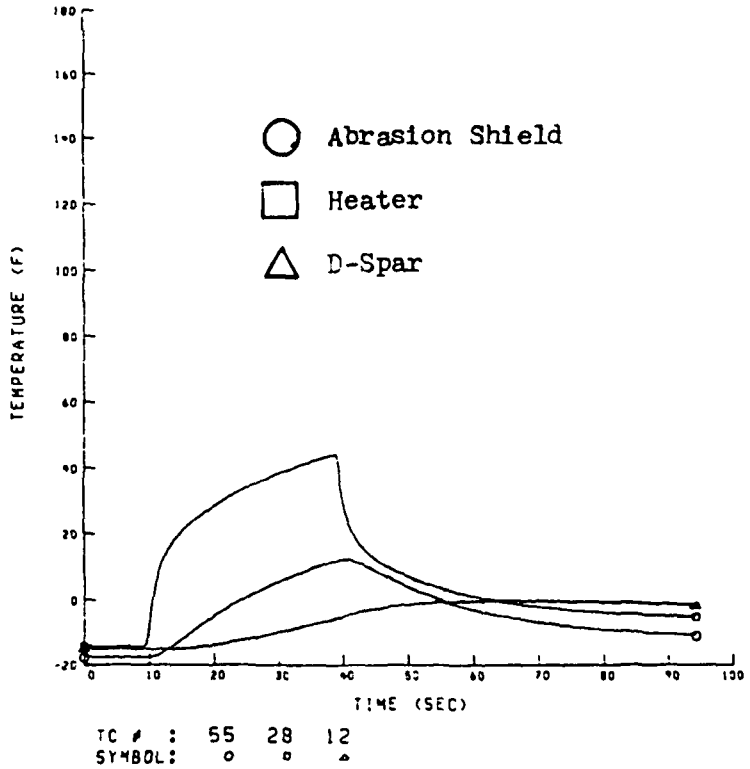

g. Position 7

Figure 21. (Reading 92 Continued)

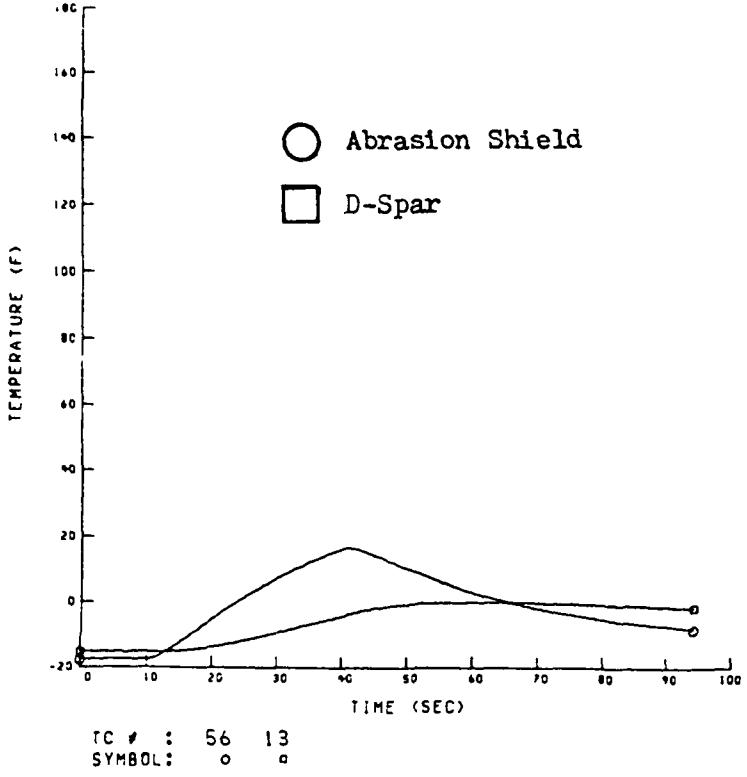

h. Position 8

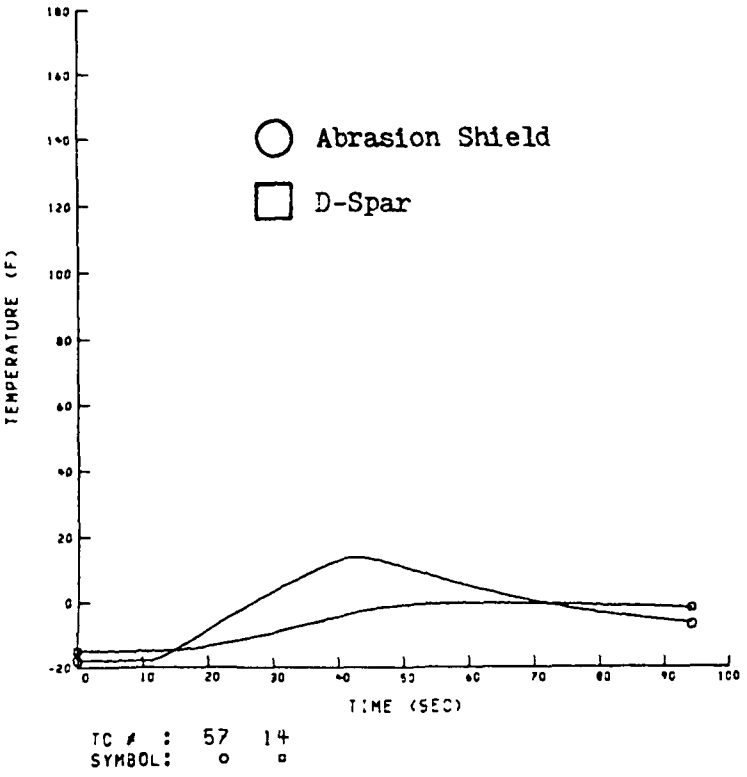

i. Position 9

Figure 21. (Reading 92 Continued)

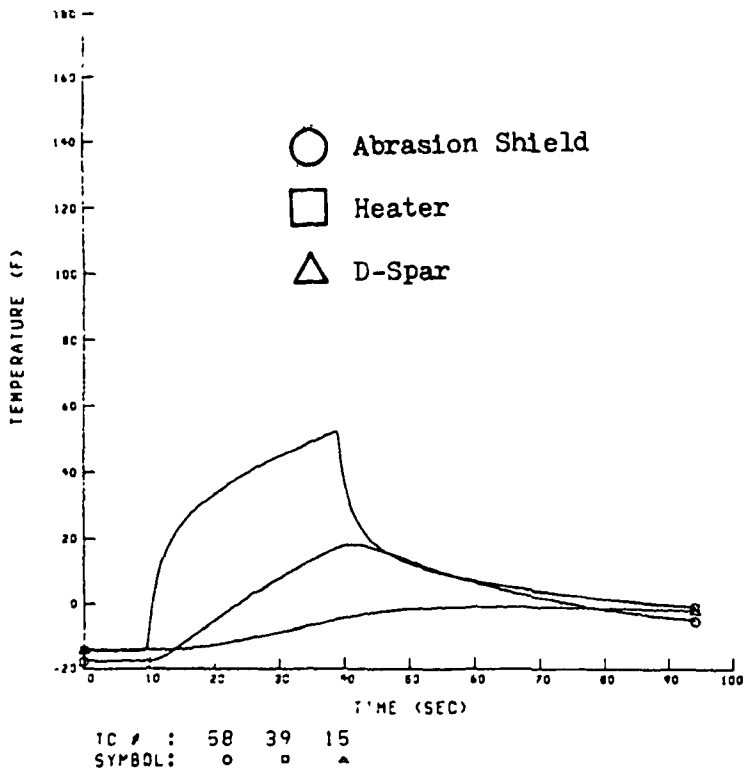

j. Position 10

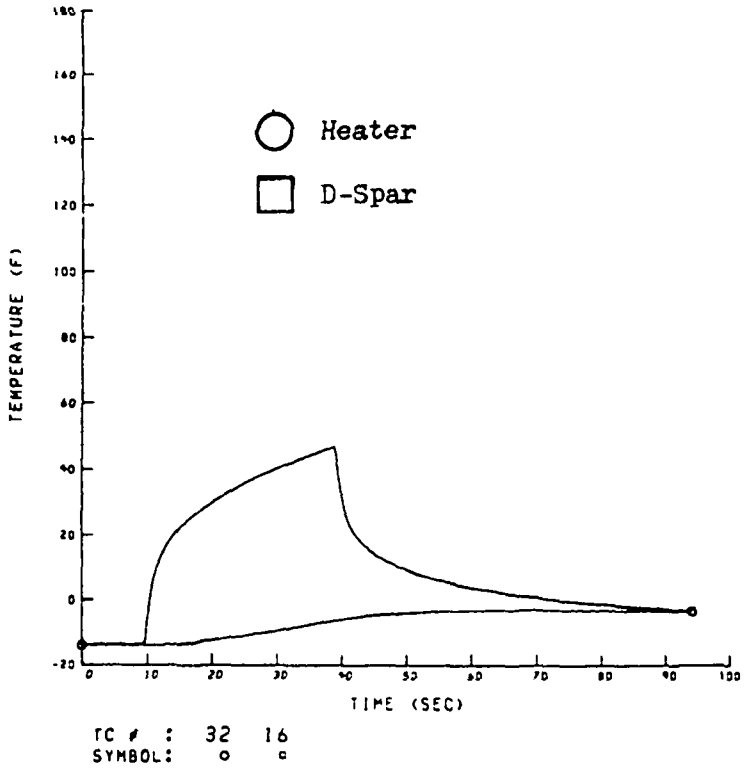

k. Position 11

Figure 21. (Reading 92 Continued)

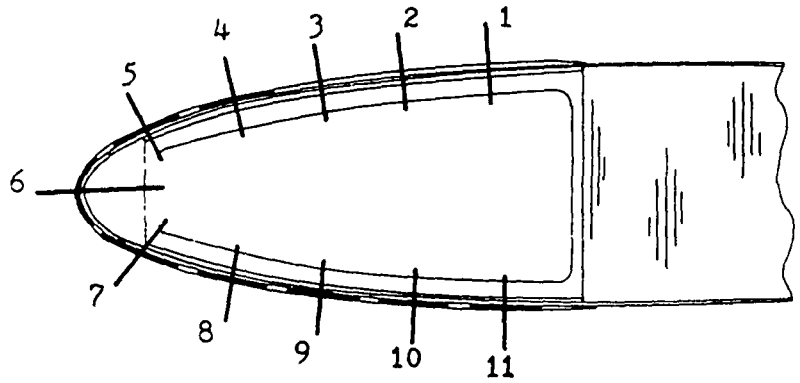

Position Around Blade

V_∞ = 120
T_∞ = -15
α = 0
P = 16.0
t_{on}/t_{off} = 30/30
n = 1

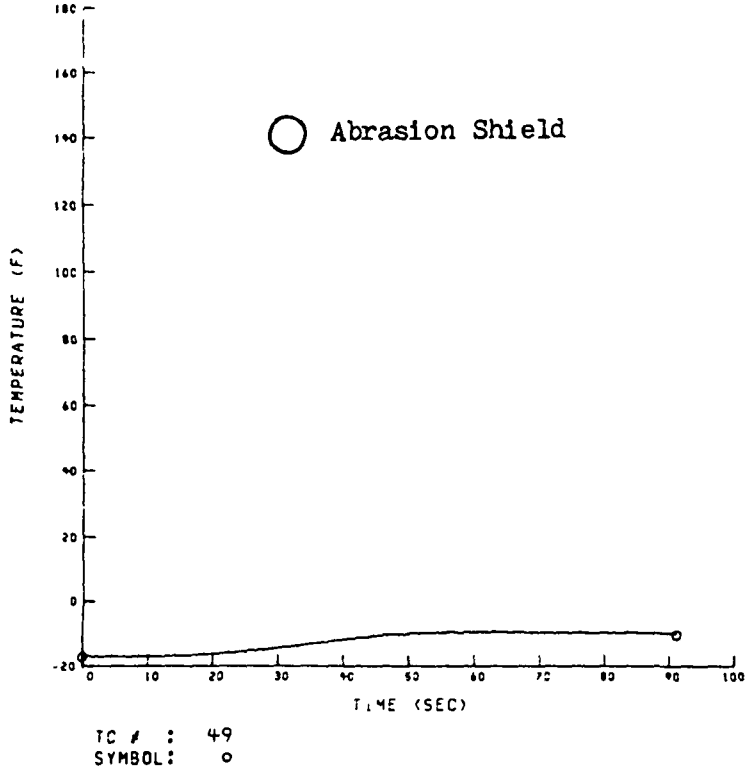

a. Position 1

Figure 22. Response of Selected Thermocouples for Escort Reading 93

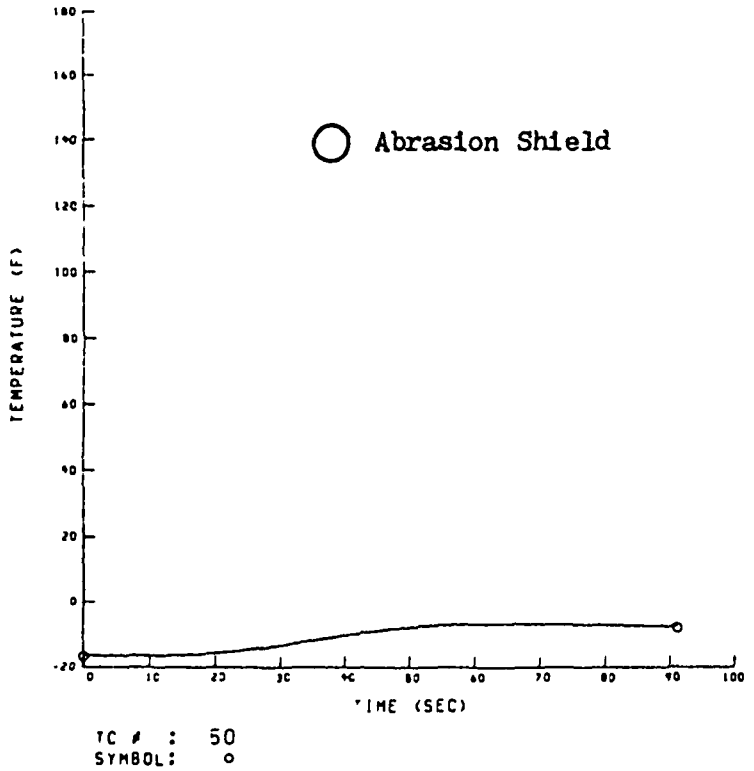

b. Position 2

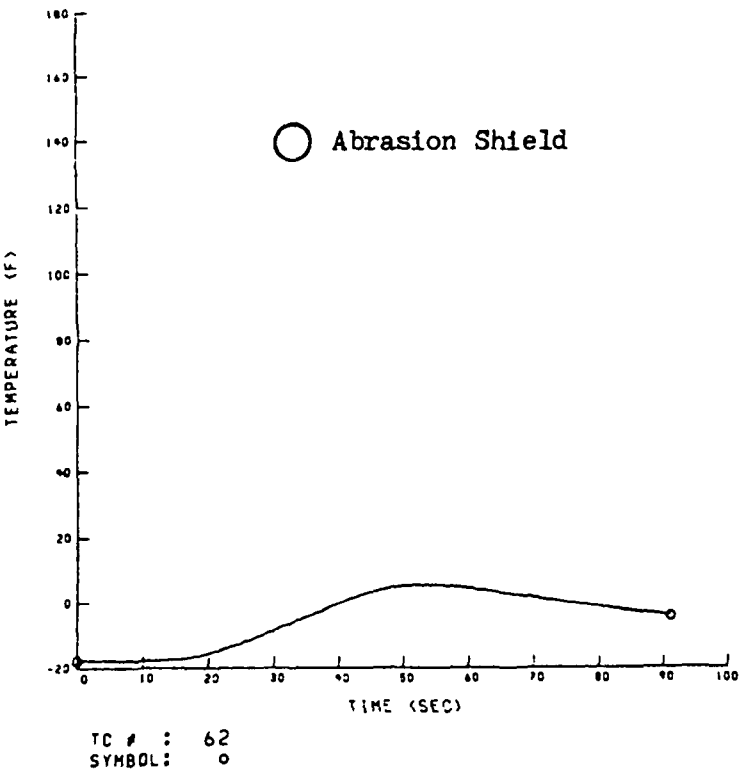

c. Position 3

Figure 22. (Reading 93 Continued)

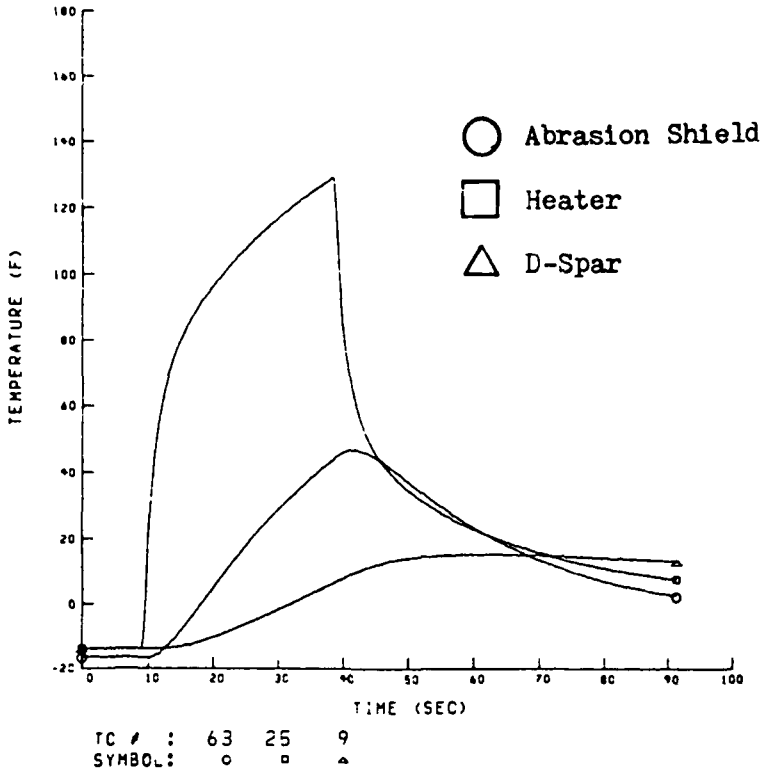

d. Position 4

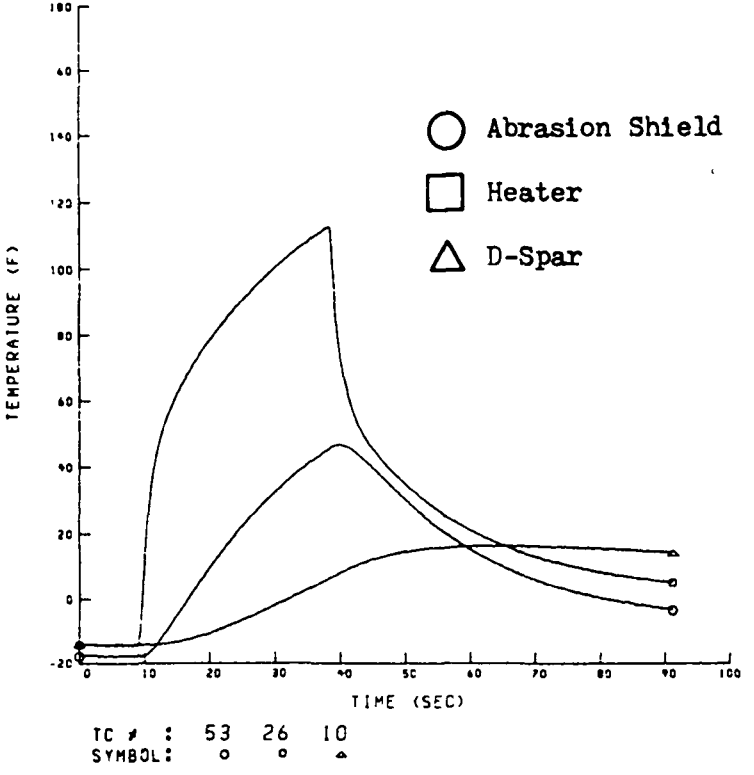

e. Position 5

Figure 22. (Reading 93 Continued)

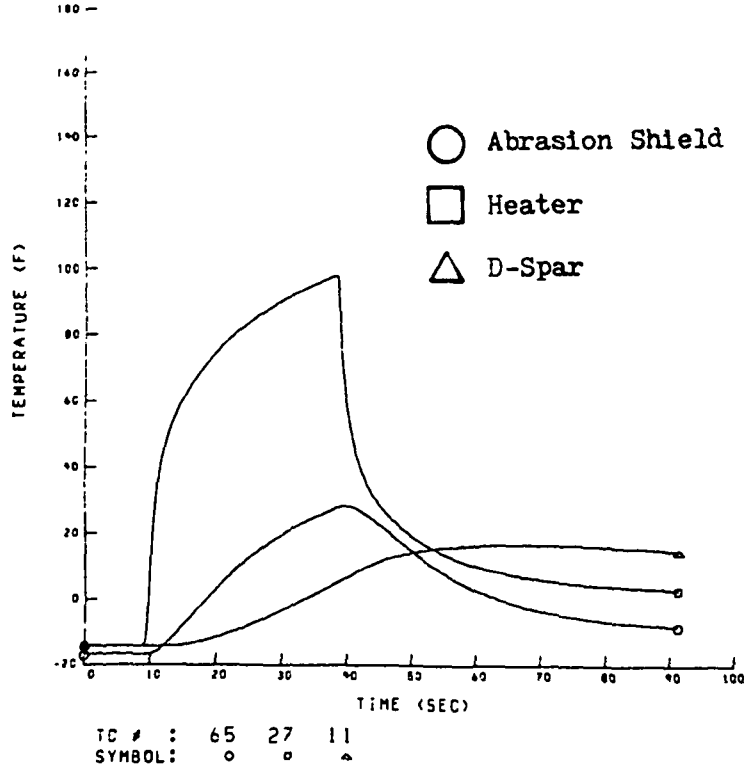

f. Position 6

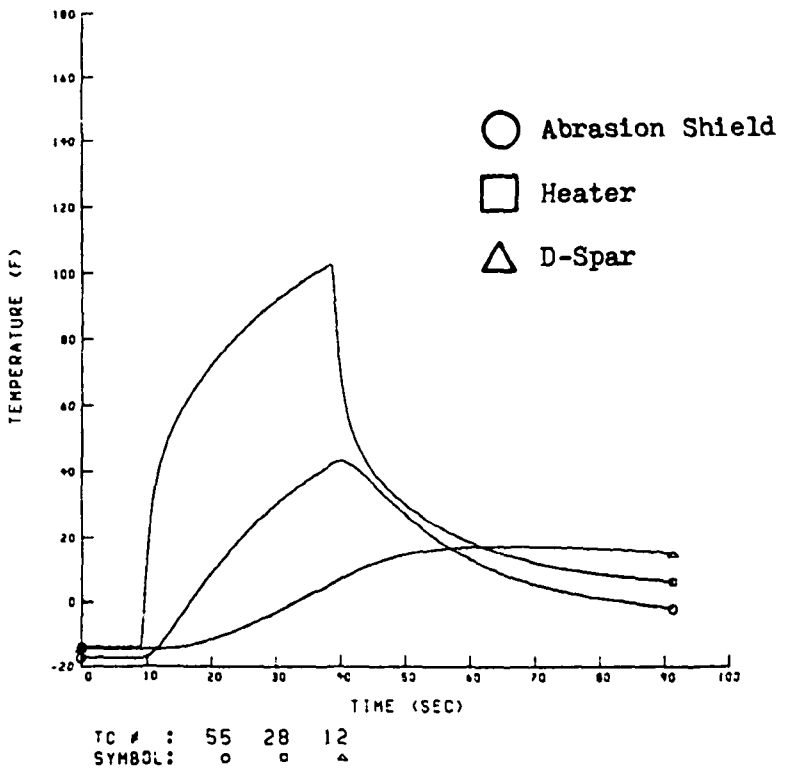

g. Position 7

Figure 22. (Reading 93 Continued)

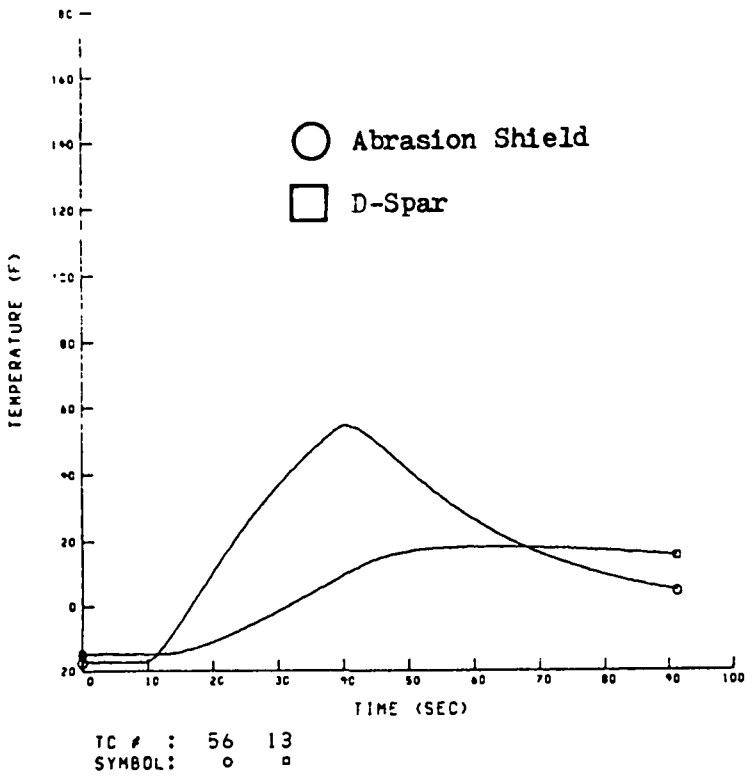

h. Position 8

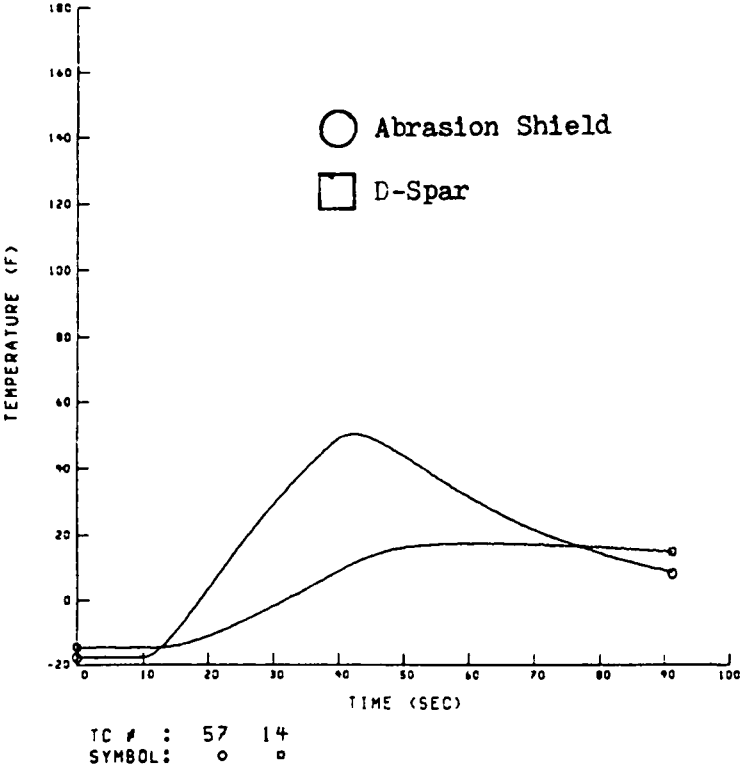

i. Position 9

Figure 22. (Reading 93 Continued)

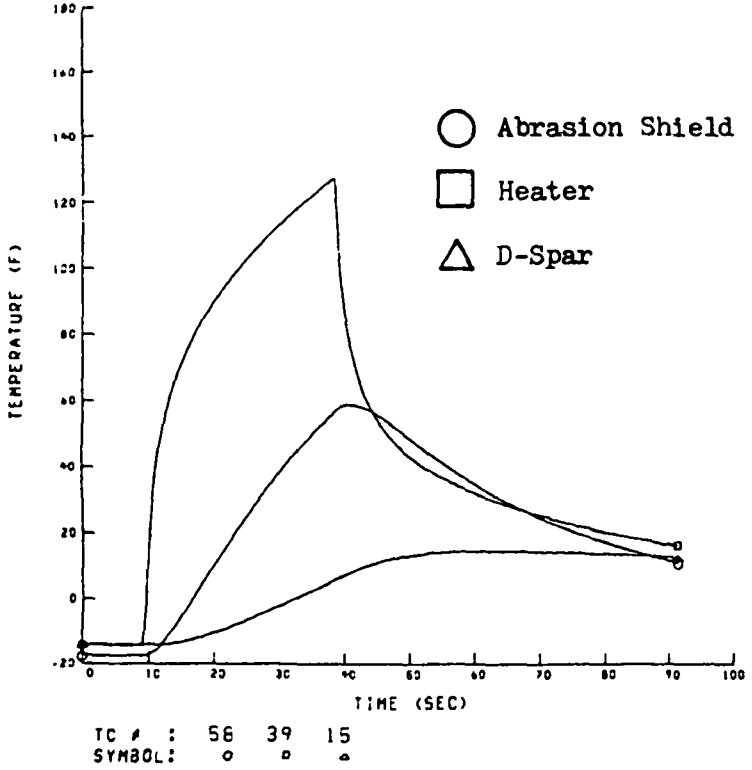

j. Position 10

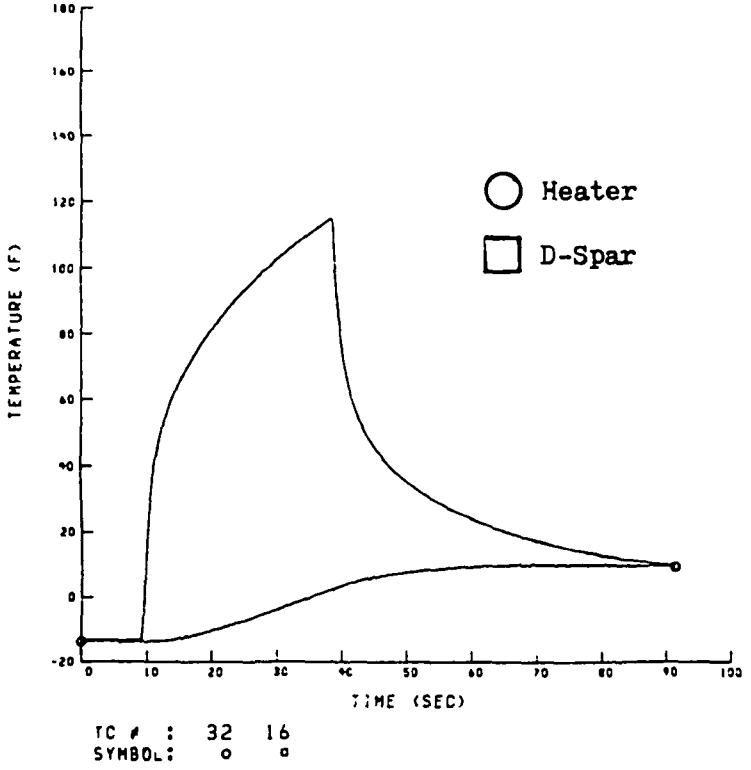

k. Position 11

Figure 22. (Reading 93 Continued)

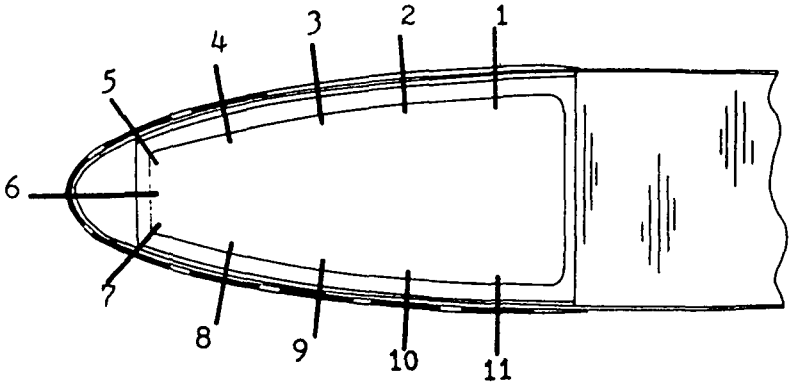

Position Around Blade

V_∞ = 120
T_∞ = -15
α = 0
P = 24.0
t_{on}/t_{off} = 20/30
n = 1

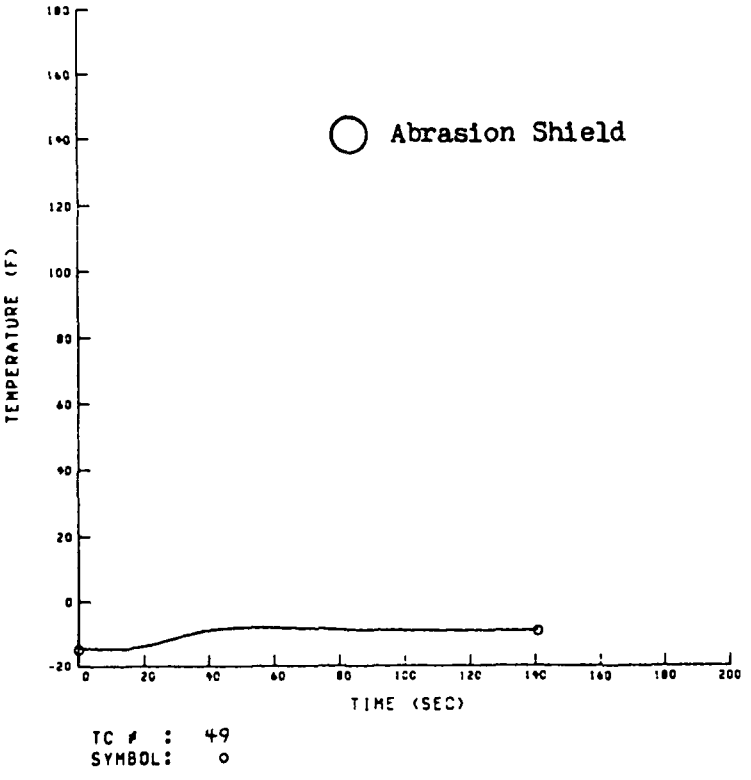

a. Position 1

Figure 23. Response of Selected Thermocouples for Escort Reading 94

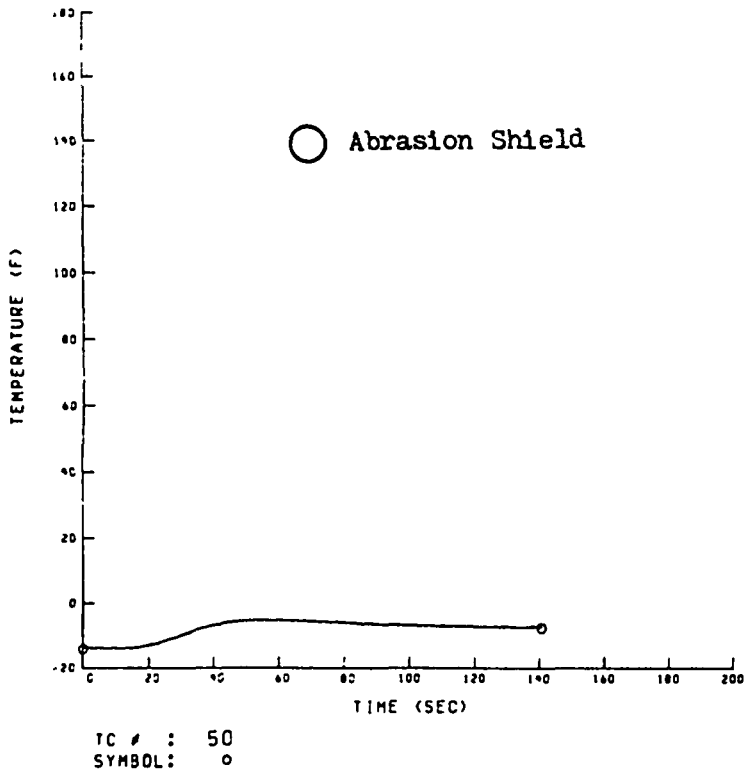

b. Position 2

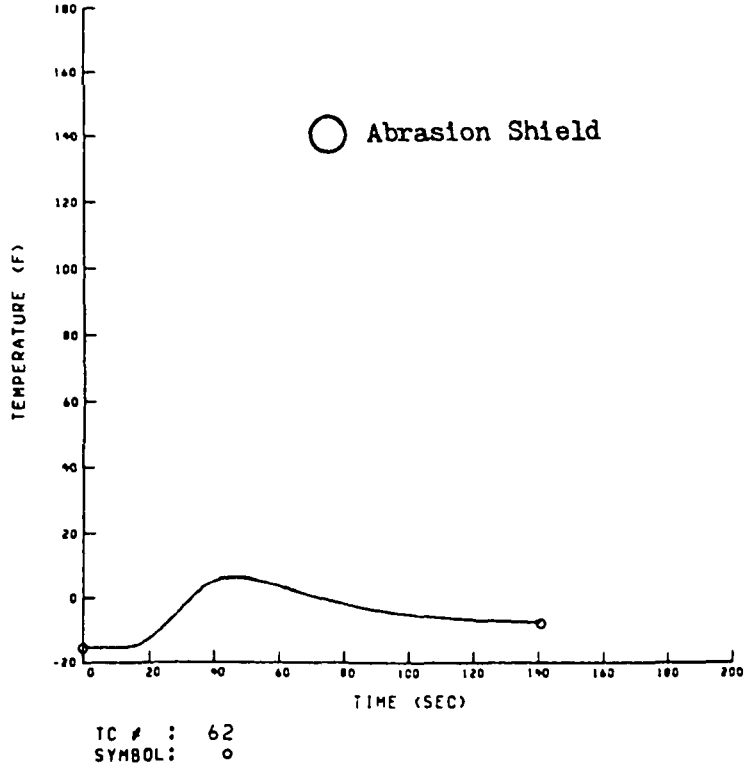

c. Position 3

Figure 23. (Reading 94 Continued)

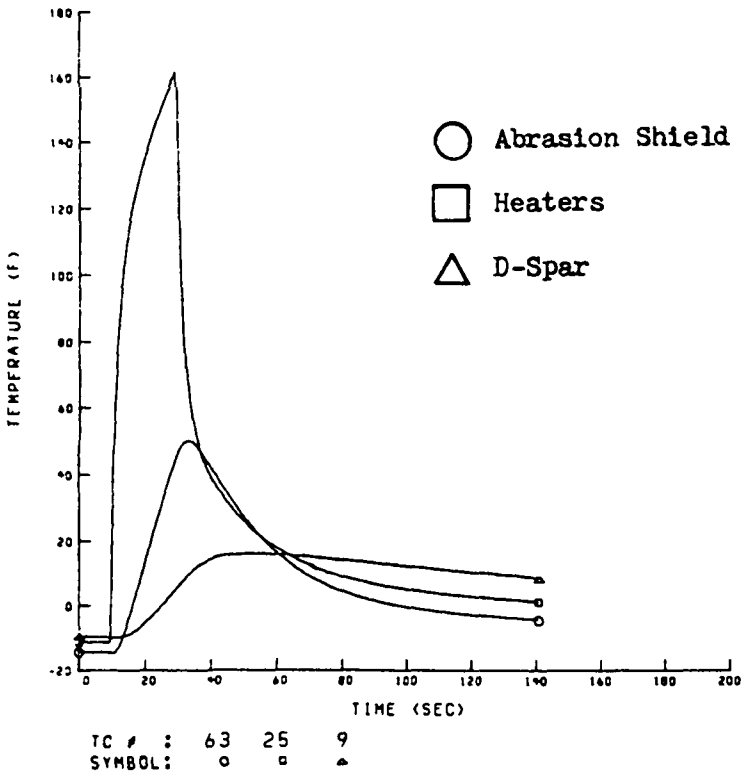

d. Position 4

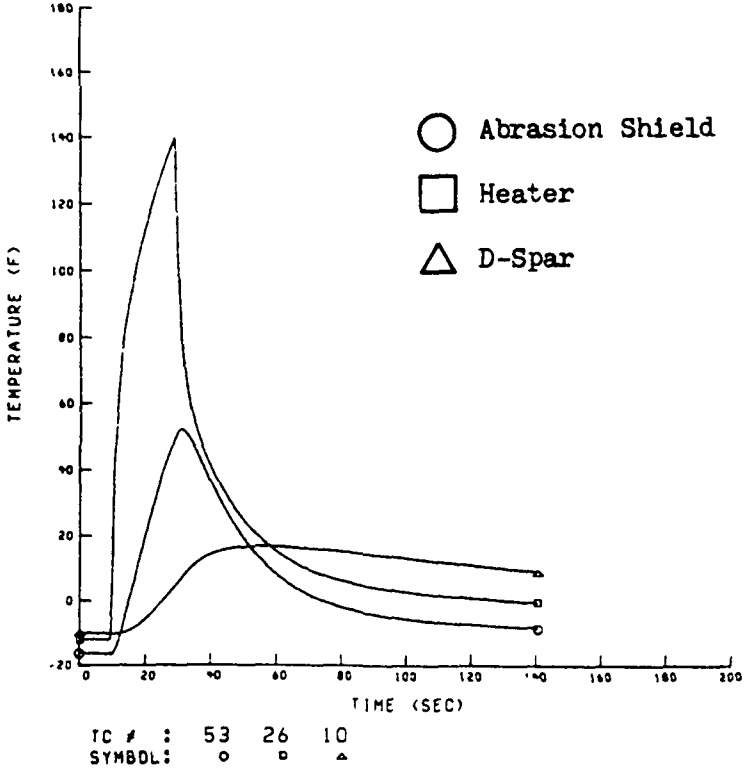

e Position 5

Figure 23. (Reading 94 Continued)

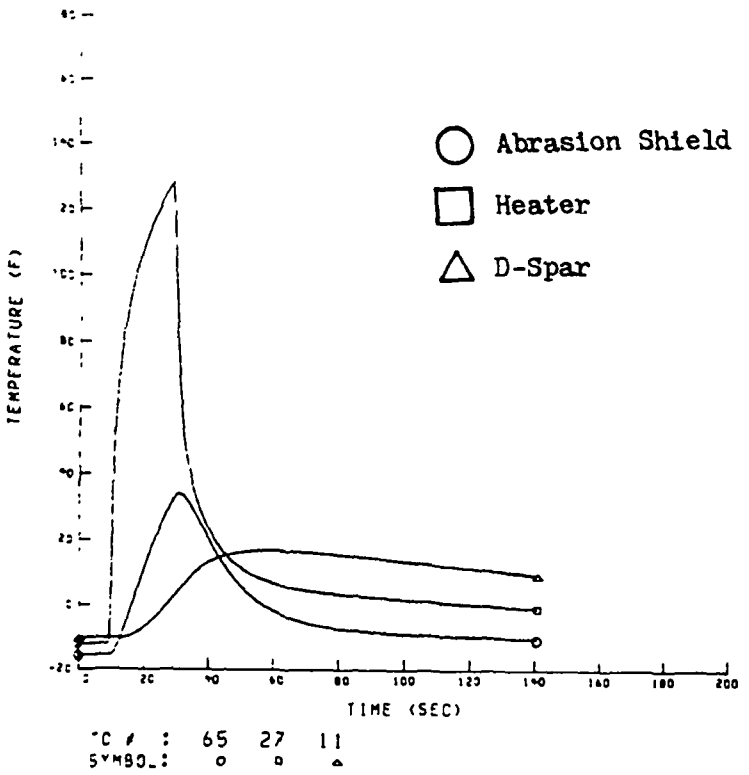

f. Position 6

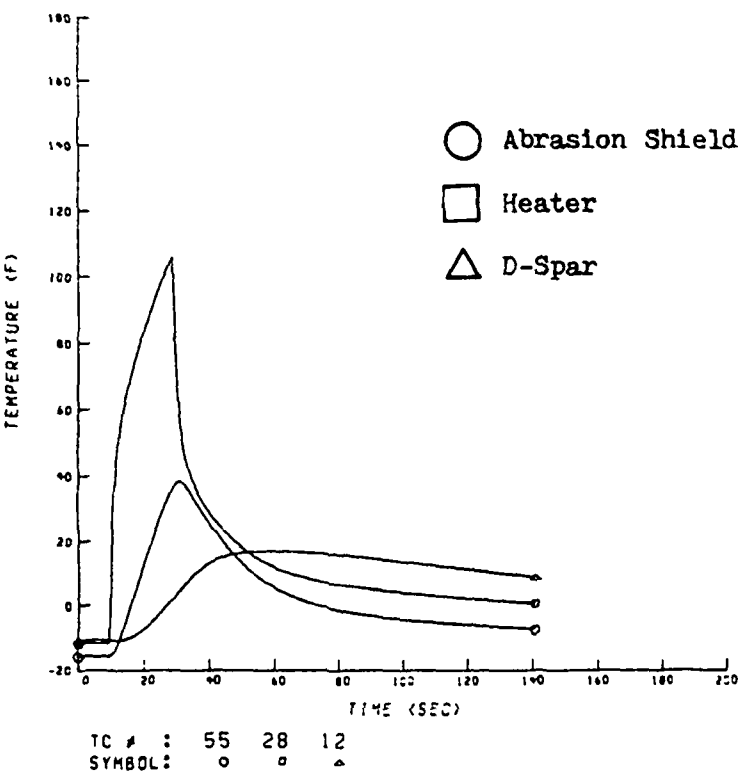

g. Position 7

Figure 23. (Reading 94 Continued)

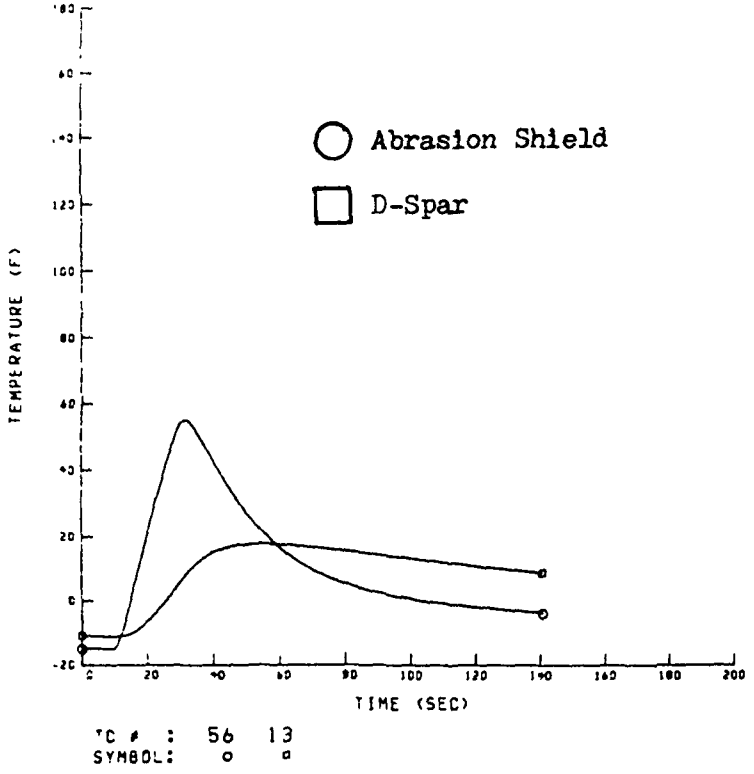

h. Position 8

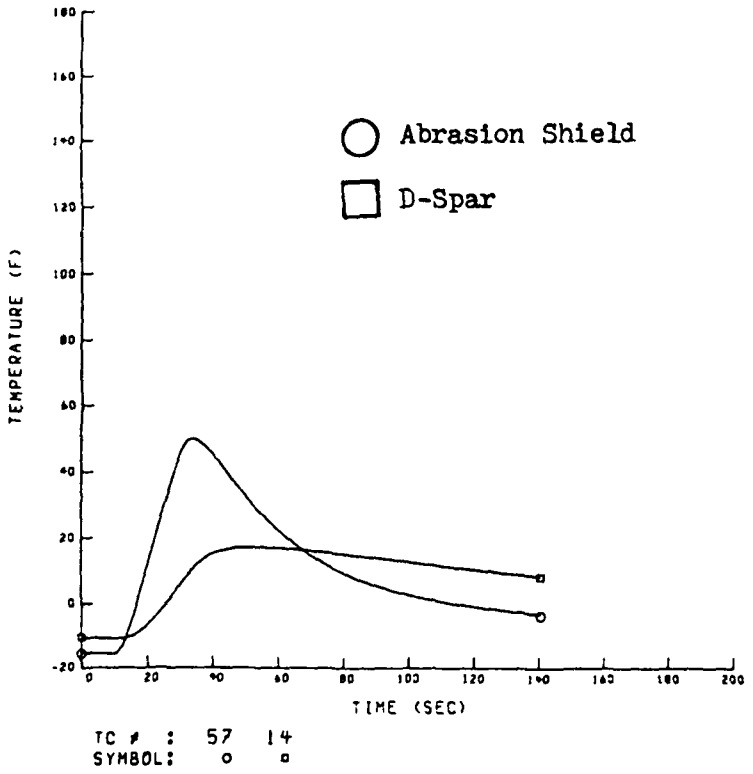

i. Position 9

Figure 23. (Reading 94 Continued)

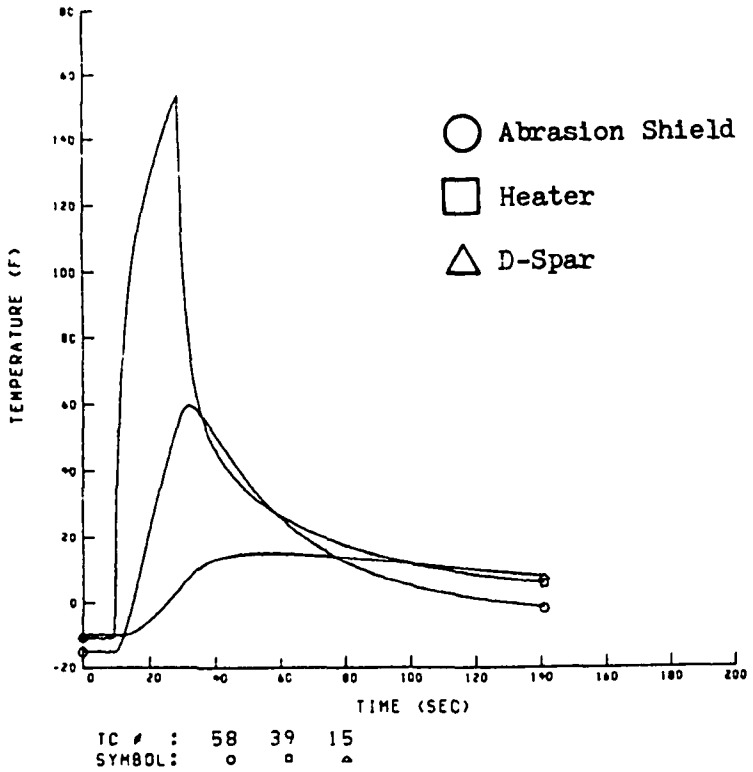

j. Position 10

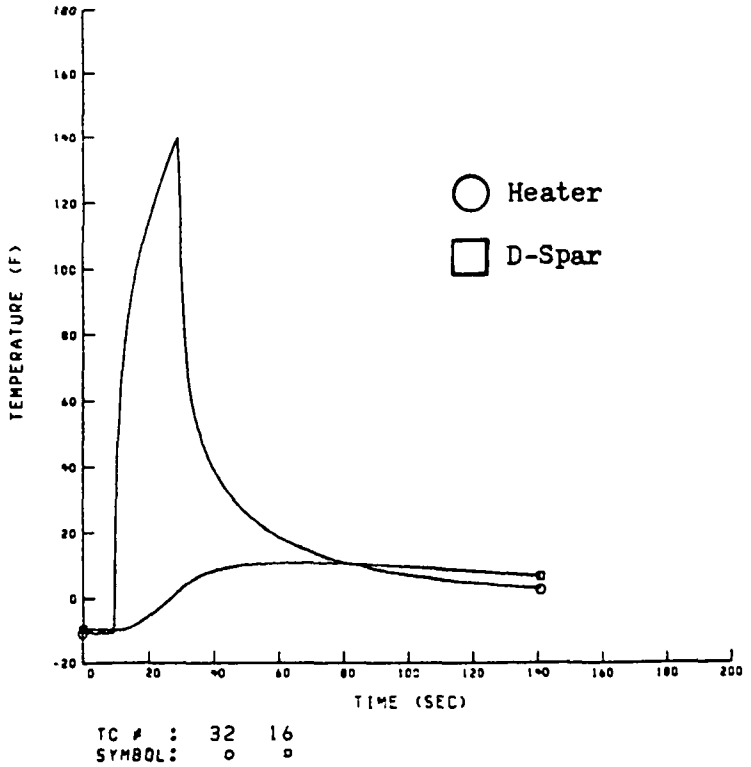

k. Position 11

Figure 23. (Reading 94 Continued)

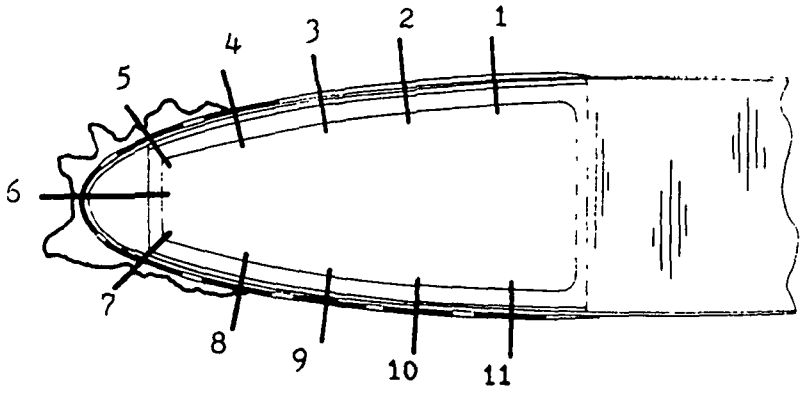

Position Around Blade

V_∞	=	200
T_∞	=	31
α	=	0
P	=	16.0
t_{on}/t_{off}	=	10/30
n	=	2
LWC	=	1.2
$\bar{d}$	=	18.4
t_{ice}	=	5

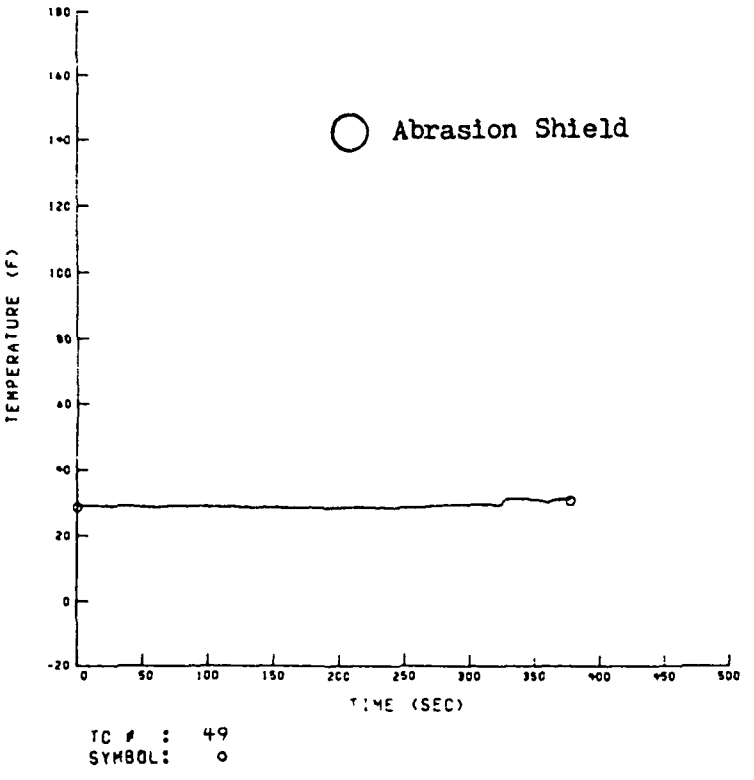

a. Position 1

Figure 24. Response of Selected Thermocouples for Escort Reading 197

C-3

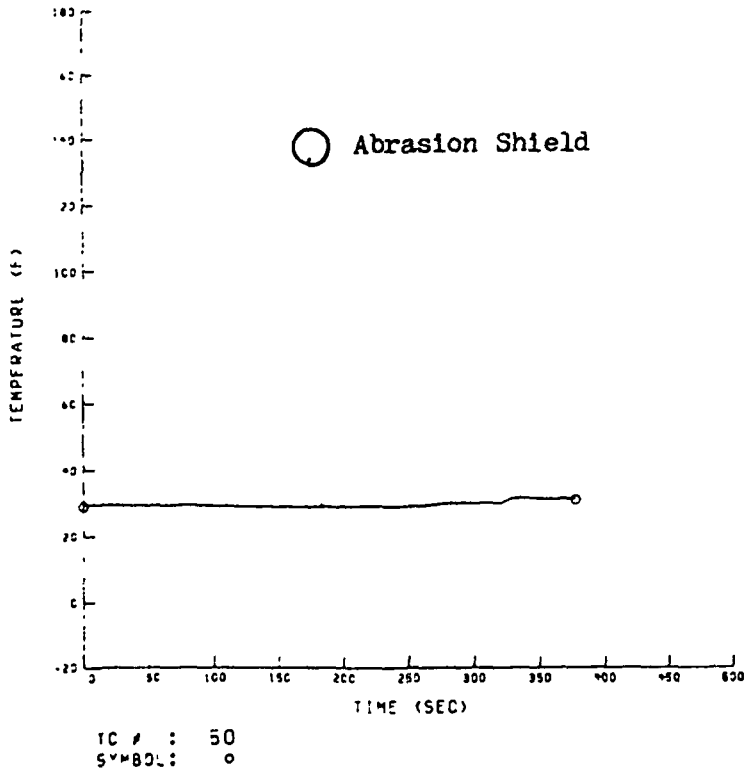

b. Position 2

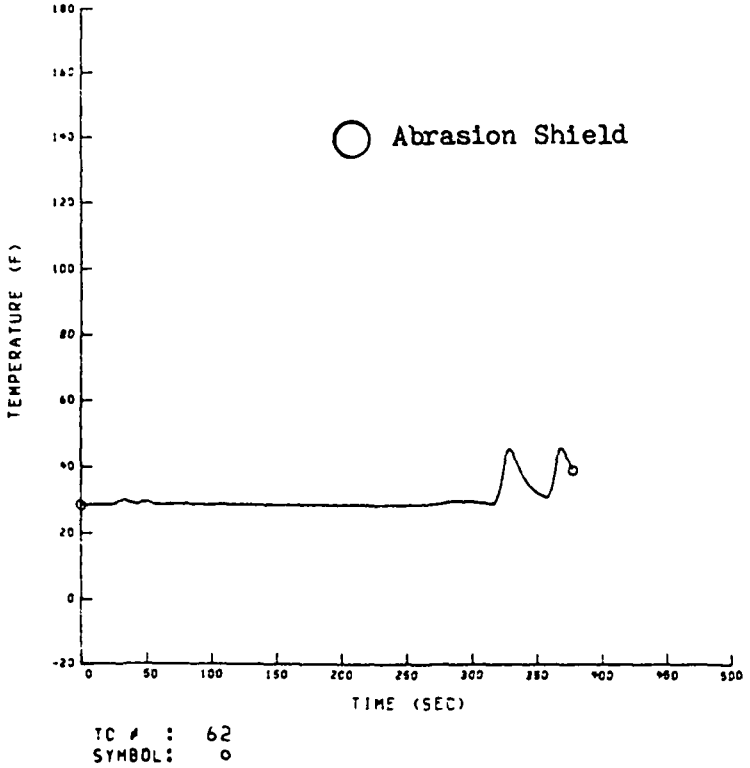

c. Position 3

Figure 24. (Reading 197 Continued)

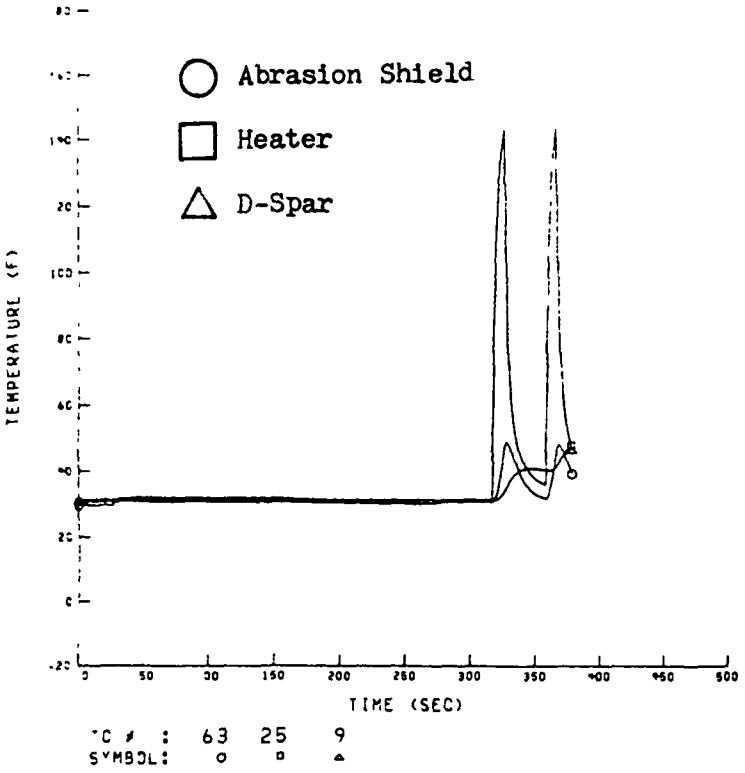

d. Position 4

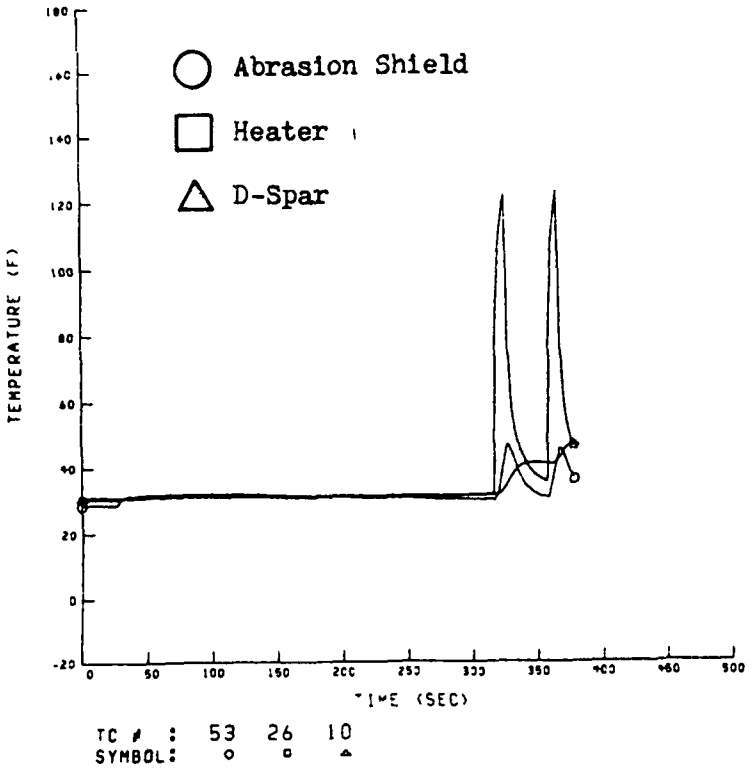

e. Position 5

Figure 24. (Reading 197 Continued)

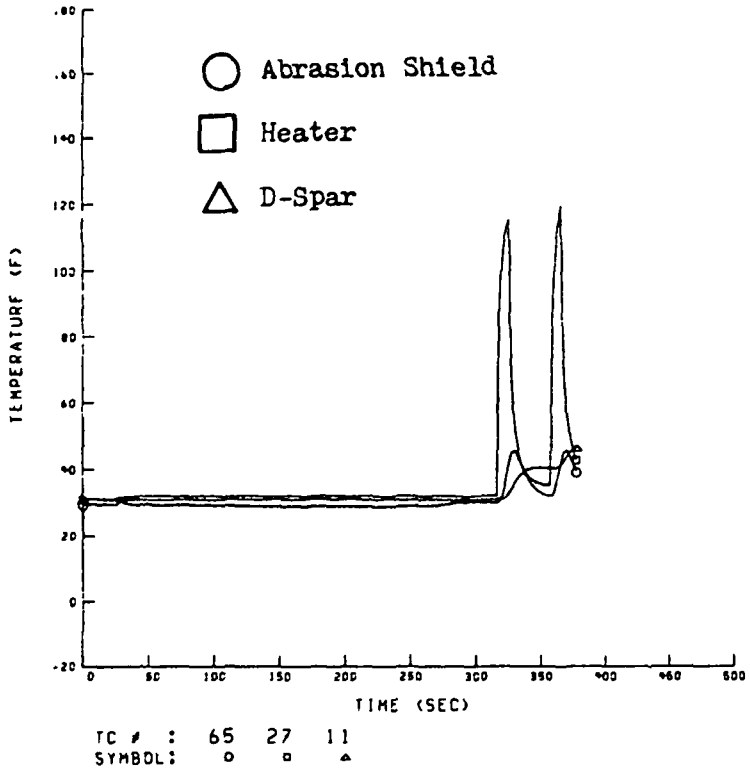

f. Position 6

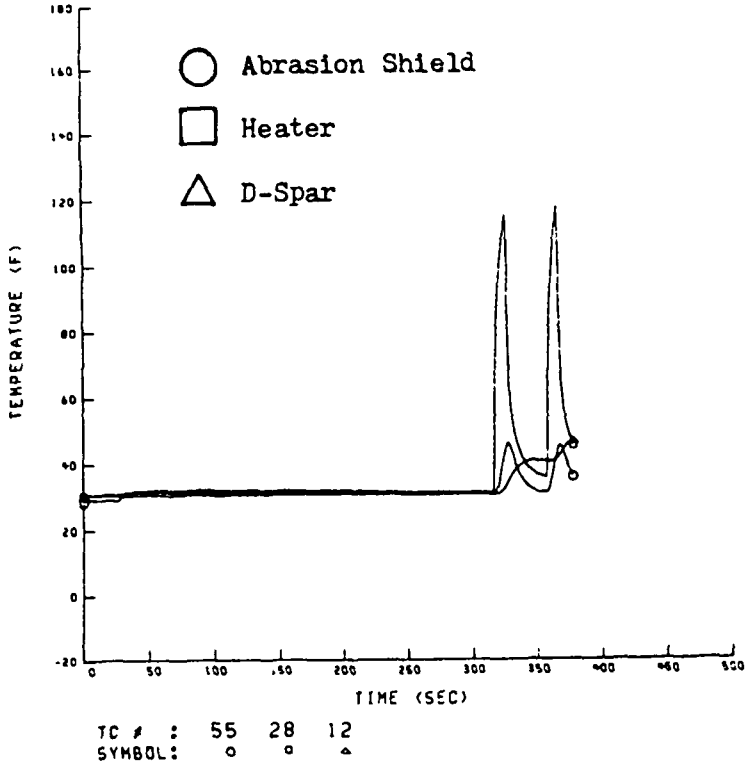

g. Position 7

Figure 24. (Reading 197 Continued)

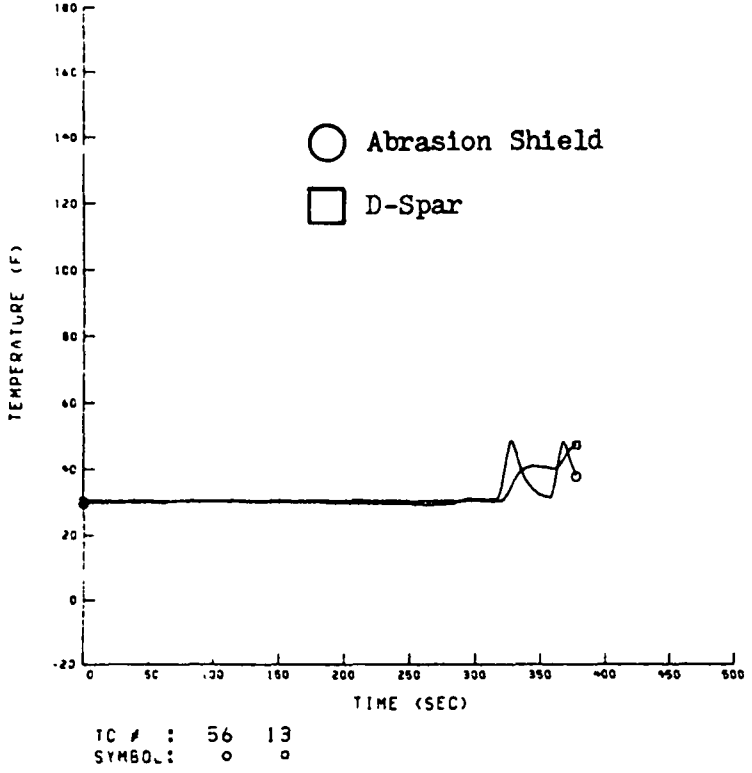

h. Position 8

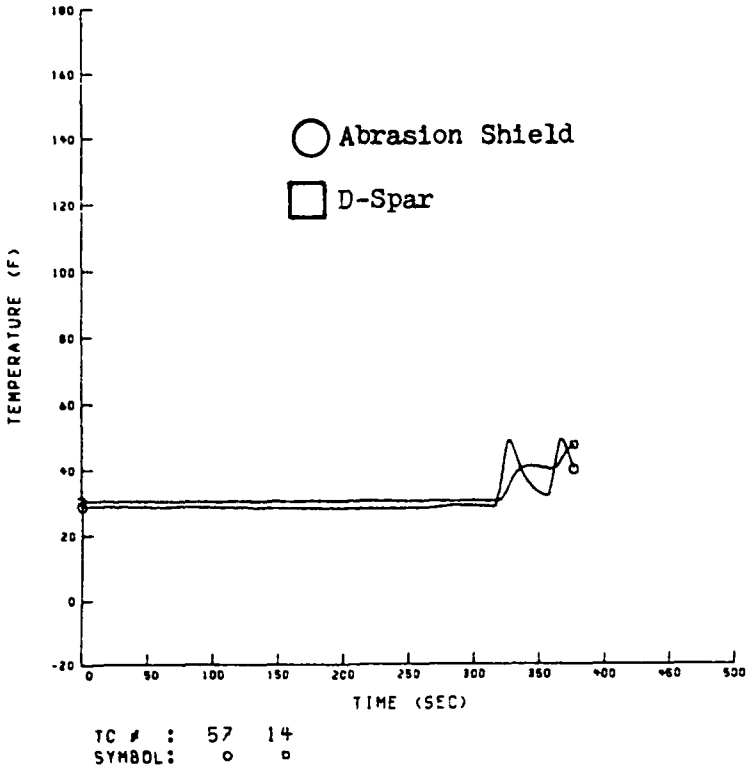

i. Position 9

Figure 24. (Reading 197 Continued)

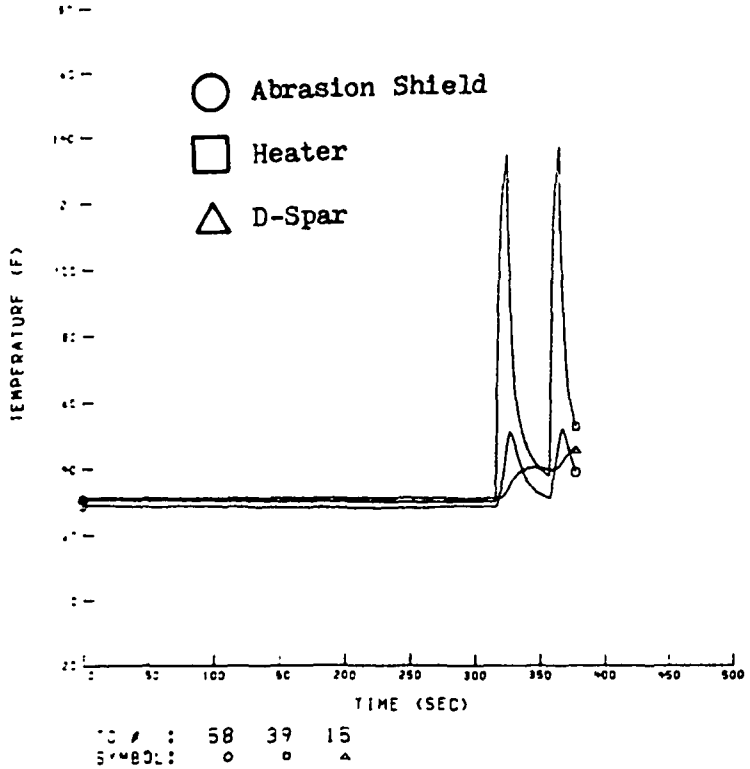

j. Position 10

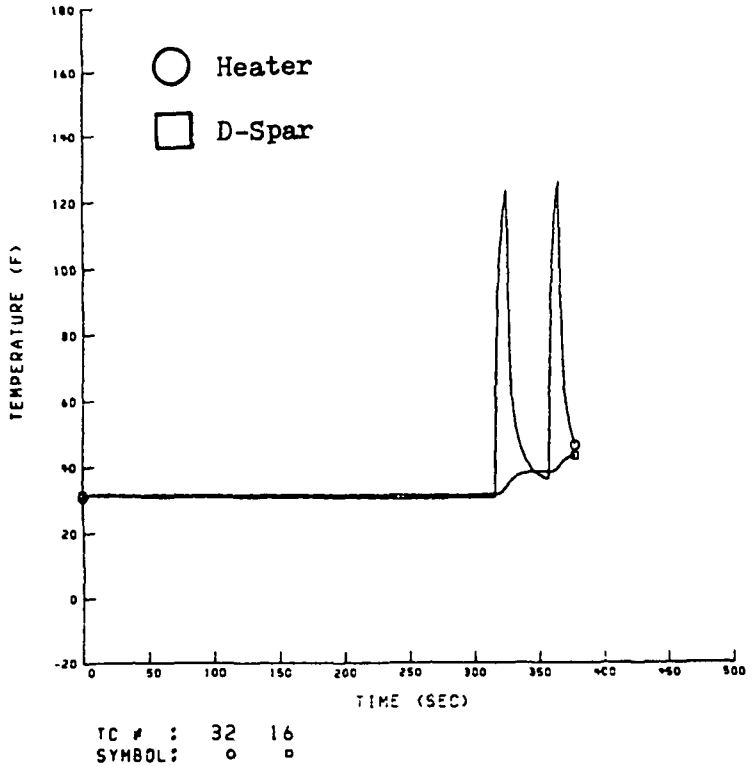

k. Position 11

Figure 24. (Reading 197 Continued)

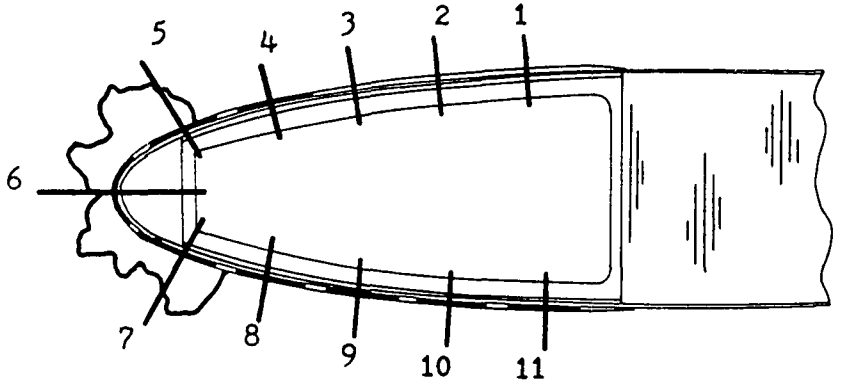

Position Around Blade

V_∞	=	250
T_∞	=	28
α	=	0
P	=	16.0
t_{on}/t_{off}	=	10/60
n	=	3
LWC	=	1.0
$\bar{d}$	=	20.0
t_{ice}	=	5

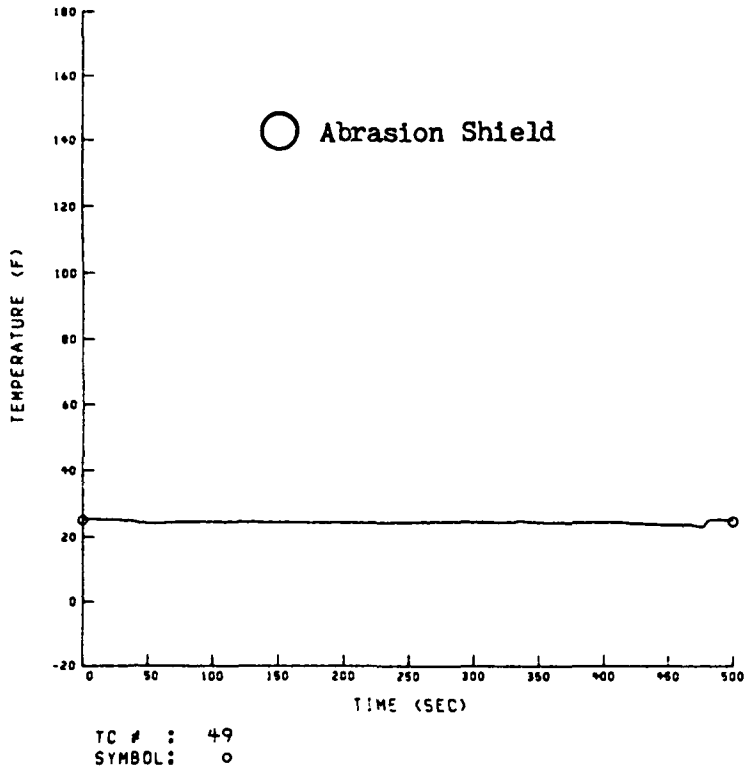

a. Position 1

Figure 25. Response of Selected Thermocouples for Escort Reading 209

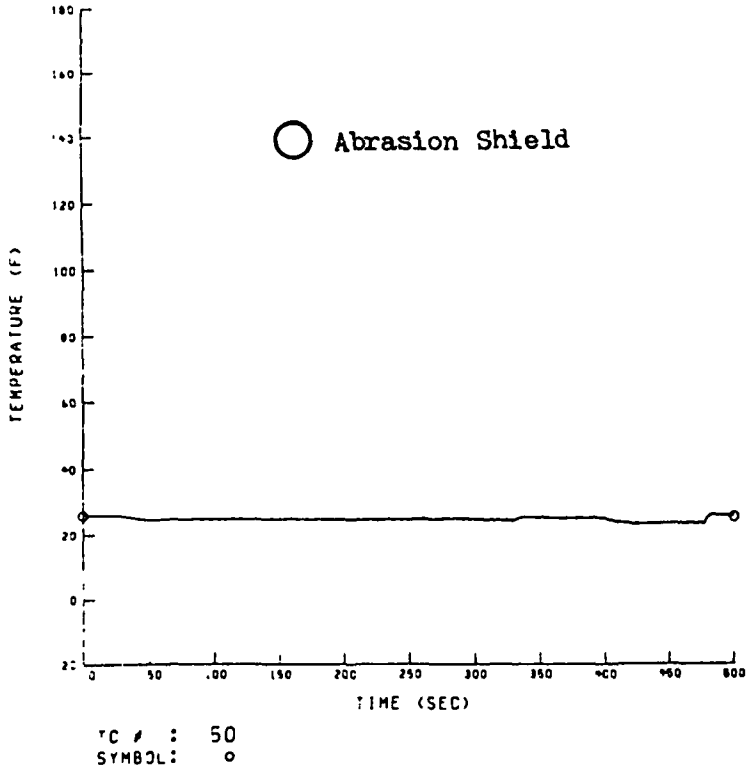

b. Position 2

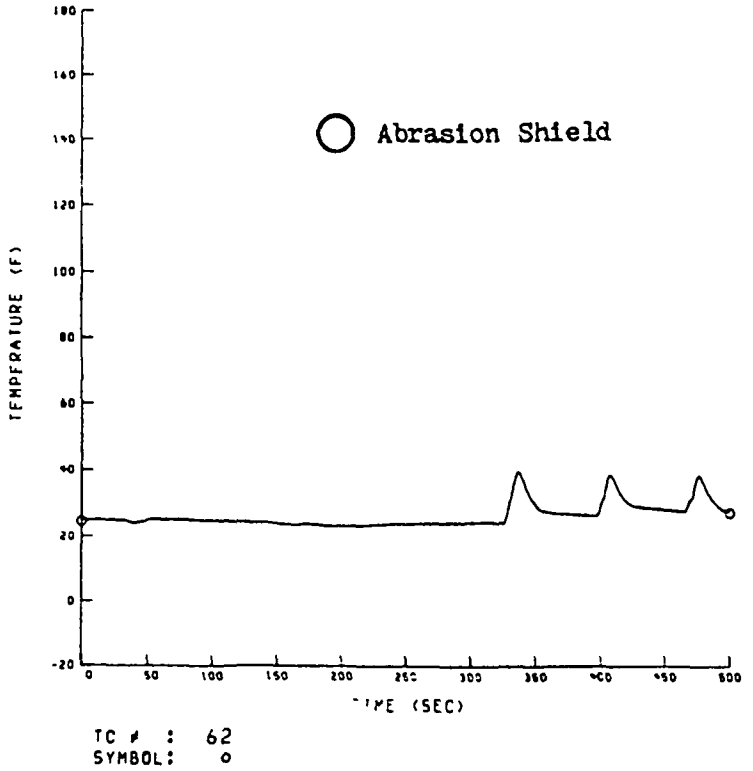

c. Position 3

Figure 25. (Reading 209 Continued)

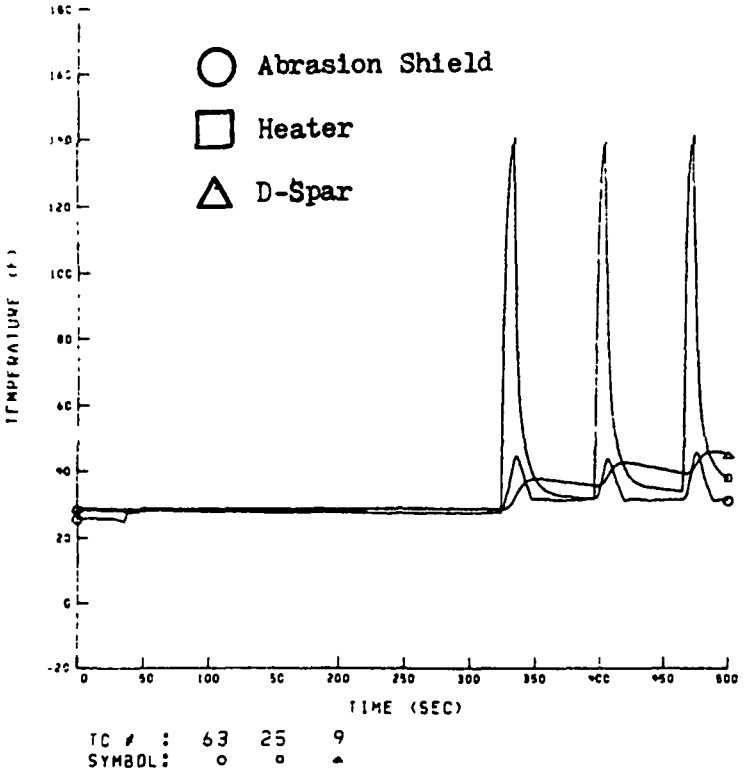

d. Position 4

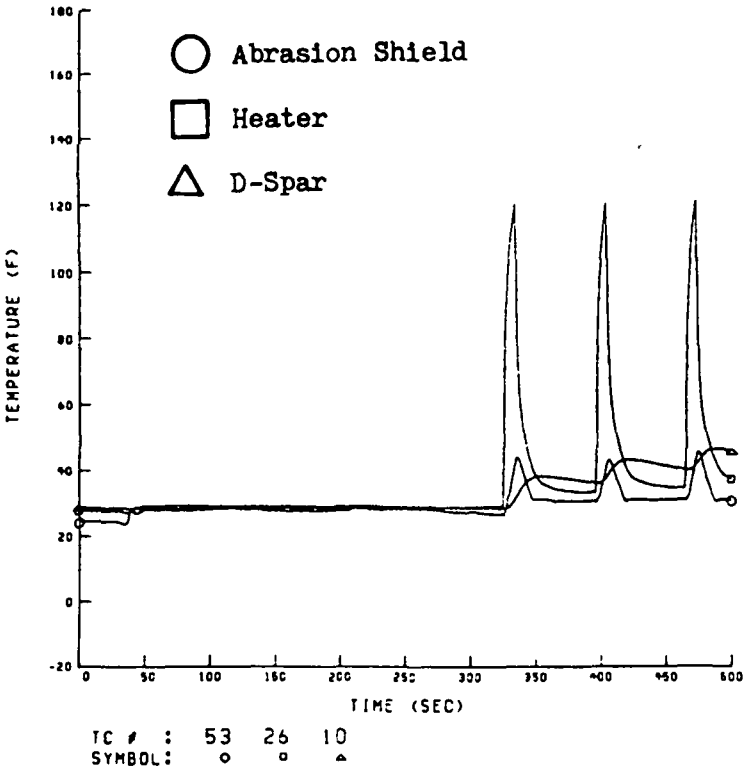

e. Position 5

Figure 25. (Reading 209 Continued)

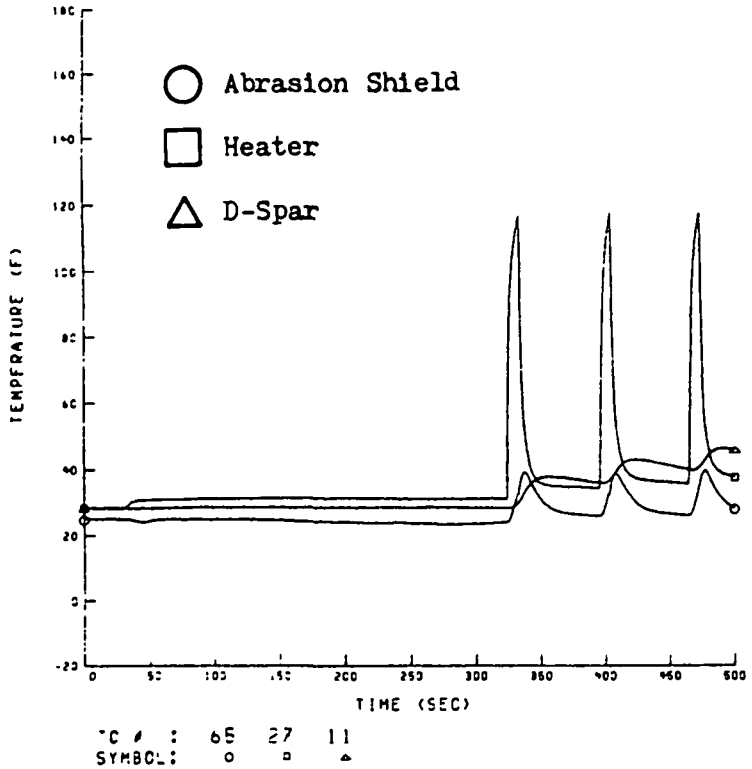

f. Position 6

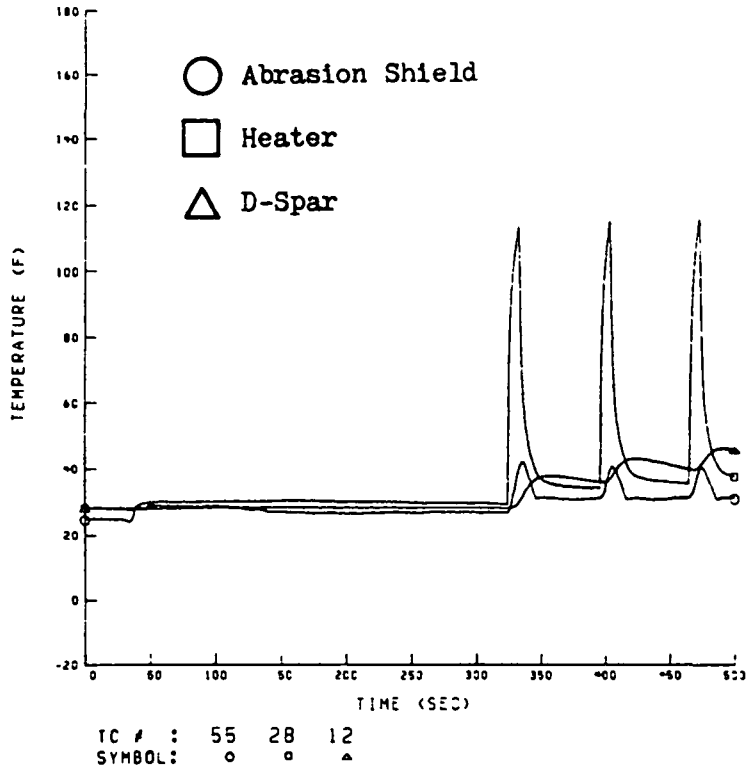

g. Position 7

Figure 25. (Reading 209 Continued)

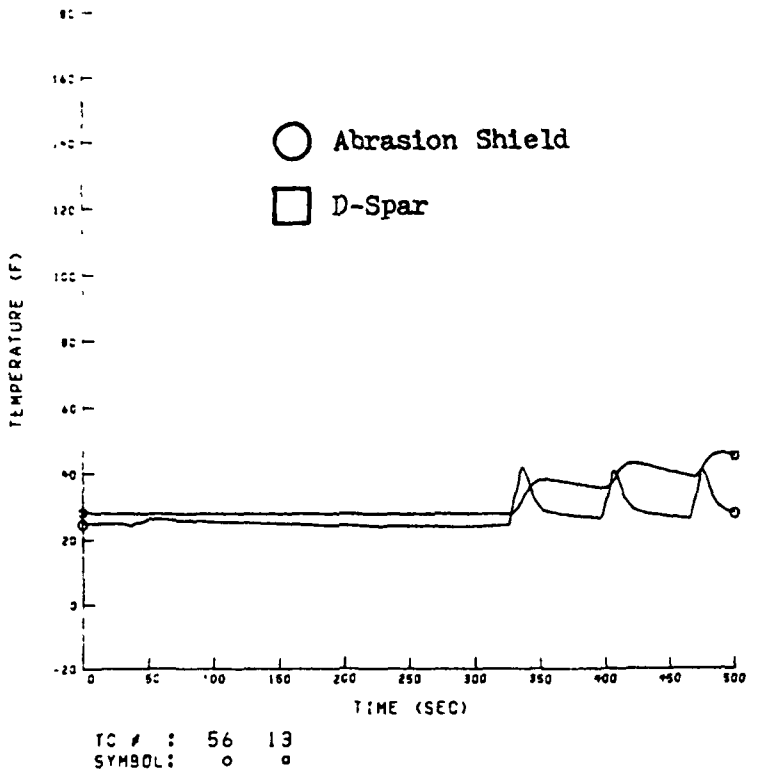

h. Position 8

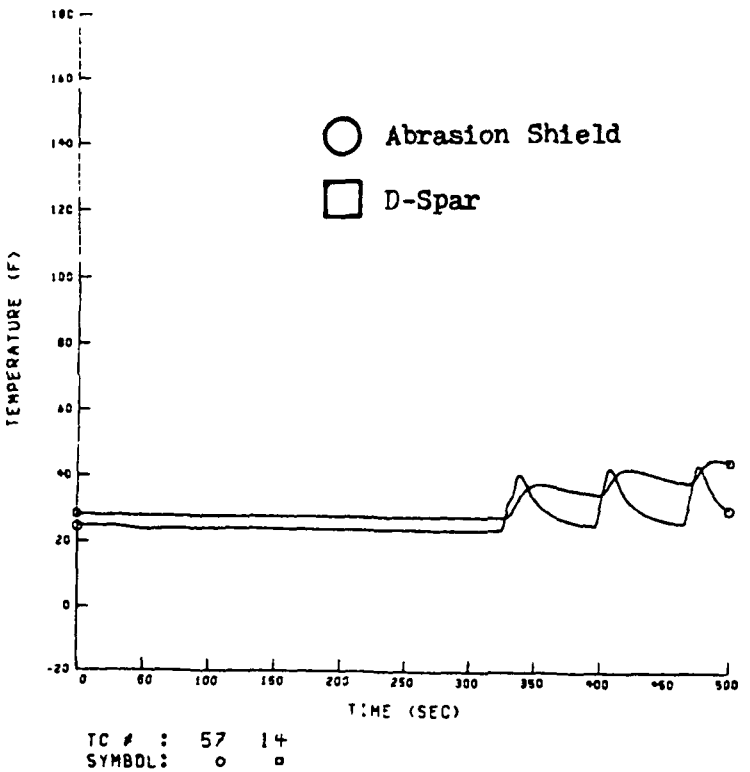

i. Position 9

Figure 25. (Reading 209 Continued)

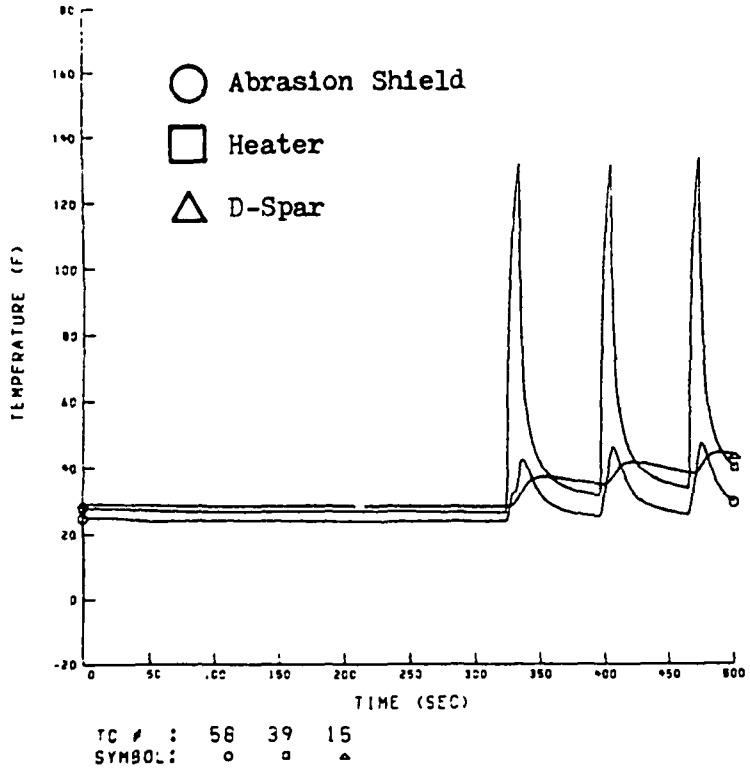

j. Position 10

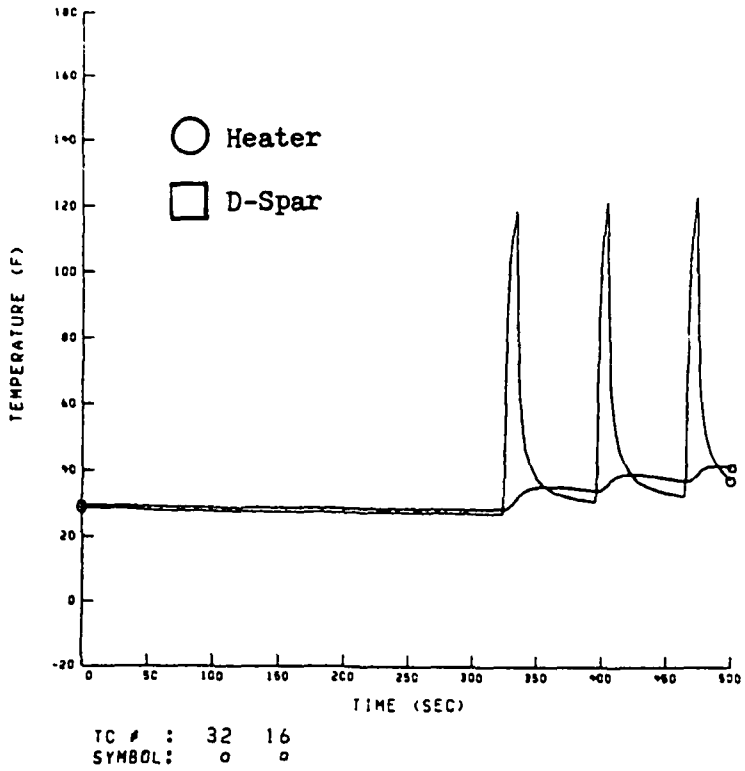

k. Position 11

Figure 25. (Reading 209 Continued)

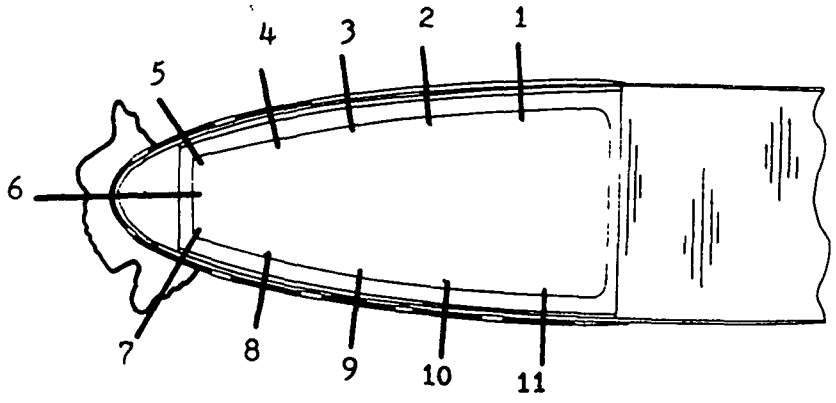

Position Around Blade

V_∞	=	200
T_∞	=	24
α	=	0
P	=	16.0
t_{on}/t_{off}	=	20/60
n	=	3
LWC	=	1.0
$\bar{d}$	=	20.0
t_{ice}	=	5

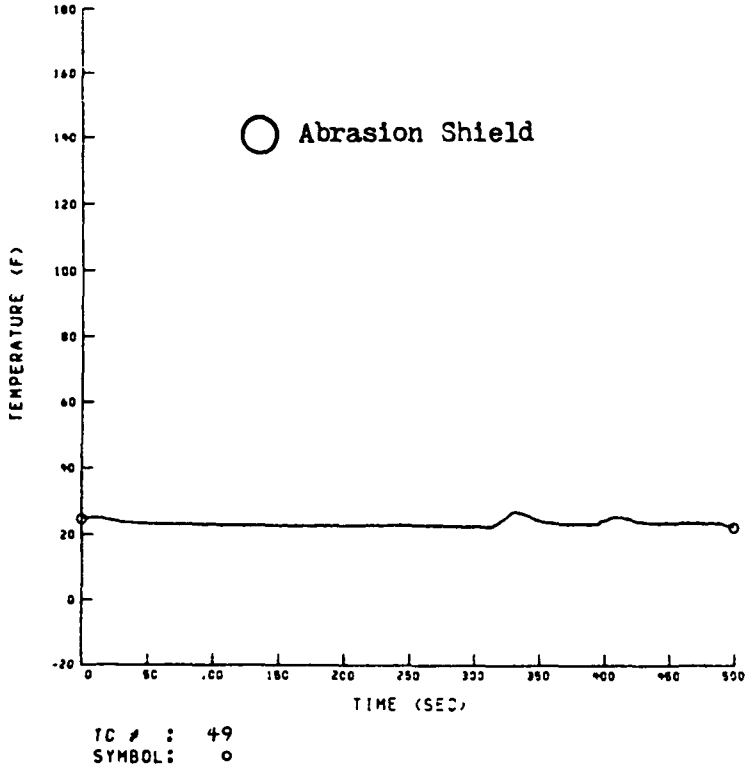

a. Position 1

Figure 26. Response of Selected Thermocouples for Escort Reading 213

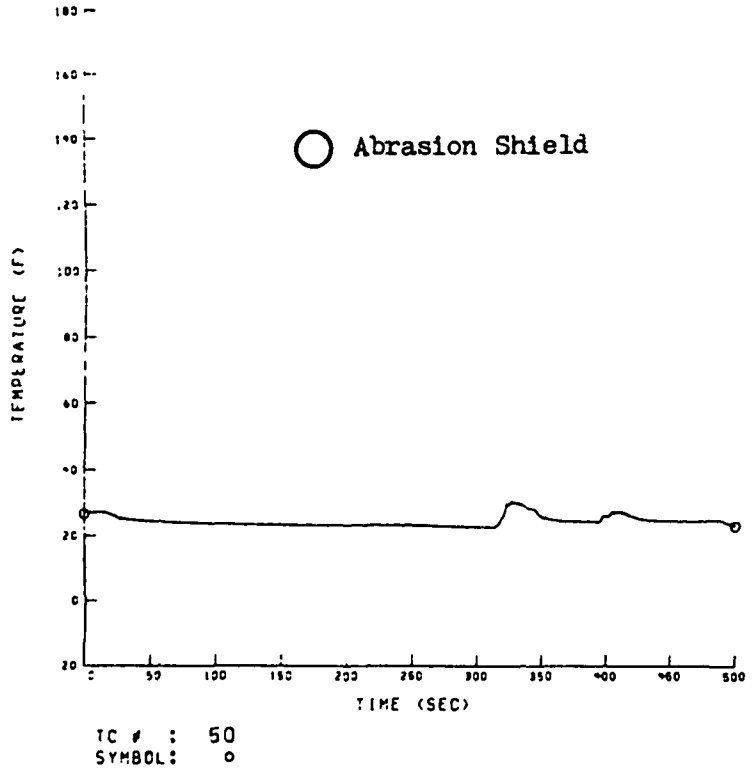

b. Position 2

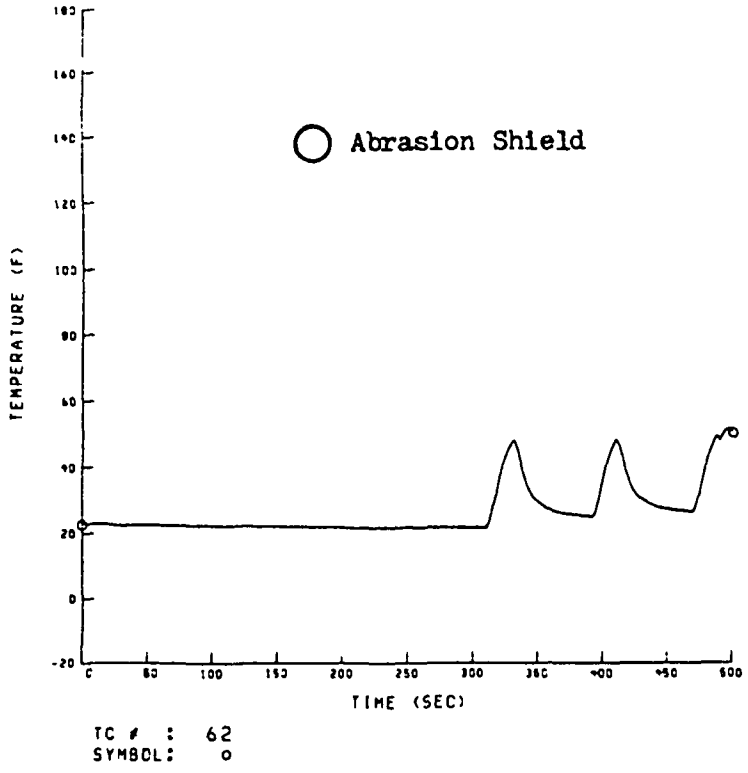

c. Position 3

Figure 26. (Reading 213 Continued)

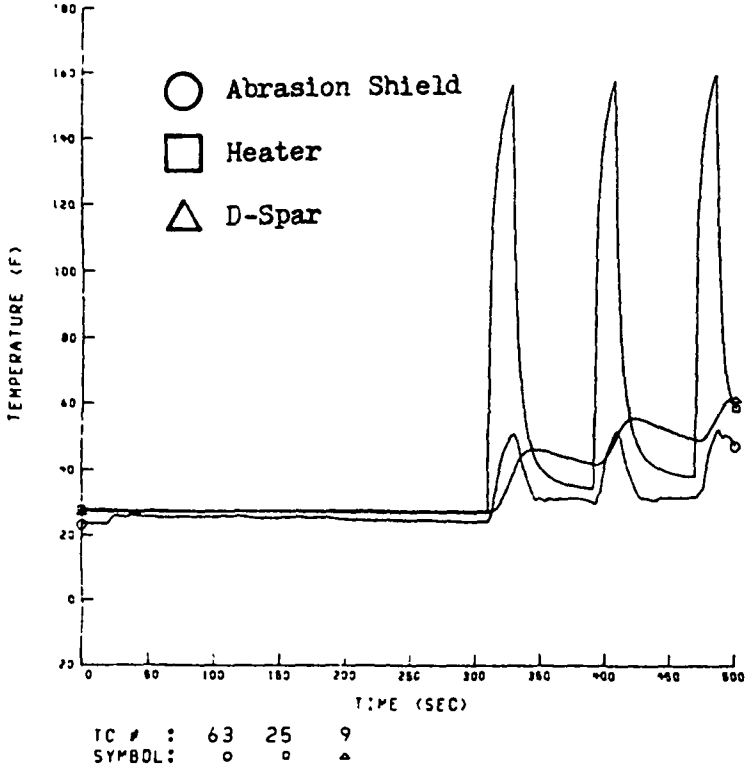

d. Position 4

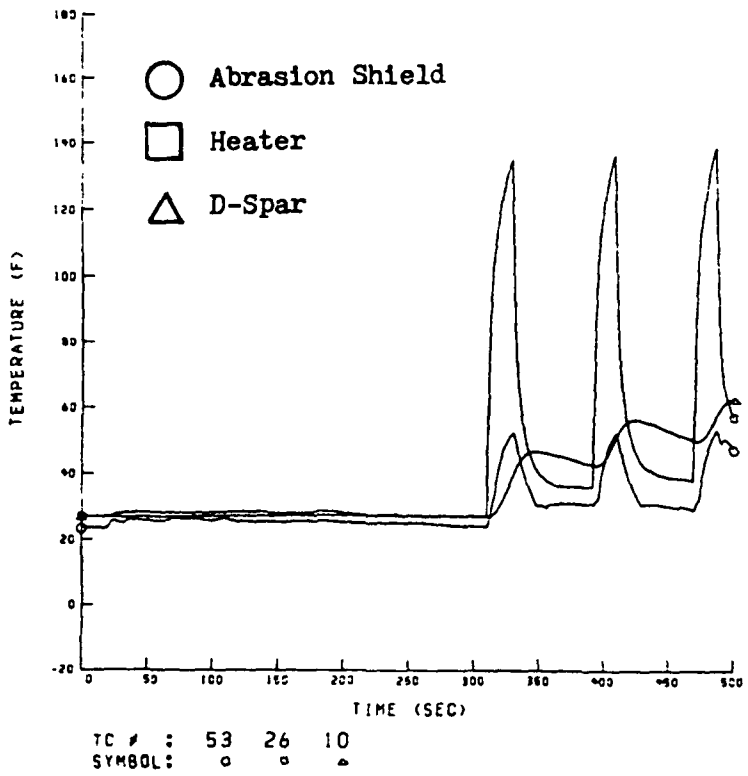

e. Position 5

Figure 26. (Reading 213 Continued)

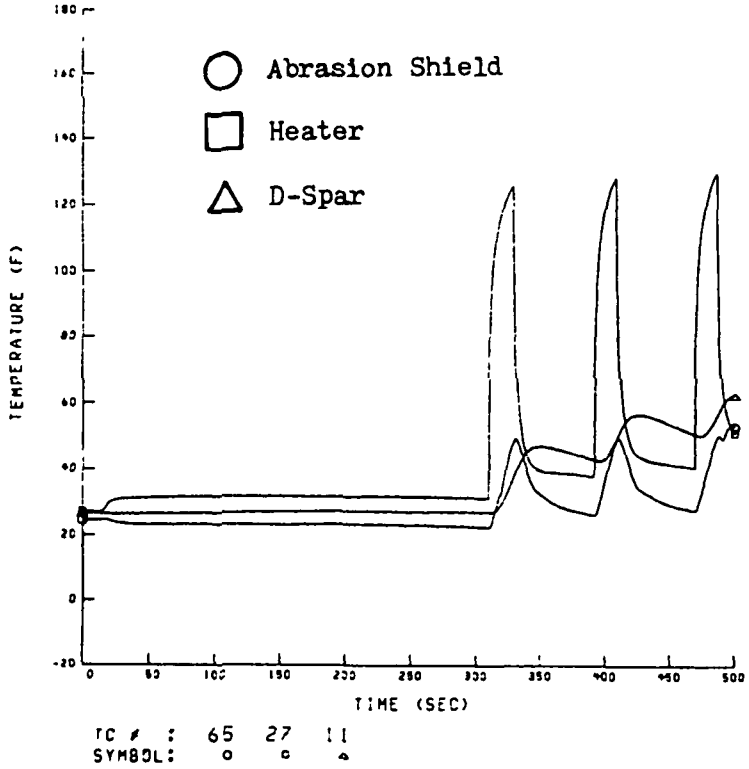

f. Position 6

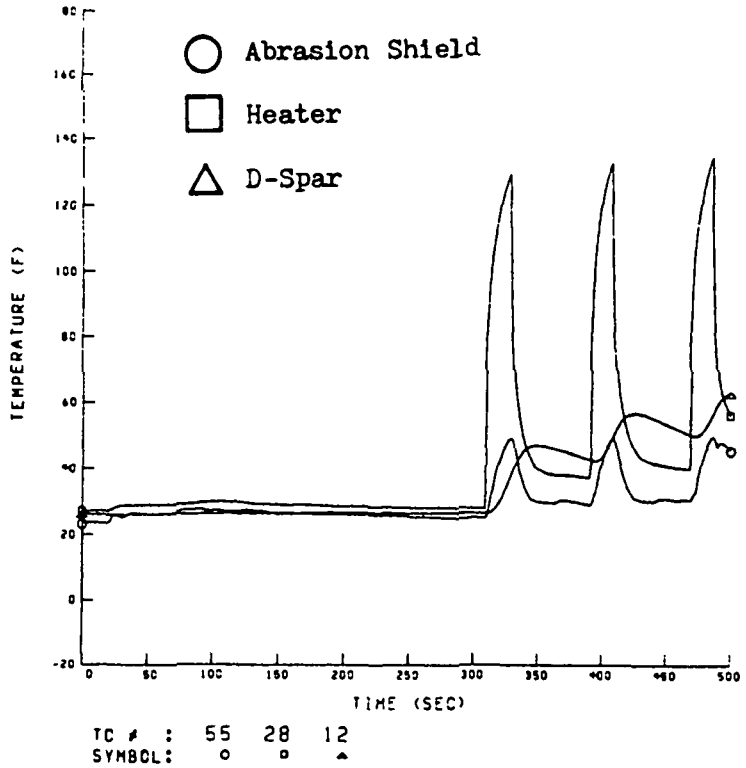

g. Position 7

Figure 26. (Reading 213 Continued)

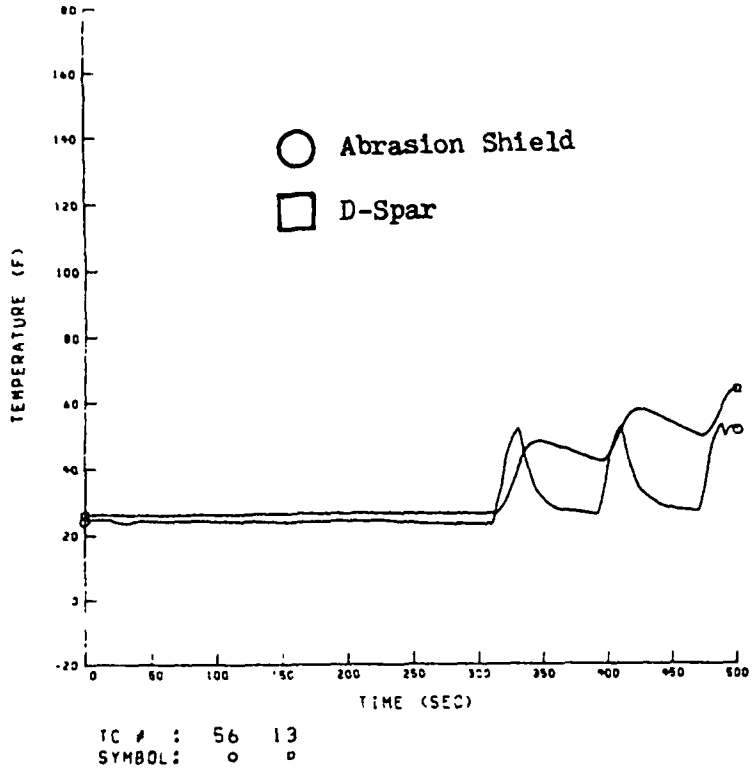

h. Position 8

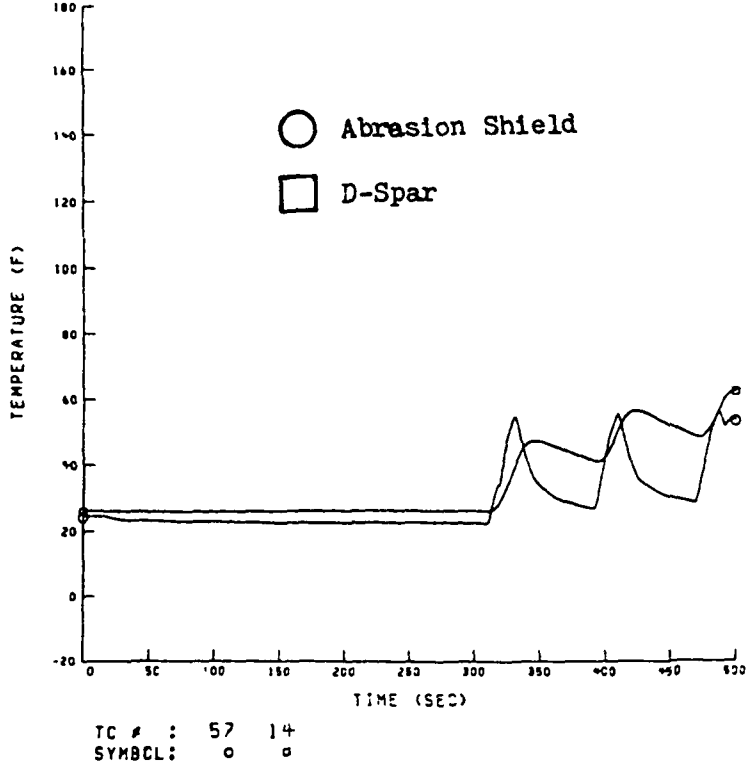

i. Position 9

Figure 26. (Reading 213 Continued)

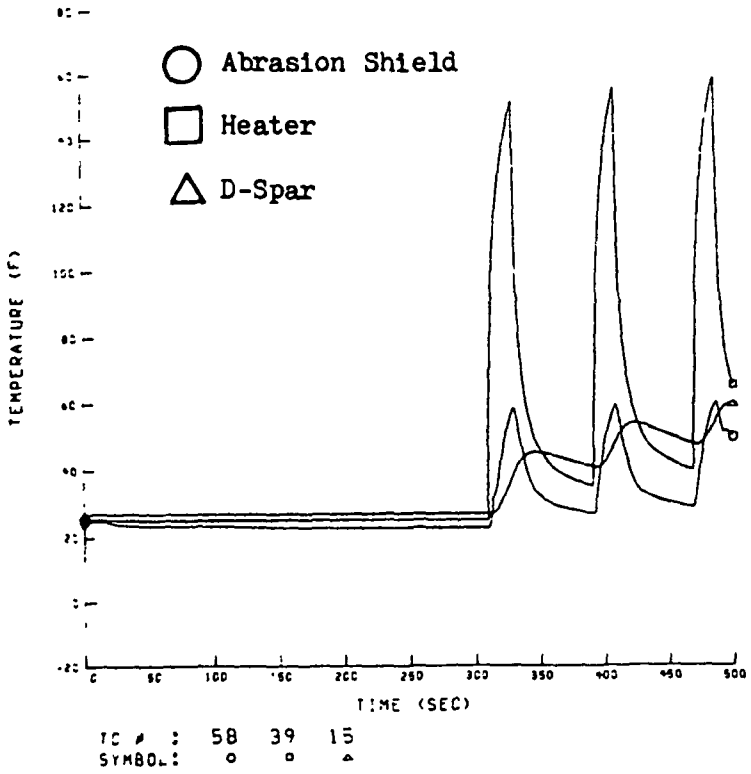

j. Position 10

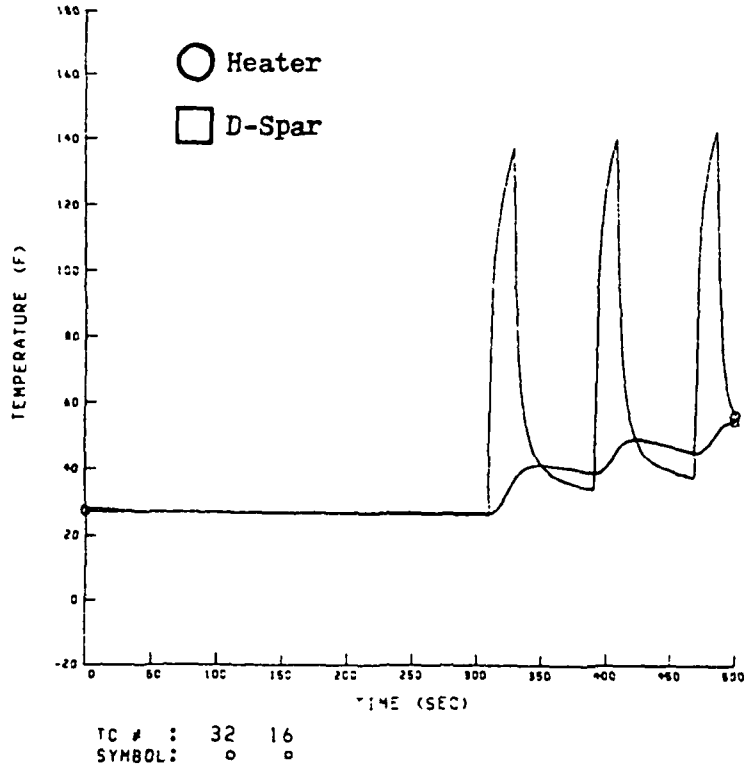

k. Position 11

Figure 26. (Reading 213 Continued)

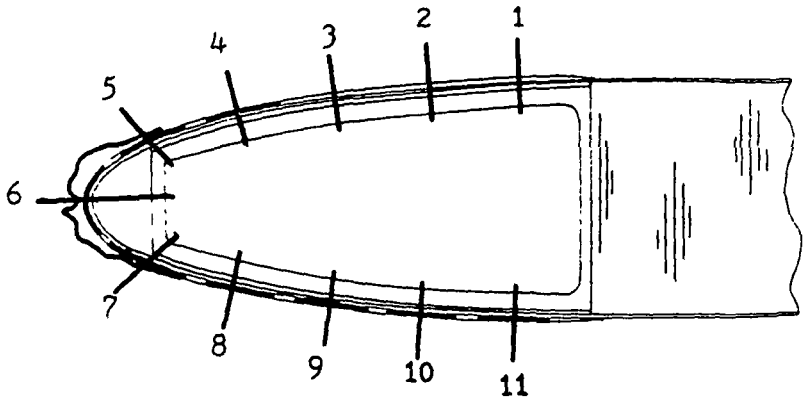

Position Around Blade

V_∞	=	100
T_∞	=	16
α	=	0
P	=	8.0
t_{on}/t_{off}	=	20,30/60
n	=	3
LWC	=	2.2
$\bar{d}$	=	19.2
t_{ice}	=	2.5

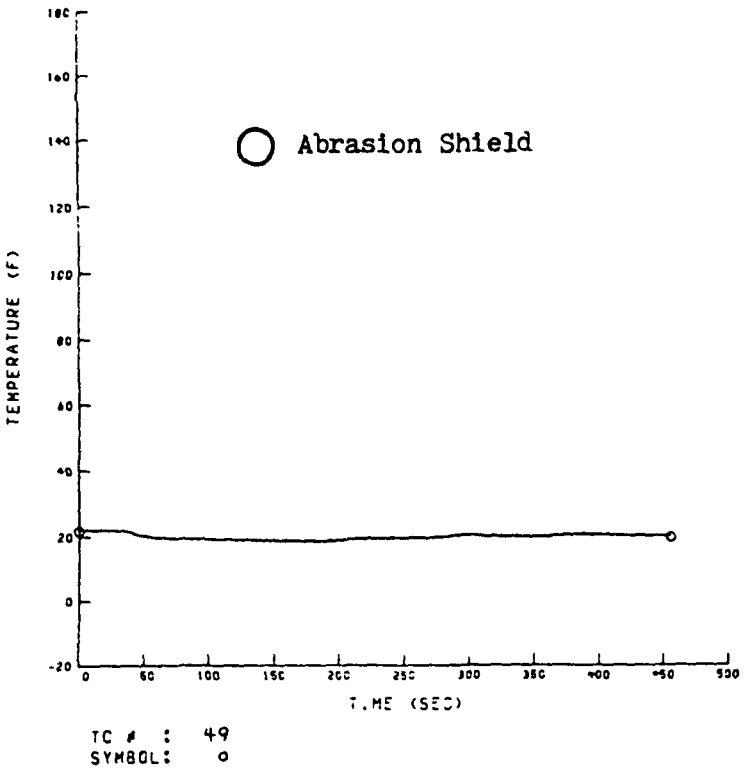

a. Position 1

Figure 27. Response of Selected Thermocouples for Escort Reading 234

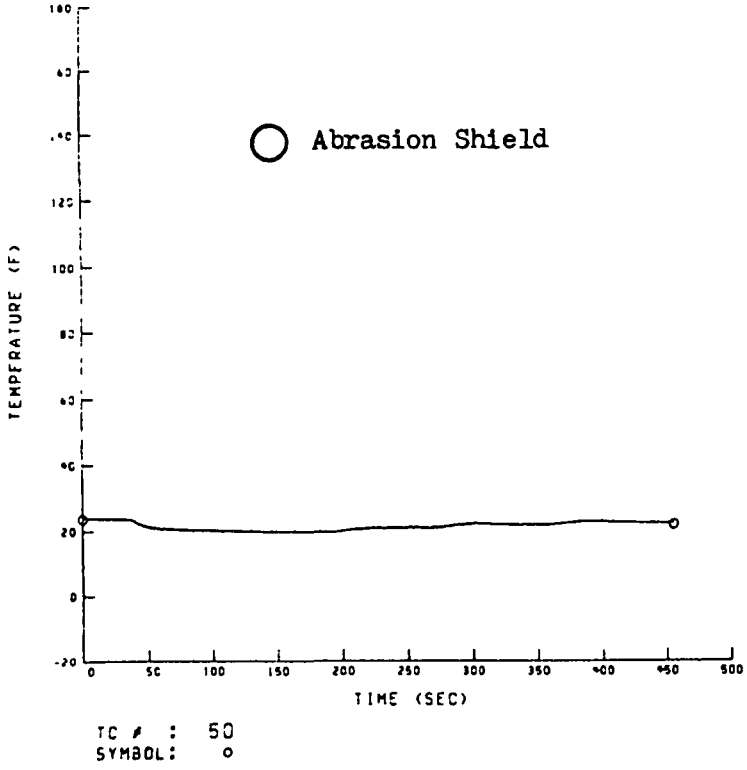

b. Position 2

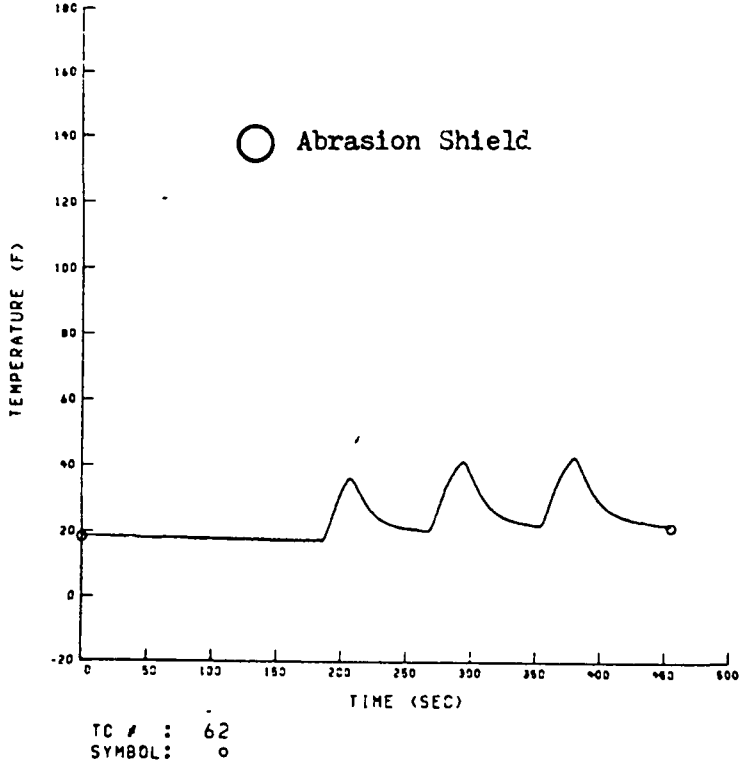

c. Position 3

Figure 27. (Reading 234 Continued)

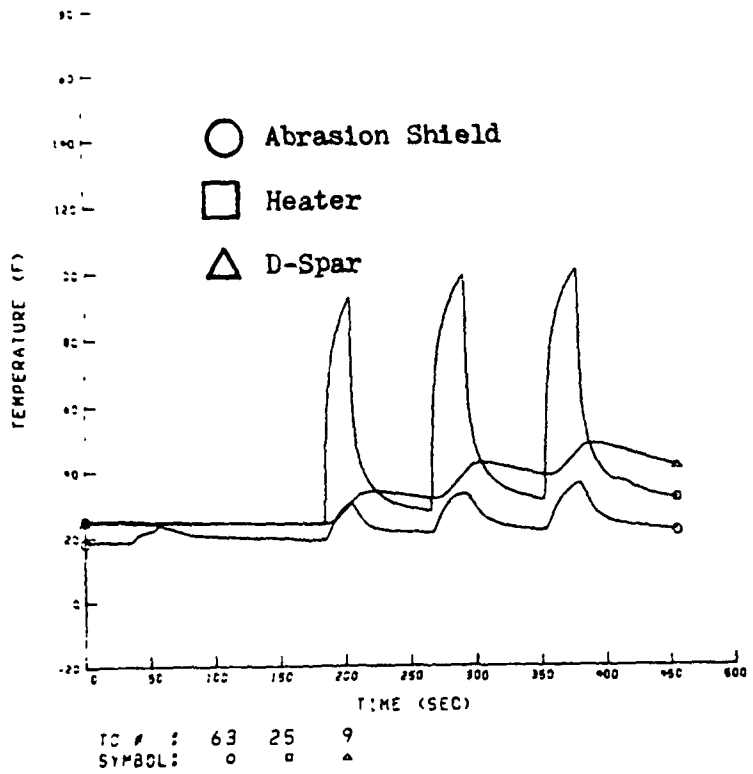

d. Position 4

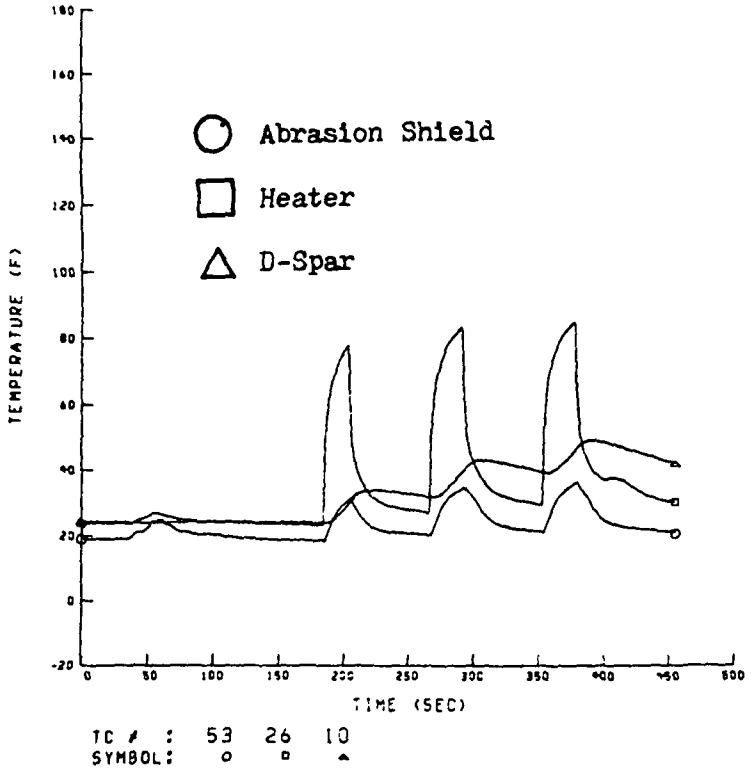

e. Position 5

Figure 27. (Reading 234 Continued)

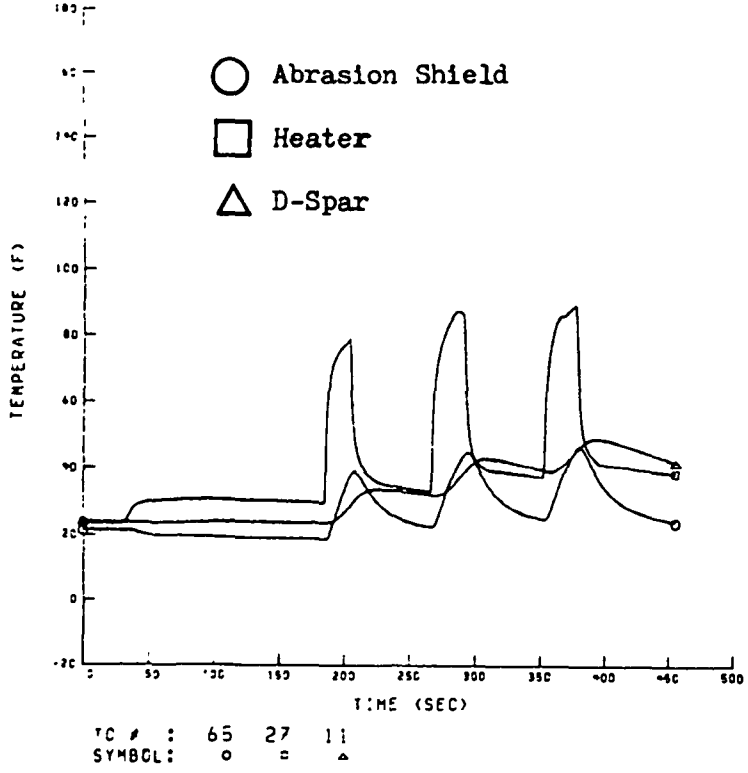

f. Position 6

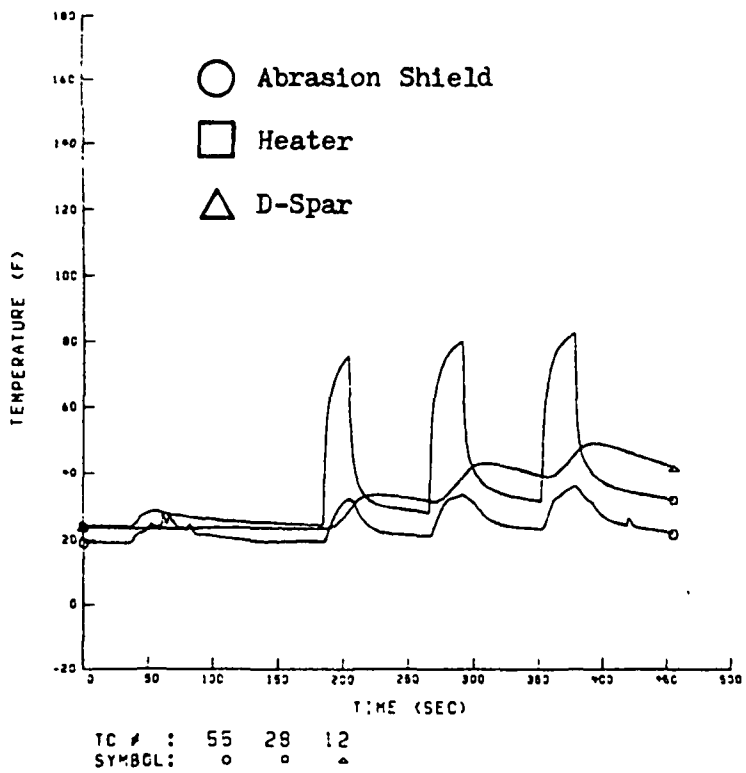

g. Position 7

Figure 27. (Reading 234 Continued)

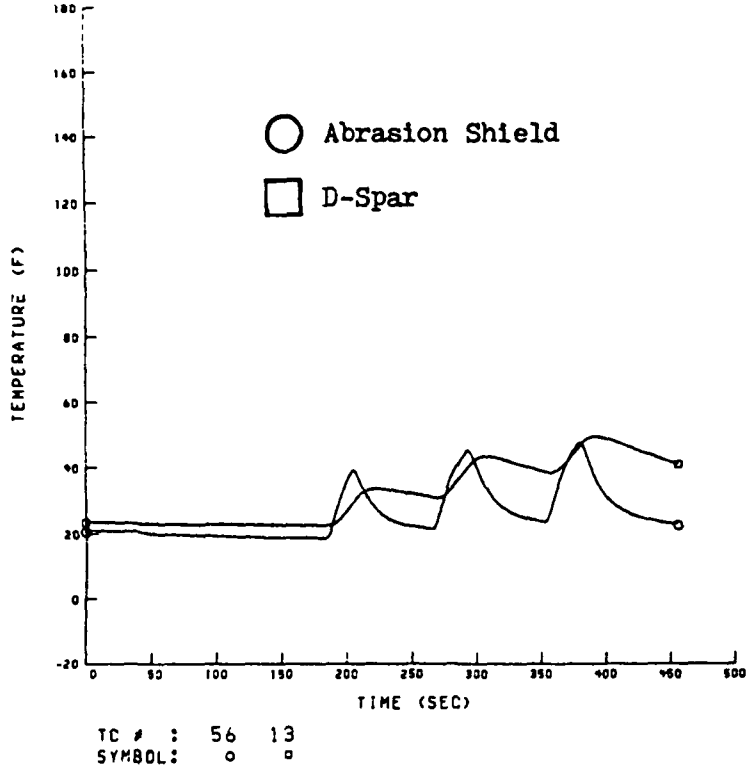

h. Position 8

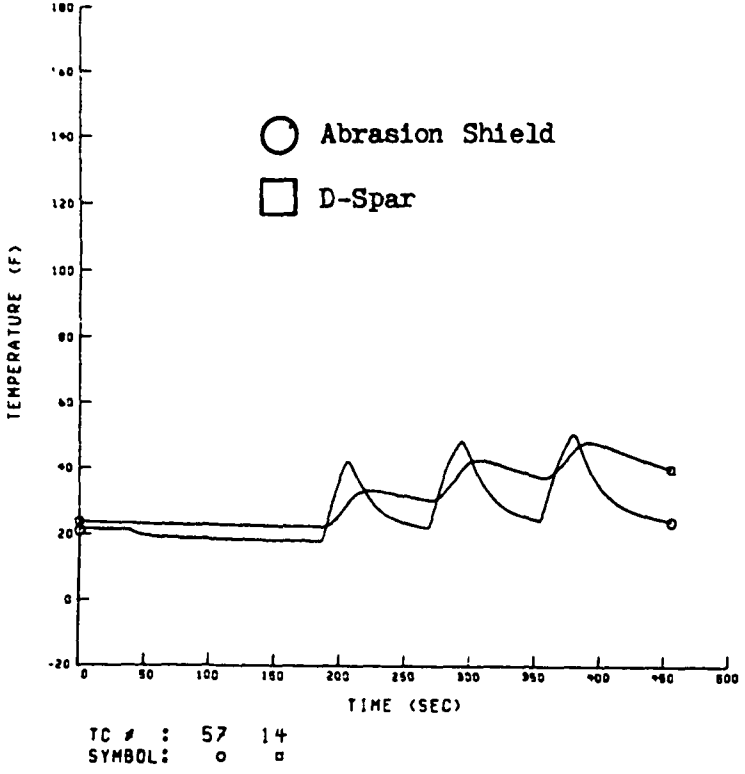

i. Position 9

Figure 27. (Reading 234 Continued)

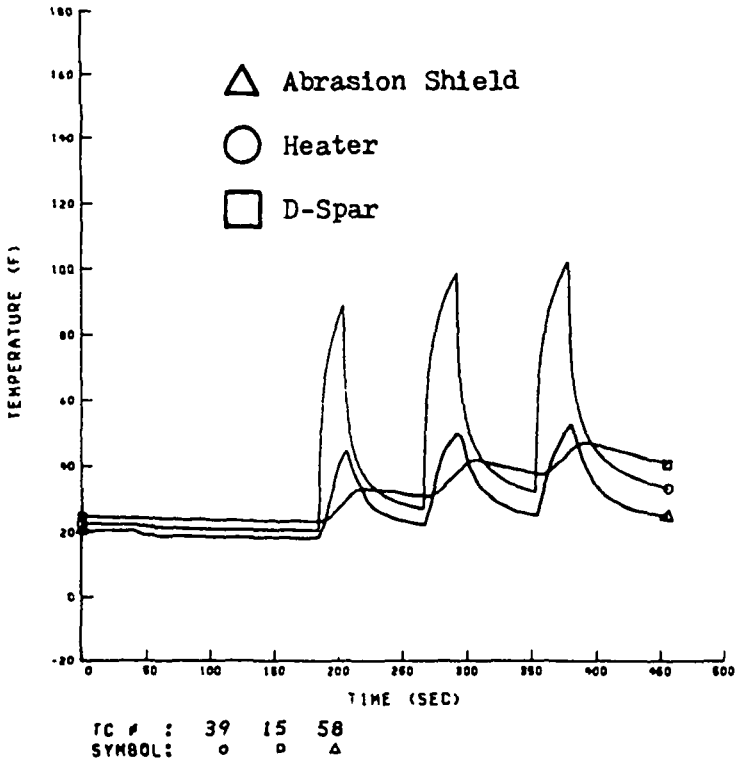

j. Position 10

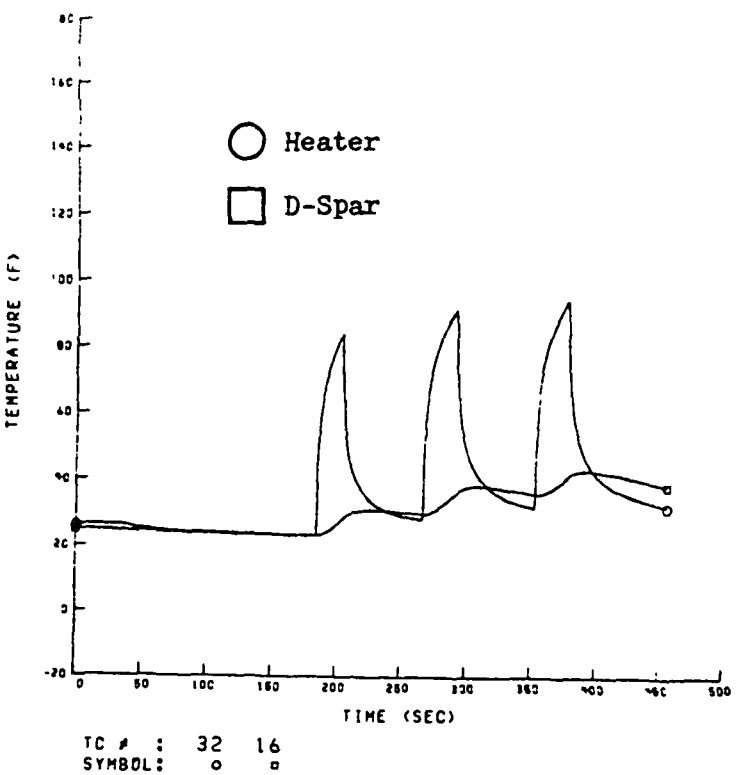

k. Position 11

Figure 27. (Reading 234 Continued)

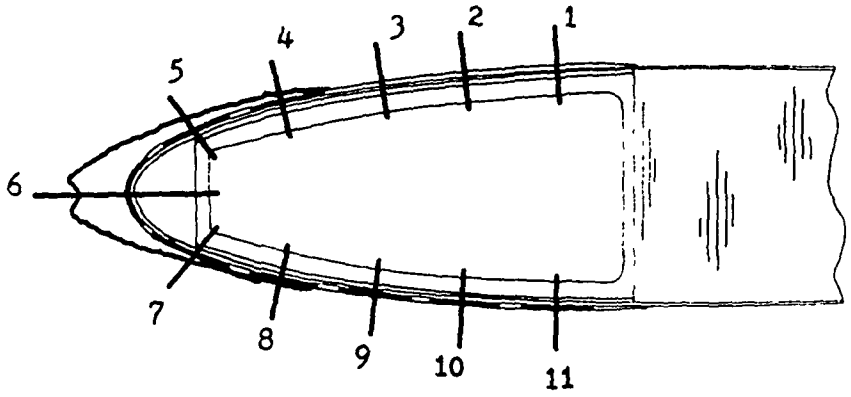

Position Around Blade

V_∞	=	250
T_∞	=	-3
α	=	0
P	=	24.0
t_{on}/t_{off}	=	10/30
n	=	3
LWC	=	1.2
$\bar{d}$	=	20.0
t_{ice}		2.5

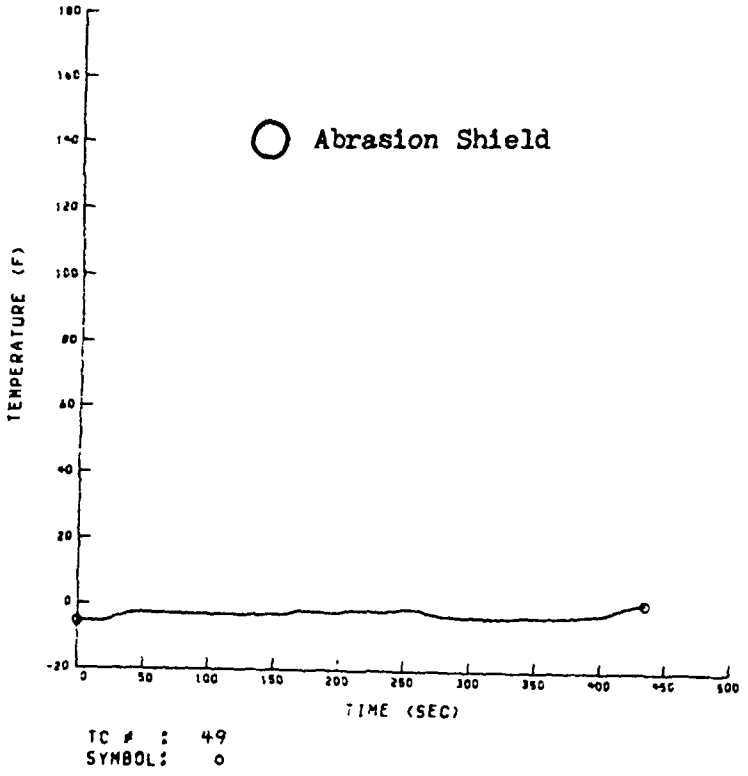

a. Position 1

Figure 28. Response of Selected Thermocouples for Escort Reading 275

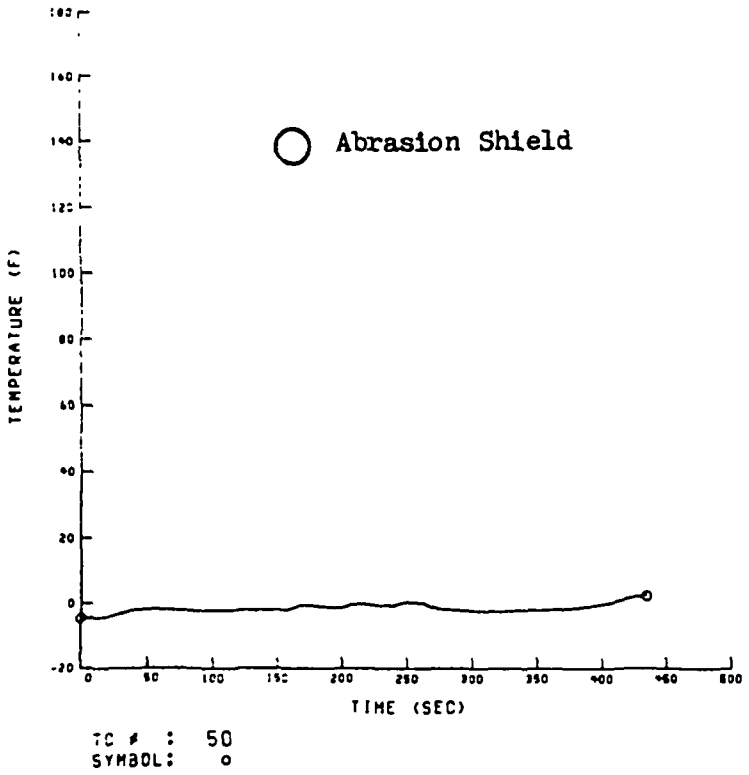

b. Position 2

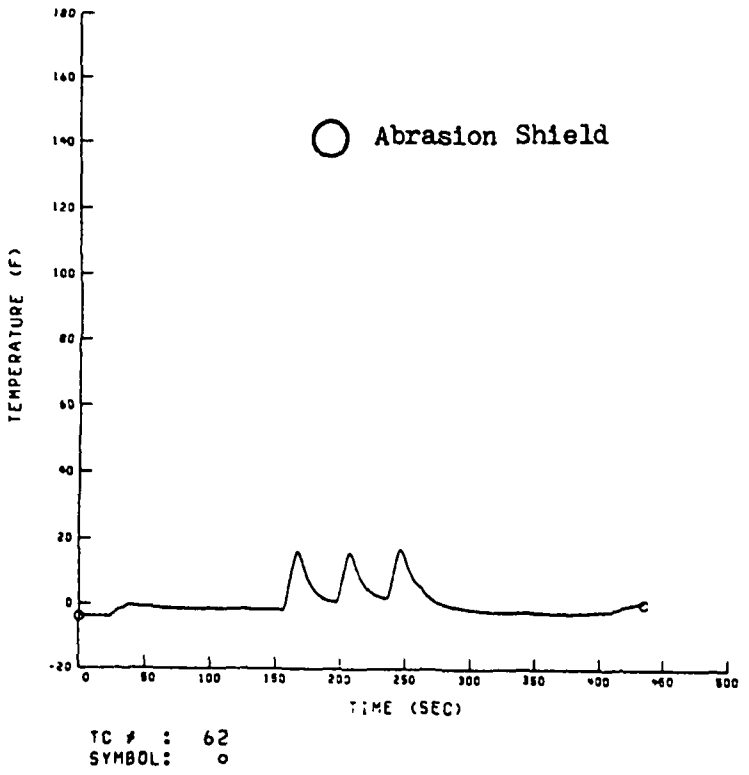

Position 3

Figure 28. (Reading 275 Continued)

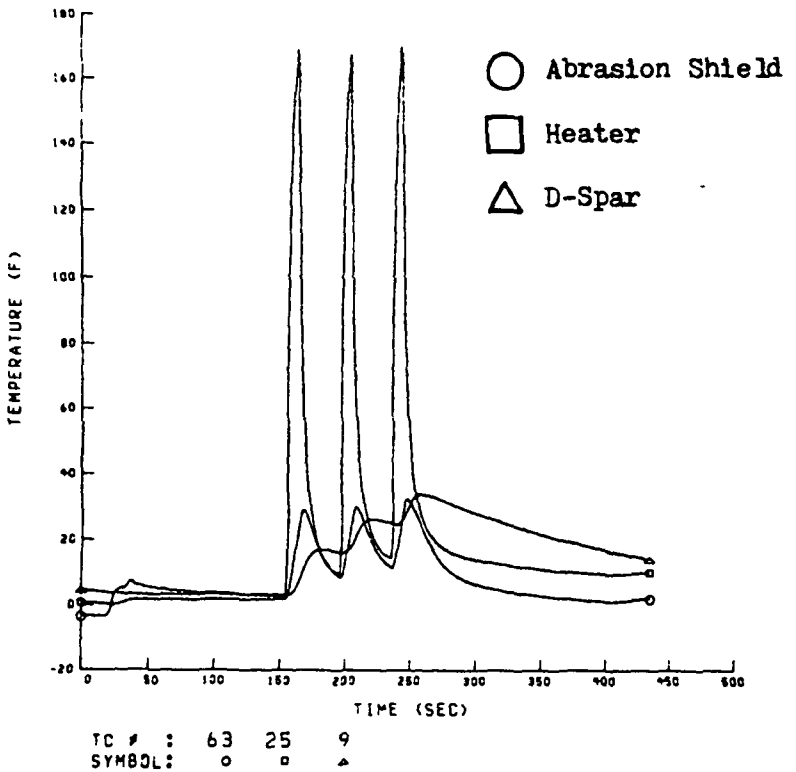

d. Position 4

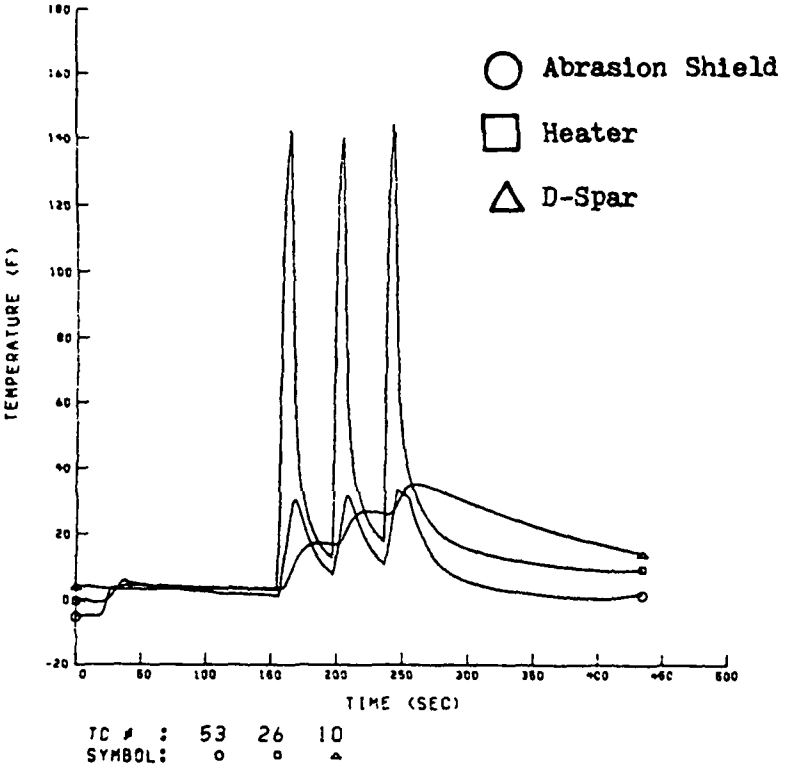

e. Position 5

Figure 28. (Reading 275 Continued)

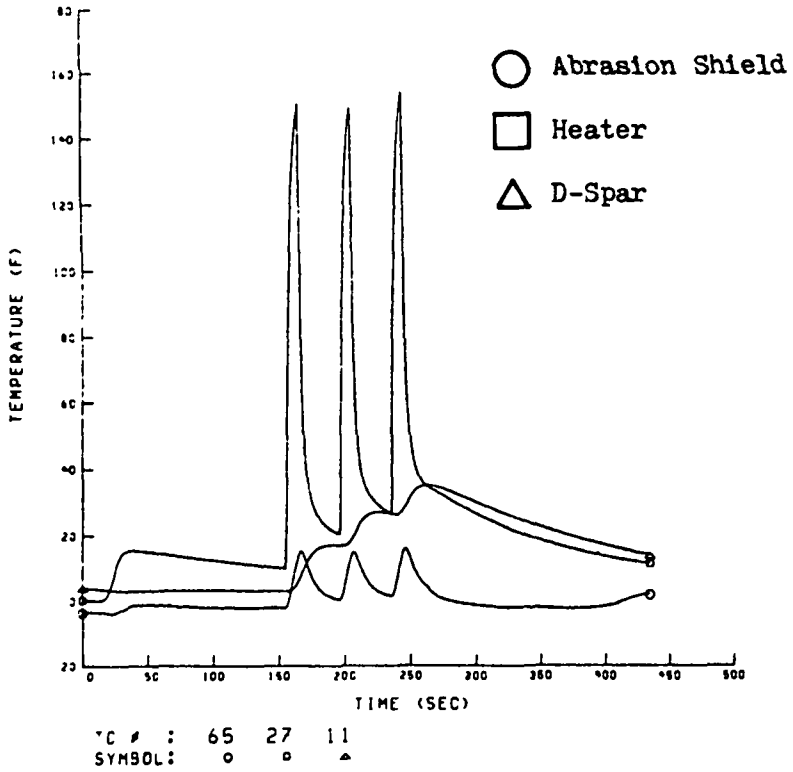

f. Position 6

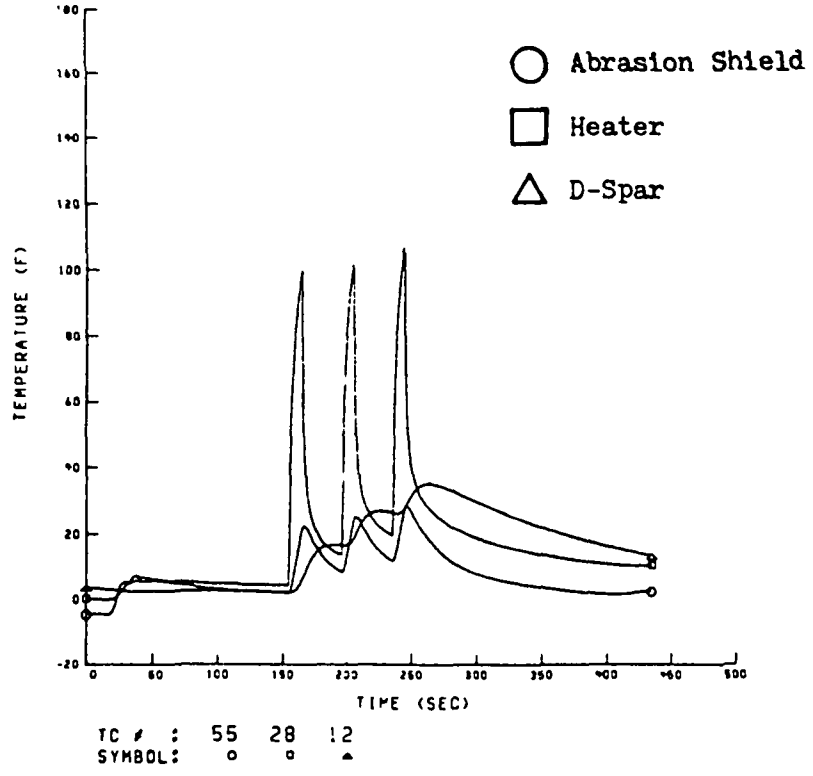

g. Position 7

Figure 28. (Reading 275 Continued)

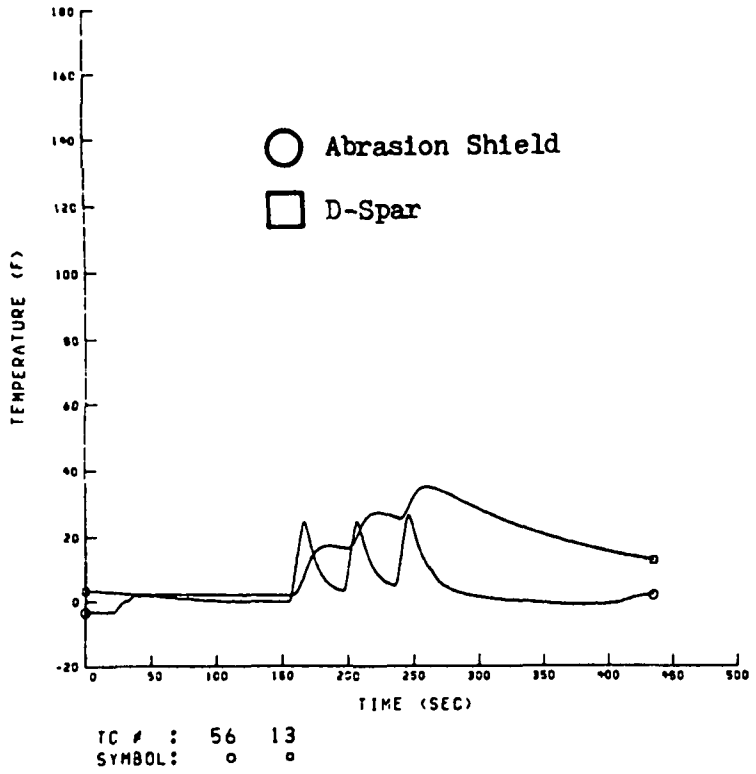

h. Position 8

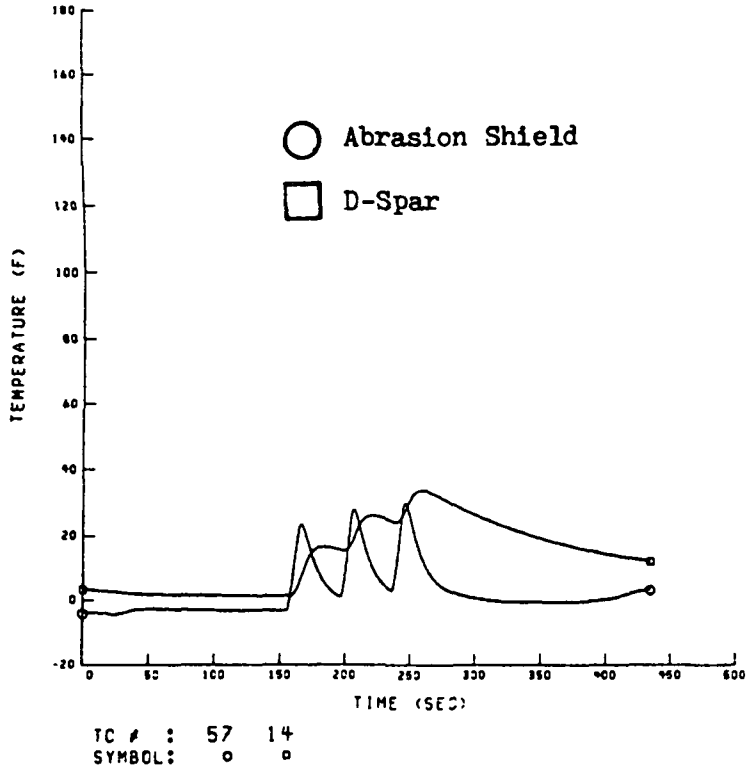

i. Position 9

Figure 28. (Reading 275 Continued)

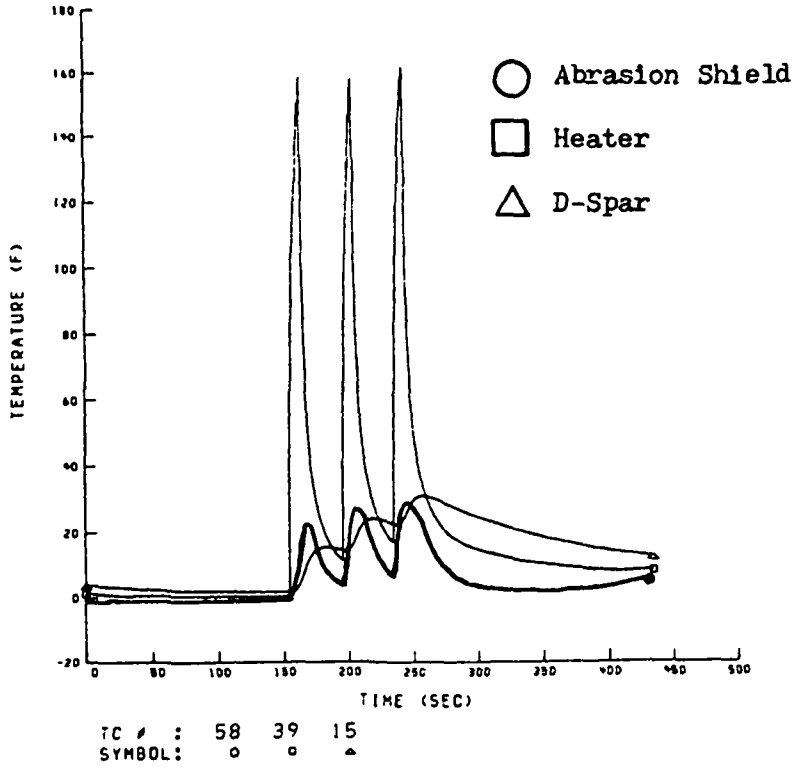

j. Position 10

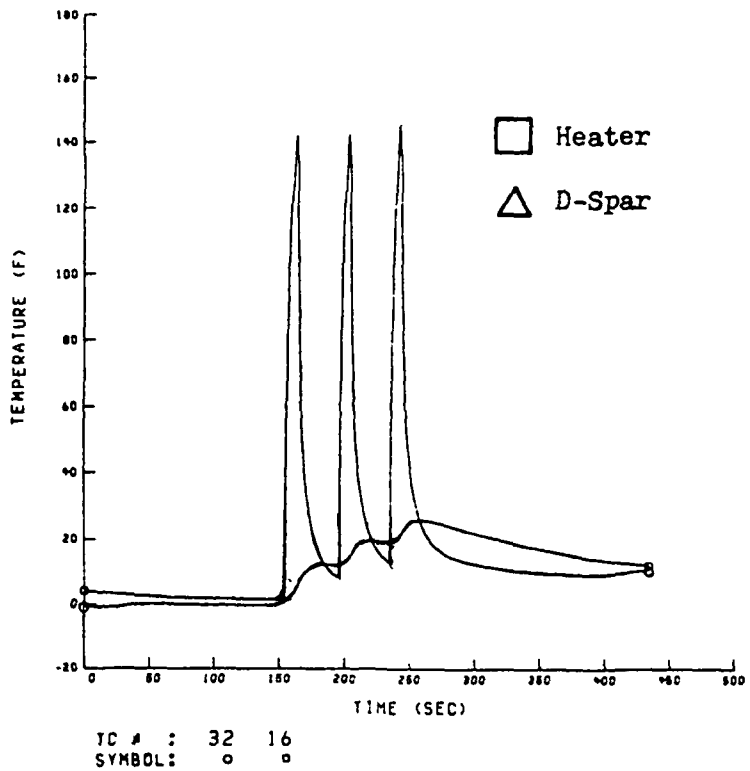

k. Position 11

Figure 28. (Reading 275 Continued)

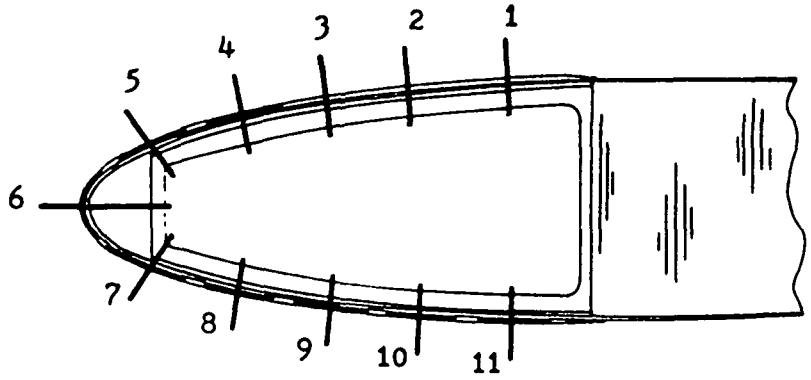

Position Around Blade

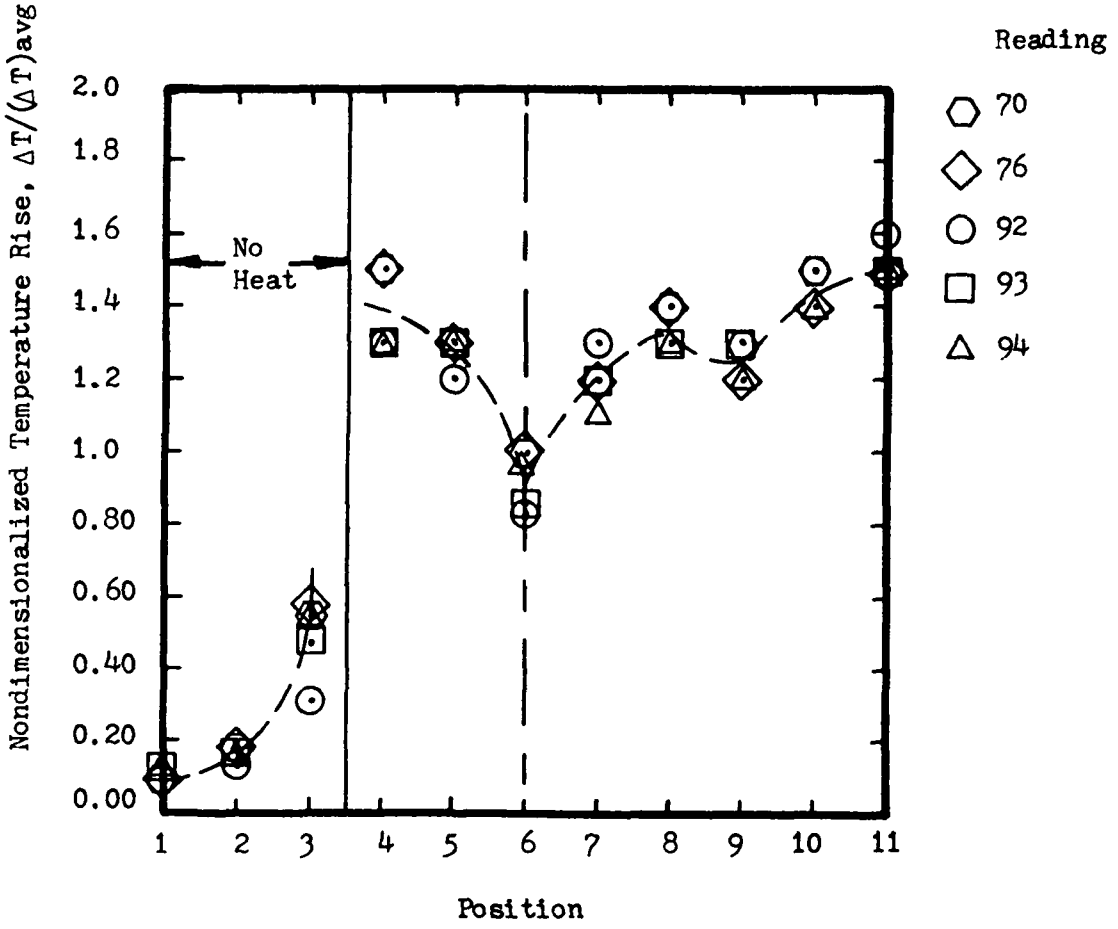

Figure 29. Presentation of Positional Trends at the Abrasion Shield for the Dry Runs

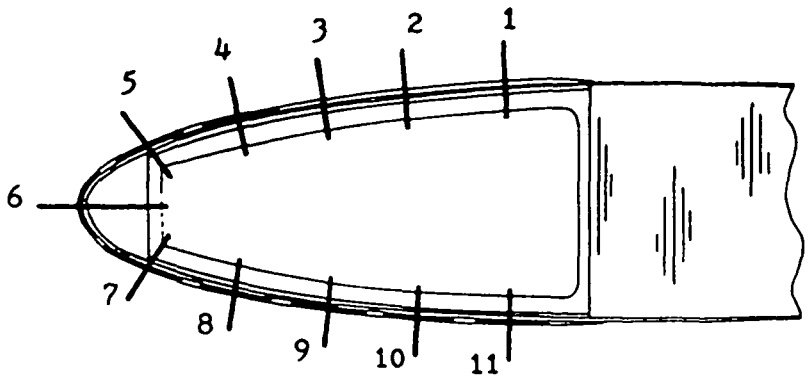

Position Around Blade

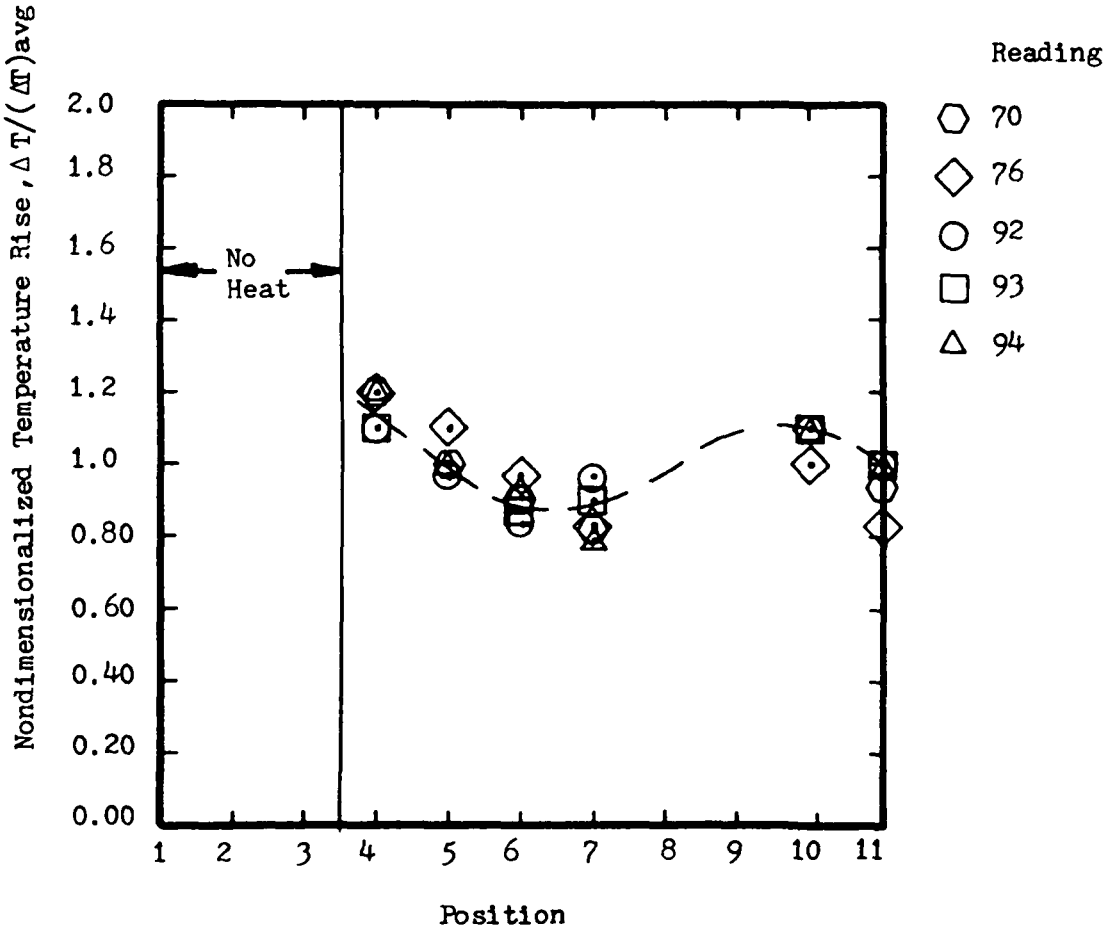

Figure 30. Presentation of Positional Trends at the Heater for the Dry Runs

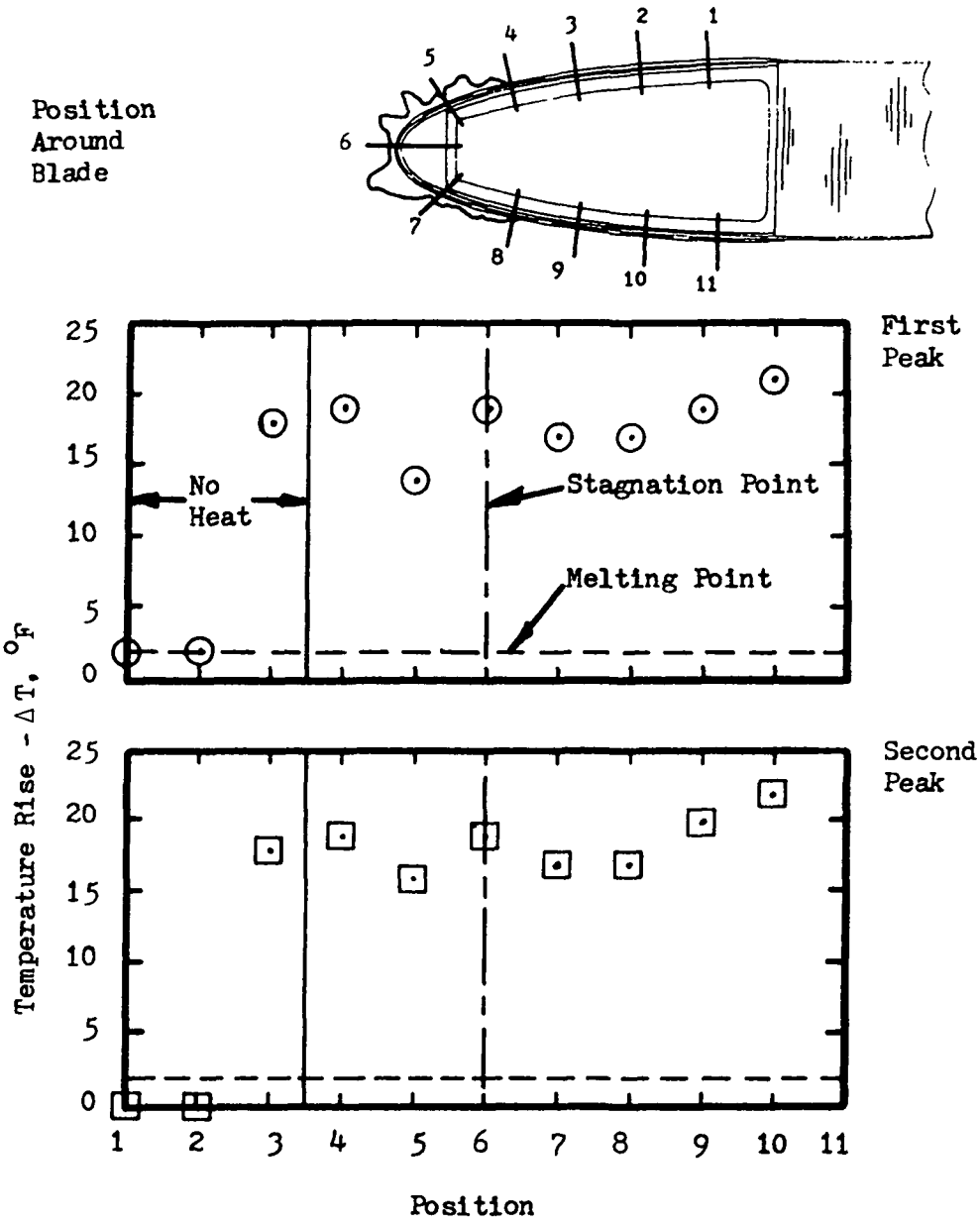

Figure 31. Presentation of Positional Trends at the Abrasion Shield for Reading 197

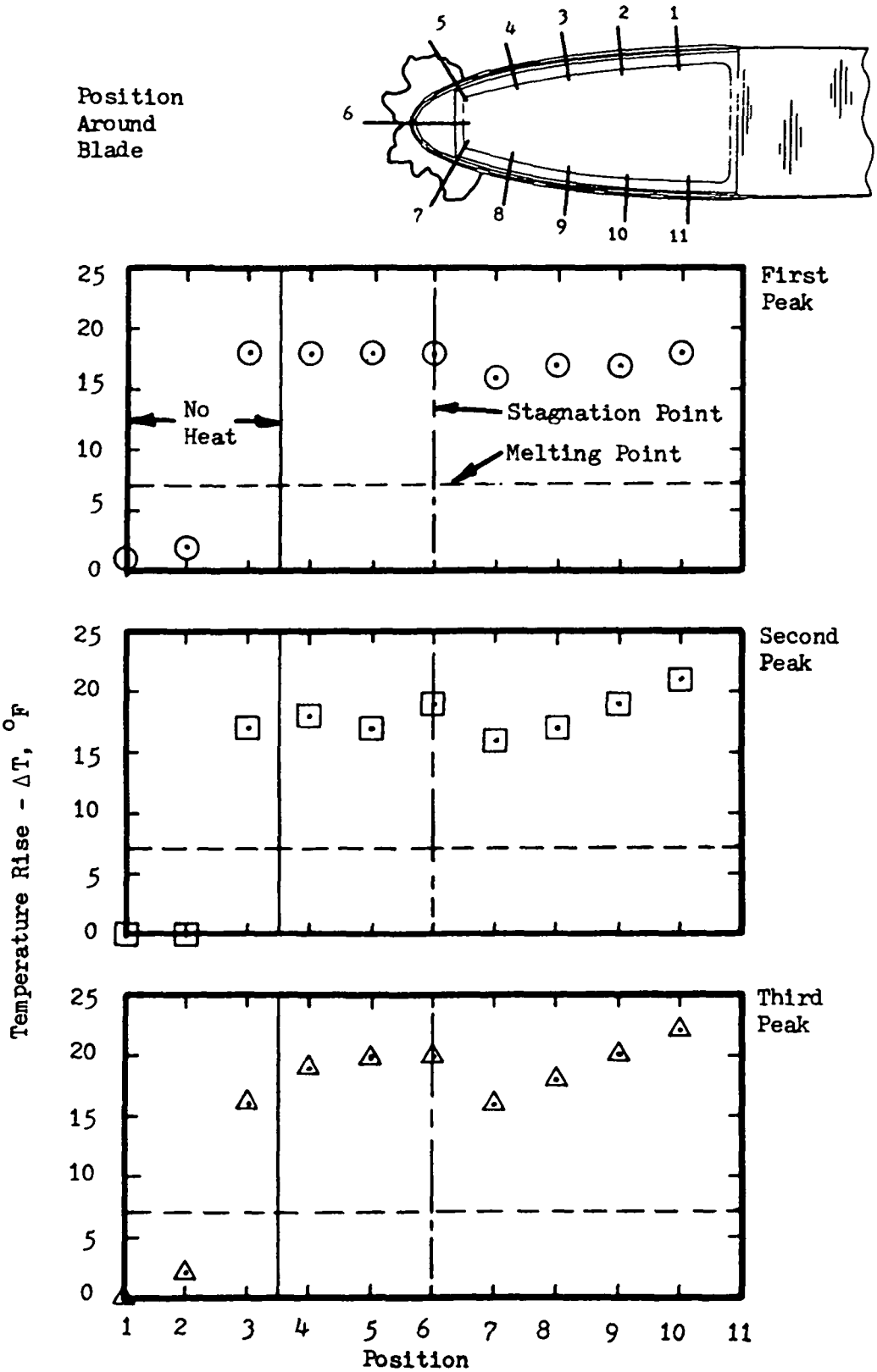

Figure 32. Presentation of Positional Trends at the Abrasion Shield for Reading 209

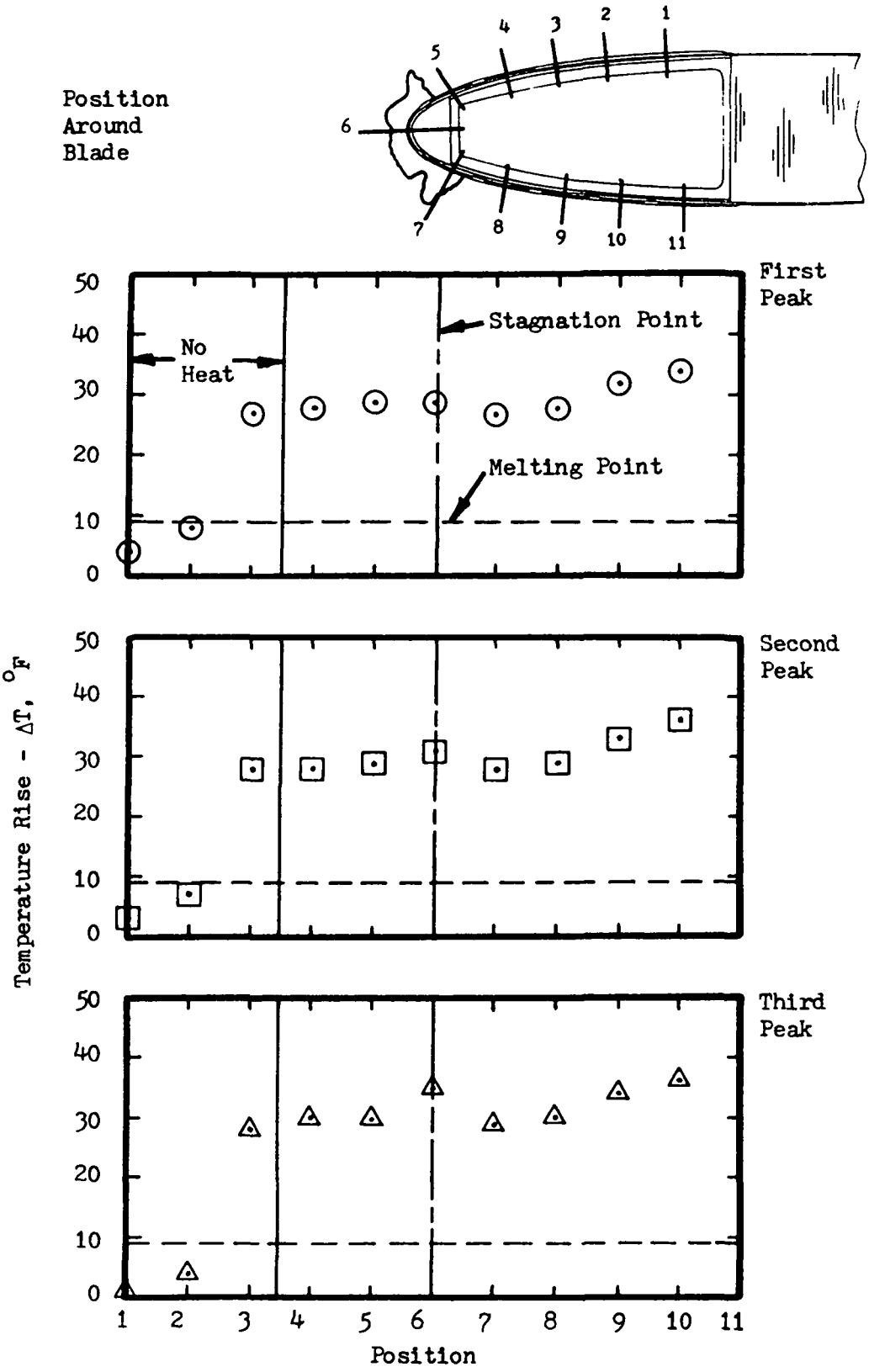

Figure 33. Presentation of Positional Trends at the Abrasion Shield for Reading 213

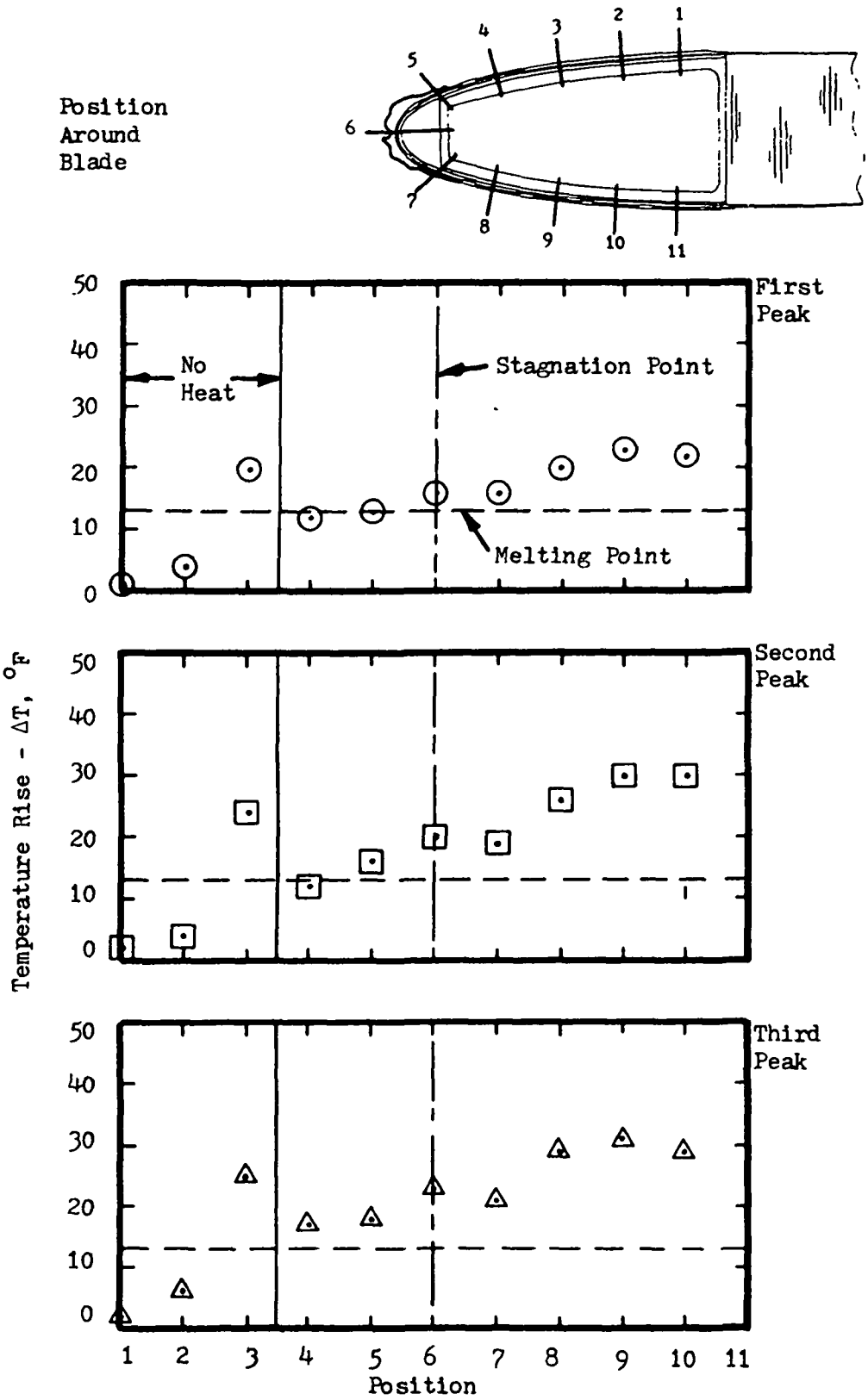

Figure 34. Presentation of Positional Trends at the Abrasion Shield for Reading 234

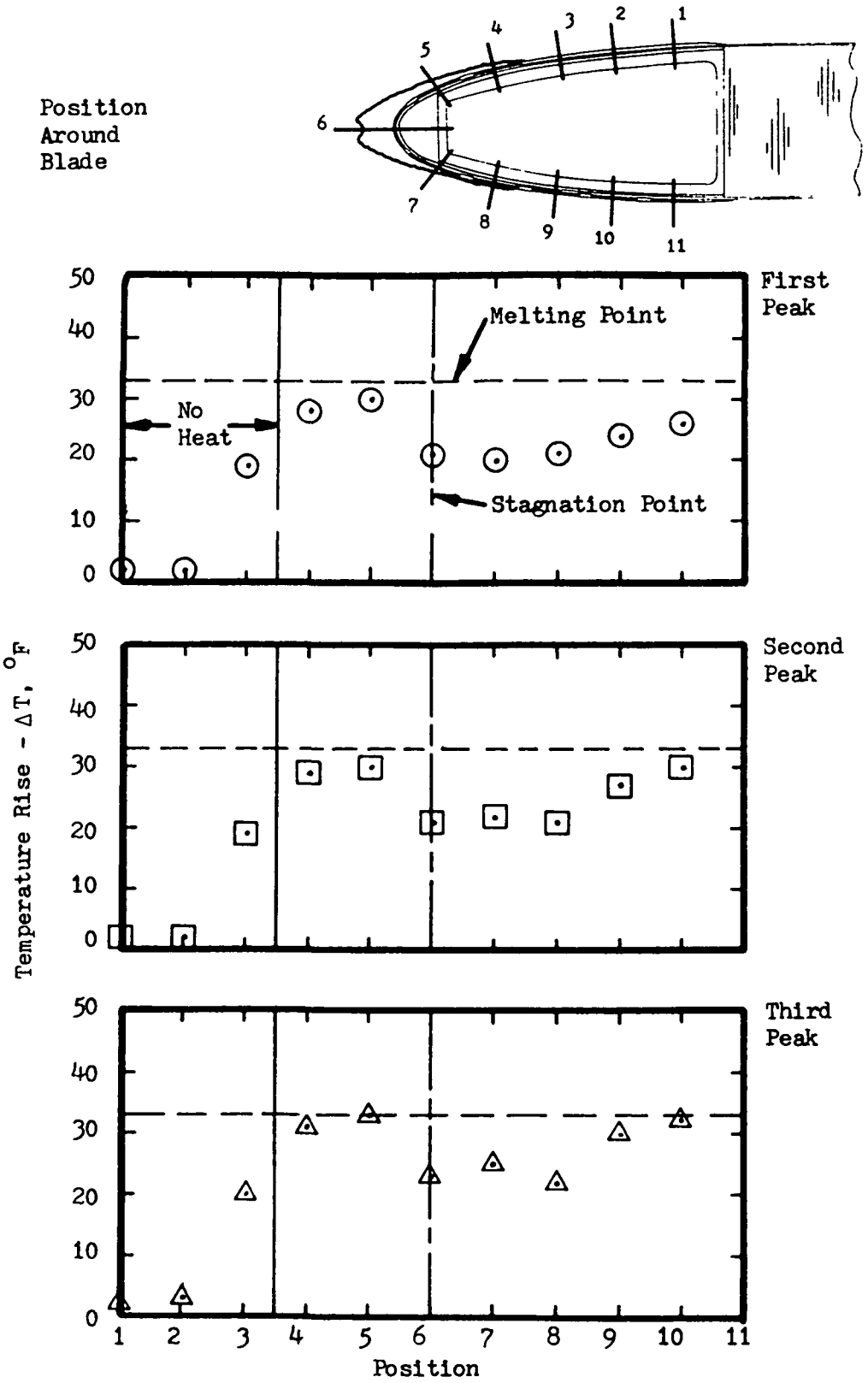

Figure 35. Presentation of Positional Trends at the Abrasion Shield for Reading 275

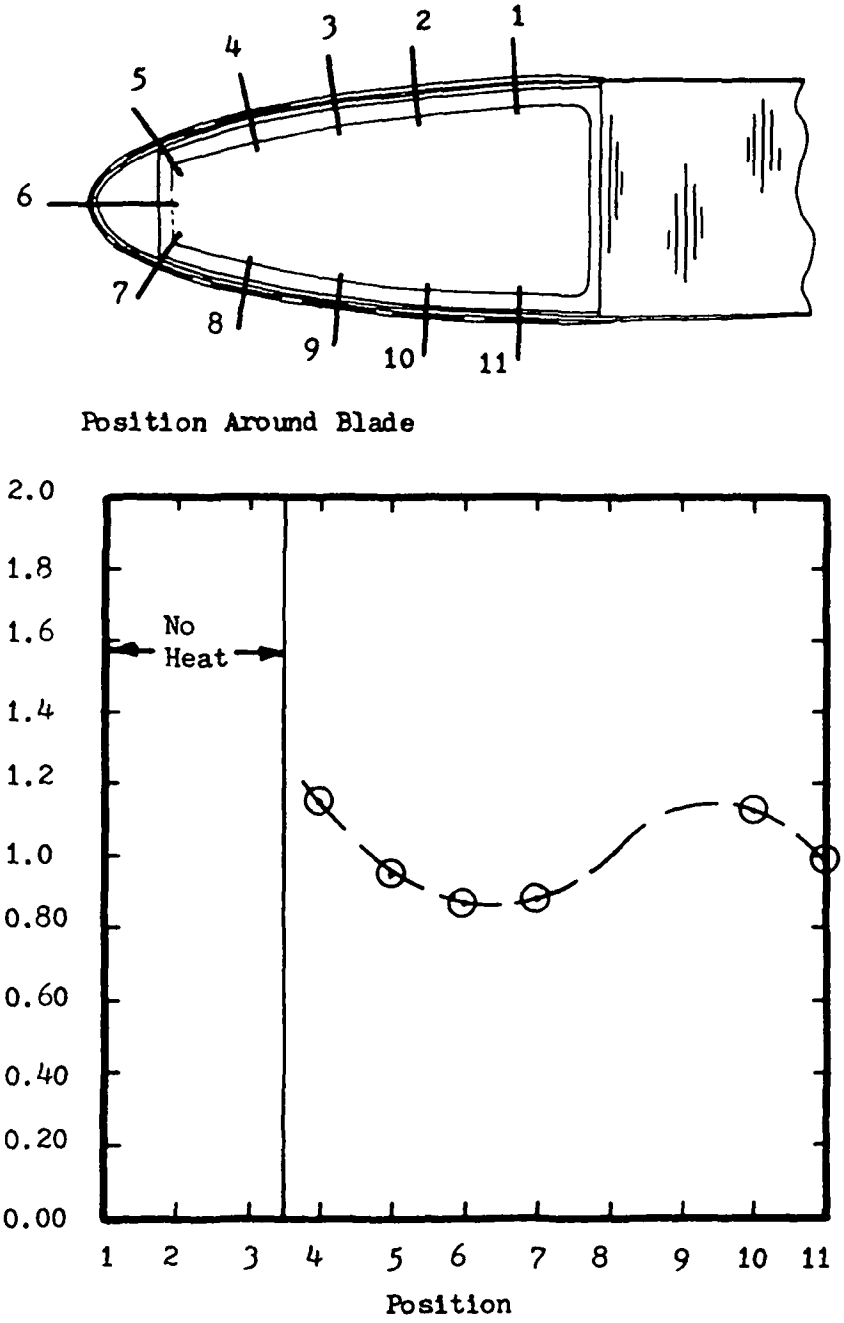

○ Average of all three cycles and all five deicing runs.

Figure 36. Presentation of Positional Trends at the Heater for the Deicing Runs

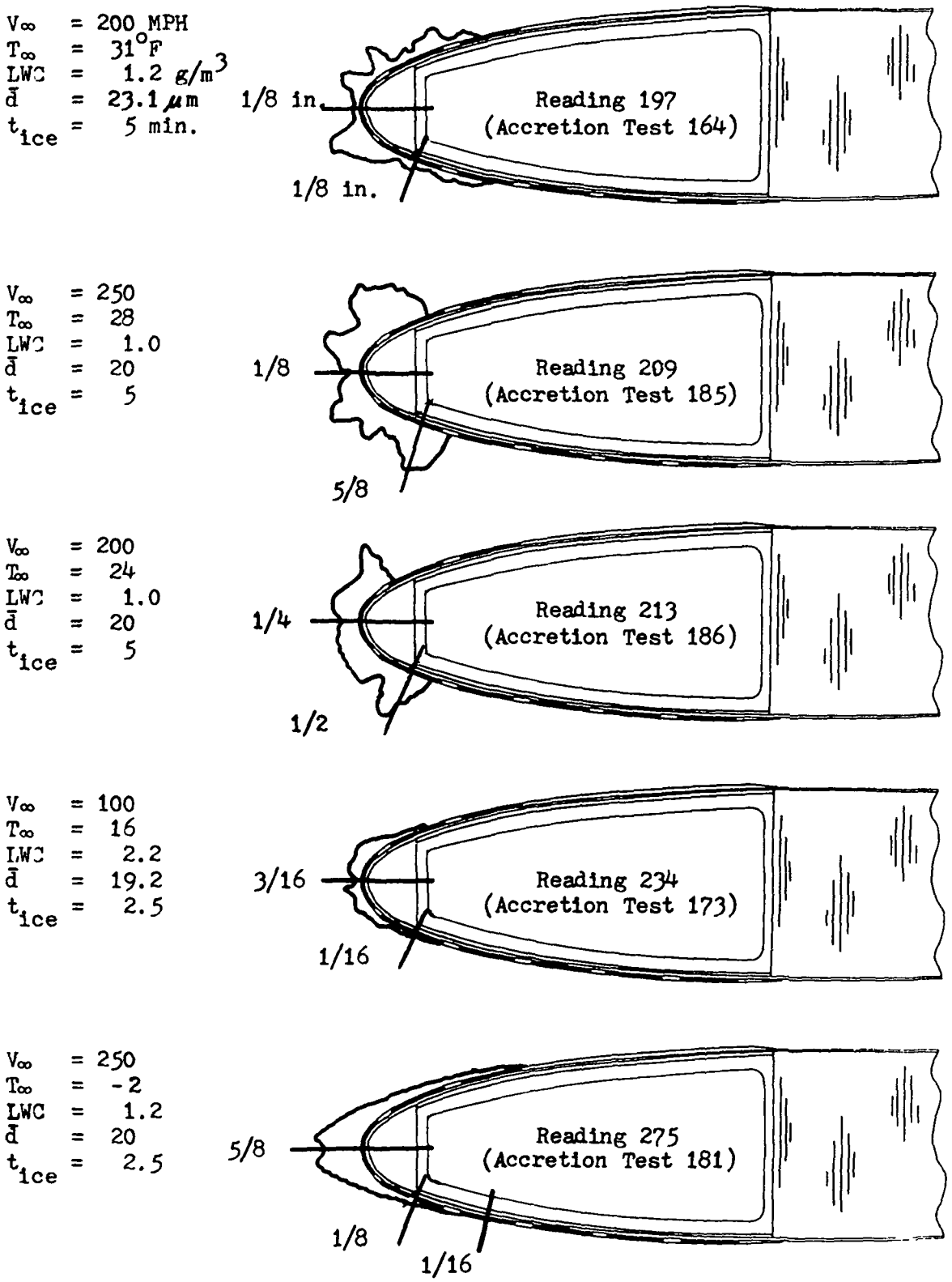

Figure 37. Approximate Ice Shapes for the Five Deicing Runs (Zero Degree Angle of Attack)

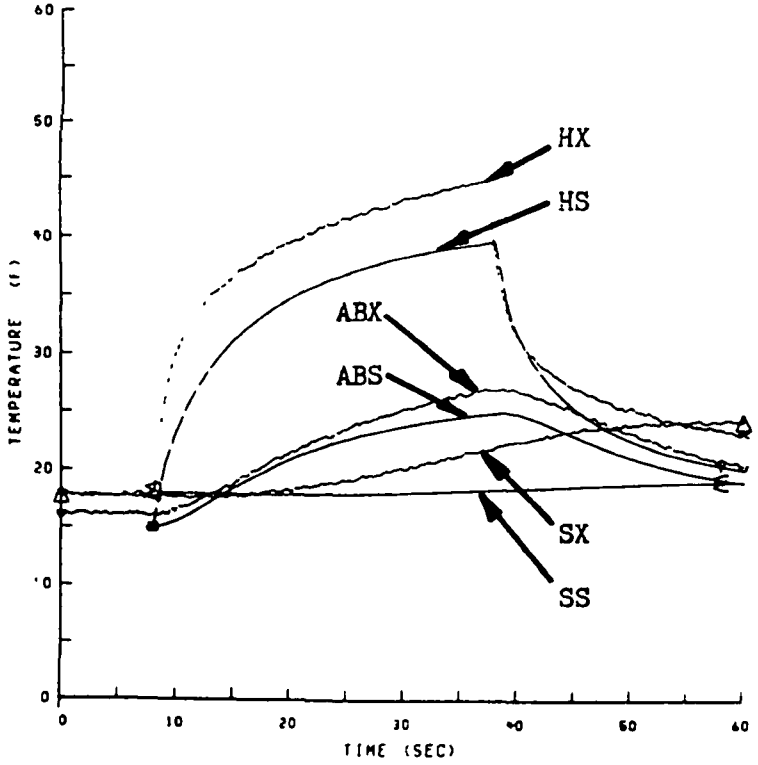

a. Position 6

$T_\infty = 17$ $t_{on} = 30$
$Pz = 2.86$ $x_{on} = 0$
$h_o = 65.7$ $Re_x = 0$

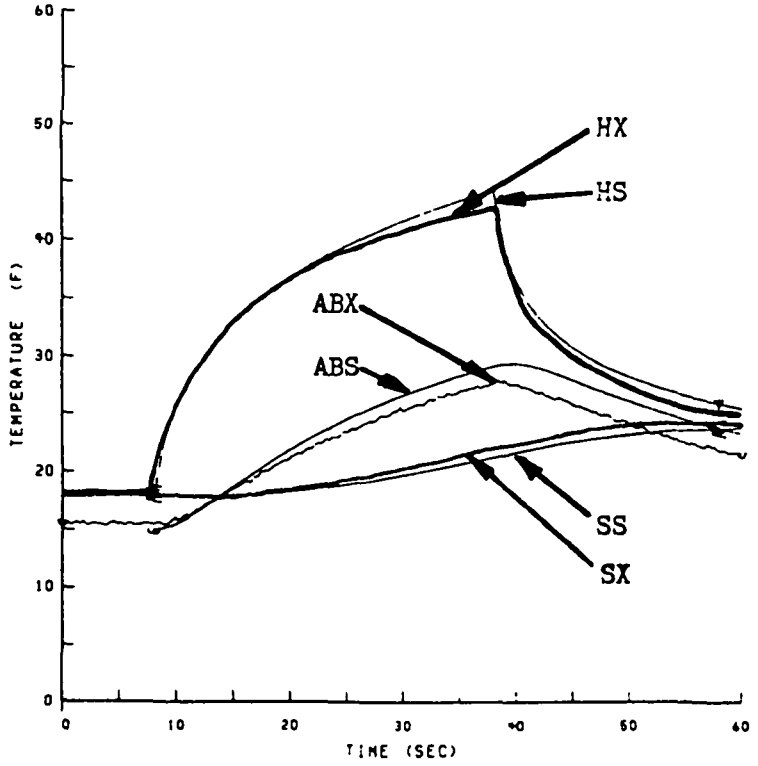

b. Position 7

$T_\infty = 17$ $t_{on} = 30$
$Pz = 2.89$ $x_{on} = 1$
$h_o = 32.7$ $Re_x = 1.23 * 10^5$

Figure 38. Numerical and Experimental Comparison for Reading 70

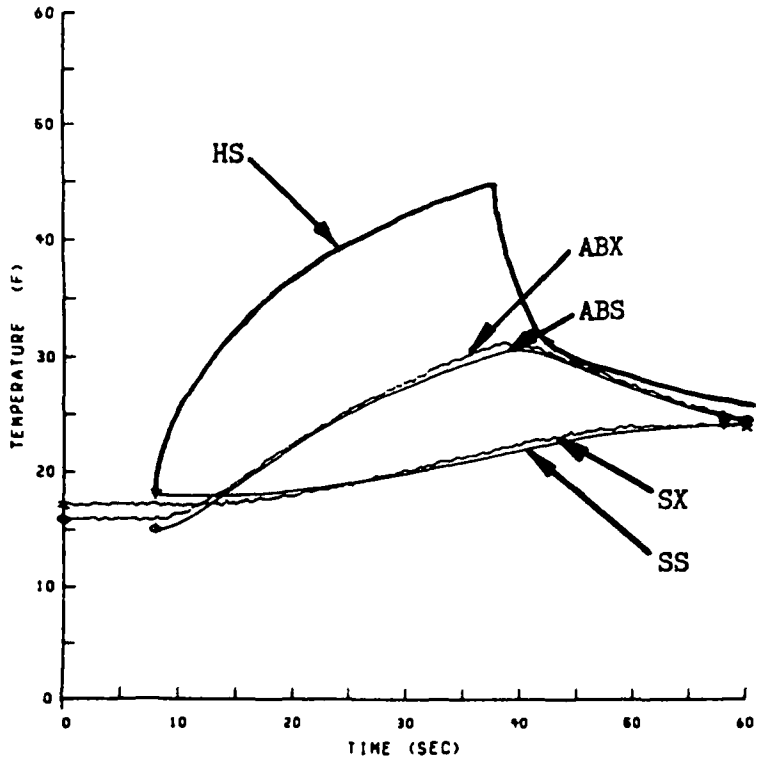

c. Position 8

T_∞ = 17 t_{on} = 30
Pz = 2.96 x_{on} = 2
h_o = 28.7 Re_x = 2.49 *10^5

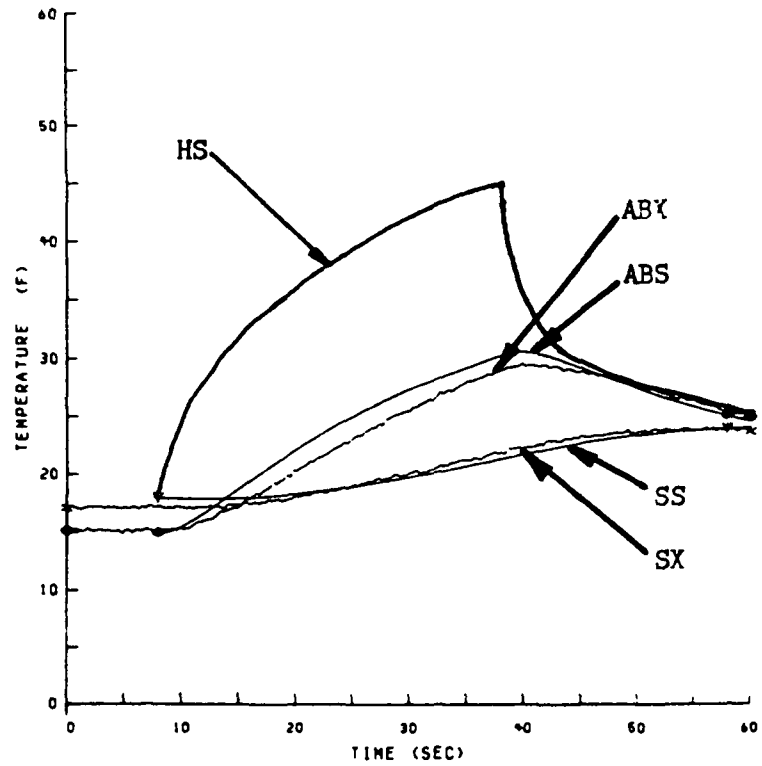

d. Position 9

T_∞ = 17 t_{on} = 30
Pz = 2.91 x_{on} = 3
h_o = 26.5 Re_x = 3.73 *10^5

Figure 38. (Reading 70 Continued)

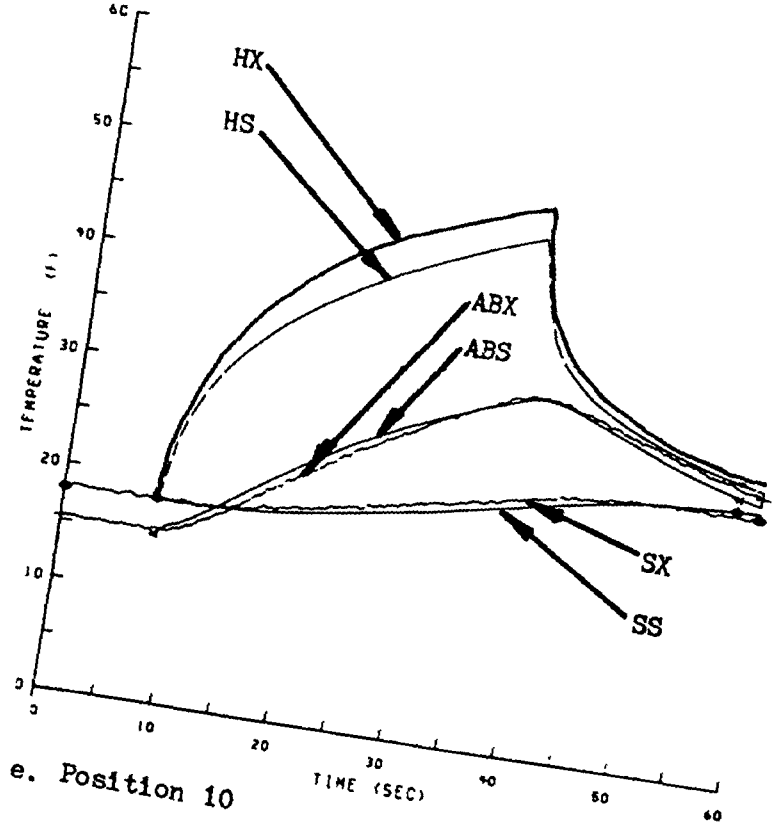

e. Position 10

$T_\infty = 17$
$Pz = 2.97$
$h_o = 25.0$

$t_{on} = 30$
$x = 4$
$Re_x = 4.97 * 10^5$

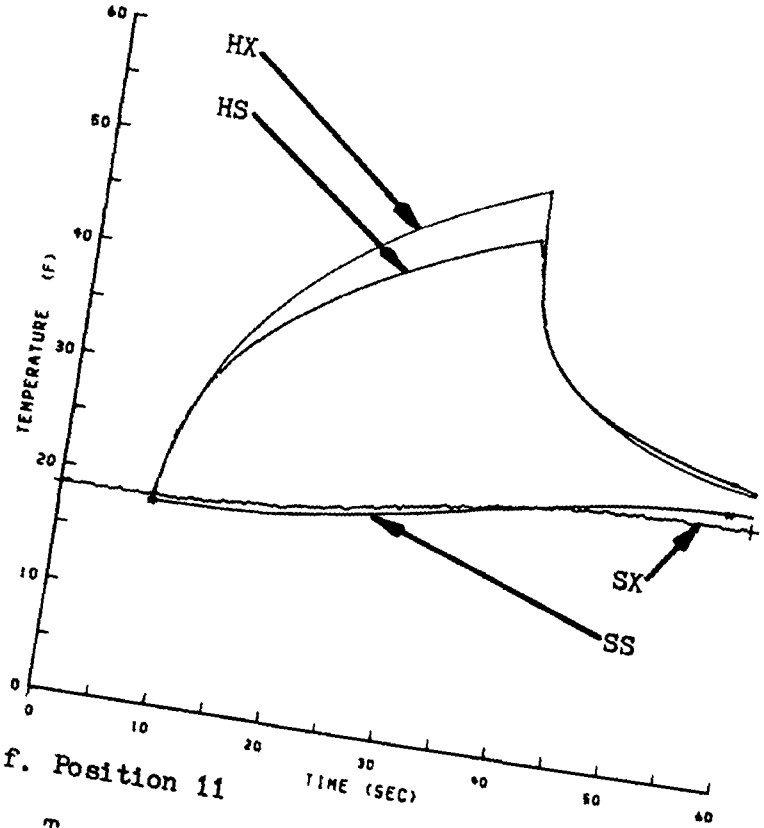

f. Position 11

$T_\infty = 17$
$Pz = 2.97$
$h_o = 23.7$

$t_{on} = 30$
$x = 5$
$Re_x = 6.17 * 10^5$

Figure 38. (Reading 70 Continued)

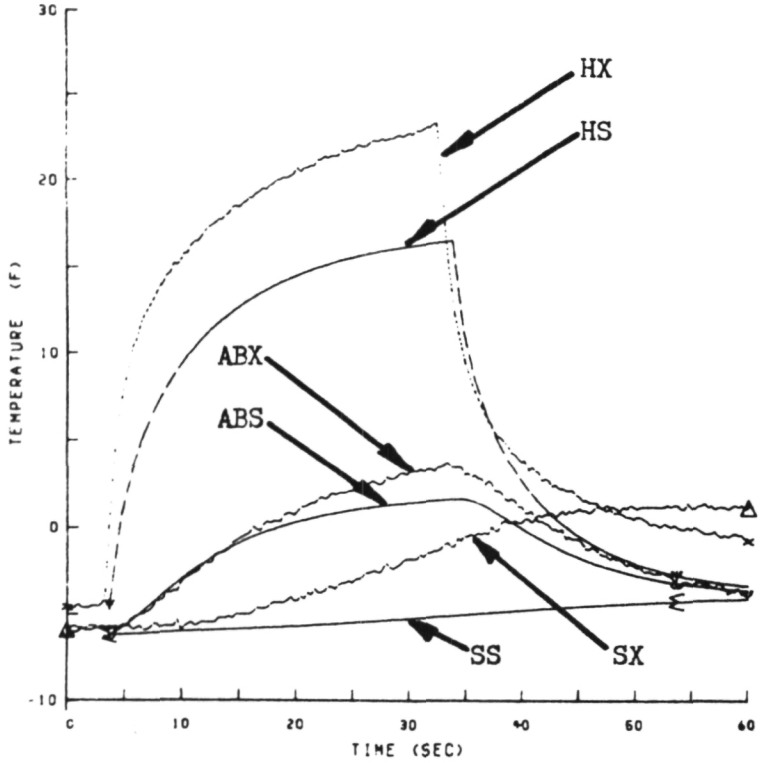

a. Position 6

T_∞ = -4
Pz = 2.86
h_o = 99.4

t_{on} = 30
x_{on} = 0
Re_x = 0

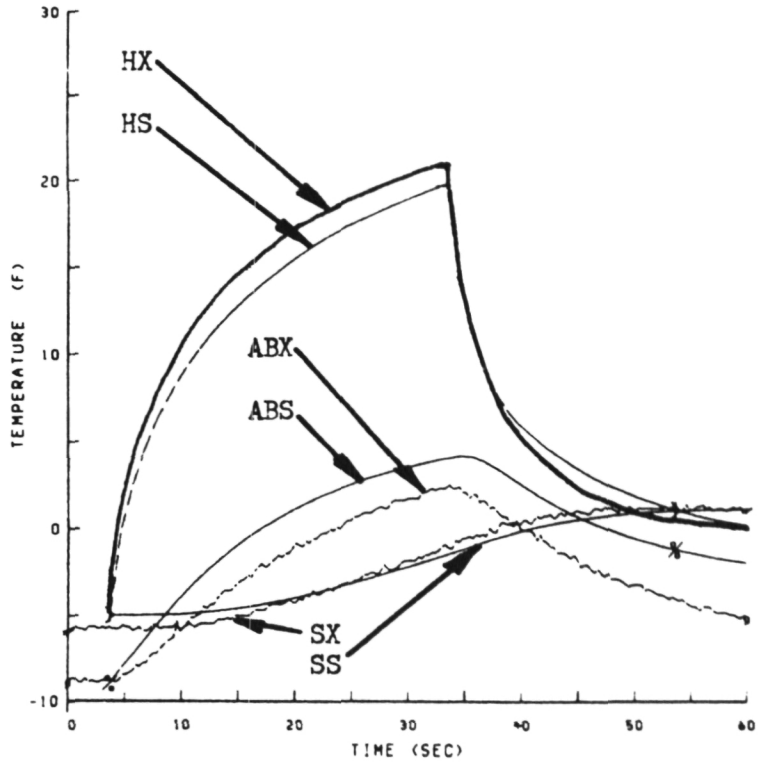

b. Position 7

T_∞ = -4
Pz = 2.89
h_o = 65.9

t_{on} = 30
x_{on} = 1
Re_x = $3.12 * 10^5$

Figure 39. Numerical and Experimental Comparison for Reading 76

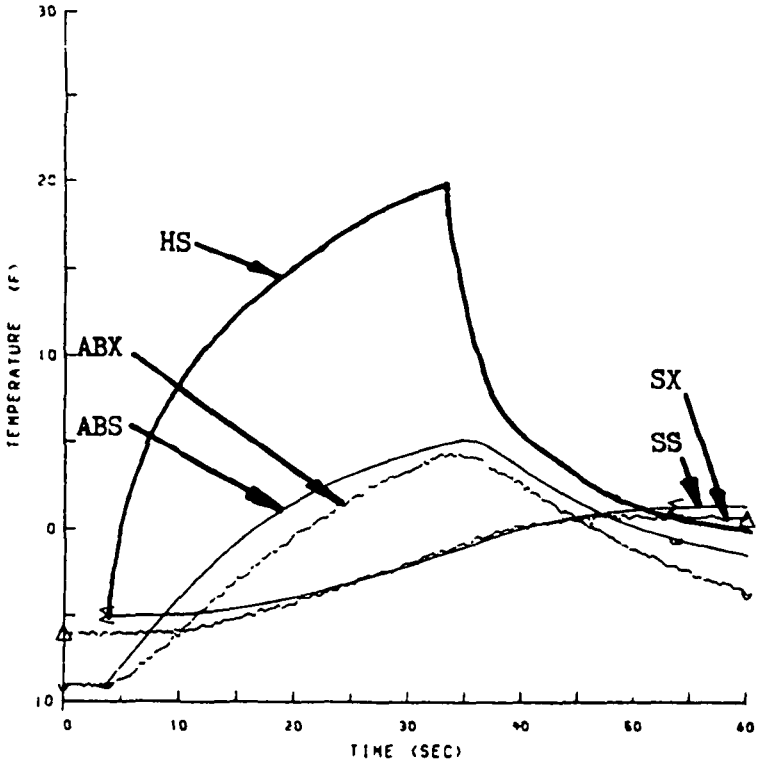

c. Position 8

$T_\infty = -4$ $t_{on} = 30$
Pz = 2.96 $x_{on} = 2$
$h_o = 57.5$ $Re_x = 6.32 * 10^5$

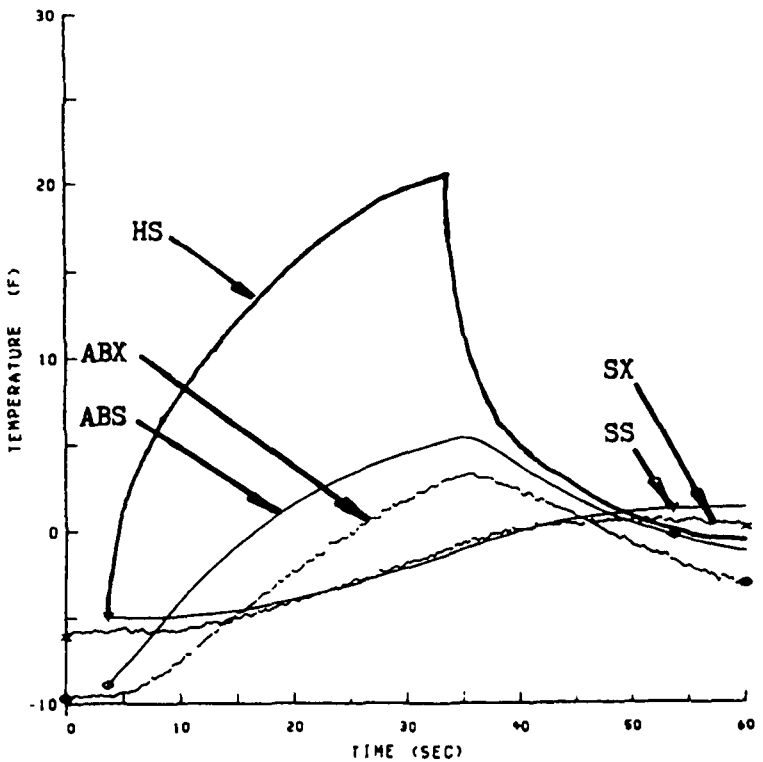

d. Position 9

$T_\infty = -4$ $t_{on} = 30$
Pz = 2.91 $x_{on} = 3$
$h_o = 53.3$ $Re_x = 9.48 * 10^5$

Figure 39. (Reading 76 Continued)

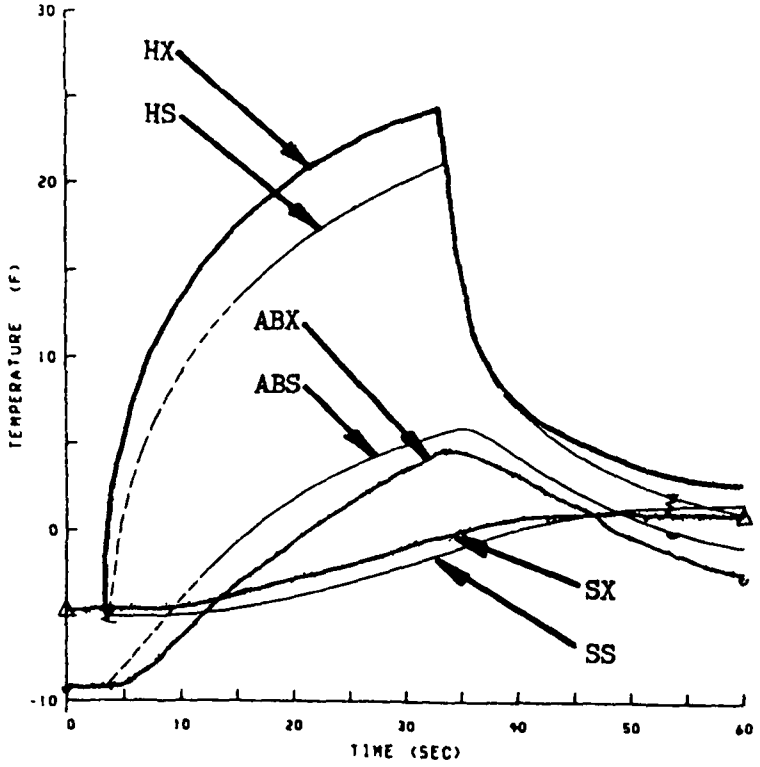

e. Position 10

T_∞ = -4
Pz = 2.97
h_o = 50.4

t_{on} = 30
x = 4
Re_x = 1.26 *10^6

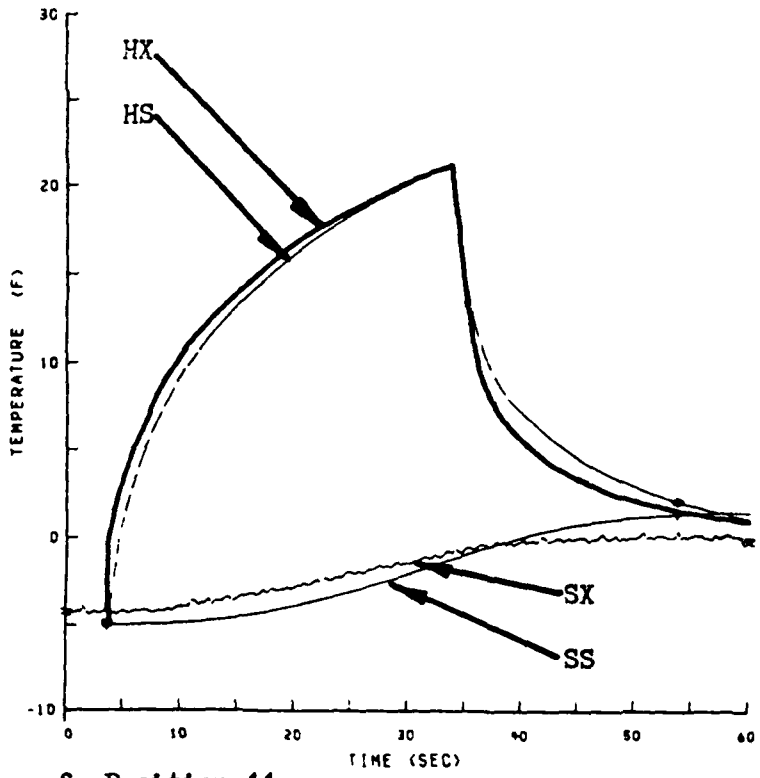

f. Position 11

T_∞ = -4
Pz = 2.97
h_o = 47.9

t_{on} = 30
x = 5
Re_x = 1.57 *10^6

Figure 39. (Reading 76 Continued)

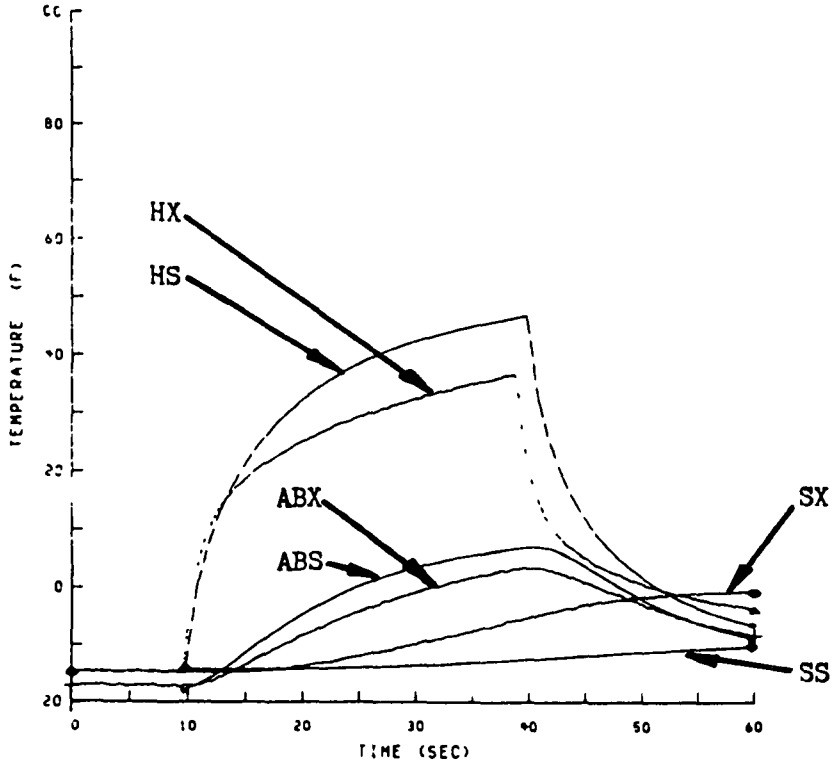

a. Position 6

T_∞ = -15 t_{on} = 30
Pz = 7.87 x_{on} = 0
h_o = 65.9 Re_x = 0

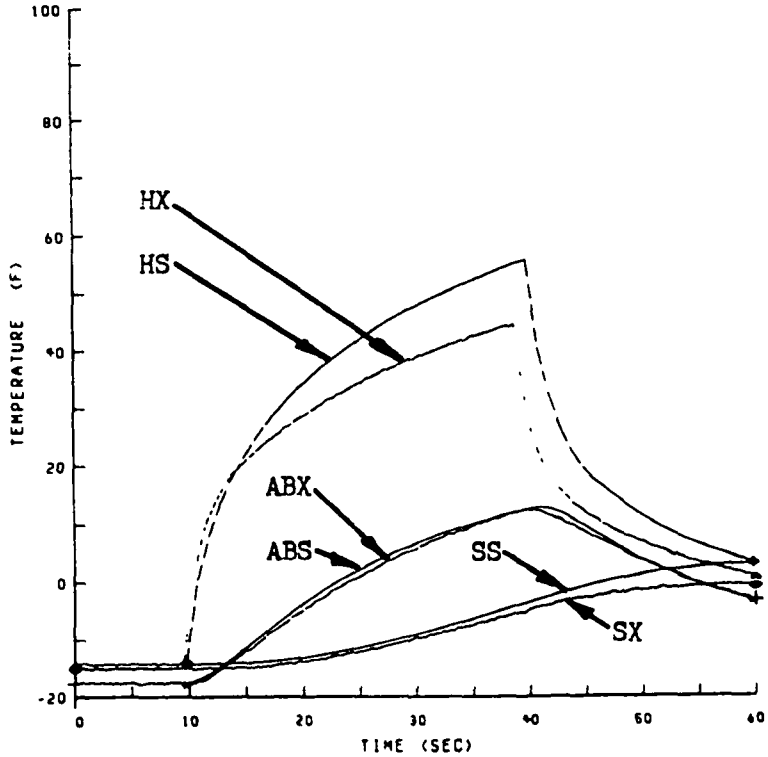

b. Position 7

T_∞ = -15 t_{on} = 30
Pz = 7.97 x_{on} = 1
h_o = 52.5 Re_x = $1.38 * 10^5$

Figure 40. Numerical and Experimental Comparison for Reading 92

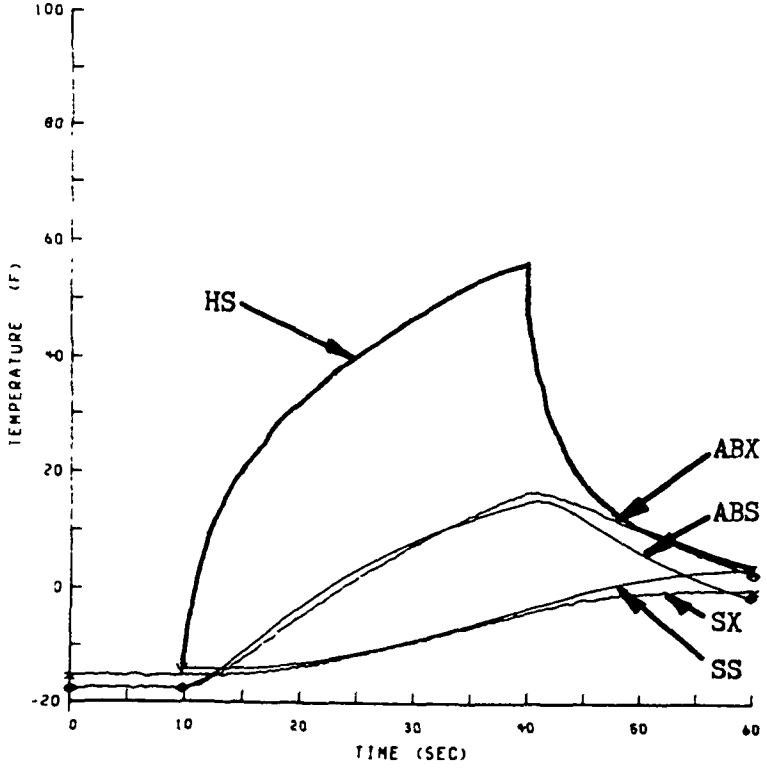

c. Position 8

T_∞ = -15 t_{on} = 30
Pz = 8.14 x_{on} = 2
h_o = 46.0 Re_x = 2.78 *10^5

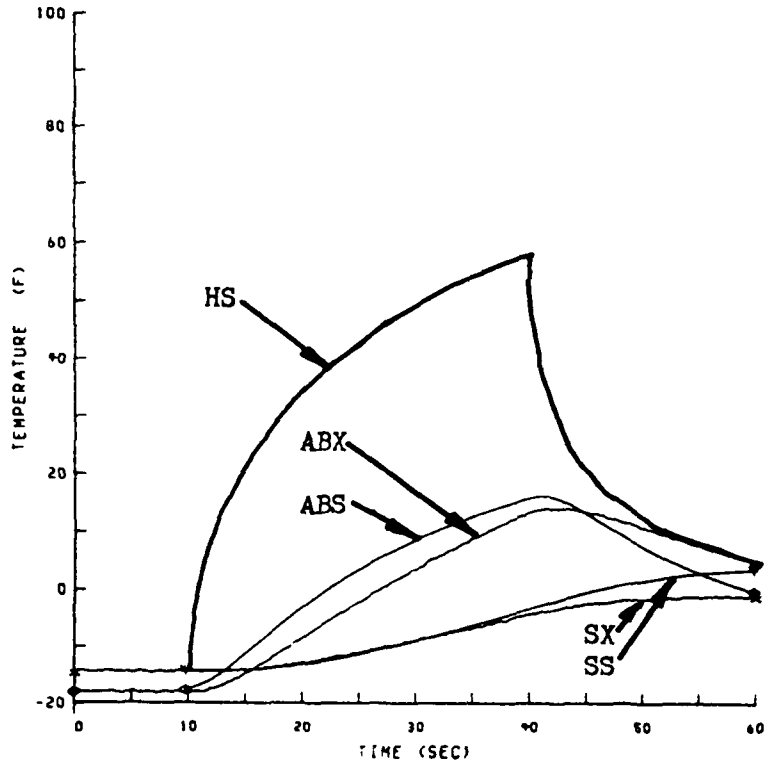

d. Position 9

T_∞ = -15 t_{on} = 30
Pz = 8.03 x_{on} = 3
h_o = 42.5 Re_x = 4.17 *10^5

Figure 40. (Reading 92 Continued)

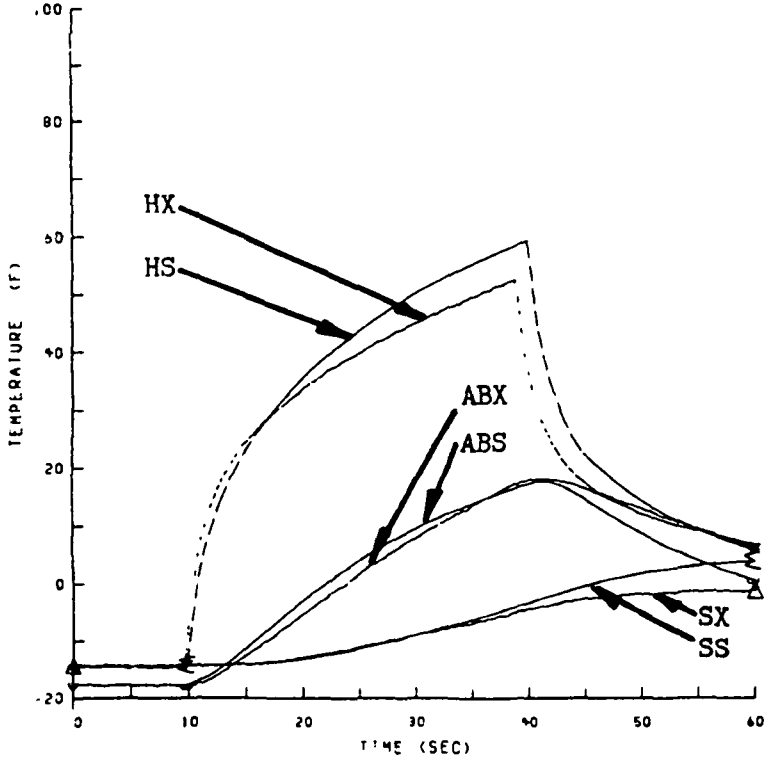

e. Position 10

T_∞ = -15
Pz = 8.20
h_o = 40.0

t_{on} = 30
x_{on} = 4
Re_x = 5.51 *10^5

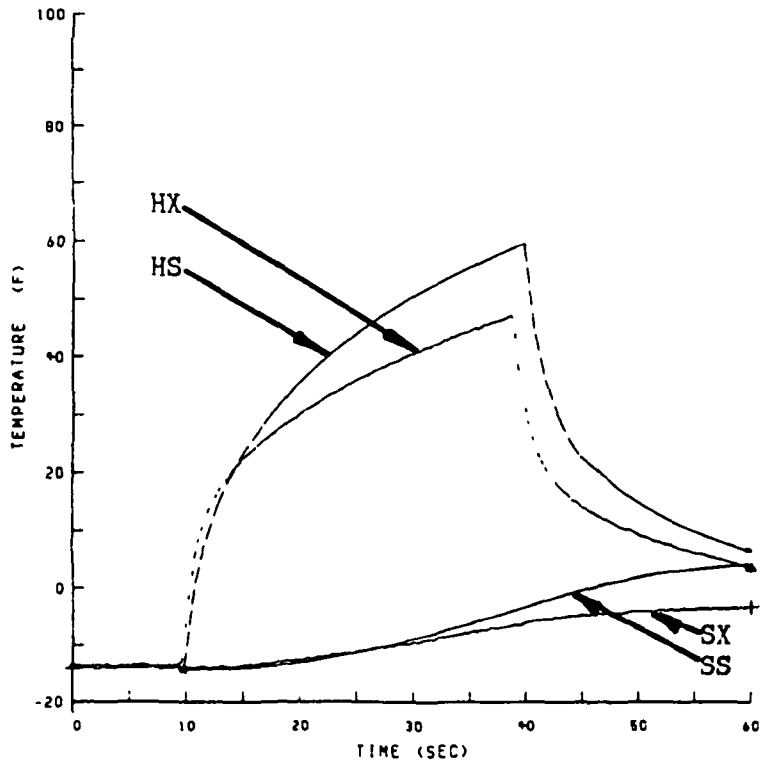

f. Position 11

T_∞ = -15
Pz = 8.20
h_o = 38.0

t_{on} = 30
x_{on} = 5
Re_x = 6.83 *10^5

Figure 40. (Reading 92 Continued)

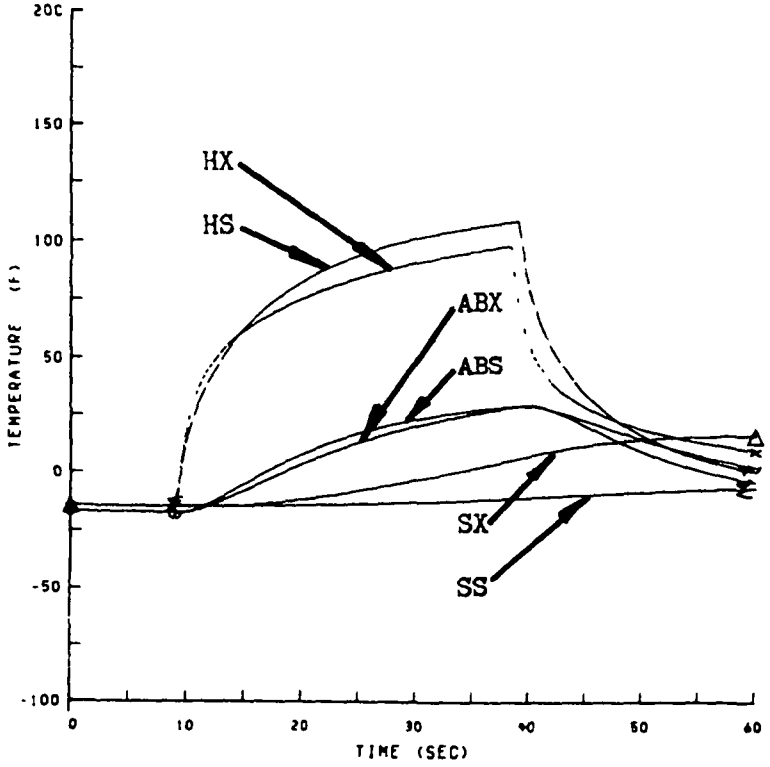

a. Position 6

T_∞ = -15 t_{on} = 30
Pz = 15.8 x_{on} = 0
h_o = 65.7 Re_x = 0

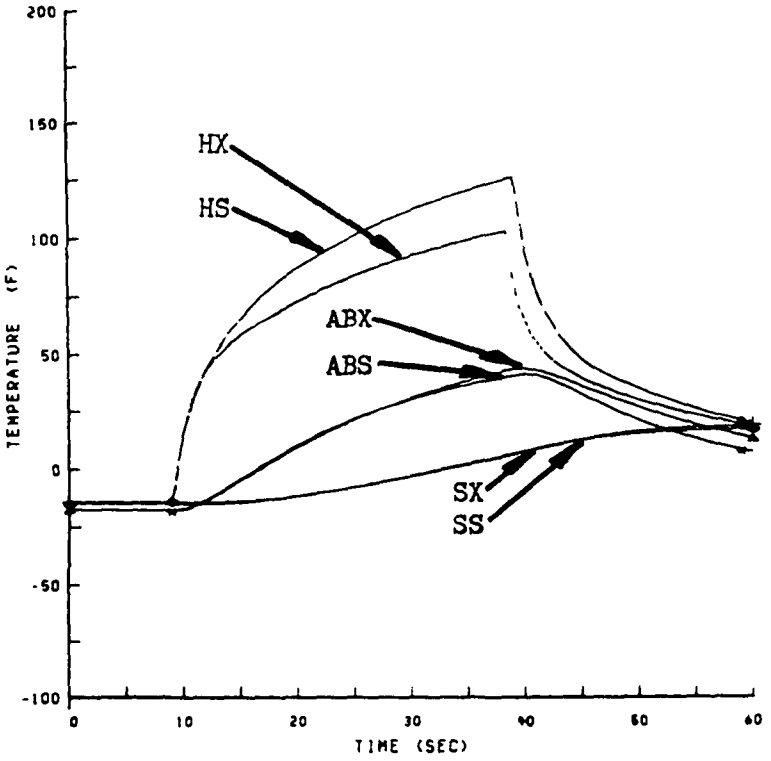

b. Position 7

T_∞ = -15 t_{on} = 30
Pz = 16.0 x_{on} = 1
h_o = 51.4 Re_x = $1.27 * 10^5$

Figure 41. Numerical and Experimental Comparison for Reading 93

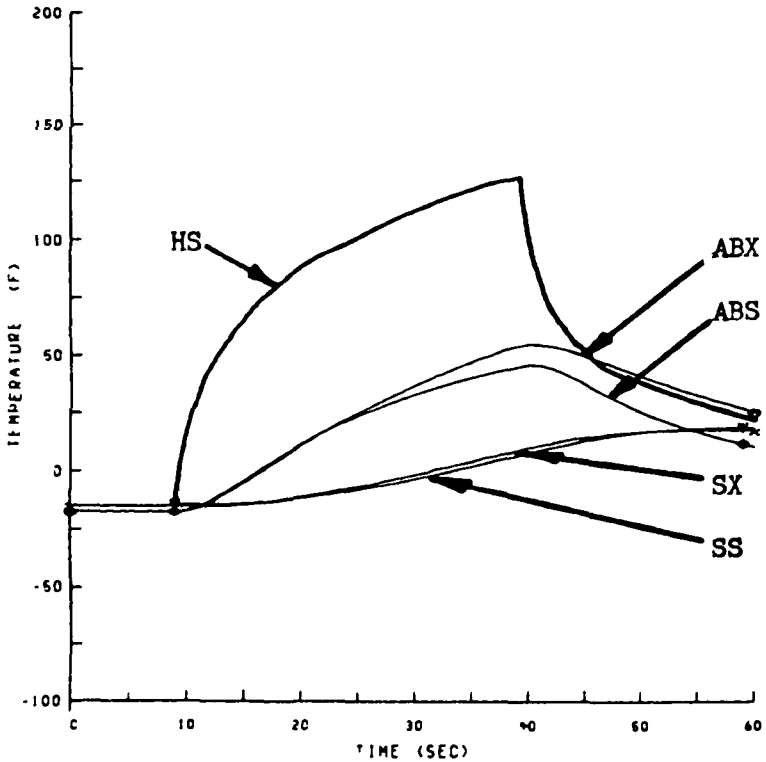

c. Position 8

T_∞ = -15
Pz = 16.3
h_o = 45.2

t_{on} = 30
x_{on} = 2
Re_x = 2.58 *10^5

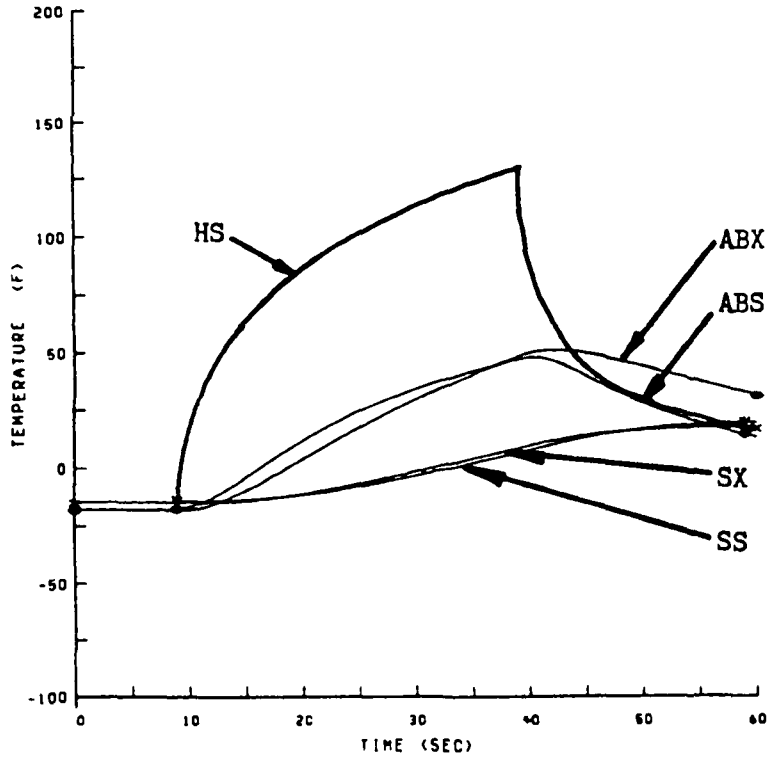

d. Position 9

T_∞ = -15
Pz = 16.1
h_o = 41.7

t_{on} = 30
x_{on} = 3
Re_x = 3.86 *10^5

Figure 41. (Reading 93 Continued)

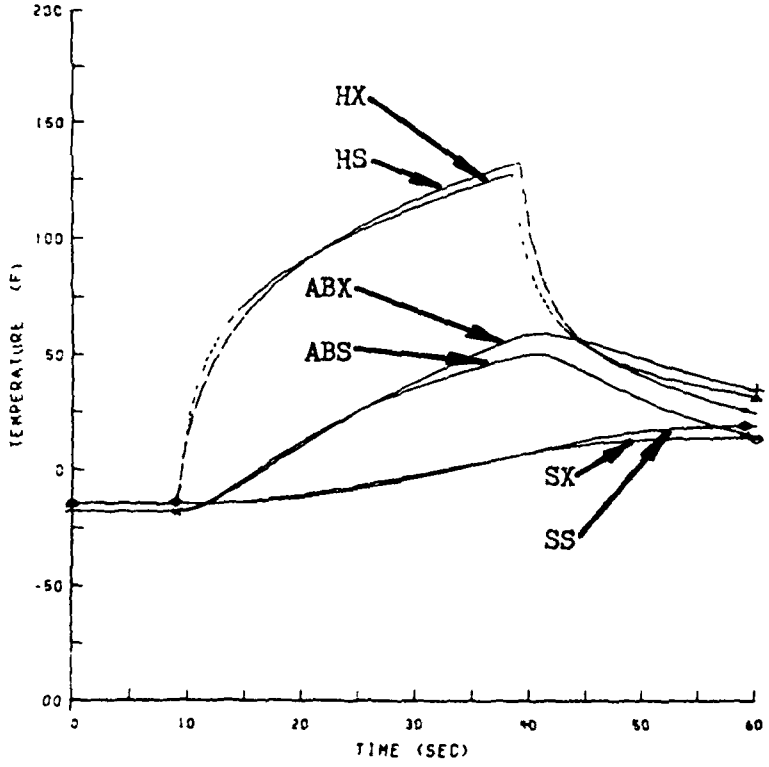

e. Position 10

T_∞ = -15 t_{on} = 30
Pz = 16.4 x_{on} = 4
h_o = 39.4 Re_x = 4.97 *10^5

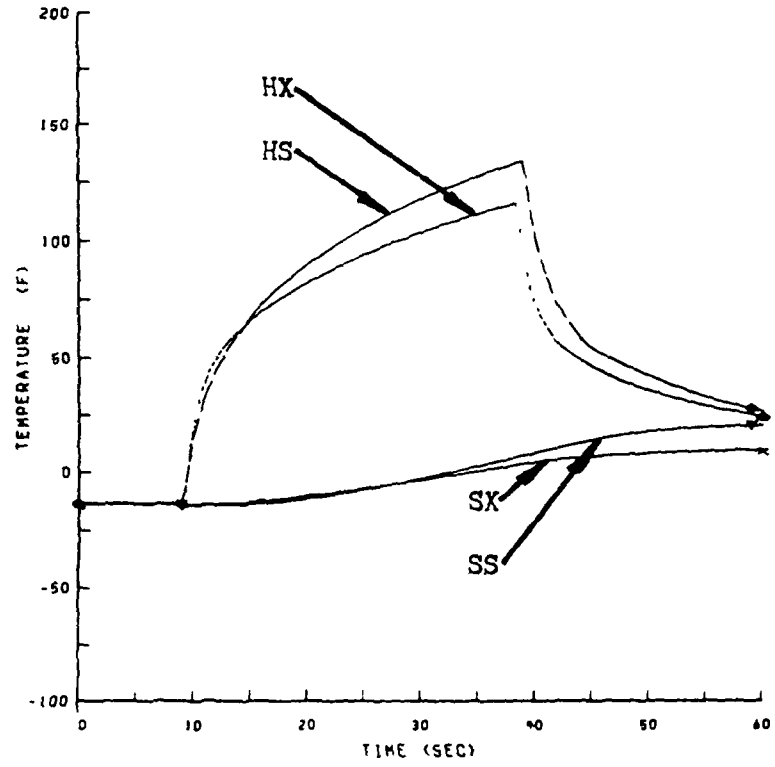

f. Position 11

T_∞ = -15 t_{on} = 30
Pz = 16.4 x_{on} = 5
h_o = 37.4 Re_x = 6.17 *10^5

Figure 41. (Reading 93 Continued)

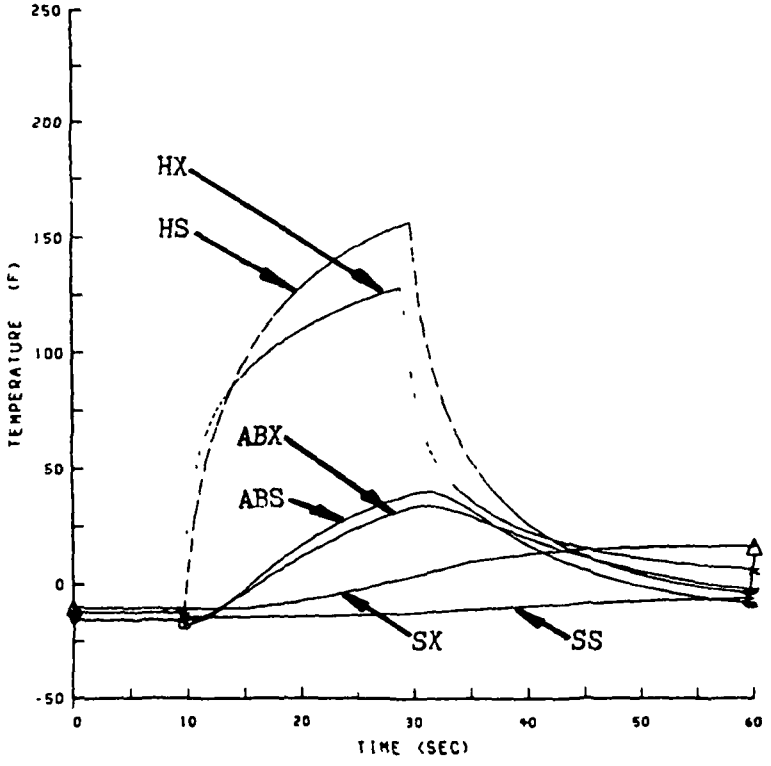

a. Position 6

T_∞ = -15 t_{on} = 20
Pz = 23.7 x_{on} = 0
h_o = 68.2 Re_x = 0

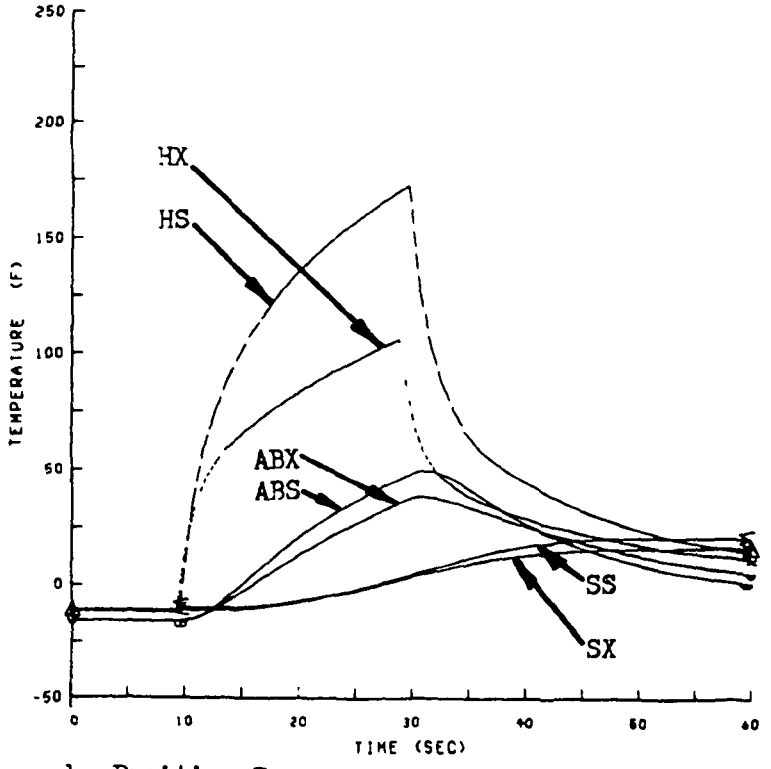

b. Position 7

T_∞ = -15 t_{on} = 20
Pz = 24.0 x_{on} = 1
h_o = 57.4 Re_x = 1.27 $*10^5$

Figure 42. Numerical and Experimental Comparison for Reading 94

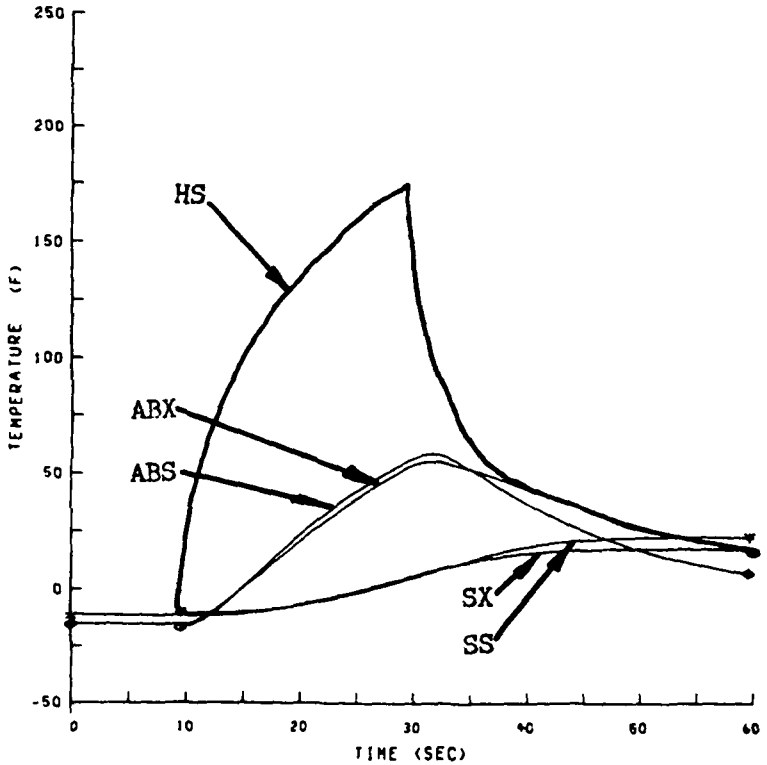

c. Position 8

T_∞ = -15 t_{on} = 20
Pz = 24.5 x = 2
h_o = 45.1 Re_x = 2.57 *10^5

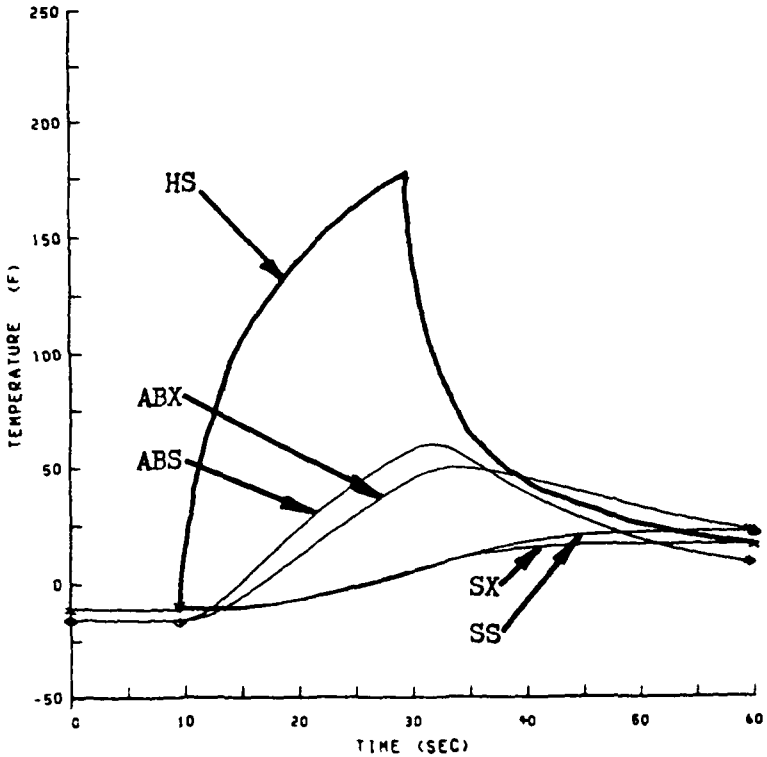

d. Position 9

T_∞ = -15 t_{on} = 20
Pz = 24.2 x = 3
h_o = 41.6 Re_x = 3.86 *10^5

Figure 42. (Reading 94 Continued)

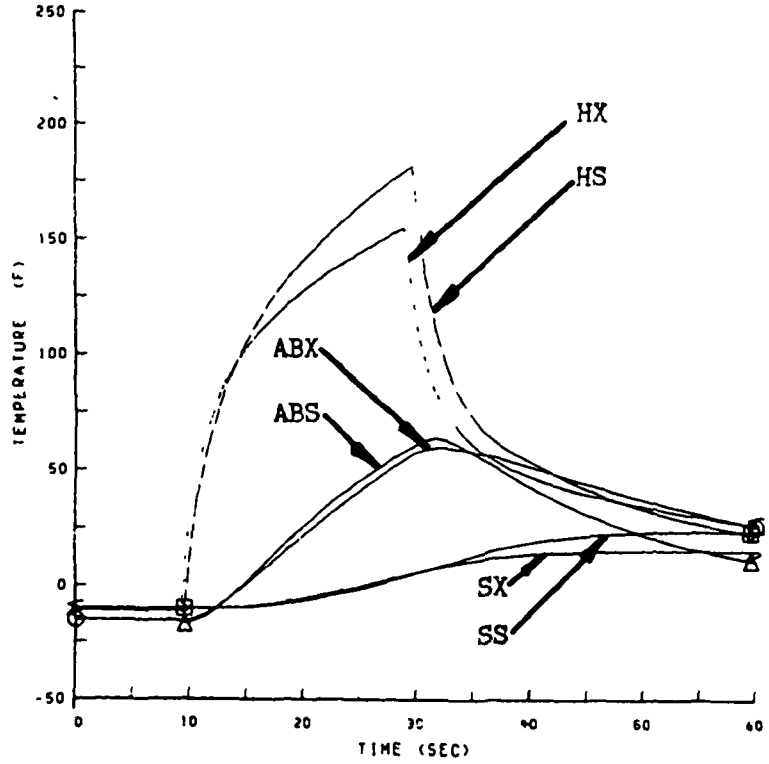

e. Position 10

T_∞ = -15
Pz = 24.7
h_o = 38.8

t_{on} = 20
x^{on} = 4
Re_x = 4.97 *10^5

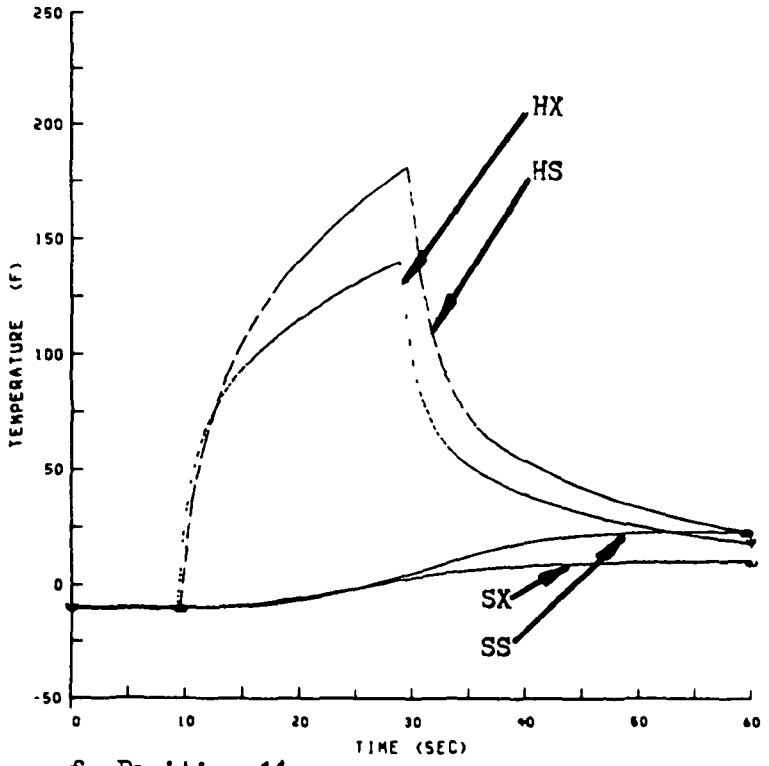

f. Position 11

T_∞ = -15
Pz = 24.7
h_o = 36.9

t_{on} = 20
x^{on} = 5
Re_x = 6.17 *10^5

Figure 42. (Reading 94 Continued)

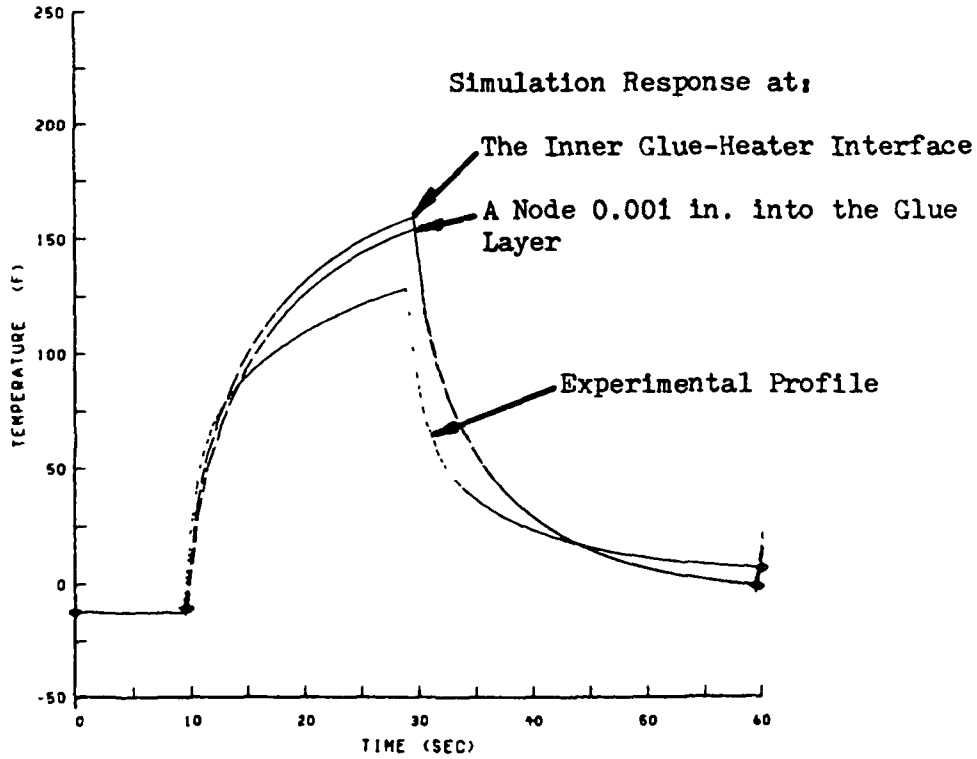

Conditions for Reading 94 at Position 6

Figure 43. Presentation of the Capton Effect

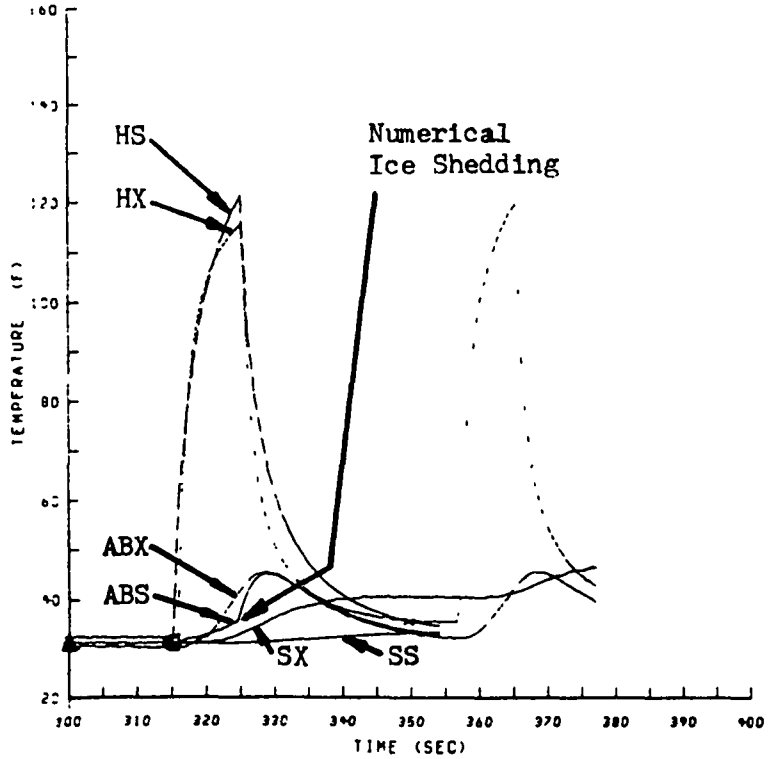

a. Position 6, First Cycle

T_∞ = 31 FT = 1/8
Pz = 15.8 DI = 5
h = 84.6 MT = $5.6 * 10^{-3}$
t^o_{on}/t_{off} = 10/30

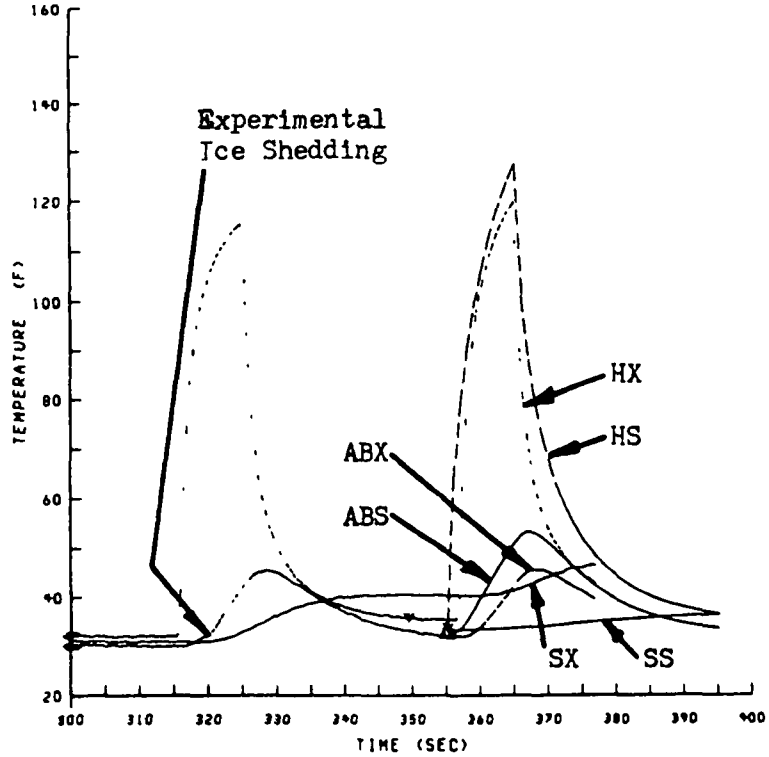

b. Position 6, Second Cycle

T_∞ = 31
Pz = 15.8
h = 84.6
t^o_{on}/t_{off} = 10/30

Figure 44. Numerical and Experimental Comparison for Reading 197

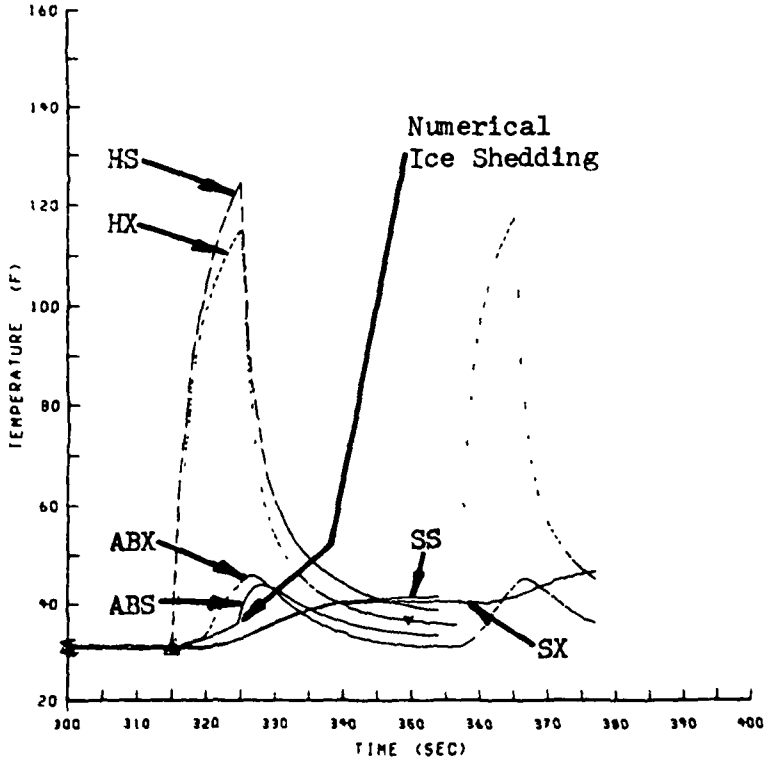

c. Position 7, First Cycle

T_∞ = 31 IT = 1/8
Pz = 16.0 DI = 5
h = 116 MT = $5.55 * 10^{-3}$
t^o_{on}/t_{off} = 10/30

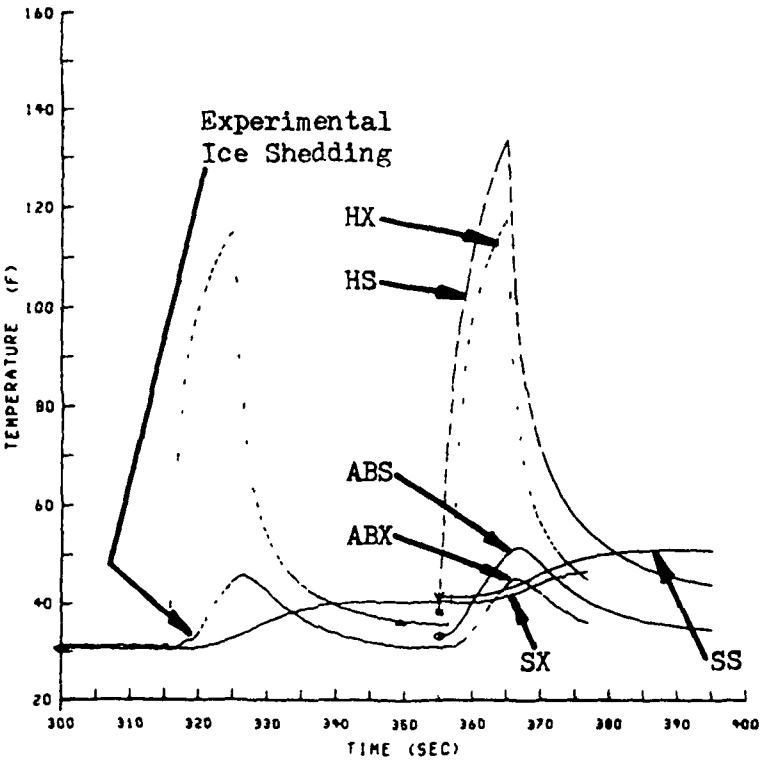

d. Position 7, Second Cycle

T_∞ = 31
Pz = 16.0
h = 116
t^o_{on}/t_{off} = 10/30

Figure 44. (Reading 197 Continued)

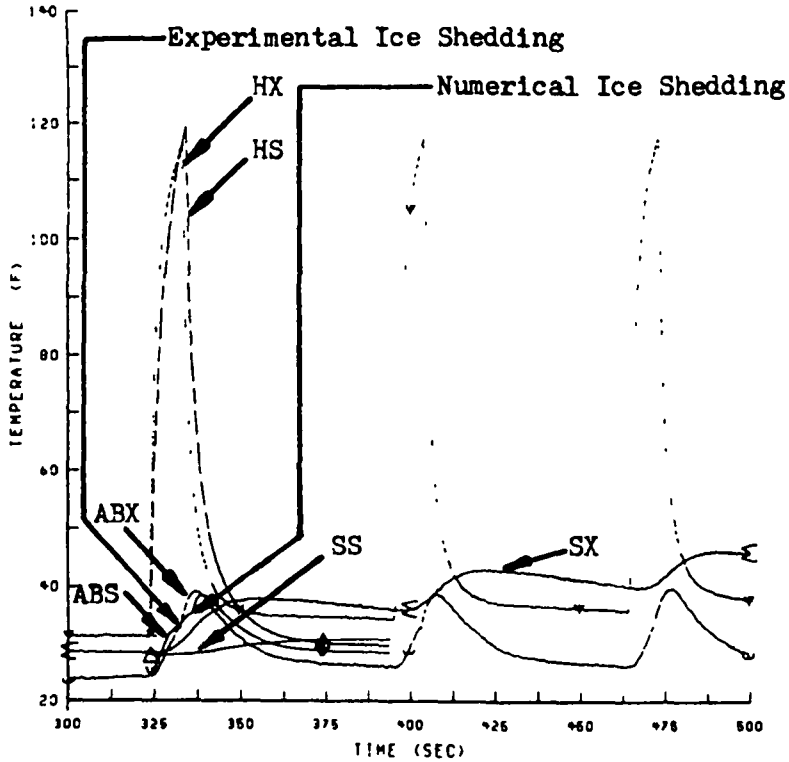

a. Position 6, First Cycle

T_∞ = 28 IT = 1/8
Pz = 15.8 DI = 5
h_o = 94.8 MT = $5.55 * 10^{-3}$
t_{on}/t_{off} = 10/60

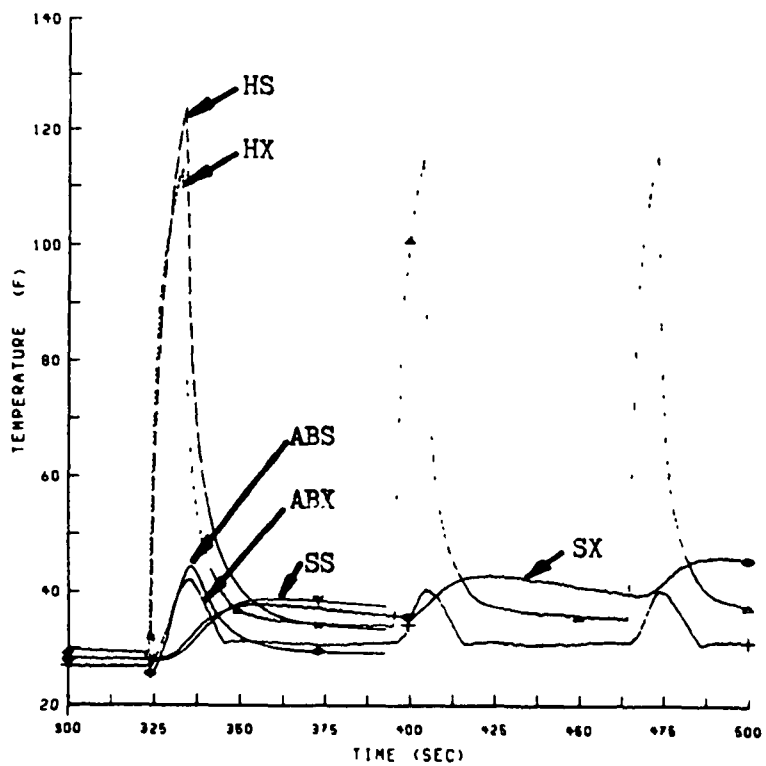

b. Position 7, First Cycle

T_∞ = 28 IT = 5/8
Pz = 16.0 DI = 1
h_o = 141 MT = 0
t_{on}/t_{off} = 10/60

Figure 45. Numerical and Experimental Comparison for Reading 209

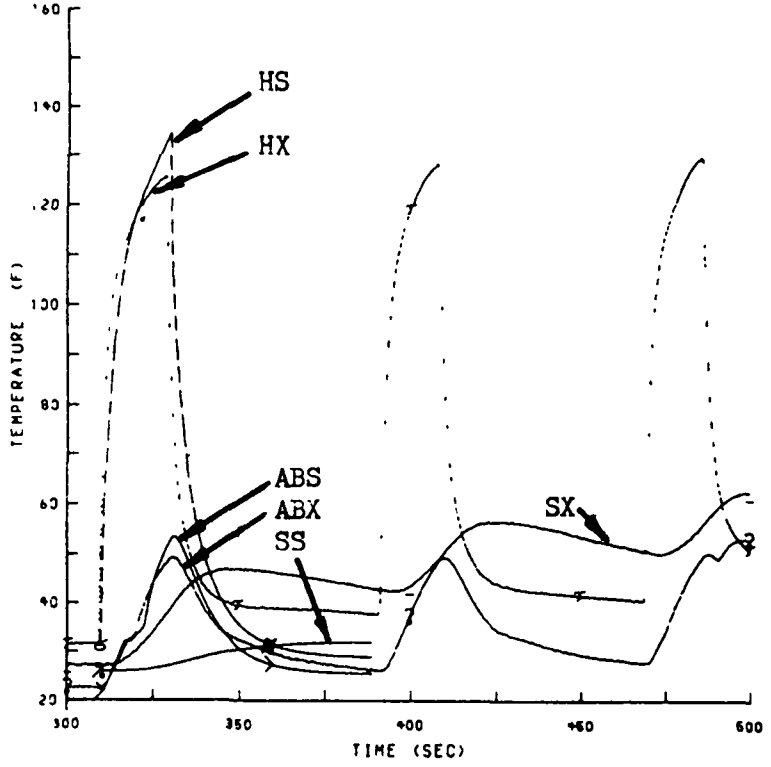

a. Position 6, First Cycle

T_∞ = 24 IT = 1/4
Pz = 15.8 DI = 2
h = 84.8 MT = $4.2 * 10^{-3}$
t_{on}^{o}/t_{off} = 20/60

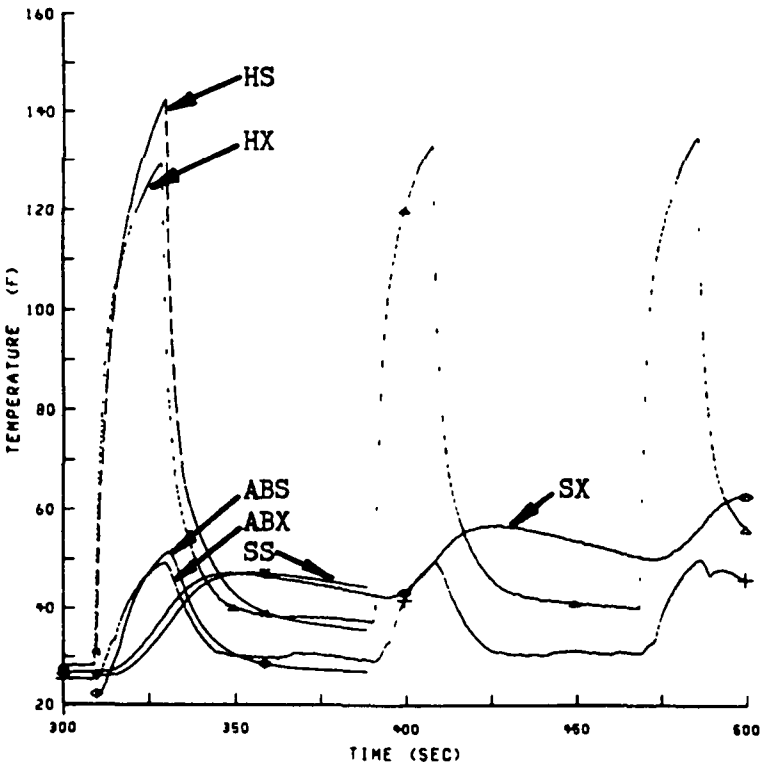

b. Position 7, First Cycle

T_∞ = 24 IT = 1/2
Pz = 16.0 DI = 1
h = 118 MT = 0
t_{on}^{o}/t_{off} = 20/60

Figure 46. Numerical and Experimental Comparison for Reading 213

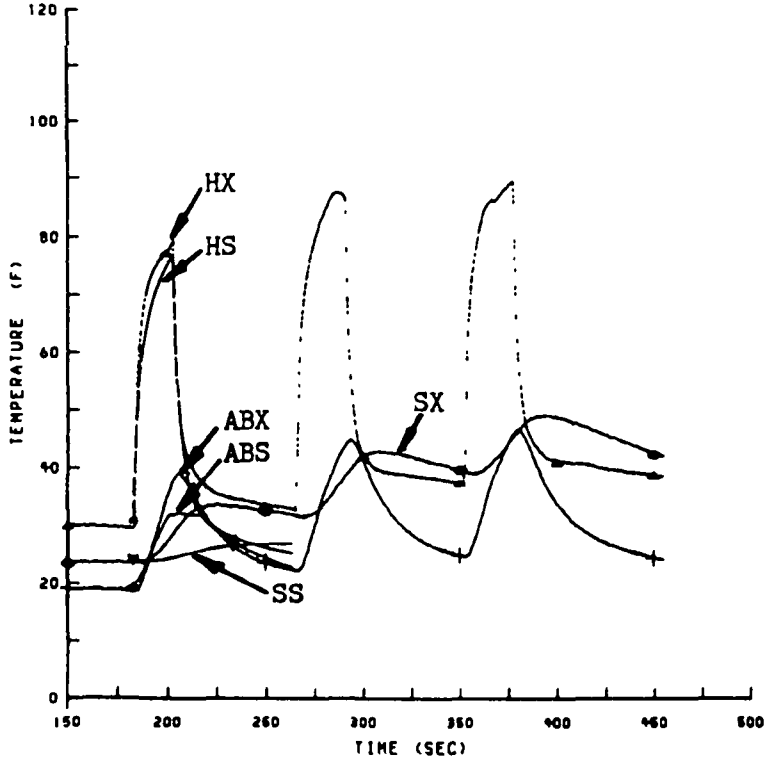

a. Position 6, First Cycle

T_∞ = 16 IT = 3/16
Pz = 7.87
h_o = 60.0
t_{on}/t_{off} = 20/60

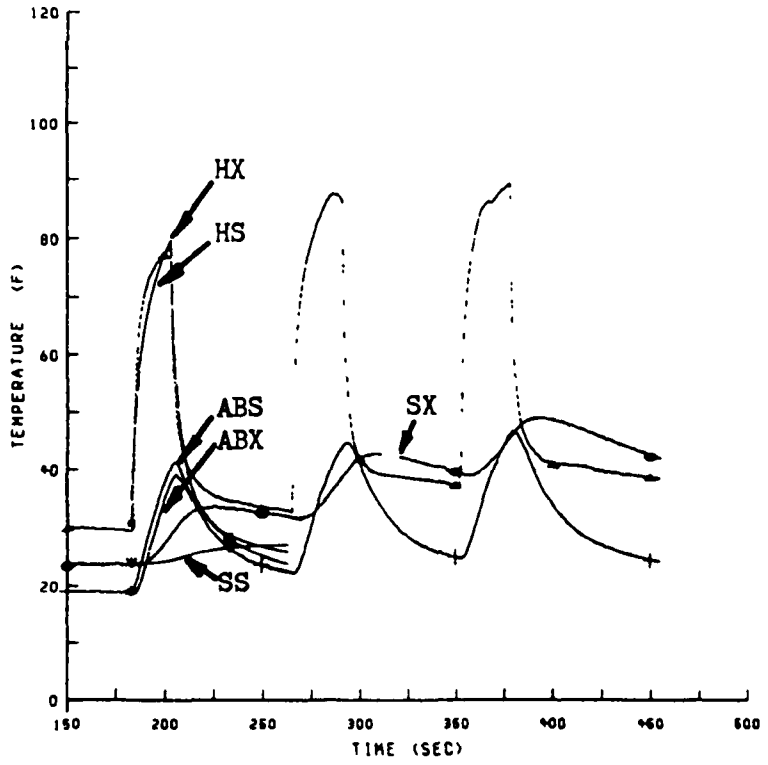

b. Position 6, First Cycle

An air gap, 0.002 in. thick, has been placed at the abrasion- ice interface in the simulation. The test conditions are the same.

Figure 47. Numerical and Experimental Comparison for Reading 234

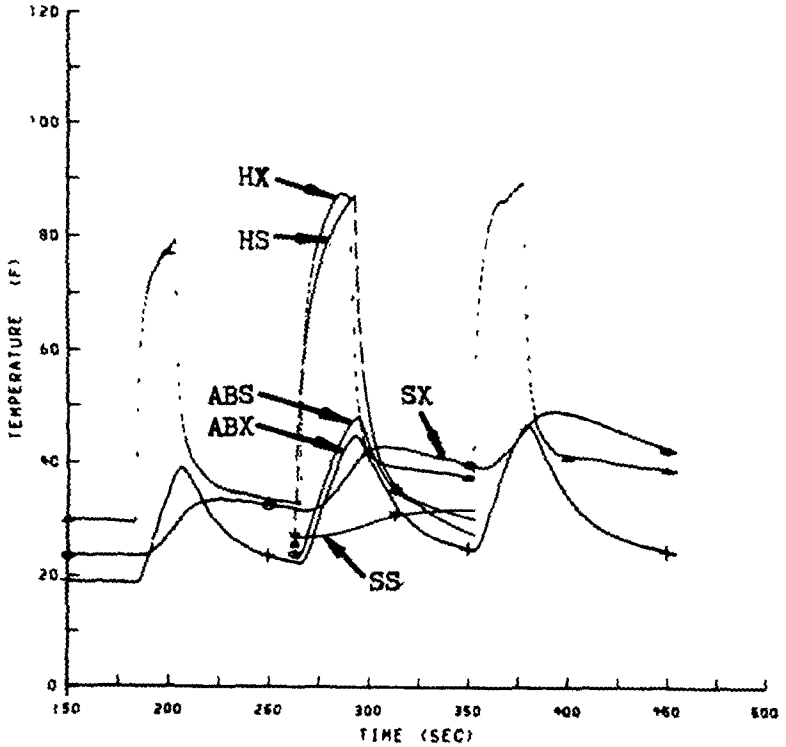

c. Position 6, Second Cycle

Same Conditions as b

t_{on}/t_{off} = 30/60

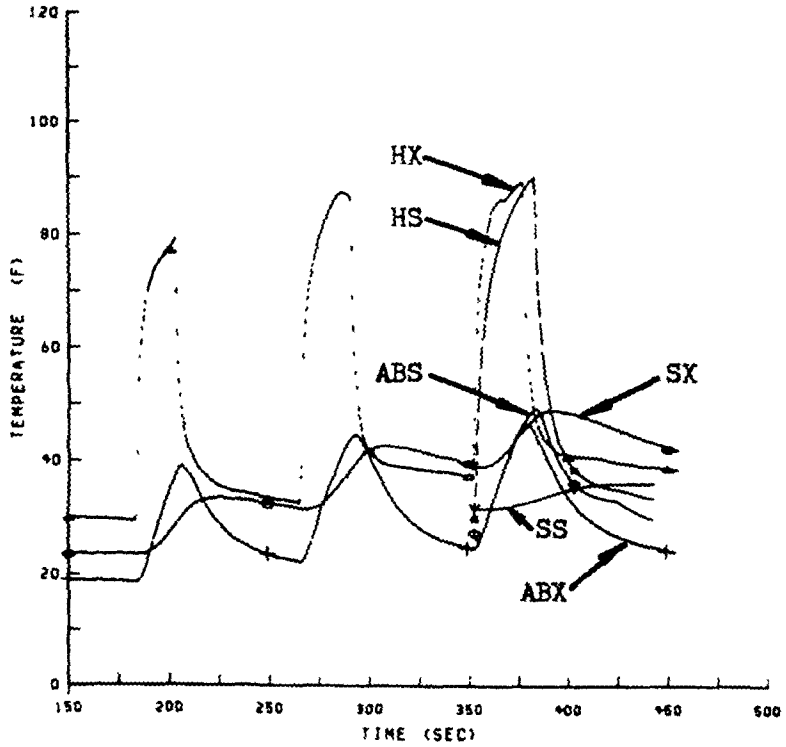

d. Position 6, Third Cycle

Same Conditions as b

t_{on}/t_{off} = 30/60

Figure 47. (Reading 234 Continued)

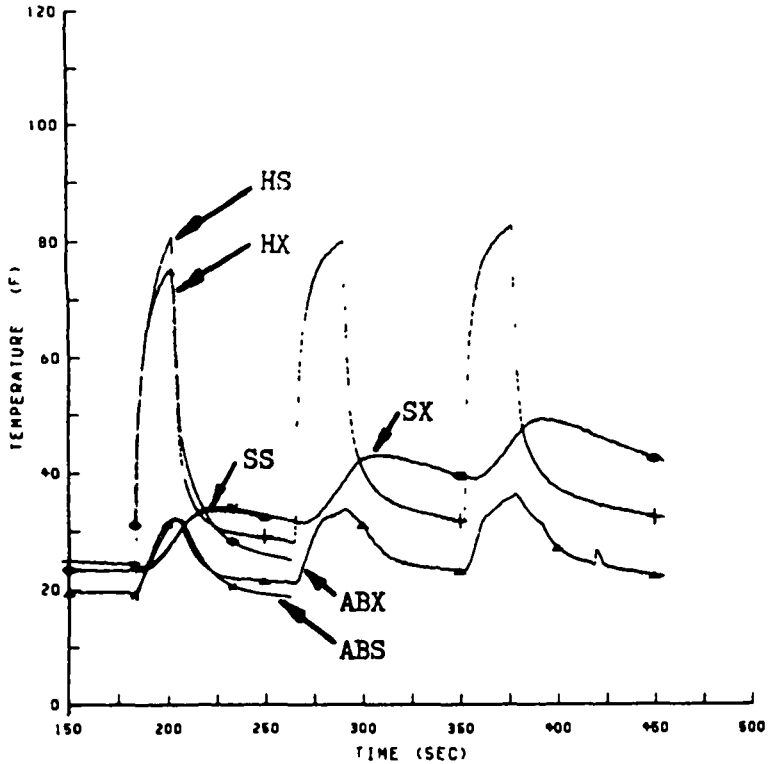

e. Position 7, First Cycle

T_∞ = 16 IT = 1/16
Pz = 7.97
h = 145
t^o_{on}/t_{off} = 20/60

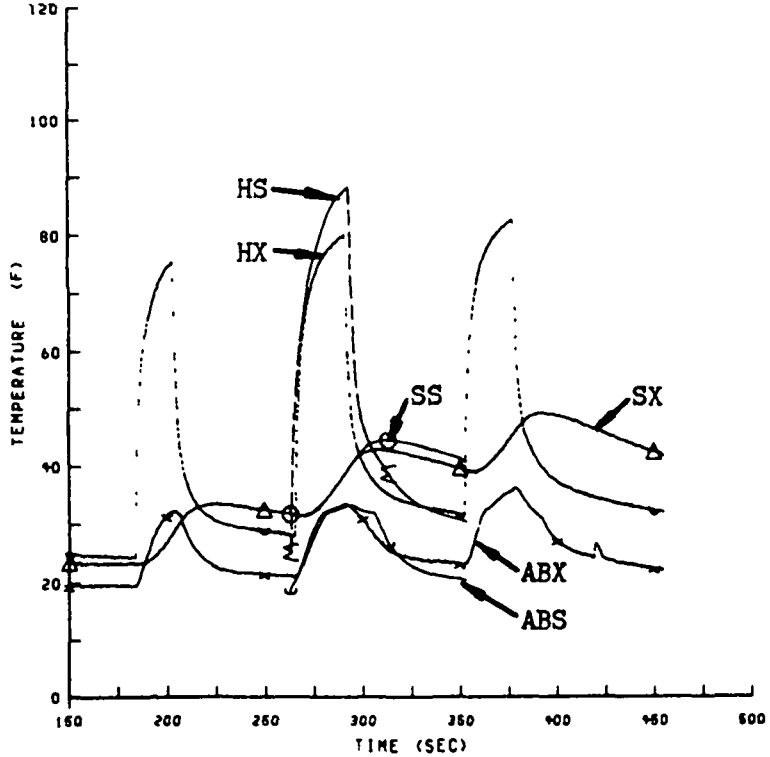

f. Position 7, Second Cycle

Same Conditions as e

t_{on}/t_{off} = 30/60

Figure 47. (Reading 234 Continued)

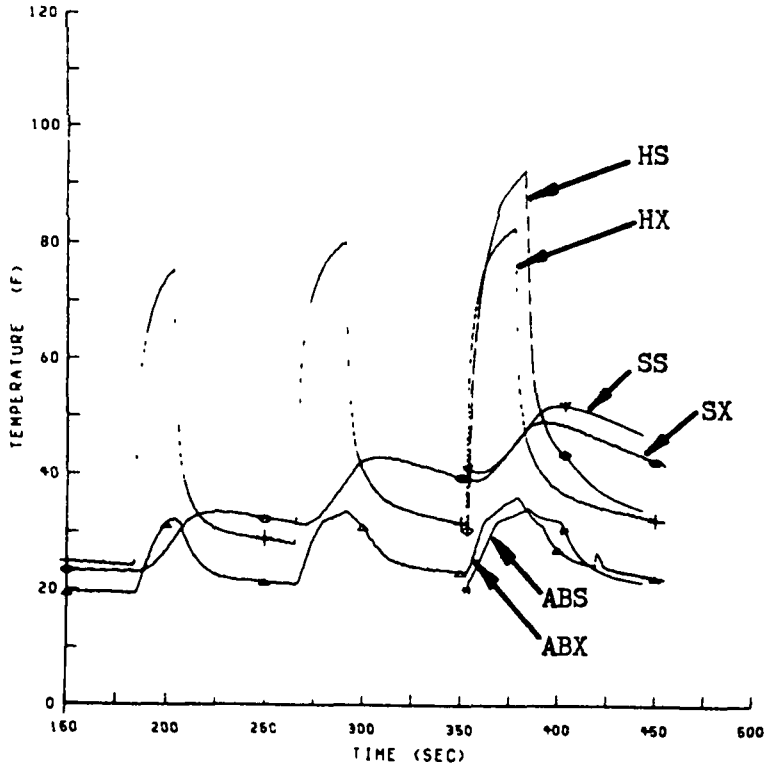

g. Position 7, Third Cycle

Same Conditions as e

t_{on}/t_{off} = 30/60

Figure 47. (Reading 234 Continued)

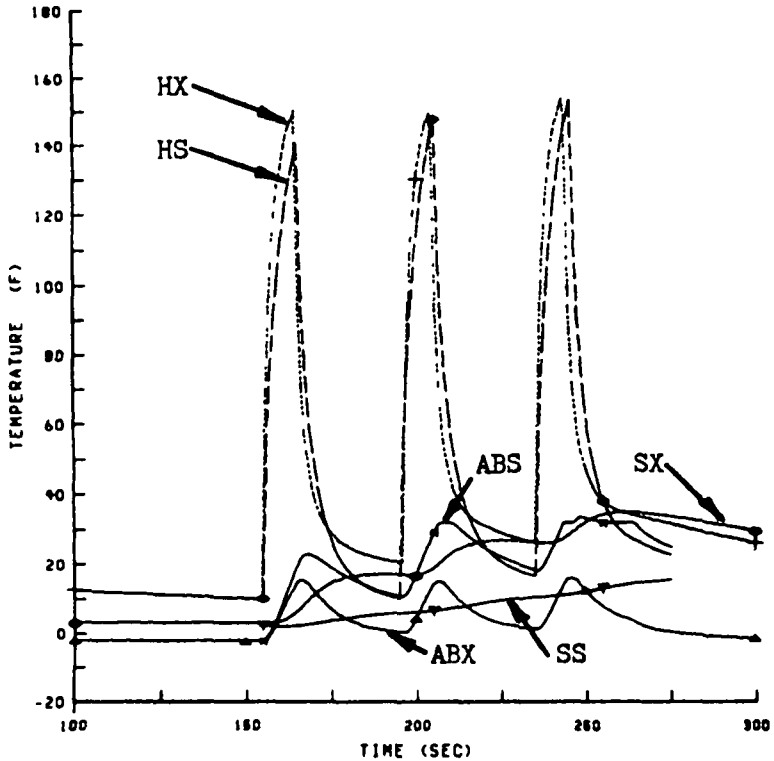

a. Position 6

T_∞ = -3 IT = 5/8
Pz = 23.7
h_o = 95.1
t_{on}/t_{off} = 10/30

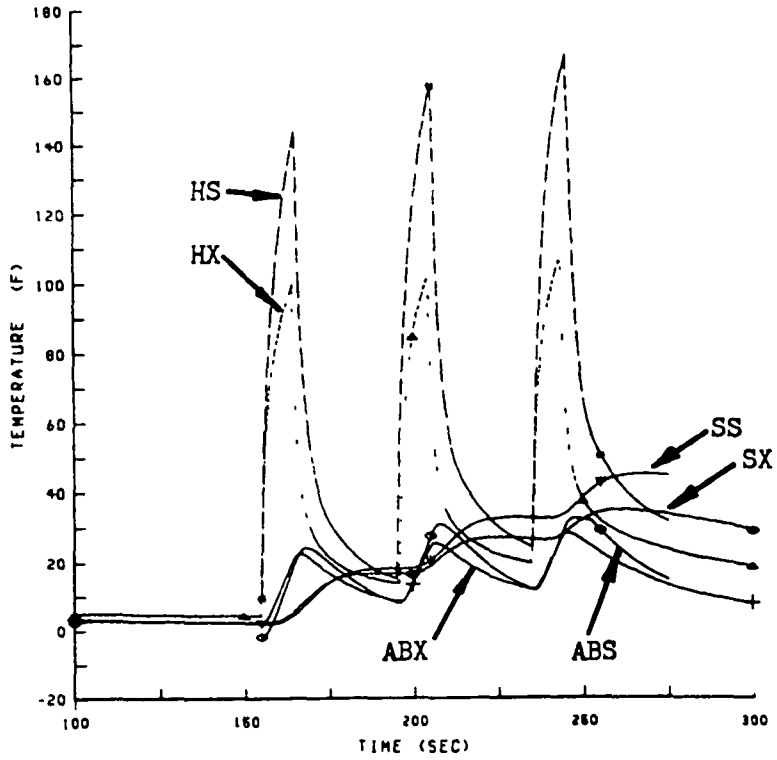

b. Position 7

T_∞ = -3 IT = 1/8
Pz = 24.0
h_o = 145
t_{on}/t_{off} = 10/30

Figure 48. Numerical and Experimental Comparison for Reading 275

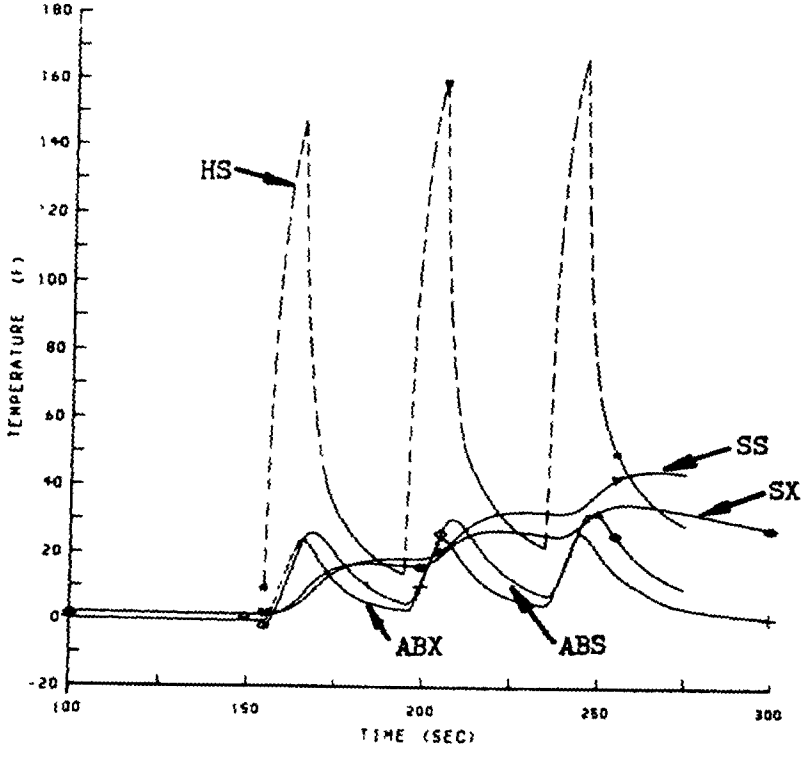

c. Position 8

T_∞ = -3 IT = 1/16
Pz = 24.5
h_o = 127
t_{on}/t_{off} = 10/30

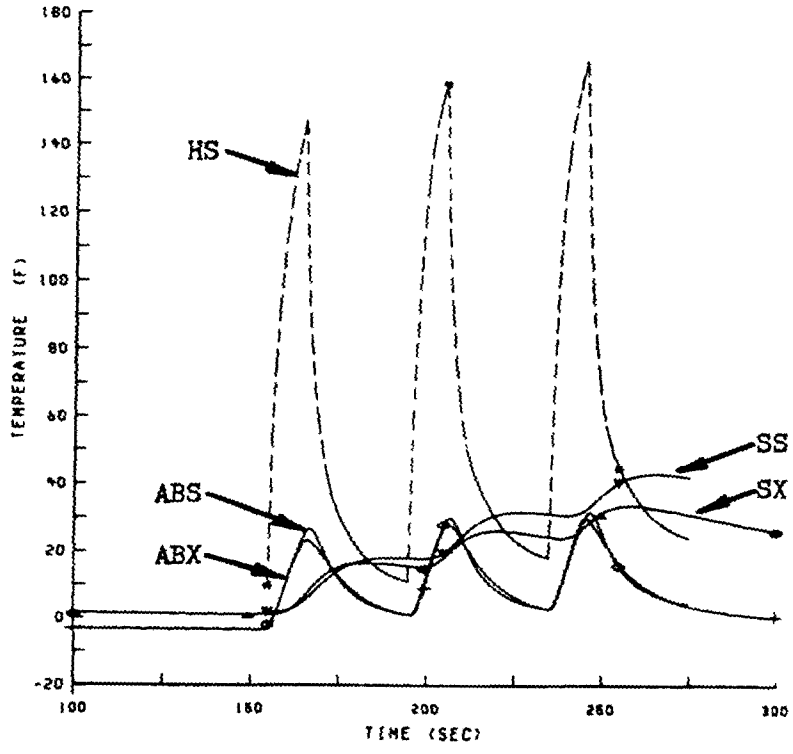

d. Position 9

T_∞ = -3 IT = 0
Pz = 24.2
h_o = 117
t_{on}/t_{off} = 10/30

Figure 48. (Reading 275 Continued)

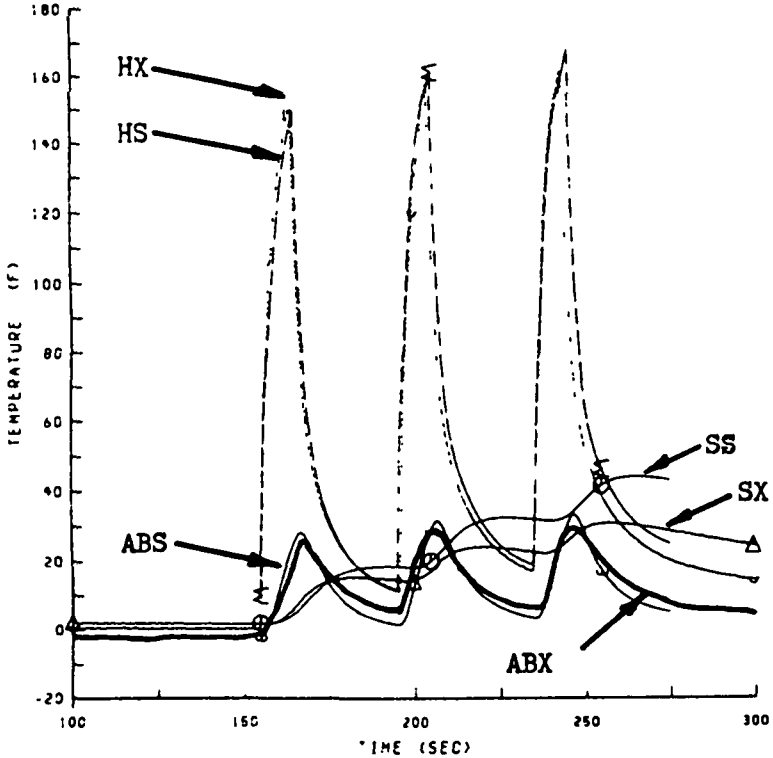

e. Position 10

T_∞ = -3 IT = 0
Pz = 24.7
h_o = 111
t_{on}/t_{off} = 10/30

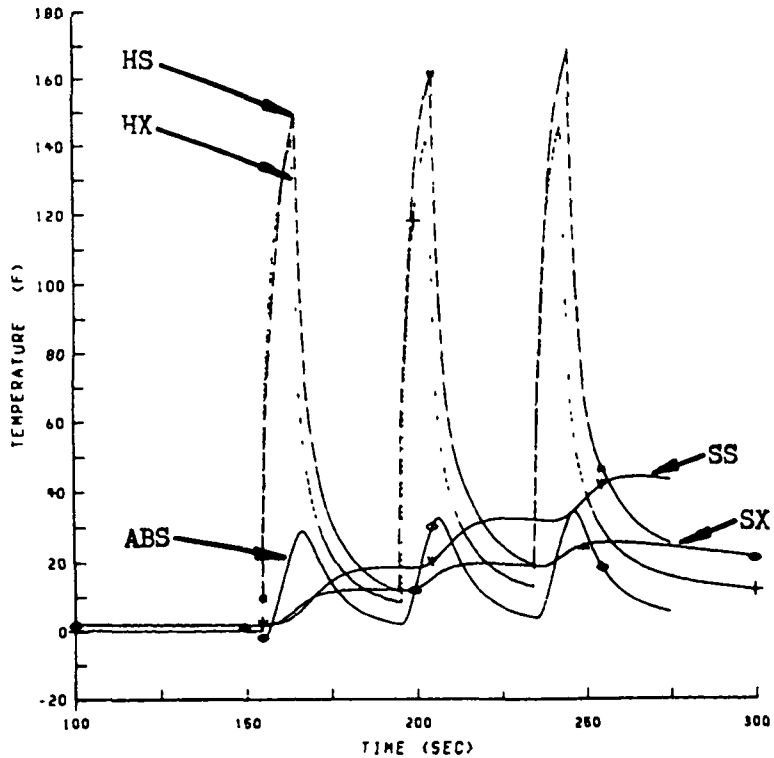

f. Position 11

T_∞ = -3 IT = 0
Pz = 24.7
h_o = 105
t_{on}/t_{off} = 10/30

Figure 48 (Reading 275 Continued)

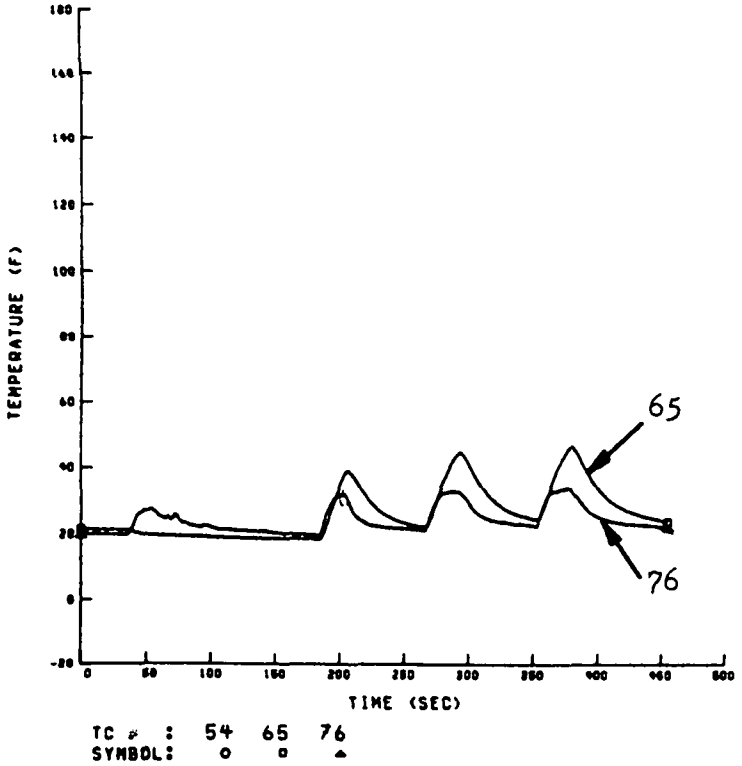

a. Position 6

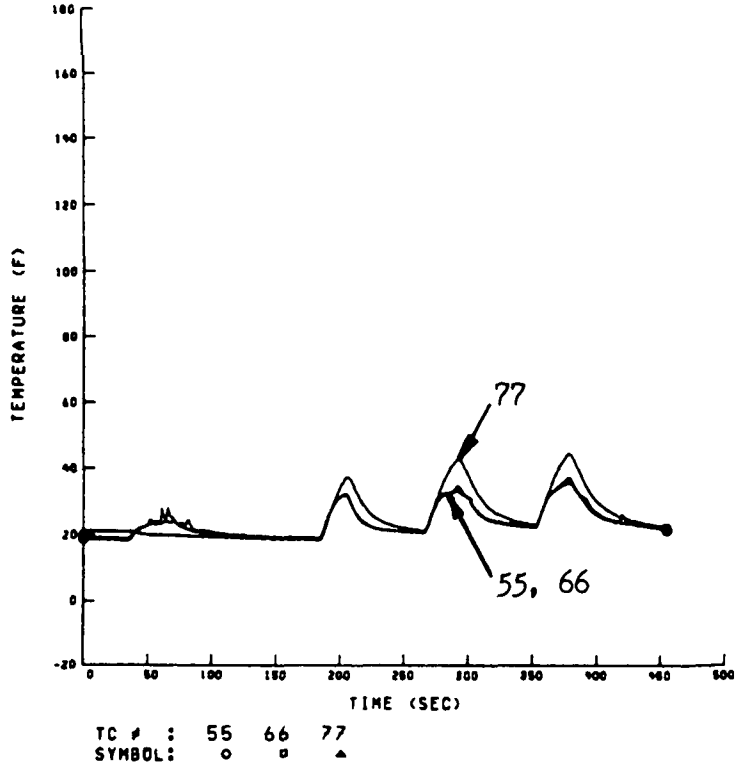

b. Position 7

Figure 49. Response of Thermocouples at Positions 6 and 7 for Reading 234

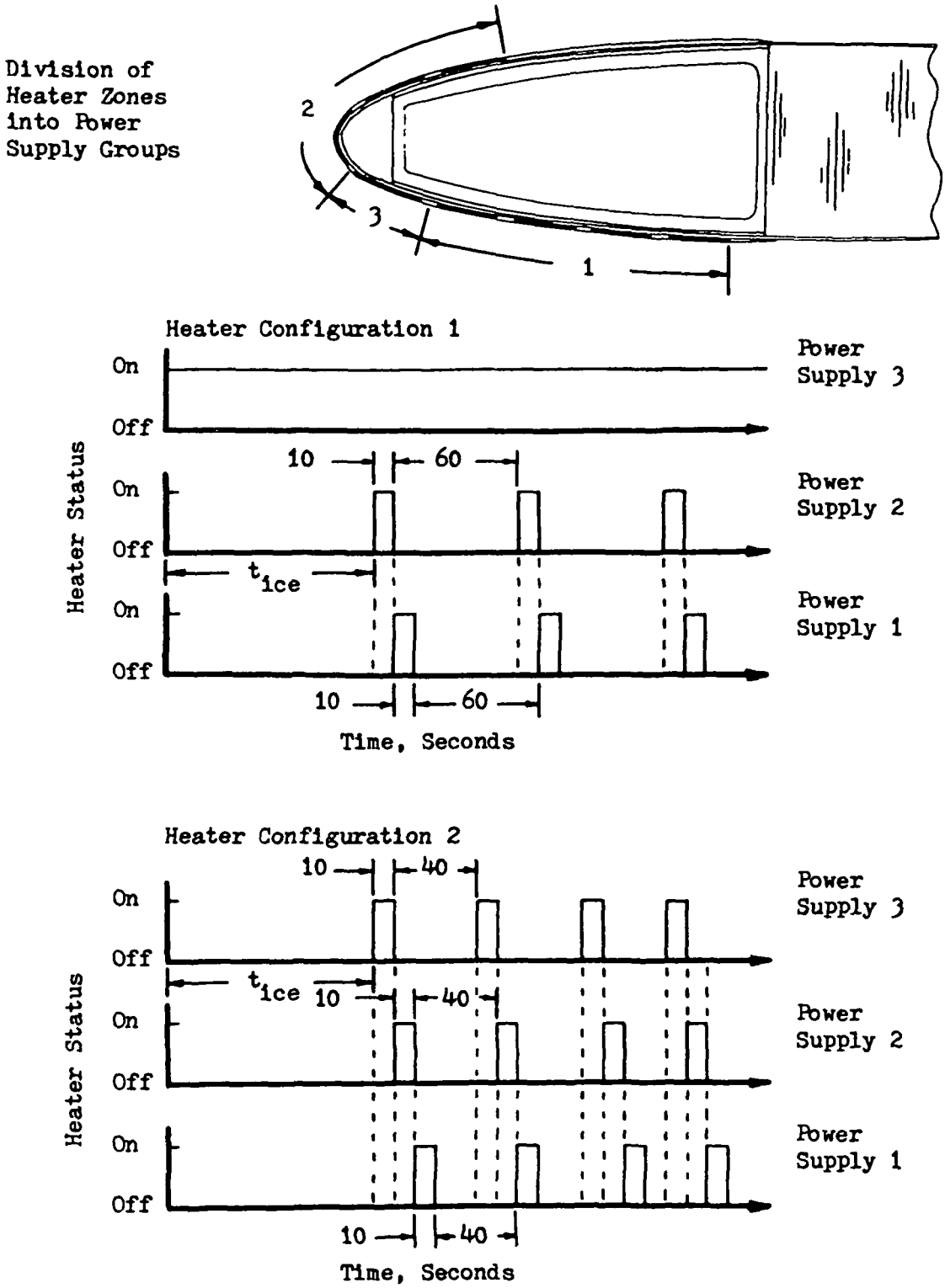

Figure 50. Phased Heater Cycling
Test Configurations

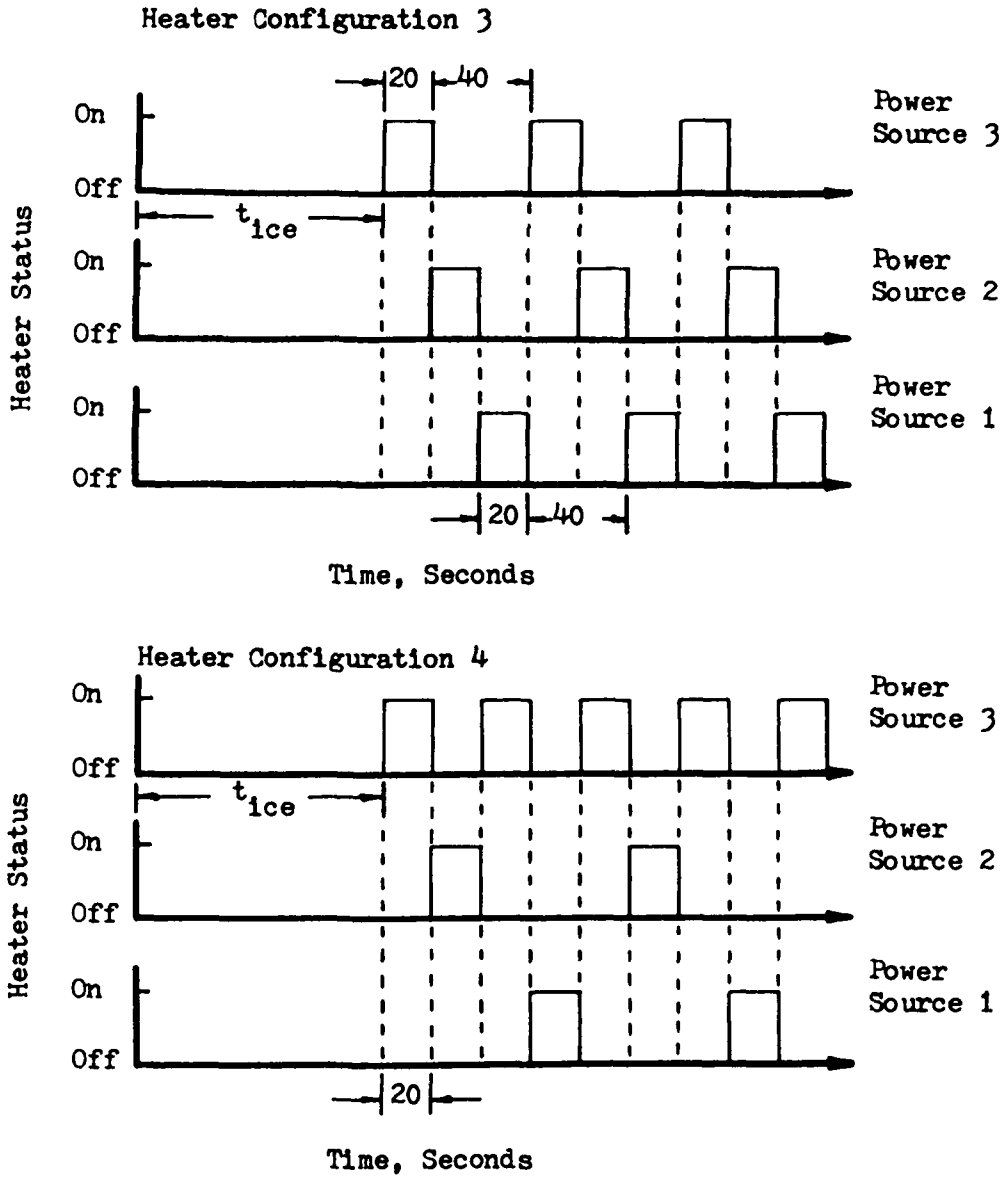

Figure 50. (Continued)

Appendix A

The Enthalpy Method simulation of a phase change process has been shown to give reliable results, as documented in Marano [1A]. However, due to the finite distance between nodes in a finite-difference formulation of a problem, the numerical results for the temperature versus time behavior of a node that undergoes a phase change may show an unrealistic response after melting begins. This will occur unless a very large number of nodes are used in the ice layer.

As illustrated in Figure 1Aa (Figure 12 of [1A]) for the abrasion shield ice interface temperature response for a deicer pad, the temperature, after it reaches 32°F, remains at 32 °F for a certain time and then oscillates after complete melting occurs. Both the plateau and the oscillation frequency are nodal dependent . This can be seen by comparing the two curves for 20 and 60 nodes in the ice layer. These oscillations are attributed to the fact that a node in the ice layer remains at the melting point for a finite period of time until the volume of ice represented by the node has entirely melted.

Voller and Cross [2A,3A] have shown, by comparing analytical and numerical solutions to simple phase change problems

using the Enthalpy Method, that the numerical solutions oscillate around the true solutions. They have also developed a criterion for determining the points of correspondence between the true and oscillating solutions. By finding these points of correspondence, accurate response curves can be obtained.

In Essence, Voller and Cross have shown that the liquid-solid interface is exactly located at the center of a node when the nodal enthalpy is Hsmp + (Hlmp - Hsmp)/2. For the ice-water system, this value is [925.63 + (9032.31)/2] = 5441.79 BTU/ft^3. By plotting the abrasion shield surface temperature at these specific times, the true solution is obtained. This procedure was used to replot the 20 and 60 node curves in Figure 1Aa, as well as to plot data for 30, 40 and 90 nodes in the ice layer. The result is shown in Figure 1Ab (Figure 13 of [1A])

To be more specific, the 90 node curve in Figure 1Ab was obtained in the following manner. At 4.9 sec., the interface node begins to melt. At 7.23 sec., the enthalpy for the second node reaches 5441.79 BTU/ft^3, meaning that the ice-water interface is exactly at the second node. The first triangle in Figure 1Ab was taken at this time, when the abrasion shield surface temperature was 36.66 °F. At 9.13 sec., the enthalpy of the third node reaches this same value, and the surface temperature at that time is plotted

as the second triangle. This procedure is repeated as time increases. As stated in Marano [1A], 30 nodes per 0.25 inches of ice was found to be the practical minimum number of nodes for sufficient accuracy.

Finally, as stated above, this temperature plateau and the succeeding oscillations can be completely eliminated by using a very large number of nodes in the ice layer. This would enable the direct program output to be plotted instead of following the procedure described in the preceeding paragraph.

1A. Marano, J. J., "Numerical Simulation of an Electrothermal De-Icer Pad", M.S. Thesis, The University of Toledo, 1982.

2A. Voller, V. and M. Cross, Int. J. Heat & Mass Trans. 24, 545, 1981.

3A. Voller, V. and M. Cross, Int. J. Heat & Mass Trans. 24, 1457, 1981.

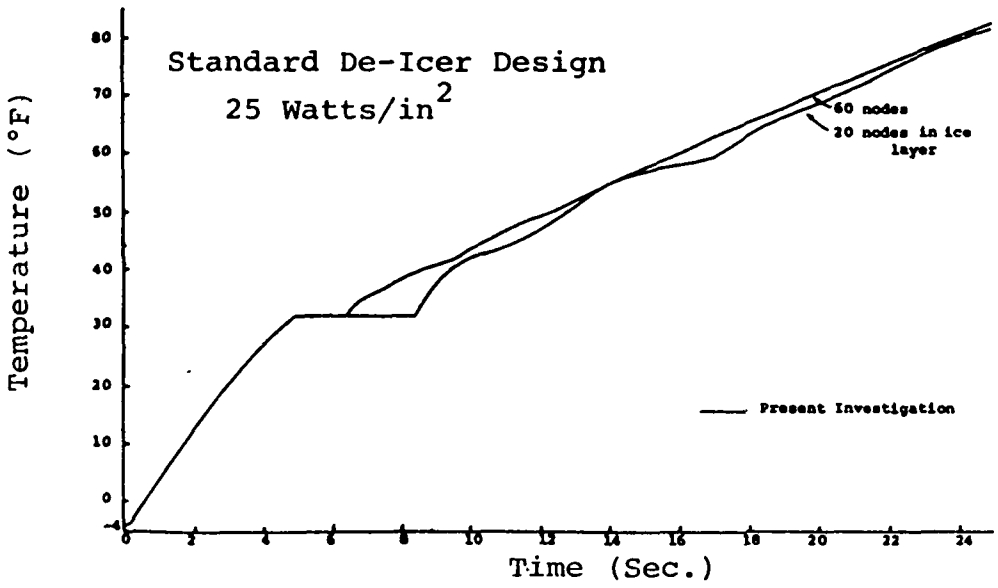

Figure 1Aa. Interface Temperature with Phase Change

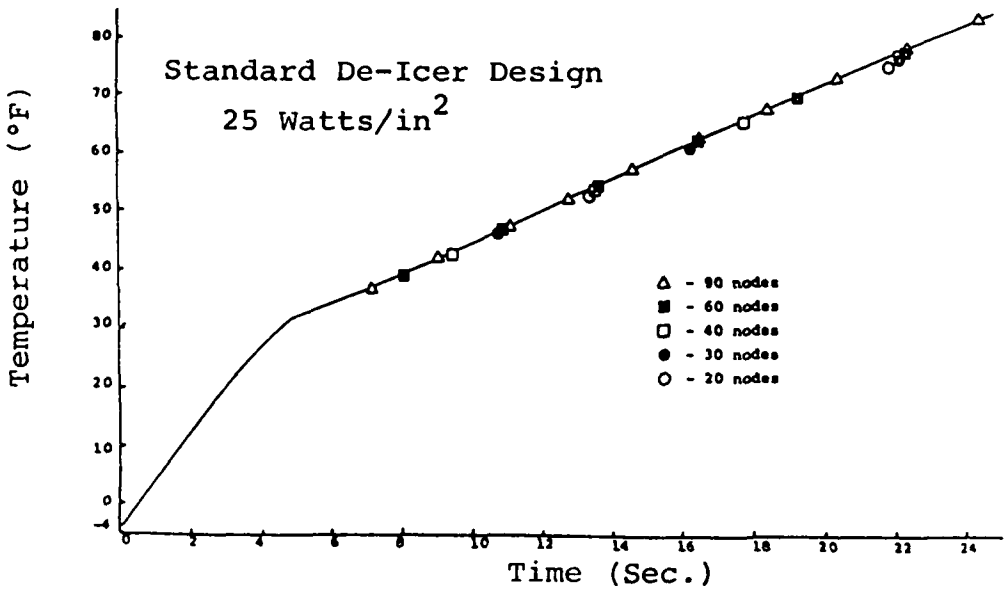

Figure 1Ab. Interface Temperature Following Plotting Method of Voller and Cross

☆U S GOVERNMENT PRINTING OFFICE 1986/646-114/20421

1 Report No.	2 Government Accession No	3 Recipient's Catalog No
NASA CR-175024		

4 Title and Subtitle	5 Report Date
A Numerical and Experimental Investigation of Electrothermal Aircraft Deicing	January 1986
	6 Performing Organization Code
7 Author(s)	8 Performing Organization Report No
Kevin L. Leffel	None
	10 Work Unit No
9 Performing Organization Name and Address	11 Contract or Grant No
The University of Toledo College of Engineering Toledo, Ohio	NAG 3-72
	13 Type of Report and Period Covered
12 Sponsoring Agency Name and Address	Contractor Report
National Aeronautics and Space Administration Washington, D.C. 20546	14 Sponsoring Agency Code 505-68-11

15 Supplementary Notes

Final report. Project Manager, Robert J. Shaw, Propulsion Systems Division, NASA Lewis Research Center, Cleveland, Ohio 44135. This report was a thesis submitted to the University of Toledo in partial fulfillment of the requirements for the degree of Master of Science in Mechanical Engineering in September 1985.

16 Abstract

This study was composed of three parts. The first part involved the extension of an existing transient two-dimensional numerical code for an electrothermal deicer so that it would simulate the situation where a variable thickness ice layer existed at the outer surface. The Enthalpy Method was used to simulate the phase change, and Gauss-Seidel iteration was used to solve the resulting system of finite difference equations. A set of criteria were developed for determining when a variable thickness ice layer had an effect on deicer performance. The second part of this study was the acquisition and analysis of experimental data. The test model was a section of a Bell UH-1H helicopter blade equipped with an electrothermal deicer manufactured by the B. F. Goodrich Company. A total of fifty-two thermocouples were utilized to document the thermal response of the blade and deicer assembly. The tests were conducted in the Icing Research Tunnel at the NASA Lewis Research Center, and consisted of four phases: dry air tests; wet air tests; ice accretion tests; and deicing tests. A total of two hundred and eleven tests were run, from which ten readings, five dry runs and five deicing runs, were selected for further analysis. This reduced set of data were examined for thermocouple response consistency and, within experimental error, the thermocouple readings were found to be independent of the three cross-sections on the blade where measurements were taken. The dry run temperature responses at the abrasion shield showed test independence when correlated as $\Delta T/(\Delta T)avg$ versus position. For both the dry and the deicing runs, the heater response, when correlated in the same manner, showed test independence for all ten runs. This behavior was a physical characteristic of the blade. In contrast, the response of the D-spar thermocouples was found to be almost entirely independent of position within each test. In the deicing runs, the experimental temperature response data clearly showed when melting, shedding or refreezing occurred. These tests illustrated that the criterion for shedding in the three cases where it did occur was that the abrasion shield interface temperature was 32-34 °F. The third part of this study concerned the validation of a one-dimensional transient thermal model of an electrothermal deicer by comparison of the predictions with the experimental data. The Enthalpy Method was found to effectively model the phase change which occurred, and the ice shedding algorithm employed in the simulation was also evaluated. In general, the one-dimensional code showed good comparison with the experimental data, with the comparisons being better at the higher free-stream temperatures.

17 Key Words (Suggested by Author(s))	18 Distribution Statement
Aircraft icing; Electrothermal deicing; Computer analysis	Unclassified - unlimited STAR Category 03

19 Security Classif (of this report)	20 Security Classif (of this page)	21 No of pages	22 Price*
Unclassified	Unclassified	266	A12

*For sale by the National Technical Information Service, Springfield, Virginia 22161